Synthesis and characterization of highly non-stoichiometric garnet oxides

Weiwei Cao

UNIVERSITÉ D'ORLÉANS

ÉCOLE DOCTORALE ÉNERGIE MATÉRIAUX SCIENCES DE LA TERRE ET DE L'UNIVERS

CEMHT-CNRS

THÈSE présentée par :

Weiwei CAO

soutenue le : **16 Décembre 2021**

pour obtenir le grade de : **Docteur de l'Université d'Orléans**

Discipline/ Spécialité : Chimie

Synthesis and characterization of highly non-stoichiometric garnet oxides

THÈSE dirigée par :

M. Mathieu Allix	Directeur de Recherche, CEMHTI CNRS
M. Michael J. Pitcher	Chargé de Recherche, CEMHTI CNRS

RAPPORTEURS :

Mme. Veronique Jubera	Maître de Conf. HDR, ICMCB Université de Bordeaux
Mme. Marie Colmont	Maître de Conf. HDR, UCCS Université de Lille

---

JURY :

Mme. Ana Isabel Becerro	Président du jury, Directeur de Recherche, CSIC, Materials Science Instituto of Seville
Mme. Veronique Jubera	Maître de Conf. HDR, ICMCB Université de Bordeaux
Mme. Marie Colmont	Maître de Conf. HDR, UCCS Université de Lille
M. Mathieu Allix	Directeur de Recherche, CEMHTI CNRS
M. Michael J. Pitcher	Chargé de Recherche, CEMHTI CNRS
Mme. Cécile Genevois	Ingénieure de Recherche, CEMHTI CNRS
M. Jianqiang Li	Professeur, University of Science and Technology Beijing

Acknowledgements

Many thanks to CSC (China Scholarship Council) for giving me three-year financial support, and many thanks to CNRS (Centre National de la Recherche Scientifique) for the last-stage financial support and its hosting through my PhD studies.

I'd like to thank the reviewers, Véronique Jubera (ICMCB, Bordeaux) and Marie Colmont (UCCS, Lille), and the examiners Ana Isabel Becerro (ICMS, Spain) and Jianqiang Li (USTB, China) for accepting to review my work.

I'd like to express my deep and sincere gratitude to my supervisors Mathieu Allix and Michael Pitcher who were positive to my questions on my project, showed their willing for discussion and shared their perspectives, I thank their professional and patient guidance during my 39-month study, and give me space to conduct the experiments and the space to expand the knowledge on the area of inorganic oxides, allowing me to have deeper understanding in this project and in related scientific questions. I also appreciate Mathieu Allix's help with easing the communication on this project, Michael Pitcher's guidance on Structural refinement for the YAG samples and many of their other kind actions. I would also like to sincerely thank Cécile Genevois for her dedicated conduction of the STEM measurements and analysis of the STEM results, and always welcoming my questions, and Emanuel Véron who helped me a lot to conduct the XRD and SEM measurements, and gave me sincere help and encouragement, Ida Di Carlo (ISTO lab) who conducted the microprobe measurements. My thanks also go to Ana Isabel Becerro who conducted the luminescence measurements and analyzing the data, and Victor Castaing together with Ana who conducted the luminescence measurements on YAG disks and data analysis. I also thank Pierre Florian for conducting the NMR measurements, Franck Fayon for performing the structural simulations, Didier Zanghi and Louis Hennet for arranging the EXAFS measurements, and also Alessio Zandonà and Aurélien Canizarès who helped me with Raman measurements.

I'd also like to acknowledge the help from Argonne laboratory (USA) for conducting the synchrotron X-ray powder diffraction (SPD) measurements and Synchrotron Soleil for conducting the EXAFS measurements. I thank Marina Licheron and Vincent Sarou-Kanian for teaching me how to conduct cooling experiment on the aerodynamic levitation apparatus. I thank Sandra Ory, Sévrine Brassamin and Rachelle Omnée for helping with experimental supplies and for their warming regards. I am grateful to all the members in our CERAM group for giving me moral help and support.

Scientific production

Patent

Ceramic material with garnet structure showing a nonstoichiometry, synthesis and uses thereof. ALLIX Mathieu, BECERRO Isabel Ana, *CAO Weiwei* and PITCHER Michael. European patent (2021) n° EP21305159.2.

Publications

1. **Extended B-Site Vacancy Content Range and Cation Ordering in Twinned Hexagonal Perovskites $Ba_8Cr_{4-x}Ta_{4+0.6x}O_{24}$**. *Weiwei Cao*, Xiaoyan Yang, Cécile Genevois, Mathieu Allix and Xiaojun Kuang. *Inorganic Chemistry* (2021) 60, 3282-3290. DOI: 10. 1021/acs.inorgchem.0c03707.

2. **Highly non-stoichiometric YAG ceramics with modified luminescence properties**. *Weiwei Cao*, Ana Isabel Becerro, Pierre Florian, Franck Fayon, Didier Zanghi, Emmanuel Véron, Alessio Zandonà, Cécile Genevois, Michael J. Pitcher and Mathieu Allix, (to be submitted).

Communication

1. **Highly non-stoichiometric YAG with modified luminescence properties (poster)**. The online 15th International Conference on Materials Chemistry (MC15) held by Royal Society of Chemistry (Dublin, Ireland), July 12-15, 2021.

Abstract

In this work, highly non-stoichiometric $Y_{3+x}Al_{5-x}O_{12}$ ($0 \leq x \leq 0.4$) garnet ceramics were synthesized by combining direct crystallisation from melt and glass crystallisation methods. Their average and local structures were determined by using a combination of different characterization methods including powder diffraction, high resolution transmission electron microscopy, nuclear magnetic resonance spectroscopy and EXAFS. The effect of nonstoichiometry on luminescence properties was mainly studied on Ce^{3+} single doped and Yb^{3+}/Er^{3+} co-doped stoichiometric (s-) and non-stoichiometric (ns-) YAG materials.

From cooling experiments of the $Y_{3.2}Al_{4.8}O_{12}$ (x = 0.2) garnet sample using the ADL technique, we show that these metastable non-stoichiometric garnets are accessible for a 400−550 °C s^{-1} cooling rate range. Cooling rates > 550 °C s^{-1} and <400 °C s^{-1} respectively produce glassy materials (which can be further turned into crystalline garnet) and biphasic $YAlO_3/Al_2O_3$.

The $Y_{3+x}Al_{5-x}O_{12}$ garnets average structure was determined by Rietveld refinement from synchrotron powder diffraction data. The lattice parameters in this range vary from 12.0071(1) Å to 12.1354(1) Å, with the excess of Y^{3+} locating at octahedral sites usually occupied by Al. The six-fold coordinated yttrium concentration evolves in a linear trend and follows with theoretical expectation all along the $Y_{3+x}Al_{5-x}O_{12}$ solid solution. The excess of Y^{3+} occupying the garnet B site was detected at the atomic scale by STEM-HAADF and was also observed by solid-state NMR spectroscopy via the appearance of a $^{[6]}Y$ chemical shift signal. EXAFS measurements also led to a clear signature $^{[6]}Y$.

The luminescence properties of the Yb^{3+}/Er^{3+} co-doped and Ce^{3+}, Dy^{3+} and Mn^{4+} single-doped direct crystallized in stoichiometric (s) and non-stoichiometric (ns) garnets. The effect of 6-coordinated excess Y^{3+} on the samples' emission properties was carefully studied and discussed, especially on Yb^{3+}/Er^{3+} and Ce^{3+} doped YAGs and linked to their structure established by powder diffraction. Yb^{3+}/Er^{3+} doped ns-YAGs show enhanced emission properties compared to s-YAG with a same doping content, which was attributed to the more efficient transfer process through the shorter $Yb^{3+} \rightarrow Er^{3+}$ energy transfer path in ns-YAG. An inhomogeneous luminescence response was observed in Yb^{3+}/Er^{3+} doped s- and ns-YAG, and appeared quite pronounced in ns-YAG. These could be caused by the deviation in dopant concentration between grains and grain boundaries.

This work is the first report of highly improved luminescence properties of YAG materials through the introduction of dopant ions, by excess Y^{3+}, into the both dodecahedral and octahedral sites of the garnet structure. It is foreseen that this first example could be a guidance for further improving and studying other non-stoichiometric garnet materials.

Contents

General introduction

Glass formation generally relies on cooling a melt rapidly enough to inhibit its crystallisation. Such rapid cooling (quenching) can be achieved by aerodynamic levitation (ADL) by instantly shutting off lasers. This technique is practical for synthesizing glass and increasing the glass forming range observed using a classic melt quenching approach in a commercial furnace[1, 2]. For example, the novel high-refractive $BaTi_2O_5$ glass, having no network former, is accessible by ADL. Novel $Ba_{1-x}A_xTi_2O_5$ (A = Mg^{2+}, Ca^{2+} or Sr^{2+}) glasses[3] were also synthesized. Al_2O_3−based[4], TiO_2−based[5] and Nb_2O_5−based[6] glasses are not common and can be also synthesized by ADL method. A work from Watanabe *et al.* [7] is also a good example in which xR_2O_3−$(100-x)Al_2O_3$ ($20 \leq x \leq 60$, *R* is Y, La, Nd, Sm, Eu, Gd, Dy, Ho, Er, Tm, Yb, Lu, Pr and Tb) samples were synthesized by ADL approach. Glass, partially crystallized and fully crystallized samples were obtained in their work. ADL fully demonstrates its advantages to synthesize compounds which are not accessible by classical methods.

Glass fabrication by ADL offers chances for accessing metastable ceramics by glass-crystallisation approach via heating the glasses in the furnace at temperatures above their glass crystallisation temperature (T_g). At CEMHTI laboratory, this synthesis route has been used to produce transparent ceramics. For example, glasses of compositions $BaAl_4O_7$[8], Sr*RE*Ga_3O_7 (*RE* stands for Rare Earth)[9] and YAG-Al_2O_3[10] were fully crystallized into transparent ceramics. Moreover, these materials exhibit optical properties when doped with lanthanides and, $Ln_{1+x}Sr_{1-x}Ga_3O_{7+\delta}$ (Ln = Eu, Gd or Tb)[11] transparent ceramics were also reported to show remarkable anion-conducting properties. Another synthesis method for metastable ceramic by ADL is direct-crystallisation from the under-cooled melt. For example, Yu *et al.*[12] and Akishige *et al.*[13] reported the synthesis of $BaTi_2O_5$ crystalline material which is ferroelectric. At CEMHTI, Fan *et al.*[14] synthesized $La_2Ga_3O_{7.5}$ ceramics which exhibits a melilite structure and anionic conducting properties. Another example is $BaGa_4O_7$ [15] which could not be synthesized by solid state reaction method but was prepared by direct crystallisation from a same composition melt. In the same work, $BaGa_4O_7$ was doped with Eu^{3+} and showed strong orange−red luminescence under UV radiation, showing potential optoelectronic applications.

Compared to the “strong” glass which can be easily fabricated and appear highly transparent, for example SiO_2 and GeO_2[16, 17], $Y_3Al_5O_{12}$ (YAG) glass is considered to be “fragile“, because its undercooled liquid has highly non-Arrhenian viscosity dependence on

temperature as stated by Angell[17] and cannot be accessed by the traditional furnace synthesis, while such glass can be obtained by ADL due to the rapid cooling and clean solidification process, although it is translucent[4, 18] due to the glass inclusions whose crystallinity is debatable[4, 19-21]. To improve the transparency of YAG glass, one can have the Al_2O_3 molar ratio higher than 62.5 mol.%, for example Ma*. et al*. produced 74 mol % Al_2O_3–26 mol % Y_2O_3 glass with high transparency using ADL, S. Alahraché *et al*. added 4 wt. % SiO_2 to YAG, obtaining YAG-rich glass [22]. Chi-hoon Lee *et al*. found that the transparency of the YAG glass increases as increasing the Eu^{3+} concentration, as the Eu^{3+} improves the glass forming ability. R. Weber *et al*. reported that large lanthanum ion stabilizes the AlO_4 formation, ensuring a high-level concentration of 4-coordinate Al^{3+} and increasing the glass-forming tendency[23]. Up to now, pure YAG glass has not been reported yet and is still being explored, our ADL synthesis and the issues taken for enhancing the cooling rate of YAG, show the probability to make it.

In this work, our main focus is to use direct-crystallisation from the melt and glass-crystallisation methods to synthesize non-stoichiometric $Y_{3-x}Al_{5+x}O_{12}$ (ns-YAG) metastable materials and to study the effect of nonstoichiometry on their optical properties. The interest lies in the fact that YAG is a versatile host which can incorporate rare earth (*RE*) ions, showing optical properties and working as solid-state laser, phosphors, and scintillators. YAG has a cubic structure with *Ia-3d* space group, in which 40% of Al atoms occupy the octahedral site (Wyckoff *16a*) surrounded by six oxygen atoms and 60% Al are in tetrahedral site (Wyckoff *24d*) surrounded by four oxygen atoms. AlO_6 octahedra and AlO_4 tetrahedra are corner connected, forming 8-coordinate dodecahedral site (Wyckoff *24c*) for hosting Y atoms. Because of their large size, *RE* doping cations occupy the dodecahedral site.

Up to now, several mature synthesis methods have been reported to achieve the synthesis of crystallized YAG with different physical forms. For example Czochralski[24] process has been used for single YAG crystal preparation, solid-state reaction[25] for transparent YAG ceramics, wet-chemical sol – gel[26] for YAG powders and laser heating[10] for bulk YAG ceramic. The resulting YAG crystals are usually limited to the stoichiometric YAG composition where the Y/Al ratio is confined to 3/5. However a few reported works[27-29] state that a small deviation from this 3/5 ratio could still exhibit garnet diffraction peaks without obvious presence of impurity phase, with its lattice parameter slightly larger than that $Y_3Al_5O_{12}$ (12.008 Å). This indicates that non-stoichiometric YAG was synthesized

previously. This YAG with Y/Al atomic ratio over 3/5 ($Y_{3+x}Al_{5-x}O_{12}$ with x > 0) is defined as non-stoichiometric YAG. Many papers[29-34] have declared that nonstoichiometry in YAG crystal structure would influence on the optical properties of the *RE*-doped garnet crystalline material, as in some way the Y_{Al} lattice defect introduces *RE* ions into octahedral site, changing the ligand environment of *RE* sensitizer centers and activator centers, thus affecting optical properties. However, it is not easy to achieve non-stoichiometric YAG, as the nonstoichiometry level confirmed by simulation and experiment was up to date limited to low concentration, *e.g*. 1 mol % excess Y_2O_3 (corresponding to x = 0.08)[28]. For higher non stoichiometry, a combination of YAG glass, YAG crystalline and eutectic $YAlO_3/Al_2O_3$ phases are observed. In order to form single garnet phase, YAG crystalline should meet suitable phase formation conditions. For this, cooling experiments of YAG samples were conducted to study the phase formation conditions. For example Nagashio *et al*.[35] performed a series of cooling experiments on 75 mg samples with $Y_3Al_5O_{12}$ composition under containerless conditions using aero-acoustic levitator. They found that as the cooling rate increases, the solidification of YAP/Al_2O_3, YAG and amorphous phases were successively achieved, and two crystalline phases (YAP/Al_2O_3 and YAG) crystallize respectively at 1400-1500 °C and 1100-1300 °C.

Nevertheless, experimental attempts to synthesize non-stoichiometric YAG compounds as well as computer simulations on lattice defect were conducted. Early in 1977, Ashurov *et al*.[36] reported that stoichiometry deviation in aluminum and gallium garnet crystals were obtained from the melt whose initial composition was stoichiometric, leading to the degeneracy of structural symmetry. At CEMHTI, M. Gervais *et al*.[27]. synthesized $Y_3Al_{5-x}Ga_xO_{12}$ and $Y_{3+x}Al_{5-x}O_{12}$ by aerodynamic levitation coupled to laser heating method. Although Ga^{3+}(0.62Å) is larger than Al^{3+}(0.535 Å), excess Ga^{3+} ions tend to occupy tetrahedral rather than octahedral sites. The solid solution range of their $Y_{3+x}Al_{5-x}O_{12}$ is 30−42.5 mol % Y_2O_3 (corresponding to $-0.6 \le x \le 0.4$). In 30−37.5 mol % Y_2O_3 (corresponding to $-0.6 \le x \le 0$) range, lattice parameter of garnet does not change and almost equals to 12.008 Å of stoichiometric YAG (37.5 mol % Y_2O_3), because in the Y_2O_3−Al_2O_3 phase diagram Al−rich compositions usually exist in the form as the mixture of garnet and alumina, although the diffraction of alumina in XRD pattern is not apparent and even invisible as Al^{3+} has low scattering coefficient. While in 37.5−42.5 mol % Y_2O_3 range, the garnet lattice parameter increases from 12.008 Å to 12.052 Å, which indicates the existence of nonstoichiometric YAG, however no structural analysis was carried out. L. Zhu *et al*.[29] reported their $Y_{3+3x}Al_5O_{12+4.5x}$ (x = 0−0.13) garnets were synthesized at 1000 °C

by sol-gel combustion method, x = 0 and 0.13 compositions in their work are respectively corresponding to $Y_3Al_5O_{12}$ and $Y_{3.23}Al_{4.77}O_{12}$, lattice parameter of YAG in this solid solution range varies from 12.0253(4) Å to 12.0565(9) Å. The lattice parameter 12.0253(4) Å of $Y_3Al_5O_{12}$ is much larger than the widely accepted 12.008 Å. Except the XRD patterns and the statement on the change of lattice parameter, the formation of $Y_{3+3x}Al_5O_{12+4.5x}$ (x = 0−0.13) was not firmly proved by further characterizations. Fortunately, by studying Y−O bond length through EXAFS characterization method, they found three different Y−O bonds, two of them are typical bonds of YO_8 dodecahedron and the last one is attributed to Y_{Al16a}−O bonding of YO_6 octahedron. Patel *et al*.[28] synthesized YAG within Al-rich and Y-rich compositions, the maximum Y nonstoichiometry concentration was achieved on 0.96 mol % of Y_2O_3 (approximately corresponding to 12.045 Å of lattice parameter a of the resulted YAG), they also predicted the mechanism of nonstoichiometry of $Y_3Al_5O_{12}$ by atomistic simulation and validated it by comparing it with the observed lattice parameter trend. For Y−rich compositions, energy required for various defects were calculated. The existence of ionic void defects was excluded, because their formation demands high energy. Most importantly, the author concluded that the defect energy of Y_{Al16a} is half of that of Y_{Al24d} (1.35 eV versus 2.52 eV)[28], implying that excess Y^{3+} locate at YO_6 sites.

The further purposes of studying nonstoichiometry (or lattice defect) in YAG is to adjust the concentration of Y_{Al16a} defect in the garnet structure, as Y_{Al16a} defects has profound influence on the optical properties, this can be expanded to $Lu_3Al_5O_{12}$ and $Gd_3Ga_5O_{12}$[30, 33, 34, 37-39]. Our exploration on different types of $A_3B_5O_{12}$ garnet by direct-crystallisation and glass-crystallisation approaches would offer the candidates for lattice-defect-related optical materials.

A quotation from Ashurov's work would be good ending of this general introduction——the way of synthesis should be taken into account in studies of optical, structural, and mechanical properties of aluminum and gallium garnet crystals both without impurities and with rare-earth activators[36].

Chapter 1
Literature review

1 Literature review

1.1 Y_2O_3−Al_2O_3 system

The commonly accepted Y_2O_3−Al_2O_3 phase diagram up to now was the one developed by Abell *et al*.[40] In this phase diagram, each possible phase was identified, including the YAP phase which was ambiguous in the Y_2O_3−Al_2O_3 phase diagram of Schneider et al[41]. although it is a metastable phase, which is supposed to decompose into YAG and an unknown phase at temperatures above 1300 °C. **Figure 1.1** shows a reproduction of the Y_2O_3−Al_2O_3 phase diagram from the work of Abell[40]. In this system, there are five crystalline compounds. There are the two end members Y_2O_3 and Al_2O_3, and their reaction products of cubic garnet YAG ($Y_3Al_5O_{12}$), perovskite−like orthorhombic YAP ($YAlO_3$) and monoclinic YAM ($Y_4Al_2O_9$). These compounds have been well defined: Y_2O_3 has a cubic structure with Y atoms located in two kinds of 6-coordinate environments with different bonding lengths and α−Al_2O_3 is trigonal with one AlO_6 environment. In their work, YAP was prepared by Czocharaski crystal growth method, the resulting YAP remains stable during cooling to room temperature. This helps to make the Y_2O_3−Al_2O_3 phase diagram more comprehensive as shown in **figure 1.1**.

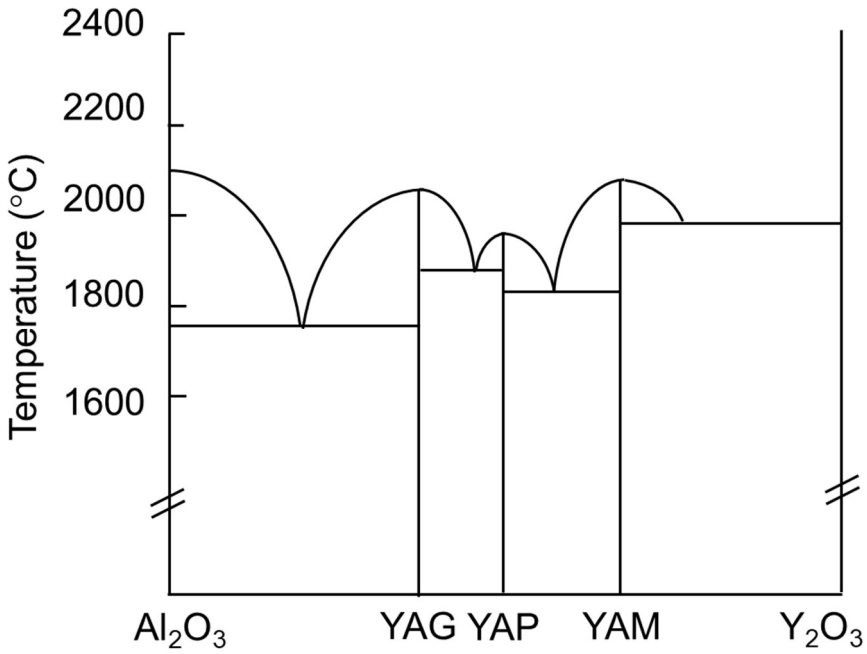

Figure 1.1. *Redrawn Y_2O_3−Al_2O_3 equilibrium phase diagram by Abell et al [40].*

As reported by M. Gervais *et al*.[27] and K. Nagashio *et al*.[35], in the ADL processed reaction of Y_2O_3−Al_2O_3 system, three typical phases are reproducibly observed: glass, single phase crystalline YAG and biphasic crystalline YAP/Al_2O_3. It was reported that YAG phase is synthesized under higher cooling rate than YAP/Al_2O_3 but lower than for glass[27, 35]. It is important to mention that the yttrium−aluminum glass is not completely transparent but translucent, as inside the sample there are many droplets embedded in glass matrix[19, 21]. To understand what leads to the phase selection in the Y_2O_3−Al_2O_3 system, the composition and chemical structure of the droplets were studied. The droplets were found to have identical composition as the surrounding glass matrix. The liquid−liquid phase separation between low−density droplets and high−density glass matrix was attributed to "density−driven"[21, 42]. The droplets can be amorphous[20] or crystallized[19, 43] as reported. Crystallized or amorphous droplets can be YAG nucleation site, and the eutectic YAP−Al_2O_3 on the sample surface can be nucleation of YAP. Single YAG phase was obtained caused by nucleation and crystal growth, and as well as by re−melting and recrystallisation, of thin YAP−Al_2O_3 layer on the surface of supercooled sample, caused by latent heat of YAG[35].

1.2 Crystal structure of YAG, YAP and YAM

$Y_3Al_5O_{12}$ (YAG) (**figure 1.2 (a)**) is a garnet structure with a body−centered cubic symmetry with lattice parameter a = 12.008 Å and space group *Ia−3d* (No. 230). Its unit cell contains 8 formula units with 160 atoms: 24 Y^{3+} locates at 8−coordinate *c* Wyckoff site, 16 Al^{3+} locate at 6−coordinate *a* Wyckoff site, 24 Al^{3+} locate at 4−cordinate *d* Wyckoff site and 96 O^{2-} at *h* Wyckoff site. There is only one oxygen environment OY_2Al_2. Numerous garnet compounds $A_3B_5O_{12}$ (*e. g.* $Gd_3Gd_5O_{12}$, $Y_3Fe_5O_{12}$, $Sm_3Al_5O_{12}$) and $A_2B_2C_3O_{12}$ (*e.g*. $Mg_3Al_2Si_3O_{12}$, $Fe_3Al_2Si_3O_{12}$, $Ca_3Fe_2Si_3O_{12}$) have been reported and exhibit the same structure.

The perovskite-type $YAlO_3$ (YAP) **(b)** is confirmed as a common by−product with metastable structure during the synthesis of YAG[35, 44]. Its structure has orthorhombic symmetry with *Pnma* space group and 5.330(2) Å ×7.375(2) Å × 5.180(2) Å unit cell, both Y and Al in this structure have one coordinating environment and they are respectively surrounded by 8 and 6 oxygen atoms. Compared to YAG, it has two oxygen environments, OY_2Al_{12} and OY_3Al_{12}. $Y_4Al_2O_9$ (YAM) **(c)** has a monoclinic structure with space group $P2_1/c$, and lattice parameters a = 7.4804(4) Å, b = 0.5461(5) Å, c = 11.2057(7) Å and β = 108.927(4) °. In this structure, Al is at two different 4−coordinate sites, Y has two

environments of YO_6 and YO_7, the ratio of these three sites is 2:2:2. Oxygen atoms are distributed in four types of environments, they are four OY_3Al, two OY_2Al, two OY_4 and one OY_2Al_2.

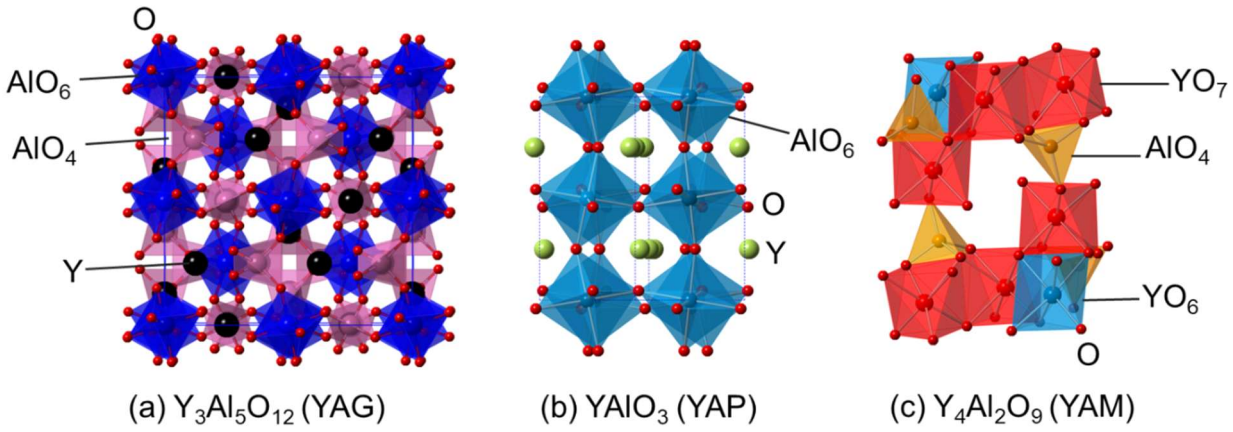

Figure 1.2. (a) *YAG crystal structure. Black and red solid spheres are respectively Y and O atoms. AlO_4 tetrahedra (pink) and AlO_6 octahedra (blue) are corner−connected and, form 8−coordinate voids where Y^{3+} atoms locate.* ***(b)*** *YAP crystal structure. AlO_6 octahedra are corner connected, Y atoms (lime green) are in 8−coordinate voids formed by AlO_6 octahedra. Red spheres are oxygen atoms.* ***(c)*** *YAM crystal structure. Al atoms locate in 4−coordinate sites, Y atoms are coordinated to six or seven oxygen atoms (red).*

1.3 Stability of YAG, YAP and YAM

Successful synthesis of $Y_3Al_5O_{12}$ (YAG) by different methods has been reported[24, 35, 45-48]. In some of these works, authors reported that during the synthesis of YAG, eutectic YAP−Al_2O_3 can be also obtained. SEM morphology of the biphasic sample implies that Al_2O_3 is distributed over the dendritic YAG crystals. In 1995, A. Ikesue *et al*.[45]19 reported the synthesis of single phase transparent YAG and Nd: YAG ceramics via solid state reaction method by sintering a pressed sample disk at high temperature using Y_2O_3, Al_2O_3 and Nd_2O_3 as staring materials[45]. When exploring suitable synthesis temperature of YAG, the products from heating treatment of the sample can be YAG, YAP−Al_2O_3 and $Y_4Al_2O_9$ (YAM), from which YAM appears as an intermediate phase which later forms YAP (**figure 1.3**). After trying different heating temperatures, YAG was the only attempt to be prepared as a single phase. This indicates, compared to the other two yttrium aluminate phases, that

YAG is a very stable phase, which was obtained at 1700 °C in their work. The reaction between YAP and Al_2O_3 takes place in a metastable solidification process at 1418±7°C, which can be attributed to the difficulty of Al to form 4−fold coordination as in YAG structure[44]. as J. L. Caslavsky *et al*. reported,

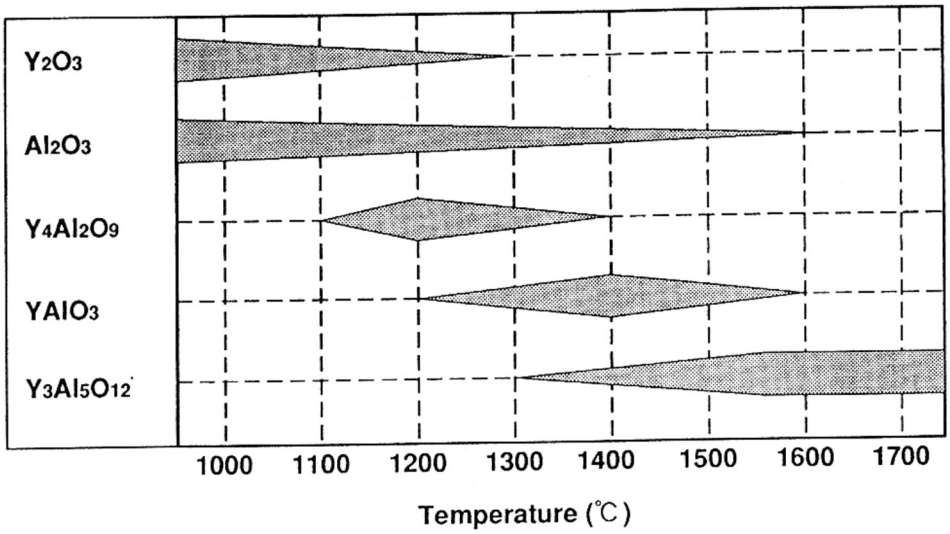

Figure 1.3. *Relationship between heating temperature and produced phases (analysis by X−ray diffraction method)[45].*

Similarly to the reactions observed in the 37.5% Y_2O_3−62.5% Al_2O_3 composition reported by A. Ikesue, Li *et al*. synthesized transparent YAG by solid state reaction under pressure in vacuum.[49] In this experiment, they found similar reaction process in this system. Three reactions take place: first the starting materials Y_2O_3 and Al_2O_3 react and produce $Y_4Al_2O_9$ (YAM), then YAM reacts with Al_2O_3 and makes $YAlO_3$ (YAP). In the last step, YAP reacts with Al_2O_3 and finally produces single phase YAG. The corresponding sintering temperature is around 1700°C. The reactions can be managed through the routes[50] and order shown in equation (1−3).

$$2Y_2O_3 + Al_2O_3 \rightarrow Y_4Al_2O_9\ (YAM) \qquad Eqn\ 1$$

$$Y_4Al_2O_9 + Al_2O_3 \rightarrow 4YAlO_3\ (YAP) \qquad Eqn\ 2$$

$$3YAlO_3 + Al_2O_3 \rightarrow Y_3Al_5O_{12}\ (YAG) \qquad Eqn\ 3$$

The synthesis of $Y_3Al_5O_{12}$ is easy to be achieved, for example, M. Gervais[27] and K. Nagashio[35] reported that they synthesized pure YAG. Their samples were heated by CO_2 lasers and directly crystallized from the melt. They could also obtain eutectic YAP−Al_2O_3, but they did not observe YAM in their samples. Its formation can be related to synthesis temperature, synthesis method, cooling rate and even to precursor type.

1.4 Synthesis of YAG

YAG in the form of single crystal, transparent polycrystalline ceramic and powders were successfully synthesized. The synthesis details are important regarding the aim of the project, they are stated in the synthesis method introduction. Single YAG crystal for laser application requires the following features: non−birefringence, negligible absorption and scattering losses, high hardness and low thermal expansion coefficient. Transparent polycrystalline YAG can be an alternative for single crystal YAG when it is designed for solid state laser applications. YAG powders can be synthesized by several low−temperature wet chemical methods like sol−gel, co−precipitation, solvothermal methods, extra. Moderate sintering temperature and repeated grinding are essential to eliminate impurities, like YAP and YAM, from YAG, for preparing pure YAG by solid state reaction.

1.4.1 YAG single crystal via Czochralski (CZ) preparation method

Czochralski (CZ) is known as the most common method to synthesize single−crystal YAG, it is an effective way to prepare large−volume or specific−shape single crystal. The growth of crystal goes through solid−liquid phase transition process as the constituent melt solidifies under controllable conditions. The solid−liquid interface moves toward solidification direction and causes the previously randomly stocked atoms to stack in an ordered way. The crystal has little intrinsic defect and impurity if the synthesis process works perfectly. Other advantages of this crystal−growth method are that crystal does not contact with crucible and reduce residual stress in it and growth of the crystal can be observed. However, this approach is costly and time−consuming, the pulling rate of single YAG crystal in the work of S. Kostić is 3mm/h (**figure 1.4**). While when dopant ions are introduced, for example Nd^{3+}, the growth of Nd: YAG single crystal becomes more complex and slower. Therefore, alternative synthesis methods are necessary.

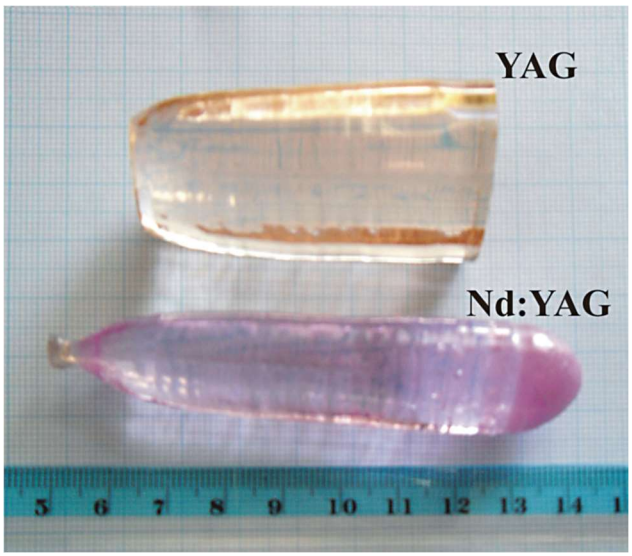

Figure 1.4. *YAG and Nd: YAG crystal prepared through Czochralski method [24]by S.Kostić.*

1.4.2 YAG transparent ceramic by solid state reaction

Solid state reaction is a commonly used method for synthesizing YAG polycrystalline ceramics. Ikesue *et al*. produced YAG and Nd: YAG (**figure 1.5**) [45] by sintering a mixture of Y_2O_3, Al_2O_3 and Nd_2O_3 powders, with ethyl silicate as a sintering aid, in vacuum above 1650°C. The synthesized YAG is dense and pore−free. Optical scattering loss of the resultant transparent Nd: YAG ceramic is as low as Nd: YAG single crystal. Its hardness, absorption and fluorescence behaviors and laser characteristics are also comparable to Nd: YAG single crystal.

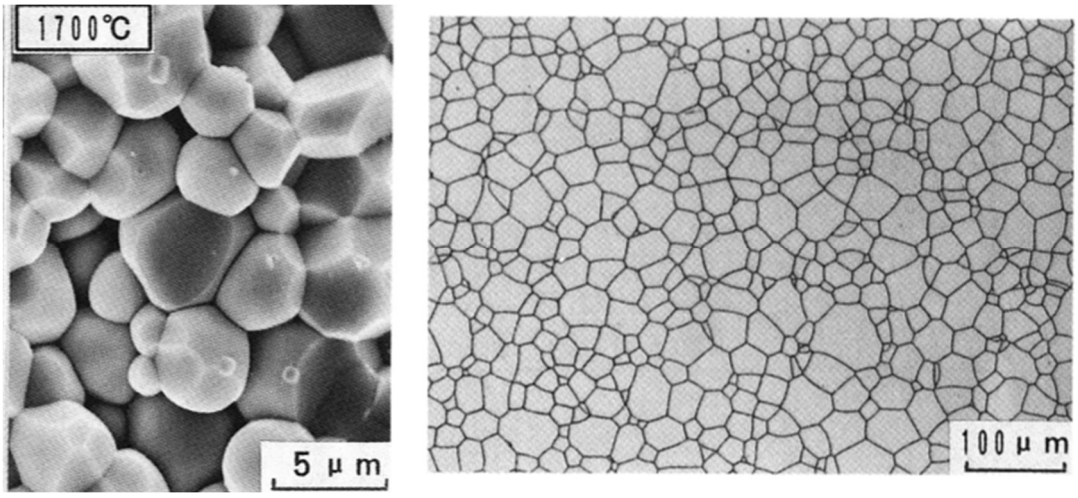

Figure 1.5. *SEM photograph of YAG synthesized at 1700 ℃ (left) and reflection microscope photograph of standard 1.1 at.% Nd: YAG polycrystalline after thermal etching, produced by Ikesue et al.[45].*

1.4.3 YAG produced by aerodynamic levitation coupled with laser heating

The idea of removing the container for material synthesis led to set up an instrument allowing contactless synthesis (**figure 1.6**), therefore levitation synthesis was designed and put into use. Aerodynamic levitation (ADL) coupled to CO_2 lasers has been exclusively applied to synthesize metal oxides, alloys and semiconductors[51]. The synthesis requires carrier gas (such as argon, oxygen and mixed gases) to levitate the sample, ensuring a non-contact synthesis process which prevent the sample from heterogeneous crystallisation when one is aiming for pure glass or single-phase ceramic, or from homogeneous crystallisation when glass is aimed for[1, 52-54]. Furthermore, the supplied gaseous environment allows to adjust the chemistry of the sample in situ[55, 56]. The working process and characteristics of this technique are detailed in in the appendix. When ADL is integrated with structural characterizing instruments, it allows to study the structure of molten materials, Greaves *et al*[57]. combined ADL with small-angle x-ray scattering (SAXS) and wide-angle X-ray scattering (WAXS) to study the in-situ phase transition of yttria-alumina melt. Hennet *et al*.[58] conducted in-situ structural study of $CaAl_2O_4$ and $MgAl_2O_4$ by X-ray and neutron diffraction when the samples were at liquid state. This can be a powerful means to study the dynamic evolution of materials.

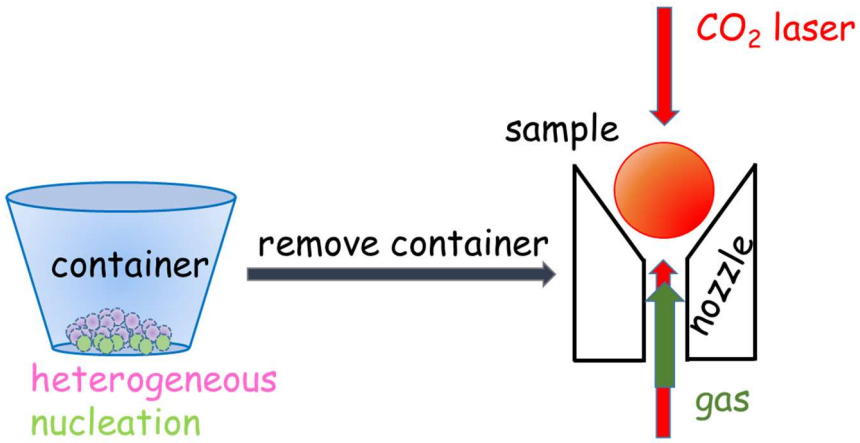

Figure 1.6. *Contactless synthesis conducted by aerodynamic levitation coupled with CO_2 lasers (right) protect the glass or ceramic sample from heterogeneous crystallisation and contamination as well.*

Samples can be heated from RT–3000 °C, the synthesis duration at this temperature range can be several minutes or seconds, which is assumed as being fast for material synthesis. Another notable advantage of ADL synthesis is that the heating and cooling processes can be precisely controlled, in most cases by setting a program which requires the desired temperatures and durations to be input for each stage. The maximum cooling rate is achieved by instantly shutting off lasers. Obviously, the fast quenching process can benefit the formation of glass and increase its forming range[1, 2]. Furthermore, changing carrier gas from one to another can also affect the cooling rate, usually less dense gas can help to facilitate the cooling process[59]. Cooling rates reached by aerodynamic levitation is at the order of ~30–1000 K/s.[1] **Figure 1.7** shows photographs of a collection of ADL prepared glass samples quenched under this cooling range, these glass beads can vary in size and color, they can be transparent or devitrified.

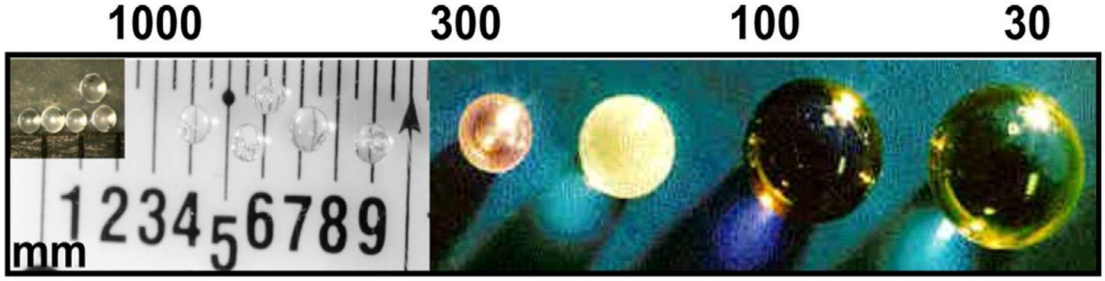

Figure 1.7. *Photographs of glass samples made by aerodynamic levitation coupled to laser heating. Left to right: aluminum silicate containing 67 mol % Al_2O_3, Mg_2SiO_4, $Er_3Al_5O_{12}$, $Y_3Al_5O_{12}$, $ErYLaAl_5O_{12}$, and $La_3Al_5O_{12}$ compositions. The scale along the top of the figure shows the approximate cooling rate in °C s^{-1}. Smaller samples have a larger surface area: volume and cool faster when the heating power is shut off. All but two of the glasses are homogeneous: the $Er_3Al_5O_{12}$ and $Y_3Al_5O_{12}$ composition liquids are homogeneous but undergo phase separation during cooling to form two−phase glasses[1].*

Laser heating by aerodynamic levitation (ADL) method can be direct or indirect synthesis method for $Y_3Al_5O_{12}$−based material, the resulted YAG sample can be glass, glass−ceramic (*i.e*. partially crystallized) or ceramic (*i.e*. fully crystallized). One interesting phenomenon but also a challenge in YAG glass preparation is that, during the quenching process, phase separation is inevitable, leading to a two-phase glass which looks translucent. While after being doped with Eu^{3+}(**figure 1.8**), the transparency of YAG: Eu glass is improved compared to non-doped YAG glass, and with more concentration Eu^{3+}, the glass becomes more and more transparent. This is because Eu^{3+} helps to increase the

glass forming ability, as the micro-sized crystals as scattering centers to visible light were diminished.

Figure 1.8. *Photographs of the as-levitated $(Y_{1-x}Eu_x)_3Al_5O_{12}$ (x = 0.001, 0.01, 0.02 and 0.04) samples; YAG (the first one) and YAG: Eu glass– ceramics with a mass of 38 mg (produced by Chi-Hoon Lee)[18].*

Thus researchers tried to introduce additives to improve the transparency of YAG-based materials. For example, the Ce: YAG−GC (glass crystallized) reported by S. Fujita *et al*.[60] contains 42.5 mol % SiO_2, 20 mol % Y_2O_3, 34 mol % Al_2O_3, 3 mol % LiO_2 and 0.5 mol % Ce_2O_3, The great amount of SiO_2 greatly improved the transparence of the resulted glass−ceramic in their work. The amount of SiO_2 can be very low but also works for making YAG glass, S. Alahraché *et al*.[22] (**figure 1.9**) managed to synthesize YAG based glass-ceramic with a minimum amount of SiO_2 – 4 wt.%, by crystalizing the glass previously made by ADL in the furnace. The small amount of SiO_2 not only ensured the vitrification of the glass, but helped to avoid to form Si-containing secondary phase, as Si^{4+} entered the tetrahedral Al site in the garnet structure.

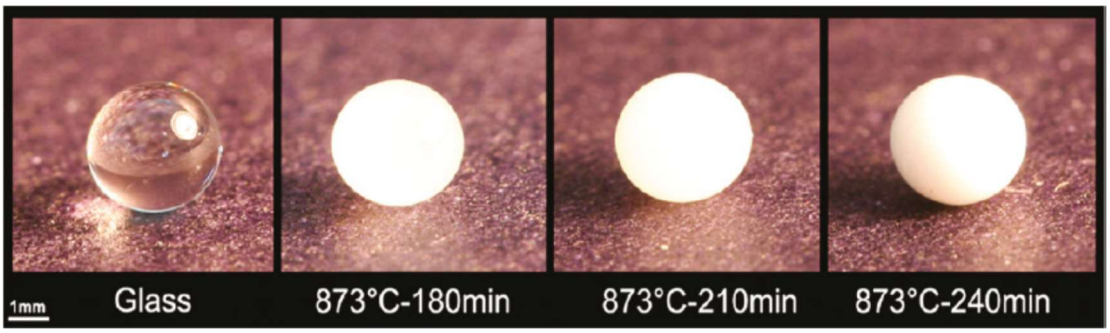

Figure 1.9. *YAG−4Si glass and glass-ceramics obtained by annealing at 873 °C, for the different indicated times[22].*

YAG−based transparent glass−ceramics reported by X. Ma *et al*.[10] were synthesized by full glass crystallisation method. The glass precursor was synthesized by ADL method which provided a fast cooling process. The composition of the as−prepared glass−ceramic started from 26% Y_2O_3−74% Al_2O_3, which has 10% more Al_2O_3 than $Y_3Al_5O_{12}$ (37.5% Y_2O_3−62.5% Al_2O_3). In the final YAG−based glass−ceramic, YAG crystals are surrounded by thin Al_2O_3 layer (**figure 1.10**). As both YAG and Al_2O_3 crystals have nanometer−scale sizes, the light scattering was reduced and led the sample to be transparent. Like YAG single crystal, this YAG−based glass−ceramic can be doped with Ce^{3+} and Nd^{3+} for phosphor and laser applications, respectively.

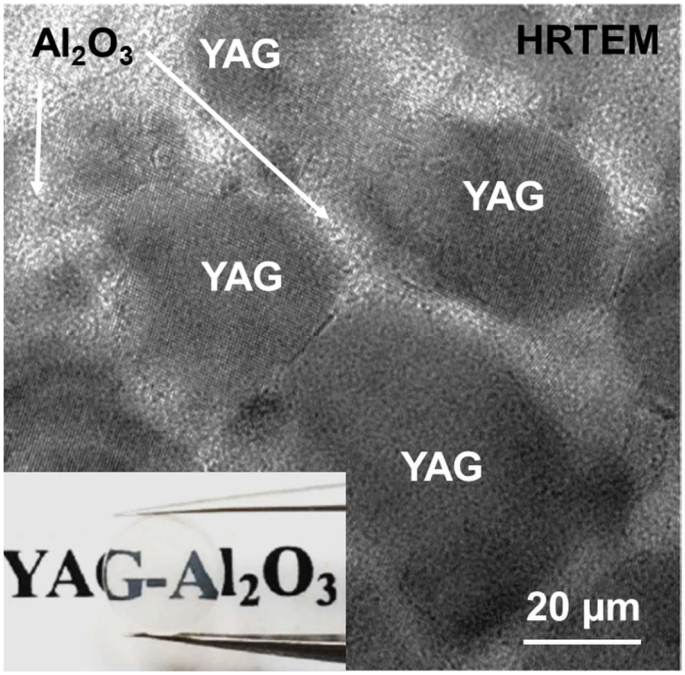

***Figure 1.10**. A HRTEM micrograph of the YAG−Al_2O_3 ceramic (bottom left corner), the YAG nanograins are surrounded by Al_2O_3. This figure combined with two cropped figures the original figure from the article of X. Ma et al [10].*

1.4.4 Wet chemical methods

Sol−gel, co−precipitation and solvothermal are wet chemical methods, they can be used to synthesize un−doped and rare−earth-doped YAG for phosphor applications. By these three methods, chemical compositions are greatly evenly mixed and achieved at a molecular level. This helps to lower the sintering temperature which is not higher than 1000°C. Sol−gel method has advantages, for example, low temperature synthesis, high possibility for uniform grain morphology and homogeneous phase dispersion. But it also has

disadvantages: difficulty in controlling the pH, high expense of starting materials and slow synthesis as well. To prepare Ce: YAG, in the work of X. Yan[46], the experiment mainly involves three steps, firstly making solution of starting material which includes Y^{3+}, Al^{3+} and Ce^{3+} cations; secondly adding additive and adjusting pH value then preparing gel by water bath; thirdly reaction and sintering. Co−precipitation method is not more facile to realise than sol−gel method. Careful solution preparation is also needed and the whole synthesis process is long[47]. G. Dantelle *et al*.[48]. reported YAG: Ce synthesized by solvothermal method. Parameters of pressure, temperature precursor concentration and reaction time were adjusted in different rounds of experiment in order find optimal synthesis conditions. YAG nanocrystals with ~100 nm size could thus be produced with a small size variation. **Table 1.1** summarizes the five above−cited synthesis procedures and the characteristics of the resultant YAG samples.

Table 1.1. Examples of YAG sample synthesized by different routes.

synthesis routes	synthesis conditions	particle size
single crystals by Czochralski method[24]	moving of solid−liquid interface driven by temperature gradient' pulling rate: 3 mm·h^{-1}	diameter:30 mm length:100 mm
solid state reaction[45]	1700 °C, 5h in vacuum	2−5 μm
laser heating[35]	cooling rate: ~ 150 K s^{-1}	2−5 μm
sol−gel[46]	800 °C, duration not given	~ 35 nm
co−precipitation[47]	900 °C, 2h	70 nm
solvothermal[48]	350 °C, 150 min	30 nm

For preparing YAG material, YAM and YAP are usually regarded as secondary phases as they are less suitable for laser and scintillator applications. YAG contains 37.5 mol % Y_2O_3 and 62.5 mol % Al_2O_3. YAP is composed of 50 mol % Y_2O_3 and 50 mol % Al_2O_3, and YAM

contains 66.7 mol %Y_2O_3 and 33.3 mol % Al_2O_3. Although in the phase diagram, YAG stays stable at a broad temperature range but is confined to an exact composition of 37.5% Y_2O_3–62.5% Al_2O_3 ($Y_3Al_5O_{12}$), many studies have reported that its content deviates from its nominal composition. This may induce Y defect at Al sites, which is commonly called anti−site (AD) defects[28, 29, 61].

1.4.5 Optical properties and applications of YAG

YAG materials have been synthesized by different routes in the form of single crystal, transparent ceramic, powder and film for diverse optical applications. It is a remarkable host with good thermal, mechanical and optical properties. neodymium-doped (Nd): YAG is known as gain medium as solid-state laser which is typically produced by Czocharaski crystal growth method, the Nd doping level is about 0.6–1 at. % depending on its use. The slightly Nd doped YAG appears less colored compared to higher higher-doped pink-purplish Nd: YAG rod[24]. The Nd doped YAG was discovered by J. Geusic[62], it has a low threshold and permits continuous operation. It replaced ruby as military rangefinders due to its higher system efficiency[63]. The Nd: doped YAG is also widely used in medical area for removing the lesion from a person's body.

The erbium (Er) doped YAG crystal is a useful laser material showing emission at around 1500 nm through $^4I_{13/2} \rightarrow {}^4I_{15/2}$ transition. It can be used for dentistry and skin treatment. While as Er: YAG has a feature of water-absorption[64] and it is not as efficient as Nd: YAG in reducing patients' pain in dental treatment[65], it is not as preferred as Nd: YAG. The transparent ceramic Nd: YAG has been reported to be synthesized by solid-state reaction method, showing comparable optical characteristics as for single crystal[45].

Since Er^{3+} in YAG structure has a low absorption cross section, limiting the pumping efficiency of the laser, this problem was solved by introducing ytterbium (Yb) ions as secondary dopant into the YAG structure, as ytterbium ions show high absorption cross section with broad absorption band. Furthermore, the $Yb^{3+} \rightarrow Er^{3+}$ energy transfer process is efficient, this reflects on higher emission intensity of the spectra. The Yb–Er co-doped YAG transparent ceramic works as media for generating 1.5 μm laser radiation[66] and shows similar optical properties as single crystal.

Cerium (Ce): YAG material can work as a phosphor for LED lighting or a scintillator for detecting radiation. The Ce: YAG phosphor emits yellow light, when it is combined with a blue GaN diode, a highly bright white LED is generated[67]. The applications of rare-earth doped YAG is more than laser medium and phosphor lighting, the dysprosium (Dy) or

samarium (Sm) doped YAG[68, 69] is a temperature-sensitive phosphor. **Figure 1.11** shows two examples of YAG applications.

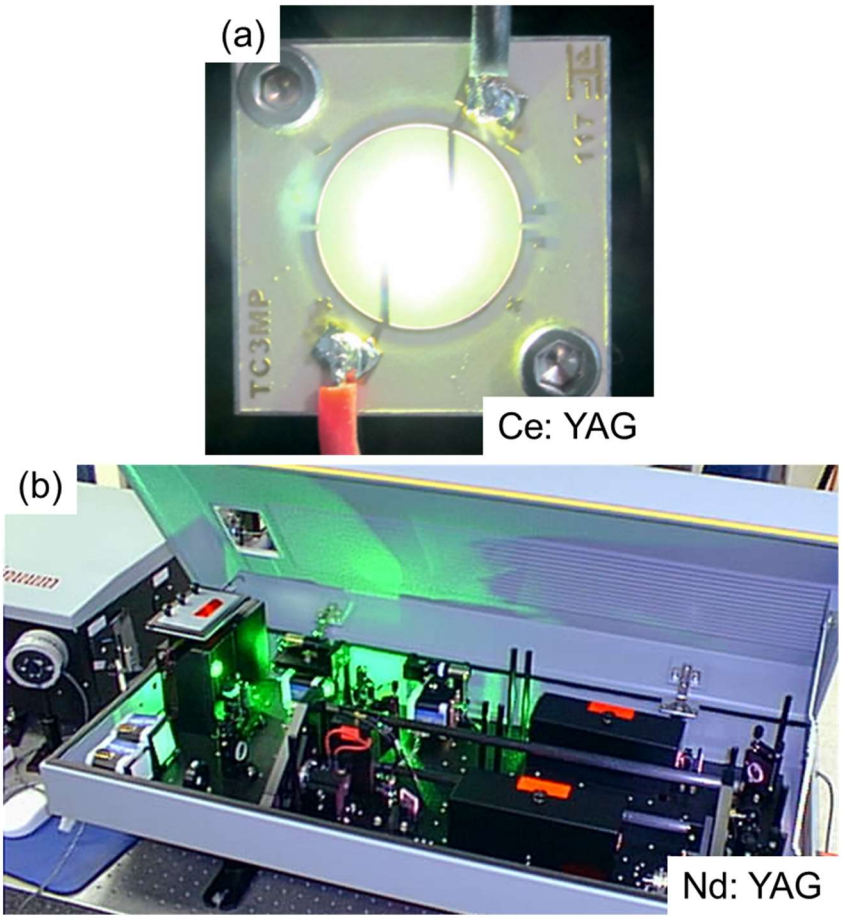

Figure 1.11 *Two examples of YAG application. (a) Ce: YAG phosphor for LED lighting[25] and (b) Nd: YAG laser[70].*

Chapter 2

Highly non−stoichiometric YAG ceramics

2 Highly non−stoichiometric YAG ceramics

2.1 Introduction

ADL synthesis offers routes towards metastable bulk oxides, this material synthesis has been well developed by the CERAM group at CEMHTI who have reported glass-crystallized transparent ceramic $BaAl_4O_7$[8] and Sr*RE*Ga_3O_7[9] for optical application, $Lu_{1+x}Sr_{1-x}Ga_3O_{7+\delta}$ (Ln = Eu, Gd or Tb)[11] and $La_2Ga_3O_{7.5}$[14] for conductivity application. Thus at the first step of the research, we tried to explore the synthesis of new compounds by glass-crystallisation or direct-crystallisation, starting with the hypothetical target compounds $Y_2Al_3O_{7.5}$ as a possible melilite as an analogue of $La_2Ga_3O_{7.5}$[14] which has a melilite structure with space group of *Ima*2, Ga^{3+} cations locate at 4- and 5-coordinate sites, La^{3+} cations are between two Ga−O_4 polyhedron layers and form La^{3+}−GaO_4 layer unit. The pentagonal rings formed by GO_4 polyhedrons supply tunnels for oxygen ions, responsible for conducting behavior. The $Y_2Al_3O_{7.5}$ sample was also directly synthesized by the same technique of aerodynamic levitation (ADL) as for $La_2Ga_3O_{7.5}$. The ADL method has been known as a useful synthesis and characterization tool for materials under high temperature and non−equilibrium condition. The feature of "contactless" of ADL enables the formation of metastable crystalline materials[1]. $La_2Ga_3O_{7.5}$ melilite, which was successfully synthesized by direct crystallisation method using ADL, was not accessible by glass crystallisation method.

Surprisingly, XRD results indicated that the resulting $Y_2Al_3O_{7.5}$ compound was a garnet phase (*i.e.*, $Y_{3.2}Al_{4.8}O_{12}$ which corresponds to the same Y/Al ratio) rather than the expected melilite. This result interested us to synthesize non-stoichiometric YAGs, to study at which site excess Y^{3+} ions locate and how lattice defect impact luminescence properties of rare earths doped YAGs.

$A_3B_5O_{12}$ is the general formula of garnet, the A site cation can be Y, Nd, Sm, Gd, Er and Yb *etc*., and the one at B site can be Al, Sc, Fe and Ga *etc*. Garnets composed of these elements may possess remarkable electrical and magnetic properties and are applied to technology and commercial areas. In $A_3B_5O_{12}$ garnet structure, A cations occupy a dodecahedral site (*24c*), 40% of the B cations are at an octahedral site (*16a*) and 60% at a tetrahedral site (*24d*). BO_6 octahedra and BO_4 tetrahedra are corner-connected, A occupies 8-coordinate voids formed by BO_n polyhedra.

$Y_3Al_5O_{12}$ (YAG), $Y_3Fe_5O_{12}$ (YIG) and $Gd_3Ga_5O_{12}$ (GGG) are of interest because of their promising commercial applications. YIG is a well−known magnetic material, Fe^{3+} ions are

distributed over 4− and 6−fold oxygen environments, the spins on the tetrahedral and octahedral sublattices are aligned antiparallel, producing a net magnetization. Due to high quality factor (*Q*) and high linearity in mid−range frequency, YIG can be applied to microwave resonators[71]. GGG is a remarkable host for rare earths and transition metal. With dopants, GGG materials exhibit optical properties. GGG based lasers, phosphors and scintillators can be applied in medical and thermal diagnosis [72, 73].

Like YIG and GGG, $Y_3Al_5O_{12}$ (YAG) is a versatile material, it is an important host material for developing solid−state lasers, LED lighting and scintillator detecting used in medical[74-77], office printing and projecting, and aerospace areas[78-80]. Since the first successful operation of ruby laser[81] and the demonstration of Nd: YAG laser operation[62], YAG based gain media materials became in the spotlight. The conventional YAG laser material was prepared as single crystals by Czochralski method[24, 82, 83], which displayed outstanding performance but demanded a long and costly synthesis process. YAG ceramics recently were synthesized by different methods of solid state reaction[25], laser heating[10], precipitation[84], sol−gel[26] *etc*. Doping of rare earths Yb, Er, Nd and Eu *etc*. make crystal lattice diverse and properties interesting for YAG. The rare earths usually substitute Y^{3+} and locate at dodecahedral sites, *e.g*. Nd^{3+} (Yb^{3+}) substitutes for Y^{3+} in single crystal Nd: YAG [24] and Yb^{3+} substitutes for Y^{3+} in Yb: YAG [26]. In addition to the type and concentration of rare earths, the localization of rare earths in the lattice is also important for optical properties. S. Geller *et al*.[39] tried to synthesize $Y_3Al_5O_{12}$ and $Gd_3Al_5O_{12}$ garnet single crystal, while the lattice parameters of these two samples are larger than that of theoretical value. After excluding the problem of starting materials purity, the enlargement of crystal lattice is likely to be attributed to the composition deviation from nominal composition, there are probably excesses of Y^{3+} and Gd^{3+} at octahedral site, whose content is about 1.5 mol %. This opened the way to synthesize non-stoichiometric garnet in the following research.

2.2 Methods

2.2.1 Synthesis procedure by solid state reaction

High−purity Y_2O_3 (99.9% Strem Chemicals) and Al_2O_3 (99.999% Strem Chemicals) were dried in an oven operating at 115 °C all the time. They were weighed following strict stoichiometry of each aimed composition. Powders were submerged in ethanol and blended using pestle and mortar for around 50 min to get a homogeneous powder mixture. The ~1 g mixture was then dried and pressed into a pellet of 12 mm in diameter. Pellets of $Y_{3+x}Al_{5-x}O_{12}$ (x = 0, 0.2 and 0.4) compositions were put in platinum crucible and

pre−sintered at 1200°C for 10h, after which the pellets were re-ground, re-pressed by the same way as for pre-sintering and then were heated at 1500 °C for 10h. The heating and cooling rates for the two sintering procedures are 10°C/min.

2.2.2 Synthesis procedure by aerodynamic levitation

Aerodynamic levitation approach (ADL) was applied, as it enables formation of glass and metastable crystalline samples[1], which can be an supplementary synthesis method to access the materials that we aimed for. Starting materials of each $Y_{3+x}Al_{5-x}O_{12}$ ($-0.1 \leq x \leq 0.45$) with an interval of 0.5) were processed by the same way as for solid state reaction synthesis before being pressed into a pellet, the compacted pellet was crushed into 10−40 mg pieces to make samples beads by ADL. Levitation gases of argon, oxygen and helium were available for selection. These three gases have different densities: argon has greater but comparable density than oxygen, and it is ten times denser than helium[59, 85]. Reducing the density of levitated gas (*e.g*. by using He or O_2 instead of Ar) can induce faster heat transfer, thus increasing cooling rate. But it can also cause severe instability of the floating sample. The sample piece was heated by gradually increasing laser power until a temperature of 2200−2500 °C was reached, monitored by pyrometer, and maintained for several seconds to get the constituents in melt homogeneous. The melting droplet was then deeply undercooled by instantly switching off lasers. The gas flow could be tuned and worked through the synthesis to stabilize the sample and protect it from contamination. Glass crystallisation was also applied to broaden the $Y_{3+x}Al_{5-x}O_{12}$ solid solution range as much as possible. The glass was prepared by laser heating in oxygen/helium.

2.2.3 Thermal stability characterization of *x* = 0.2 and 0.4 ns-YAGs

Synthesis conditions of *x* = 0.2 ns−YAG was studied by **(a)** a series of cooling experiments. Sample mass was changed over 9−39 mg with an interval of 1 mg. The experiment was realized by Manual Laser and 3Voies software together (illustrated in appendix). The Manual Laser initiated laser heating and 3Voies software was later connected with Manual Laser. The cooling started after launching a button on 3Voies software, meanwhile cooling curves were recorded on it. **(b)** high−temperature annealing on *x* = 0.2 ns−YAG at 1600 °C for 12h. As a comparison, s−YAG starting powders mixture was synthesized under the same condition. **(c)** in−situ VT−XRD from RT to 1600 °C in vacuum using D8 Advanced Bruker laboratory diffractometer (1.5406 Å Cu Kα radiation) equipped with Vantec−1 linear detector and an Anton Parr oven chamber (HTK16N). Besides, the structural stability of *x*

= 0.4 ns−YAG, which extends the YAG solid solution range, also interests us. Crystallized sample powders were measured by VT−XRD using the same heating and data collecting process as done for *x* = 0.2 ns−YAG. Platinum ribbon holder was used to diminish temperature gradient along the sample thickness.

2.2.4 Phase characterization

Preliminary phase indexation was realized by RT X−ray powder diffraction (XRD) measurement on *x* = -0.1−0.45 sample powders using a D8 Advance Bruker Bragg−Brentano diffractometer (1.5418 Å Cu Kα radiation) equipped with a Vantec−1 linear detector. To precisely work out the cell parameter and occupation of excess Y^{3+}, high−resolution synchrotron X−ray powder diffraction (SXPD or SPD) measurements were performed by high−flux (~ 5×10^{11} phs/sec at 30 keV) 11BM source (Advanced Photon Source, Argonne National Laboratory, U.S.A.) using the rapid access/mail-in service. The data were collected from 0.5 to 50 2θ with a 0.001° step size and λ = 0.458 Å of wavelength. Sample powders of each composition were taken from a single bead and loaded into a Kapton tube with a diameter of 0.8 mm before the measurement, X−ray absorption muR of this ceramic series is ~1.19–1.85 which were computed on the 11BM compute X−ray absorption web page by taking X−ray wavelength ~0.4578 Å, chemical formula $Y_{0.375}Al_{0.625}O_{1.5}$ (Z = 1), capillary radius 0.8 mm and packing fraction 0.6 (suggested). Average structure of YAG samples were determined by Rietveld structural refinement on the SPD data, the refinement was performed with corresponding refinement macros the using *TOPAS V6* software.

2.2.5 Microstructure and compositional characterization

Microstructure of polished beads was observed by scanning electron microscope Field Emission Gun-SEM MERLIN (ZEISS). Chemical content of $Y_{3+x}Al_{5-x}O_{12}$ (*x* = 0, 0.1, 0.2, 0.3 and 0.4) garnets was checked on polished bead by electron dispersive spectroscopy (EDS) equipped on SEM and by high precision microprobe (SX Five microprobes, tungsten source) work at 10 mA and 15 kV, the sampling was performed across the diameter of the polished section of the bead.

Local structures of $Y_{3+x}Al_{5-x}O_{12}$ (*x* = 0, 0.2 and 0.4) garnets were investigated by a series of measurements. Selected area electron diffraction (SAED), High Resolution Transmission Electron Microscope (HRTEM) imaging, atomic−resolution Scanning Transmission Electron Microscopy−High Angle Annular Dark Field (STEM−HAADF)

micrographs and Energy Dispersive X−ray Spectroscopy (EDS) elemental mapping were performed on a JEOL ARM200F (JEOL Ltd.) Cold FEG (Field Emission Gun) TEM (Transmission Electron Microscope) operating at 200 kV. The TEM is equipped with a double spherical aberration corrector and fitted with a JEOL SDD CENTURIO EDS system. The cationic organization was imaged at atomic scale by STEM−EDS elemental mapping and STEM−HAADF imaging mode with a 68−174.5 mrd inner−outer collection angles, using 0.13 nm and 0.1 nm probe sizes respectively. Before the measurement, the samples were fixed on a tripod and mechanically polished on inlaid diamond discs until to reach a thickness of 40 μm. The samples were then milled with argon ions using a Precision Ion Polishing System (PIPS, Gatan) until a hole was obtained. Observations and analyses were carried out on the thinnest areas locating around this hole

2.2.6 Sample preparation and ^{89}Y MAS−NMR characterization

^{89}Y solid-state MAS NMR measurement were carried out by Bruker Advanced III spectrometers operating at magnetic fields of 7.0 and 9.4 T, corresponding to ^{89}Y Larmor frequencies at 14.71 and 19.61 MHz, respectively. ^{89}Y spectra were recorded using the EASY pulse sequence that allows to efficiently remove the baseline distortion caused acoustic probe ringing occurring at low Larmor frequencies[86]. A short flip angle of 90° corresponding to a pulse duration of 28.5 μs and a recycling delay of 75 s were used to avoid saturation effects and to obtain qualitative MAS spectra. The spinning frequency was set to 6 kHz and 1152 transients were accumulated.

^{89}Y is spin-1/2 nucleus with 100% natural abundance and is very sensitive to local coordination environment, however the relaxation time of recording ^{89}Y solid-state NMR spectra is extremely long due to the low gyromagnetic ratio (γ)[87, 88], thus resulting an extremely long relaxation time. Under such condition, it is highly time consuming to record ^{89}Y solid−state NMR spectra with a large number of required transients to improve signal to noise ratio. In order to reduce the ^{89}Y relaxation time and the overall experimental time, a paramagnetic cation Gd^{3+} which can provide an effective nuclear spin source[73] was introduced into the garnet structure without forming impurities. Therefore, YAGs ceramic samples were prepared with the following process.

0.1 mol % Gd–doped directly crystallized x = 0, 0.1, 0.2, 0.25 YAGs and glass crystallized x = 0.3 and 0.4 samples for ^{89}Y NMR measurement were prepared with a general approach of diluting 1 mol % Gd–doped YAG with non-doped YAG. Taking the 0.1 mol % Gd: $Y_3Al_5O_{12}$ for example, its preparation procedures are: (1) weighing and blending starting

materials to make ~2g 1 mol% Gd: $Y_3Al_5O_{12}$ and ~2g $Y_3Al_5O_{12}$ powders; (2) the two batches of powders were respectively pressed into pellets; (3) the two pellets were calcined at 1200 °C for 10h in the furnace; (4) after calcining, the pellets were ground into fine powders before being weighed with a molar ratio of 9:1 (0.0018 mol $Y_3Al_5O_{12}$: 0.0002 mol Gd–doped $Y_3Al_5O_{12}$); (5) their powders were homogeneously blended before making a pellet; (5) the pellet was crushed into pieces and synthesized by ADL technique; (6) checking phase and waiting for NMR measurement (x = 0.3 and 0.4 samples were made into glass beads by ADL and then crystallized in the furnace); (7) powdered sample was filled in a rotor and measured by NMR (Avance III HD Bruker NMR spectrometer).

2.2.7 Sample preparation and EXAFS characterization

The coordination of excess Y^{3+} in ns−YAGs (x = 0, 0.1, 0.2, 0.25was also studied by XANES−EXAFS, and s−YAG with pure 8−coordinate Y^{3+} works as a reference. YAGs sample powders of x = 0, 0.1, 0.2 and 0.25 compositions were respectively mixed with boron nitride powders with mass ratio of 1:7. Their powders were blended in ethanol using mortar and pestle for around 50 min. The powders mixture was later pressed under 1.5 tonne isostatic pressure and into a pellet with 12mm in diameter. Mass per unit area of each pellet was determined by software to make yttrium absorbance jump equal to 1 at K edge in order to obtain strong enough signal without saturating the detector. Absorption coefficient was determined by the DIFFABS beam line at SOLEIL. The measurement was performed in an energy region of 17 – 17.985 keV with energy steps from 1 to 3 eV depending on energy region. Each sample was scanned with an acquisition of 1sec/point and four times to ensure a good signal/noise. Incident X−ray penetrates the pellet and transmit, its initial and final intensity of the beam allow for calculating the X−ray absorption coefficient μ of the sample.

$$I = I_0 e^{-\mu t}$$

Where I_0 and I are respectively intensities of incident and transmitted beam, μ is the energy dependent absorption coefficient and t is the thickness of the sample.

2.2.8 DFT computation

Plane wave based Density Function Theory (DFT) computations with periodic boundary conditions of ^{89}Y NMR parameters have been performed using the Castep code[89, 90]. An energy cutoff of 600eV was used for the plane-wave basis set expansion and the Brillouin zone was sampled using a Monkhorst−Pack grid spacing of 0.04 $Å^{-1}$. These computational

parameters were used for both geometry optimization and calculation of NMR parameters. The PAW[91, 92] and GIPAW[93] algorithms were respectively used for computing the electric field gradient (EFG) and NMR chemical-shielding tensors.

2.3 Results

2.3.1 Initial synthesis of non-stoichiometric YAG $Y_{3.2}Al_{4.8}O_{12}$ by ADL

$Y_2Al_3O_{7.5}$ was similarly synthesized by aerodynamic levitation method as done for $La_2Ga_3O_{7.5}$ to try to obtain an yttrium aluminum melilite. $Y_2Al_3O_{7.5}$ sample bead was deeply under-cooled by cutting the laser power from 2200–2300 °C. It was interesting that after many rounds of synthesis this composition obtained three kinds of beads with different looks as shown in **figure 2.1** (photo) — one translucent bead, one white smooth bead and one white smooth bead. XRD results (figure 2.2) implied that the translucent bead was "glass" (imperfect glass, which is presented in details in chapter 4) and white rough bead (the third bead) was biphasic $YAlO_3/Al_2O_3$. Amazingly the white smooth one is garnet. As $Y_2Al_3O_{7.5}$ garnet contains 40 at.% which is obviously larger than 37.5 at.% Y for stoichiometric YAG ($Y_3Al_5O_{12}$), the composition $Y_2Al_3O_{7.5}$ was probably synthesized as $Y_{3.2}Al_{4.8}O_{12}$ garnet with high nonstoichiometry or excess Y^{3+} in the garnet structure lattice. This interested us a lot to find the compositional limit of $Y_{3+x}Al_{5-x}O_{12}$ garnets.

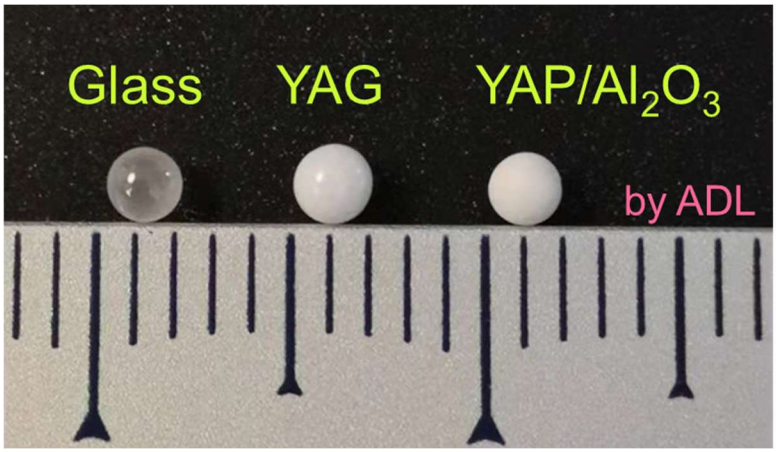

Figure 2.1. *Photo of translucent glass, gloss YAG and matt YAP/Al_2O_3 beads with composition of $Y_{3.2}Al_{4.8}O_{12}$. All the beads were prepared by direct crystallisation in argon using ADL. The size of each bead is smaller than 2 mm in diameter.*

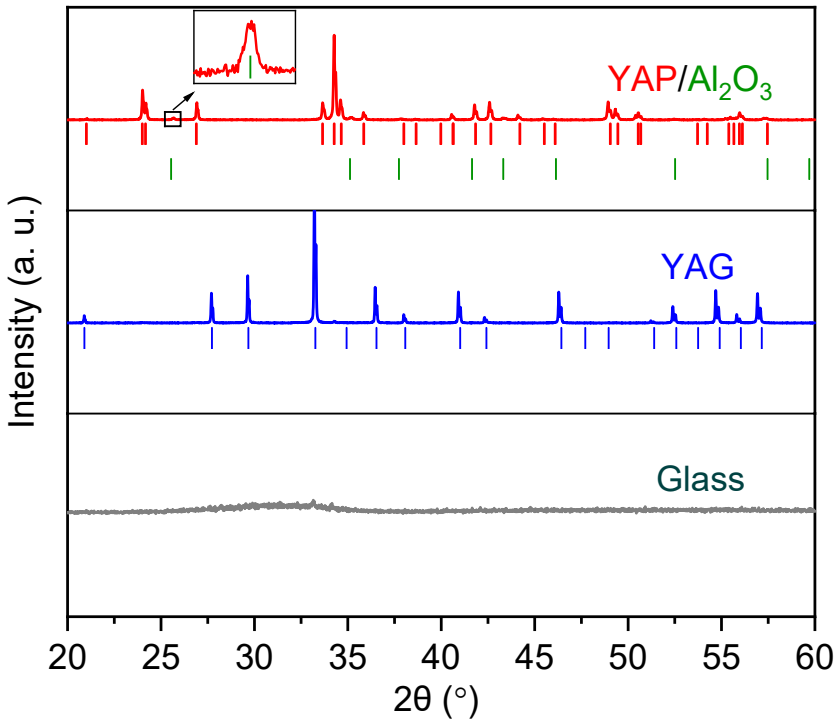

Figure 2.2. *XRD patterns of glass, YAG and biphasic YAP/Al_2O_3 prepared by ADL in argon. They all were obtained from $Y_{3.2}Al_{4.8}O_{12}$ composition which is corresponding to $Y_2Al_3O_{7.5}$. The small insert above the YAP/Al_2O_3 enlarges the diffraction peak of Al_2O_3 at 25.7° 2θ.*

2.3.2 Compositional limits of $Y_{3+x}Al_{5-x}O_{12}$ with argon carrier gas

Although it was the first time we synthesized $Y_{3.2}Al_{4.8}O_{12}$ YAG, the substitution of Y^{3+} for Al^{3+} at this stage, it was worth to synthesize other YAGs by changing the Y/Al ratio in the mixture of starting materials, to see if a systematic evolution exists, and to find the maximum level of non-stoichiometry. Then in the following work, $Y_{3+x}Al_{5-x}O_{12}$ samples with x varies in (-0.1, 0.3) were tried to be synthesized by the same approach as for $Y_{3.2}Al_{4.8}O_{12}$: directly crystallized (DC) from the melt in argon using ADL technique, they were carefully synthesized in order to obtain sample beads with glossy appearance. XRD patterns (**figure 2.3**) of these as-synthesized samples determined that $-0.1 \leq x \leq 0.29$ samples obtained single garnet phase, while $x = 0.3$ appears as a mixture of YAG, YAP and Al_2O_3. By looking at the diffraction peak of the garnet phase in 33−34° 2θ, one can confirm that as x increases, the diffraction peaks of these pure YAG phases systematically shift to lower 2θ due to the systematic increase of the cell volume, which may indicate a garnet solid solution has been obtained in the $-0.1 \leq x \leq 0.29$ range.

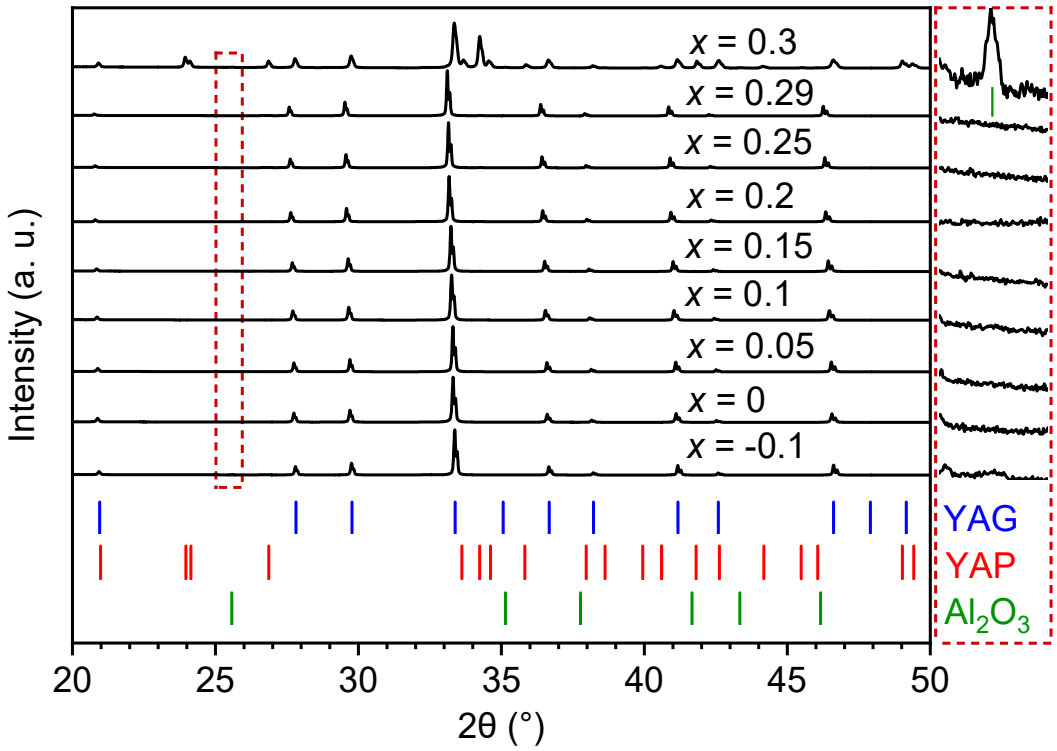

Figure 2.3. *XRD patterns of $Y_{3+x}Al_{5-x}O_{12}$ (-0.1 ≤ x ≤ 0.3) ceramics prepared by ADL in argon. Ticks in blue, red and green are respectively indicate the Bragg diffraction positions of YAG, YAP and Al_2O_3. The diffraction patterns in 25−26 °2θ range are enlarged and shown in the right dashed box. The sole peak at 25.5 °2θ in x = 0.3 indicates the presence of Al_2O_3 phase.*

2.3.3 Attempt to synthesize $Y_{3+x}Al_{5-x}O_{12}$ ($x \geq 0.3$) ns-YAG by solid state reaction method

Solid state reaction (SSR) synthesis was attempted for $Y_{3+x}Al_{5-x}O_{12}$ (x = 0, 0.2 and 0.4) garnets, to provide a comparison with results of direct crystallisation. **Figure 2.4** shows after the synthesis at 1500 °C for 10 h, x = 0 was isolated with pure garnet phase, while x = 0.2 contained 75.2(3) wt.% cubic garnet (YAG), 22.2(3) wt.% hexagonal perovskite−type $YAlO_3$ (YAP) and 2.4(2) wt.% monoclinic $Y_4Al_2O_9$ (YAM). The x = 0.4 sample contained 49.5 (3) wt.% YAG, 45.7(2) wt.% YAP, 3.1(2) wt.% YAM and a fourth phase Al_2O_3 with a content of 1.5(2) wt.%. As the Y concentrations in the three Y-containing phase are in an order of YAM > YAP > YAG, the concentration distribution of the three phases in the x = 0.2 and 0.4 sample are reasonable. Lattice parameter of YAG phase in these two compositions were 12.0007(1) Å and 12.0008(1) Å, they are the same to that of stoichiometric YAG. Which means under the applied synthesis conditions, there was no ns−stoichiometric YAG produced from x = 0.2 and 0.4 nominal compositions. It agrees with

the unshifted diffraction peaks of garnet phase in these two compositions compared to that of x = 0 YAG phase.

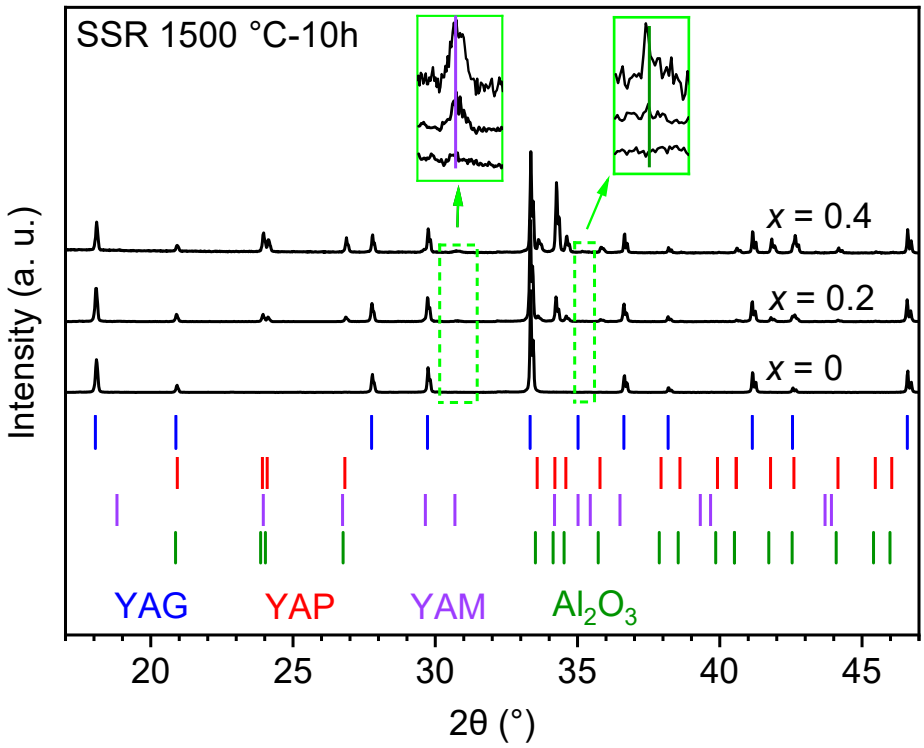

Figure 2.4. *XRD patterns of $Y_{3+x}Al_{5-x}O_{12}$ (x = 0, 0.2 and 0.4) synthesized by solid state reaction (SSR) method at 1500°C. The four series of vertical ticks indicate the Bragg diffraction positions of YAG, YAP YAM and Al_2O_3. The two small inserts respectively enlarge the diffraction peaks at around 30.8° and 35.2° 2θ, confirming the existence of YAM in x = 0.2 and 0.4 compositions and Al_2O_3 in x = 0.4.*

2.3.4 Effect of cooling rate on $Y_{3+x}Al_{5-x}O_{12}$ phase formation

Synthesis conditions of directly crystallized $Y_{3.2}Al_{4.8}O_{12}$ (x = 0.2) YAG were explored by cooling experiment using ADL technique in argon and essential software. The cooling rate was controlled by changing the sample mass over 9−39 mg with 1 mg interval. **Figure 2.5** shows cooling curves of these samples, the samples were gradually heated up to 2200−2300 °C. Three distinctive cooling curves were obtained (**figure 2.5**). The grey ones drop smoothly after shutting down lasers and show no peak caused by temperature recalescence in crystallisation process. The blues ones show sharp peaks where cooling process is fast after the temperature recalescence. Temperature recalescence in red cooling curves appears earlier than that in blues curves, and is followed with sluggish

cooling curve tail. These three kinds of cooling curves respectively result in glass, YAG and YAP/Al_2O_3 samples as in **figure 2.1**.

The temperature at ascending point just before the temperature recalescence represents the crystallisation temperature. It enables us to see the difference in crystallisation temperature between YAG and YAP/Al_2O_3. YAG crystallizes at 880−1000 °C (as the pyrometer was not calibrated, there could be a difference between the measured and real temperature) and YAP crystallizes at 1220−1320 °C. Both crystallisation temperature ranges are below the equilibrium melting temperature[44]. Cooling rate in figure 2.6 is defined by $\Delta T/\Delta t$ in 2100−1300 °C, this temperature range was chosen as it covers the cooling process of all the samples before their crystallisation and ensures that the concerned cooling range is as broad as possible to make the cooling rates of the three sets of samples comparable. From **figure 2.6**, we see that glass was obtained when the cooling rate exceeds 550 °C s^{-1}, YAG is inaccessible below 400 °C s^{-1}, and garnet can only be isolated by direct crystallisation in 400−550 °C s^{-1}. We can also find that from glass to YAG and to YAP, the cooling rate has a trend of monotone decreasing, which implies that the evolution trend of cooling rate is the result of sample mass and the structure of the sample as well.

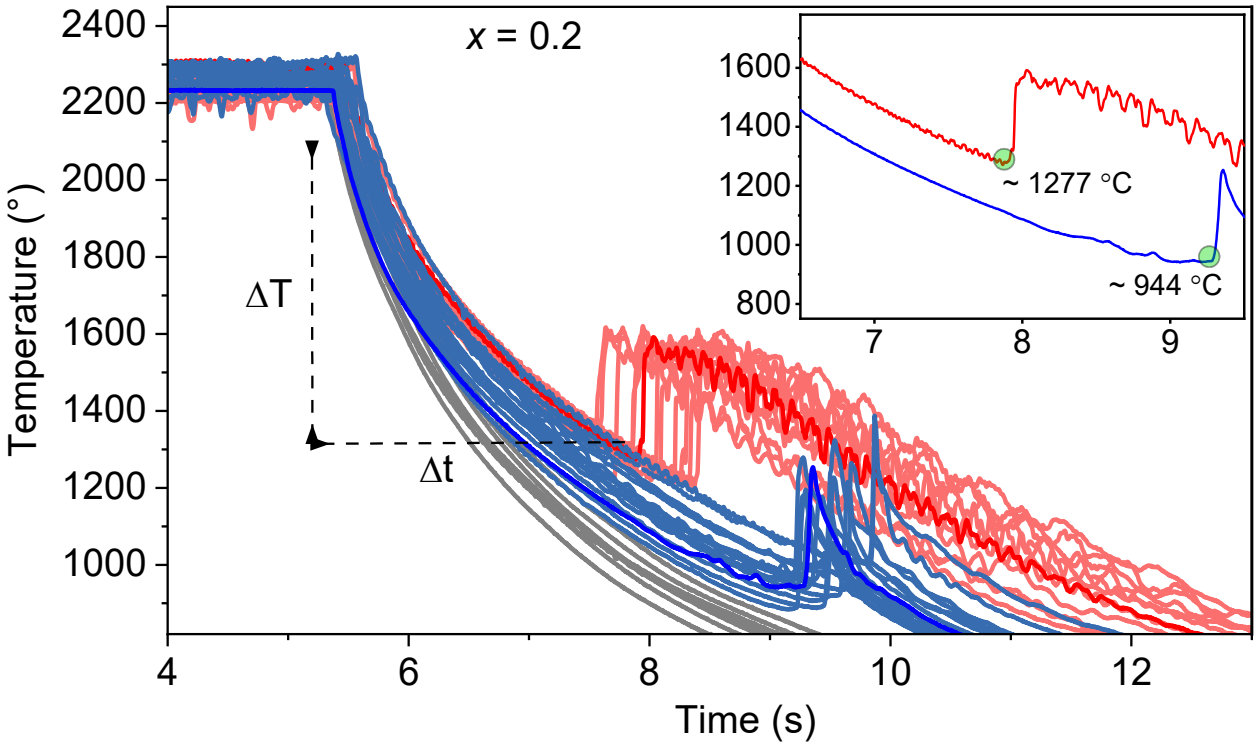

Figure 2.5. *Cooling curves of 9−39 mg x = 0.2 samples with 1 mg interval. The dark grey, dark blue and dark red curves are representatives clearly showing the shapes of these three groups of curves, they resulted in glass, garnet and biphasic YAP/Al_2O_3. The insert enlarges a fraction of the cooling process of the blue and red curves stressed in main figure, it indicates the resulted YAG and biphasic YAP/Al_2O_3 respectively crystallized at around 944 ℃ and 1277 ℃. After crystallisation. Temperatures were monitored by pyrometer.*

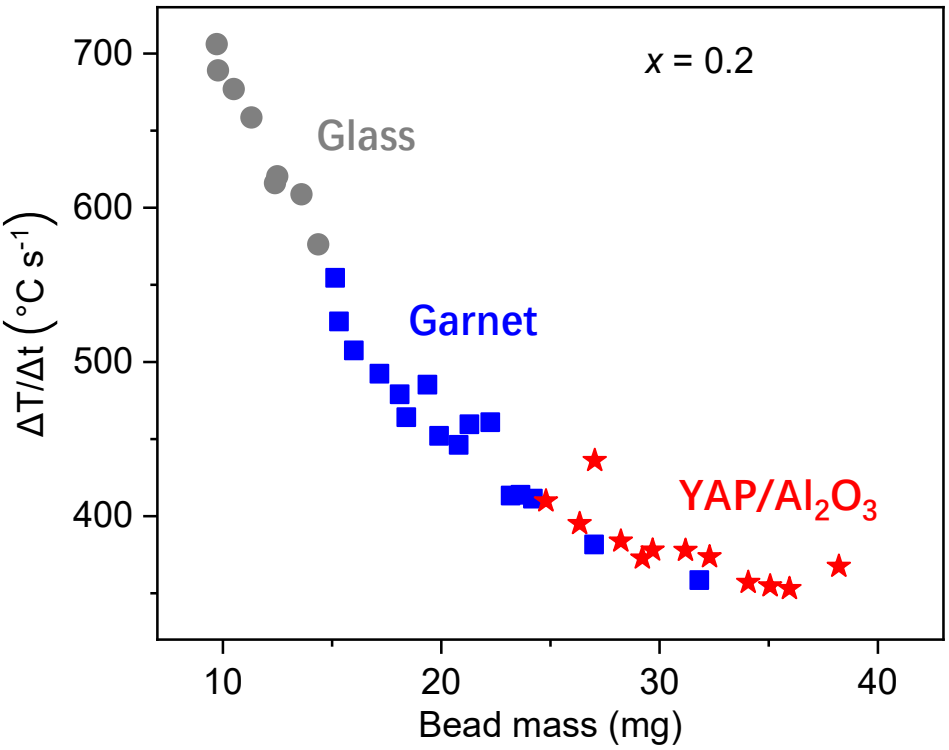

Figure 2.6. *Cooling rate versus bead mass of x = 0.2 ($Y_{3.2}Al_{4.8}O_{12}$). These cooling rates were processed from the cooling curves in figure 2.5 The cooling rate was calculated by dividing 2100−1300 ℃ temperature difference by the corresponding cooling duration each sample underwent.*

2.3.5 Effect of enhanced cooling rates on the compositional limits of $Y_{3+x}Al_{5-x}O_{12}$

As the formation of *x* = 0.2 ns−YAG is related to cooling rate, it inspired us to synthesize *x* = 0.3 ns−YAG by heating a sample as small as possible, but the resulting phase was still a mixed phase of YAG, YAP and Al_2O_3. Then we thought lighter levitating gas may help to enhance the cooling rate, which can be more efficient than decreasing the sample mass. The cooling experiments to find the most efficient way to enhance cooling rate were performed on both *x* = 0 and 0.2 compositions. Levitated gases of argon, oxygen and helium were used for the two compositions. All sample masses were controlled as 9 mg. The samples were heated up to 2000−2100 °C lasting for several seconds, and then were cooled down by instantly shutting down lasers. Cooling curves of *x* = 0 and 0.2 compositions are closed to each other when the same levitated gas was used. **Figure 2.7** shows that three groups of cooling curves were recorded regarding to gas type. The cooling rate of samples cooled down in oxygen is higher than in argon, but the fastest cooling rate was by far achieved using helium. The order of cooling rate ΔT/Δt under the three gases is

He > O_2 > Ar (insert of **figure 2.7**). It was enhanced from ~ 350 °C s^{-1} to ~ 900 °C s^{-1} when changing from Ar to He.

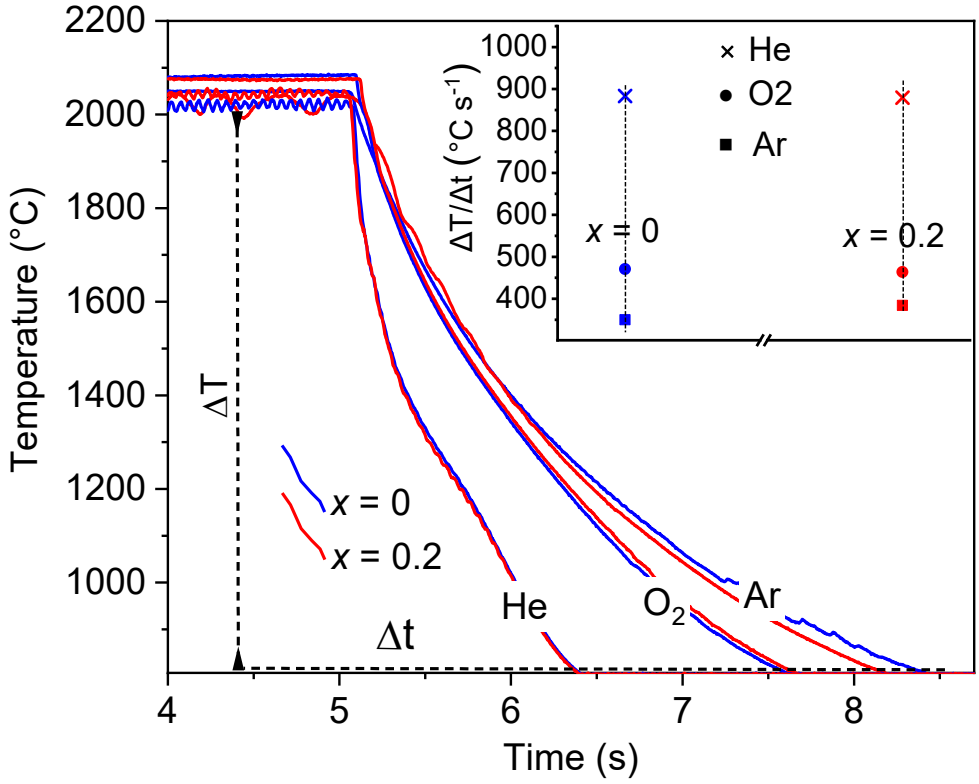

Figure 2.7. *Cooling curves of 9 mg x = 0 and 0.2 glass beads collected when samples were synthesized in Ar, O_2 and He. Cooling rate was considered in 2000−810 °C range.*

Helium was then used to synthesize x > 0.29 compositions. However, under helium the sample bead vibrates violently which lowers the probability to prepare a glass bead. Oxygen was then considered to be used as a compromise between levitation stability and cooling rate. Fortunately, x = 0.3, 0.35 and 0.4 sample beads were levitated stably in oxygen and resulted in glass samples. As glass crystallisation has been known as an effective way to synthesize aimed ceramics[8, 11, 15, 94], it was then tested as a possible method to prepare x = 0.3, 0.35 and 0.4 garnet. The x = 0.3, 0.35 and 0.4 glass compositions were heated at 1100 °C for 5h, XRD patterns of the three crystallized samples indicated that they are single YAG phase (**figure 2.8**). Although x = 0.45 was laser−heated in oxygen, it could not be prepared as a glass. It directly crystallized into a mixture of YAP, stoichiometric YAG and Al_2O_3. Helium was also tested to make a x = 0.45 glass, but it failed as the sample frequently touched the nozzle, which caused the sample to crystalize into mixture of YAG/YAP/Al_2O_3. From a global perspective, diffraction peaks

of YAG shift steadily towards lower 2θ angle as *x* values increases. $Y_{3+x}Al_{5-x}O_{12}$ solid solution range was extended from $0 \leq x \leq 0.29$ to $0 \leq x \leq 0.4$.

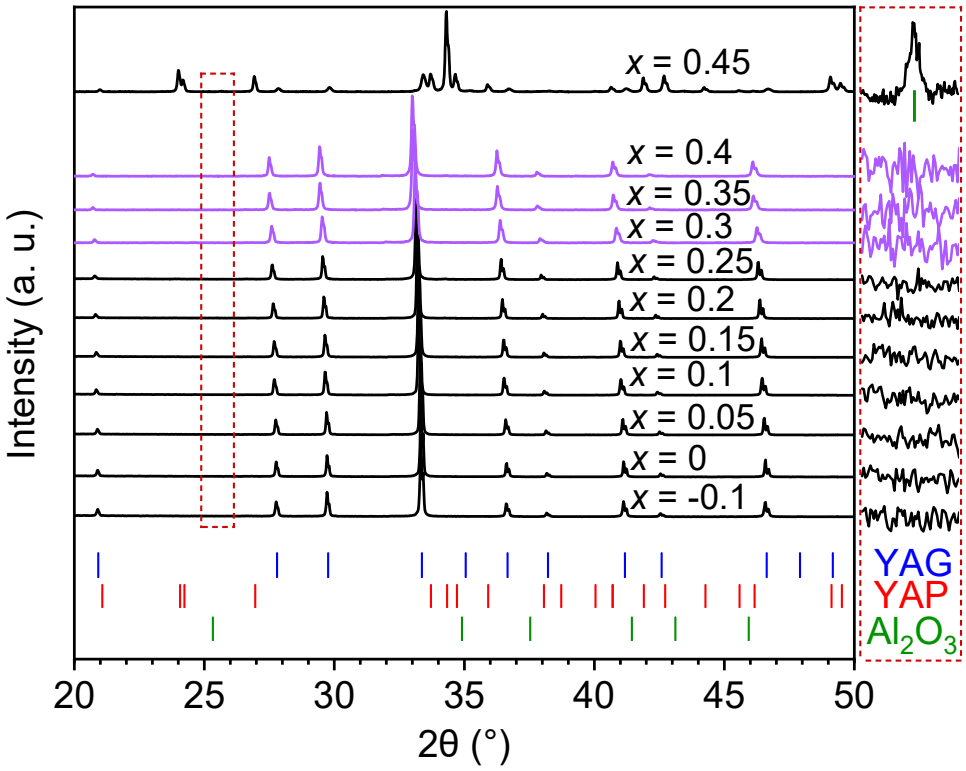

Figure 2.8. *XRD patterns of $Y_{3+x}Al_{5-x}O_{12}$ ($-0.1 \leq x \leq 0.45$) ceramics. $-0.1 \leq x \leq 0.25$ (black) were crystallized directly from melt in argon, $0.3 \leq x \leq 0.4$ (purple)were crystallized from glass which were obtained by fast cooling in oxygen. $x = 0.45$ was also prepared in oxygen and directly crystallized from melt, as it cannot be made into glass in oxygen. The blue, red and green ticks respectively indicate the Bragg diffraction positions of YAG, YAP and Al_2O_3. XRD patterns in the dashed box on the right magnifies the diffraction patterns at 25−26° 2θ range.*

2.3.6 Thermal stability of ns−YAGs

2.3.6.1 Crystallisation of ns−YAG under near−equilibrium conditions

To determine what the thermodynamically stable products are when $Y_{3+x}Al_{5-x}O_{12}$ ($x = 0$ and 0.2) are synthesized under the near-equilibrium conditions by ADL, sample mass was aimed at 65 mg which was much heavier than the 9-39mg samples for the cooling experiments shown above, aiming to slow the heat release process. Samples were heated up to around 1960 °C which was detected by pyrometer and is close to the reported melting temperature 1940±7 °C[44]. Figure 2.9 shows a temperature plateau appearing at 1840±10

°C on the cooling curves (blue for x = 0 and red for x = 0.2), it is corresponding to crystallisation. After the temperature plateau, the cooling process of x = 0.2 is slower than that of x = 0. In the 1800 °C−805 °C temperature range, x = 0.2 underwent a cooling rate of 170 °C s^{-1} which is lower than 220 °C s^{-1} of x = 0. SEM morphologies of polished 65 mg x = 0 and 0.2 beads indicate both samples are biphasic (insert of **figure 2.9**).

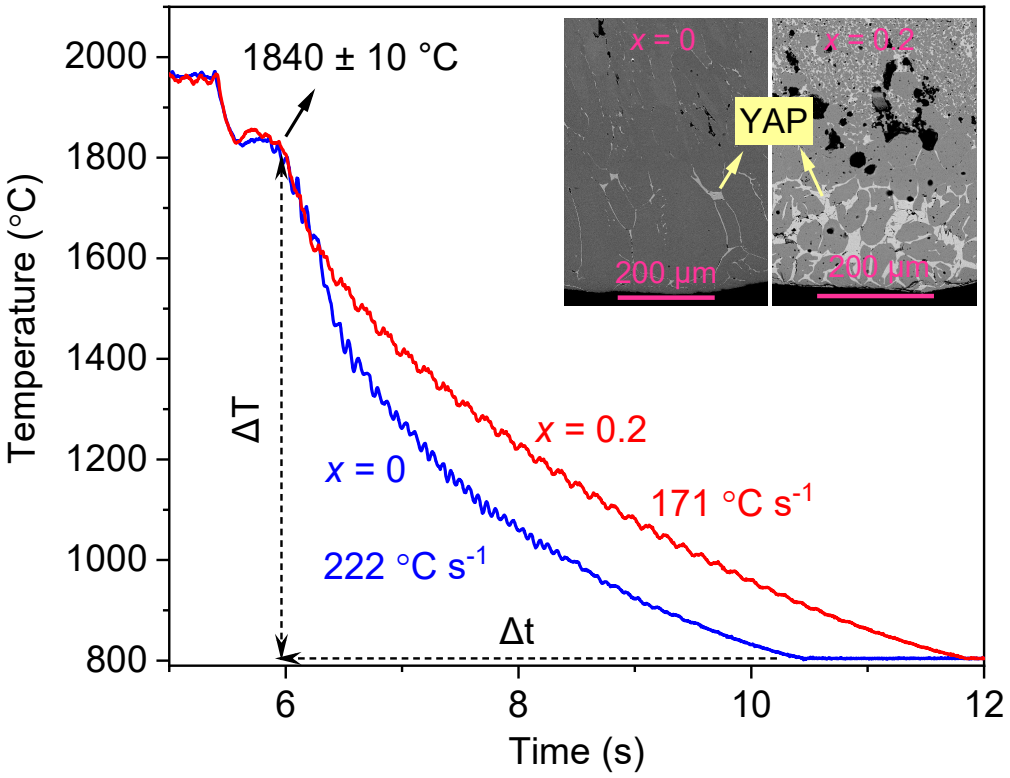

Figure 2.9. *Cooling curves of 65 mg $Y_{3+x}Al_{5-x}O_{12}$ (x = 0 and 0.2) after instantly cutting off laser power. The samples were prepared in argon. The cooling rate was calculated by (1800−805) °C/Δt, where Δt is cooling duration in 1800−805 °C temperature range. The insert shows SEM morphology of polished x = 0 and 0.2 beads. Both samples are biphasic YAG(dark grey)/YAP(light grey).*

Tables 2.1 and **2.2** are respectively EDS results of x = 0 and 0.2 samples, both implies that light and dark grey areas from SEM morphologies are respectively YAP and YAG. There is more YAP produced in x = 0.2 than in x = 0, because the original x = 0.2 composition was Y−rich. XRD patterns (**figure 2.10**) show that diffraction peaks of YAP phase in x = 0 are weak, and they are more intense for x = 0.2. Rietveld refinement on XRD data revealed x = 0 contains 96.9(2) wt.% YAG and 3.0(2) wt.% YAP, and x = 0.2 exhibits 82.3(2) wt.% YAG and 17.6(2) wt.% YAP. The refined lattice parameters of YAG phase in these two

compositions are respectively 12.0149(1) Å ~12.0157(1) Å, which are almost corresponding to the same composition of $Y_{3.03}Al_{4.97}O_{12}$, indicating that the garnet phases the two 65 mg samples may still contain tiny amount of excess Y^{3+}.

Table 2.1 EDS results of 65 mg *x* = 0 sample prepared by ADL method in argon.

	light grey		dark grey	
	Y (at. %)	Al (at. %)	Y (at %)	Al (at. %)
	20.60	19.40	15.77	24.23
	20.62	19.38	15.76	24.24
	20.66	19.34	15.72	24.28
mean	**20.63**	**19.37**	**15.75**	**24.25**

Table 2.2 EDS results of 65 mg *x* = 0.2 sample prepared by ADL method in argon.

	light grey		dark grey	
	Y (at. %)	Al (at. %)	Y (at. %)	Al (at. %)
	20.66	19.34	15.93	24.07
	20.69	19.31	15.89	24.11
	20.69	19.31	15.88	24.12
mean	**20.68**	**19.32**	**15.90**	**24.10**

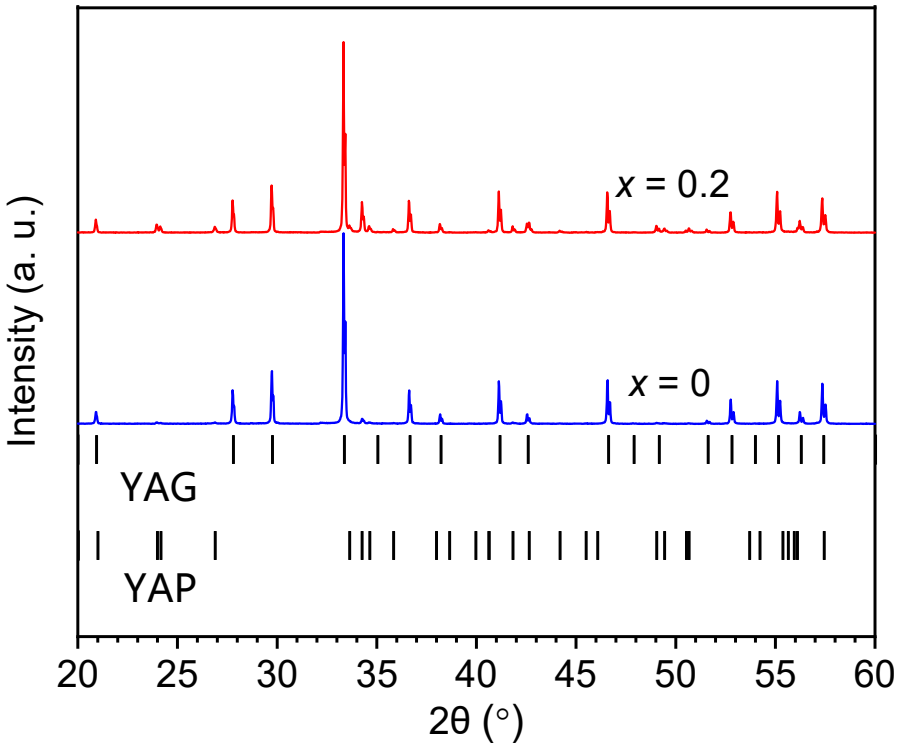

Figure 2.10. *XRD patterns of 65 mg $Y_{3+x}Al_{5-x}O_{12}$ (x = 0 and 0.2) beads resulting from cooling experiment (figure 2.5). The ticks above and below respectively indicate Bragg diffraction positions of YAG and YAP.*

2.3.6.2 Thermal decomposition of ns−YAG by ex−situ method

To see if $Y_{3+x}Al_{5-x}O_{12}$ (x = 0.2 and 0.4) ns-YAGs can sustain the high temperature on which x = 0 can be isolated with single garnet, the two ns-YAGs samples were heated at 1600 °C for 12h in the furnace with heating and cooling rates of 10 °C s^{-1}. Compared to x = 0 s-YAG, x = 0.2 decomposed into stoichiometric YAG and YAM, and x = 0.4 decomposed into YAG and YAP. Diffraction peaks of YAG for x = 0.2 and 0.4 shift to higher 2θ corresponding to Bragg peak positions of x = 0 garnet (**figure 2.11**), and lattice parameter of YAG phase in the two compositions falls respectively from 12.070 (1) Å and 12.1354(1) Å to 12.0076(1) Å and 12.0082(1) Å (**figure 2.12**).

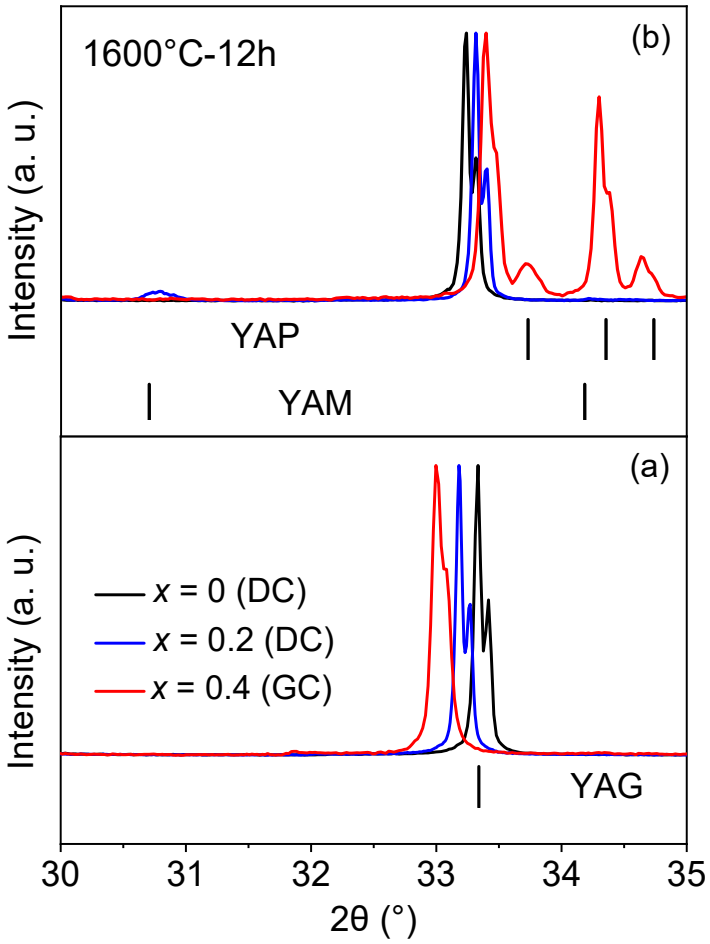

Figure 2.11. (a) *XRD patterns of directly crystallized x = 0 s−YAG and x = 0.2 and fully glass crystallized 0.4 ns−YAG.* ***(b)*** *XRD patterns of x = 0, 0.2 and 0.4 after annealing their YAGs at 1600 ℃ for 12h. The ticks indicate Bragg positions of YAP, YAM and YAG as labeled.*

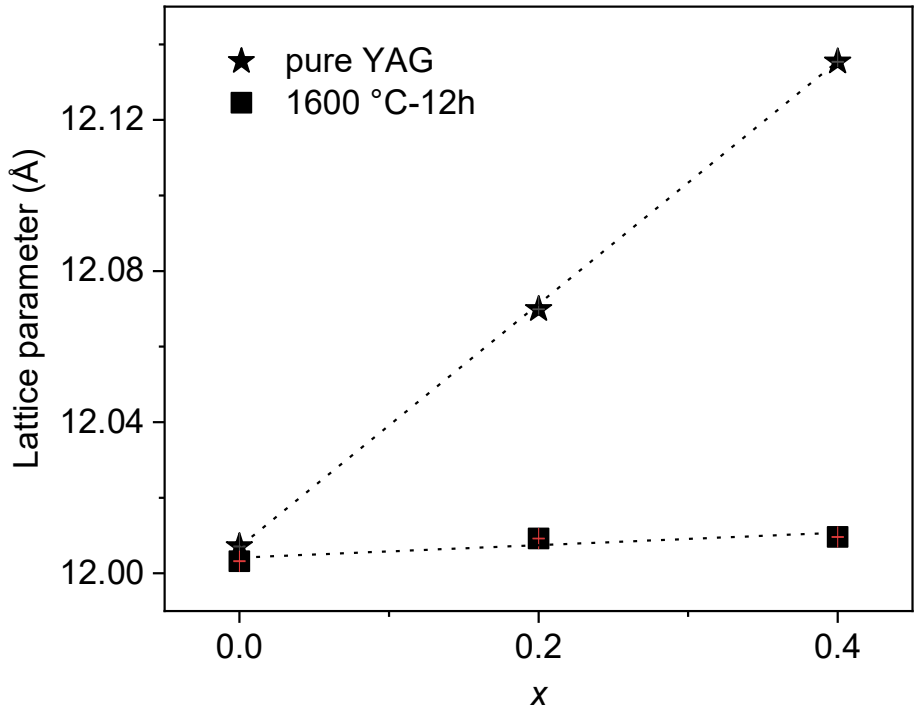

Figure 2.12. *Lattice parameter a of garnet phase in $Y_{3+x}Al_{5-x}O_{12}$ (x = 0, 0.2 and 0.4) before (star) and after (square) annealing at 1600 ℃ for 12h.*

2.3.6.3 Optimisation of the experimental set−up for in−situ VT−XRD measurements

As implied by the ex-situ decomposition experiment, x = 0.2 ($Y_{3.2}Al_{4.8}O_{12}$) and x = 0.4 ($Y_{3.4}Al_{4.6}O_{12}$) garnets are not as stable as x = 0 ($Y_3Al_5O_{12}$) as they yield a mixture of phases. In this section, x = 0.2 and 0.4 ns-YAGs were measured by in-situ VT−XRD equipped with a HTK16 furnace (detailed in appendix) aiming to determine their precise decomposition temperature. The x = 0.2 sample beads were ground into powders and mixed ethanol to make homogeneous paste for loading into a platinum sample holder with a cavity around 1 mm deep. Temperature for each data are labeled in figure 2.13. Over 1200–1600 °C, XRD patterns shift to lower 2θ angle as temperature increases, indicating a thermal expansion caused by heating. Each temperature was confirmed stable before the scanning and each scan took 30 min. **Figure 2.13** shows, in the whole temperature range, that the sample remains garnet phase, which is contradictory with the fact that the x = 0.2 ns−YAG was previously shown to decompose into stoichiometric YAG and YAM. Finally, this observation was attributed to the sample being too thick, thus inducing temperature gradients along the depth. The upper layer may have not been heated at lower than expected.

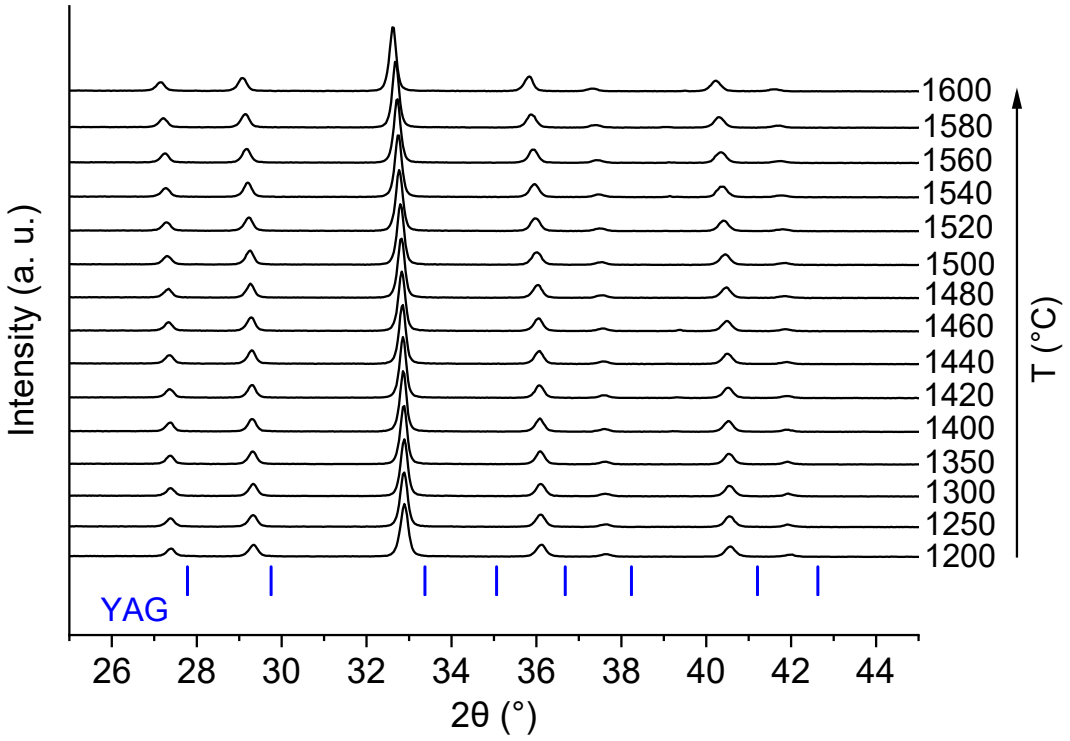

Figure 2.13. *VT−XRD patterns of x = 0.2 ($Y_{3.2}Al_{4.8}O_{12}$) ns−YAG in 1200–1600 ℃. The ticks indicate Bragg diffraction positions of YAG. The shift between ticks and peak positions of the pattern collected at 1200 ℃ is attributed to heating. No decomposition was observed, because the sample paste was too thick.*

In the second round of measurements, a platinum ribbon sample holder with a flat surface was used. Also, a vacuum environment below 10^{-4} mbar was used to prevent platinum evaporation at high temperature (especially above 1400°C)[95]. The sample paste with a certain thickness was pasted on the ribbon. After the measurement, the sample was cooled to room temperature. The sample was found to have peeled from the sample holder. This can happen as the paste could not bear the strain during the measurement, and a thinner paste may fix this problem. In the next (third) measurement, the paste was thinner than in the previous case. Unfortunately, after the same measurement process and the sample cooled to room temperature, the sample located in the middle of the ribbon was found to have melted. This can be explained from the setting of thermocouple and the sample itself. Two thermocouples are designed, one of them is placed in direct contact with the sample for accurate temperature measurement and control. As the sample paste was very thin, its part in the middle of Pt ribbon touched with thermocouple, it was under high temperature, furthermore each scan lasted for 30 minutes, it is possible for the thin sample layer in the

middle of the Pt ribbon melted. So in the last round of measurements (fourth attempt), the sample was carefully prepared with a moderate thickness. The final state of the sample after cooling was good without obvious damage (**figure 2.14**).

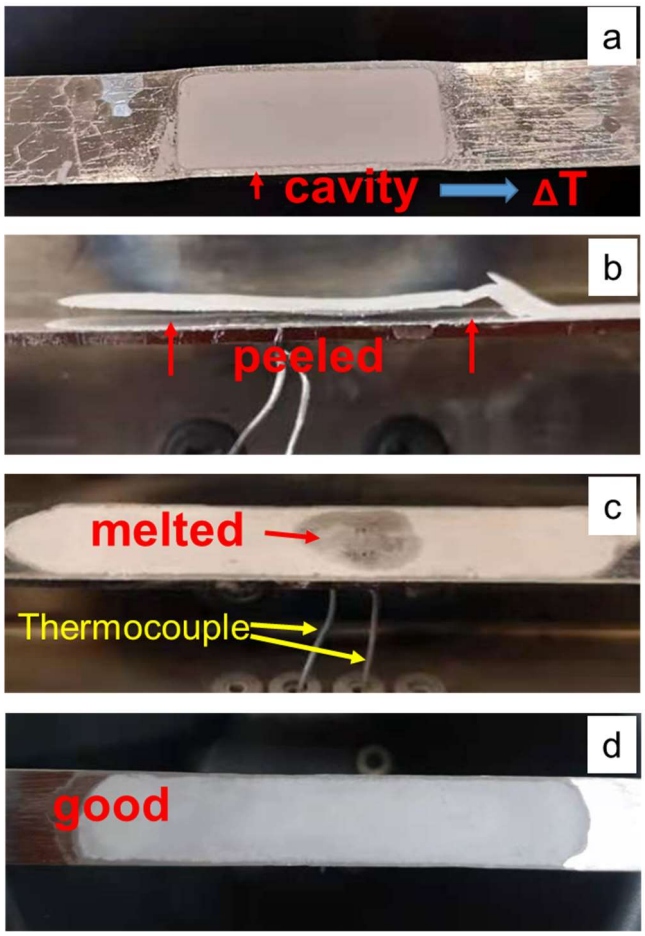

Figure 2.14. *Photos of the states of the samples after VT−XRD measurement under vacuum.* ***(a)*** *First round of measurement. Sample powders were filled in the Pt ribbon with a cavity.* ***(b)*** *Second round of measurement. Sample peeled from sample holder.* ***(c)*** *Third round of measurement. Sample melted in the middle where is close to thermocouple and heated sufficiently.* ***(d)*** *Fourth round of measurement. Sample in a good state after the measurement. The fourth round measurement produced acceptable XRD data at different temperatures and enables further analysis.*

2.3.6.4 In-situ observation of thermal decomposition of $Y_{3.2}Al_{4.8}O_{12}$ and $Y_{3.4}Al_{4.6}O_{12}$

Figure 2.15 shows VT−XRD patterns of x = 0.2 ($Y_{3.2}Al_{4.8}O_{12}$) sample from the fourth round measurement. The temperature range was extended to 30−1600 °C in order to present enough data points. Diffraction peaks of garnet phase shift to lower 2θ, caused by thermal expansion. As the temperature increases, diffraction peaks get broader due to phase

decomposition into s-YAG as heating process is going on. At 1350 °C, YAP diffraction peaks become visible and their content increases. At 1350 °C, YAM diffraction peaks emerges and their content starts to increase. At 1600 °C, the *x* = 0.2 sample becomes a mixture of 77.7(7) wt.% YAG, 8.4(3) wt.% YAP and 13.7(6) wt.% YAM (**figure 2.16**). **Figure 2.17** shows that the lattice parameter evolves in a linear growing trend up to 1350 °C where the first impurity YAM starts to grow, then it reaches a short plateau in 1350–1450 °C. The bending of the trend of the lattice parameter at 1350 °C may indicate the garnet has been transformed into stoichiometric YAG (named G2 in the figure of phase fraction), and the following dropping of the lattice parameter can be ascribed to the continuous formation of YAP and YAM impurities.

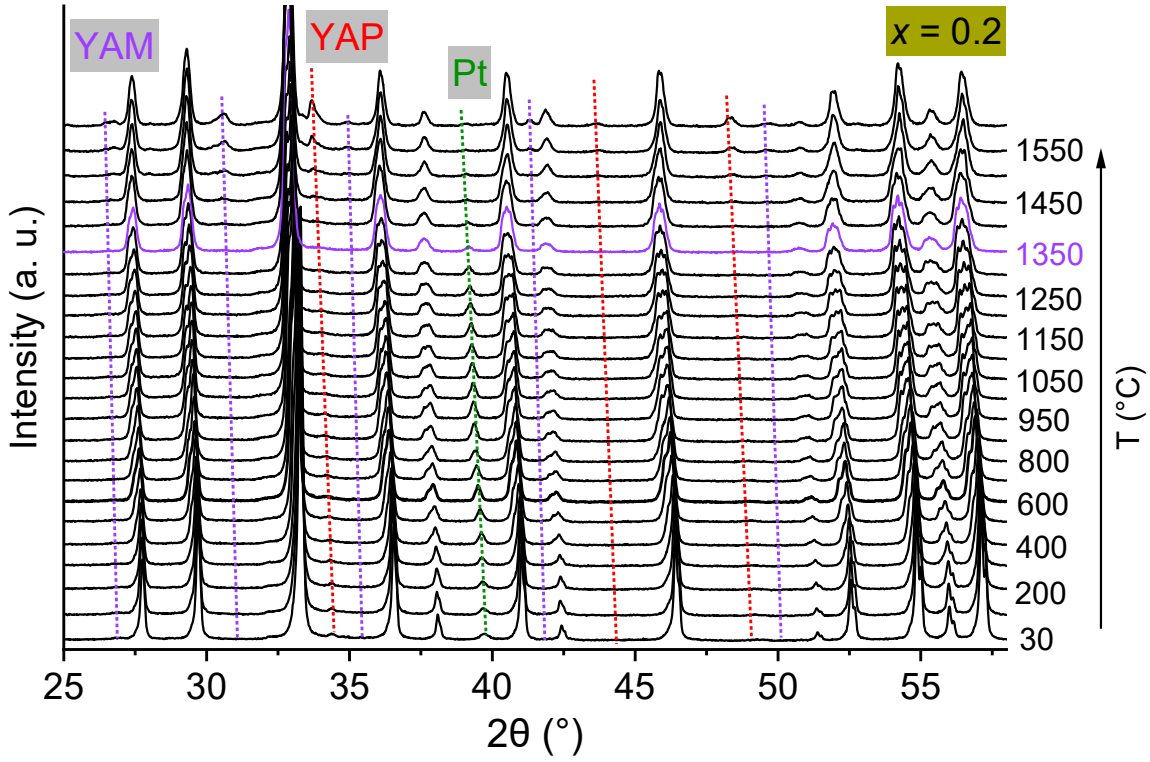

Figure 2.15. *VT−XRD patterns of x = 0.2 ($Y_{3.2}Al_{4.8}O_{12}$) ns−YAG in 30−1600 °C (from fourth measurement). In 30−900 °C range and 900 –1600 °C range, XRD data were respectively collected every 100 °C and 50 °C. Diffraction peak indexed by Pt comes from platinum ribbon used as sample holder.*

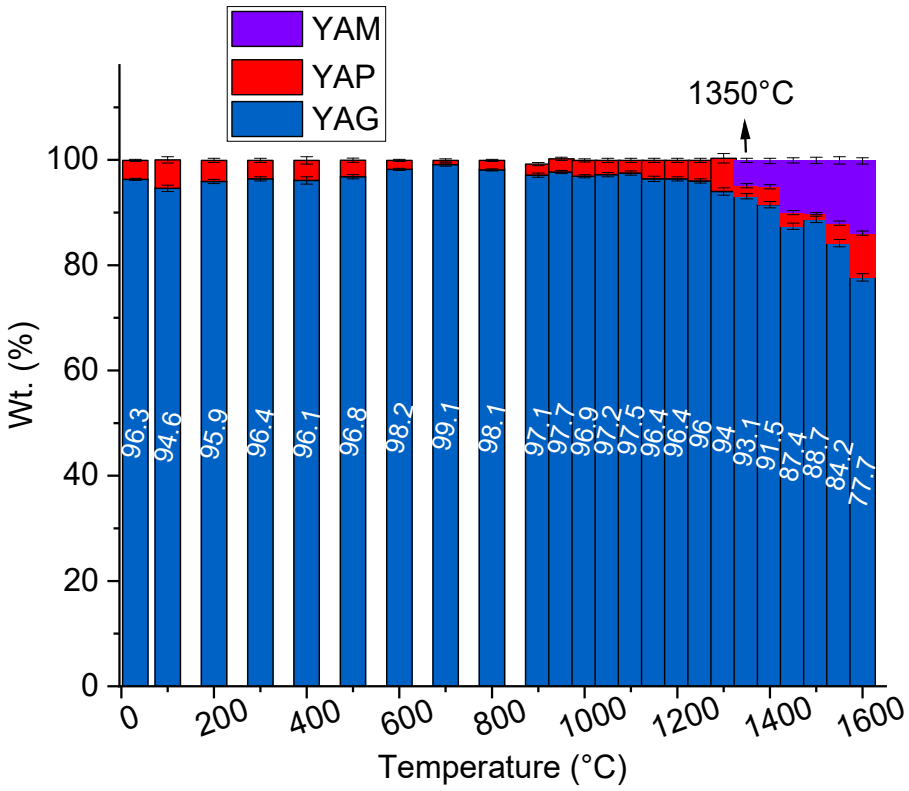

Figure 2.16. *Phase fractions of YAG(blue), secondary garnet (G2), YAP(red) and YAM (purple) in x = 0.2 ($Y_{3.2}Al_{4.8}O_{12}$) composition, they are from Rietveld structural refinement performed on XRD data collected by HTK16 VT−XRD at different temperatures.*

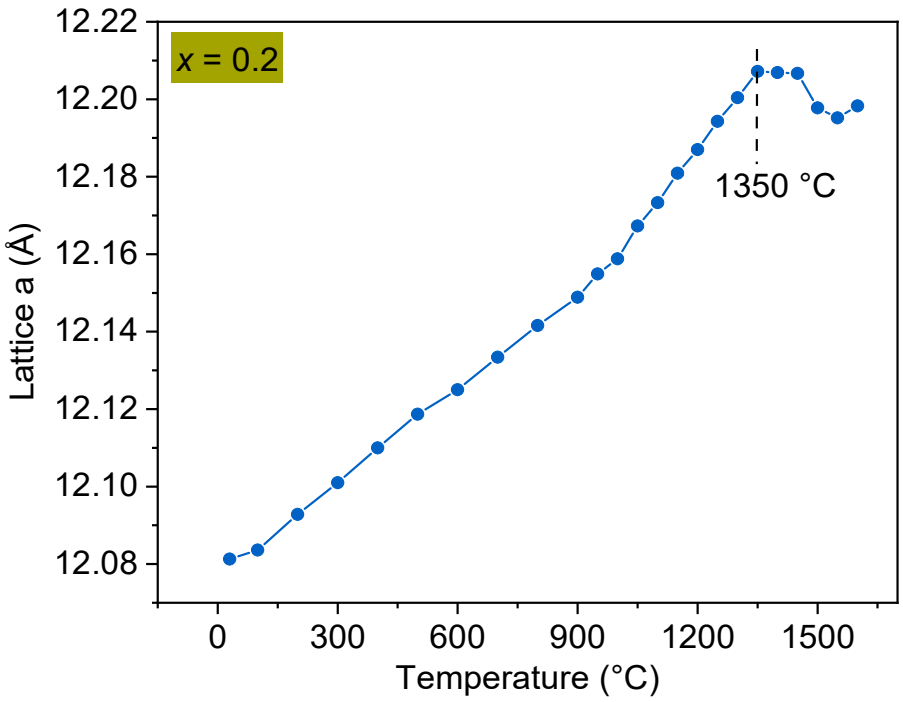

Figure 2.17. *Lattice parameter evolution of garnet in x = 0.2 ($Y_{3.2}Al_{4.8}O_{12}$) sample during the heating in 30 – 1600 ℃. Lattice parameter was obtained from Rietveld refinement.*

Similarly to x = 0.2, x = 0.4 ($Y_{3.4}Al_{4.6}O_{12}$), ns−YAG starts to decompose at 1350 °C, where x = 0.2 ns−YAG starts to decompose into YAM (**figure 2.18**). The secondary phase appears with its peaks presented on the right of the peaks of main garnet phase. This shows the start of phase transformation from ns−YAG into s−YAG, meanwhile at this temperature, YAP and YAM phase start to grow. **Figure 2.19** shows before 1350 °C, the sample is pure garnet phase. After this temperature, garnet phase decreases and, YAP and YAM fractions increase. YAM fraction reaches its maximum of 4.7(2) wt. % at 1400 °C, and peaks of garnet firmly shift to higher 2θ. Also at this temperature the YAP fraction surges by around 15 wt. %. At 1600 °C, the sample is mixed with 64.8(2) wt. % YAG and 35.1(2) wt. % YAP. Lattice parameter (**figure 2.20**) was obtained by Pawley refinement, it increases in a linear trend till 1350 °C, and then decreases due to the sudden increase of YAP.

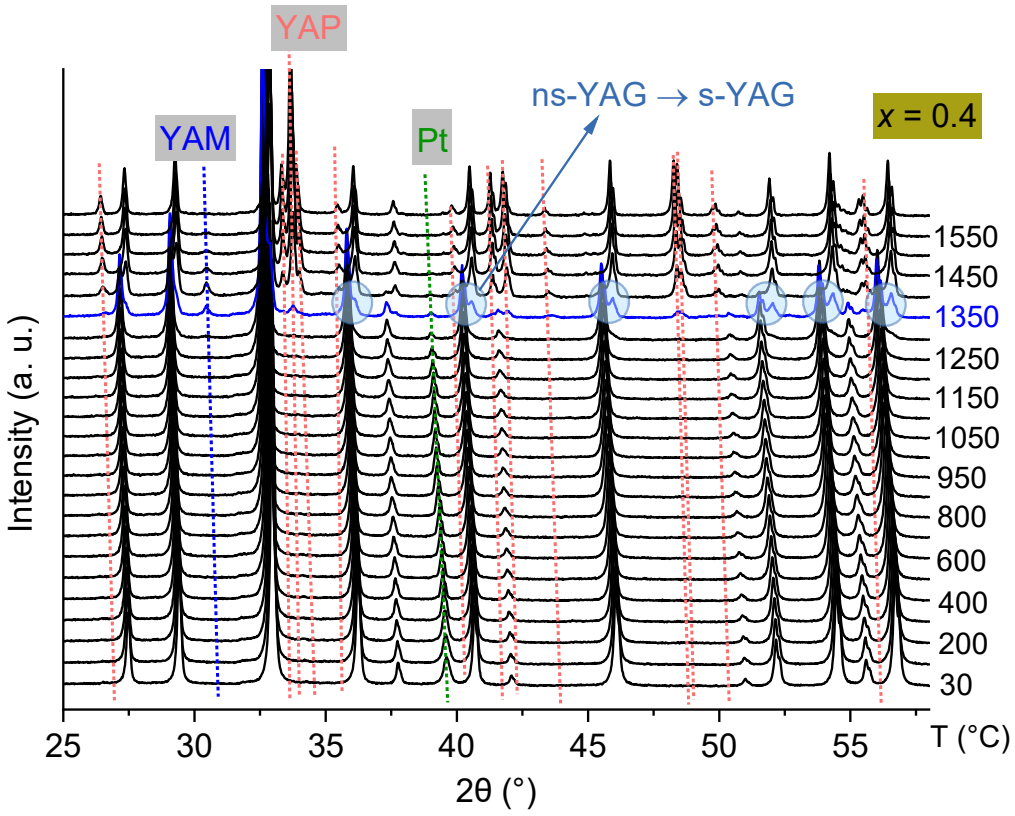

Figure 2.18. *VT−XRD patterns of x = 0.4 ($Y_{3.4}Al_{4.6}O_{12}$) ns−YAG. The XRD patterns were collected under the same heating and data collecting conditions as for x = 0.2 composition. The diffraction peak of platinum comes from the ribbon where is exposed to the X−ray scanned area.*

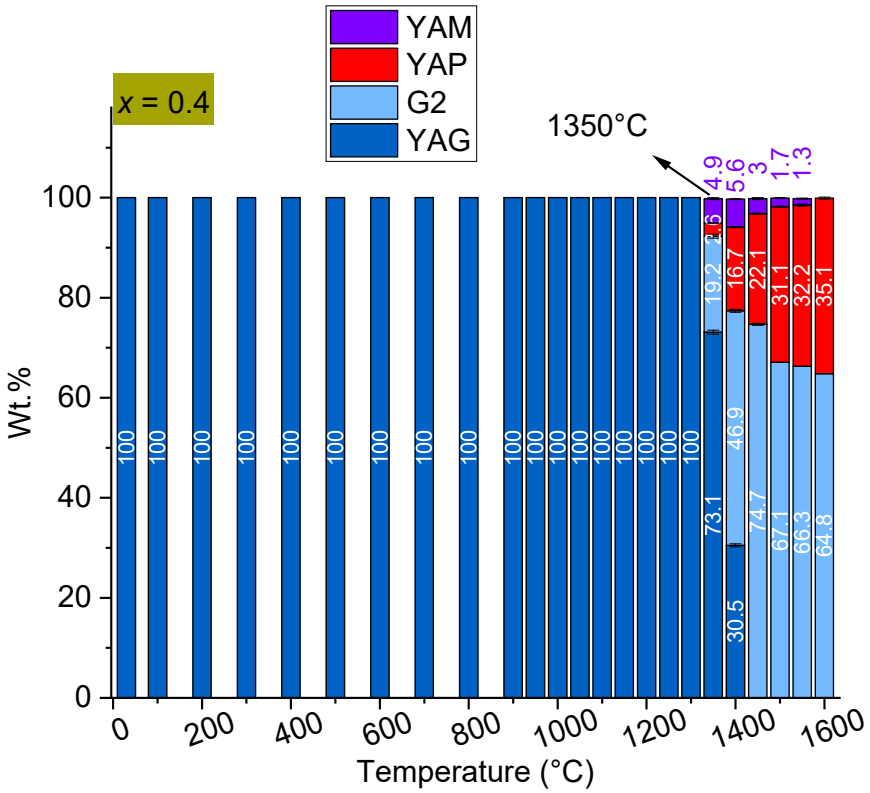

Figure 2.19. *Phase fractions of YAG (blue), YAP(red), G2 (secondary garnet, light blue) and YAM(purple) in x = 0.4 composition, they were obtained by the same process as for x = 0.2 composition.*

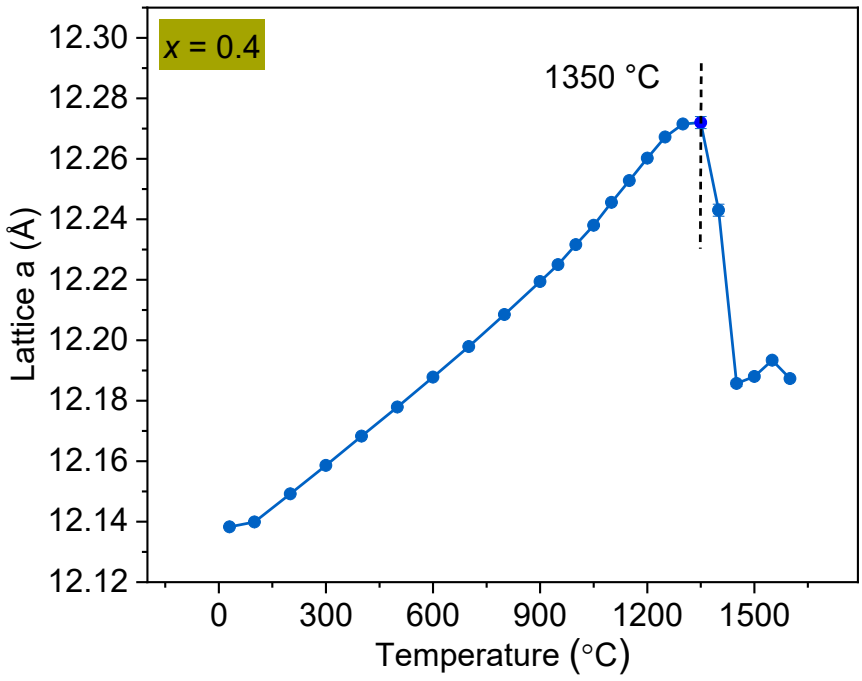

Figure 2.20. *Lattice parameter evolution of garnet in x = 0.4 along the heating in 30−1600℃. The data points were obtained from Pawley refinement.*

Both $Y_{3+x}Al_{5-x}O_{12}$ (x = 0.2 and x = 0.4) ns−YAGs stay stable up to 1350 °C and decompose into YAP and YAM phases. The thorough phase decomposition in the two compositions lead lattice parameter of YAG to decrease to ~ 12.19 Å at 1600°C. YAM and YAP in these two compositions almost form at the same temperature of 1350 °C. After this temperature, the lattice parameter of YAG in x = 0.4 composition drops sharply, while for x = 0.2, it first reached a plateau in 1350–1450°C before dropping. Finally, the lattice parameter of the garnet phase in both x = 0.2 and 0.4 compositions is around 12.19 Å, the garnet phase in the two compositions at last became stoichiometric. It should be noted that, at temperatures lower than 1350 °C, the absence of YAP in phase fraction figure of x = 0.4 was attributed to the peeling of YAP−rich surface (photo inserted in **figure 2.21**) during the crystallisation process in the furnace.

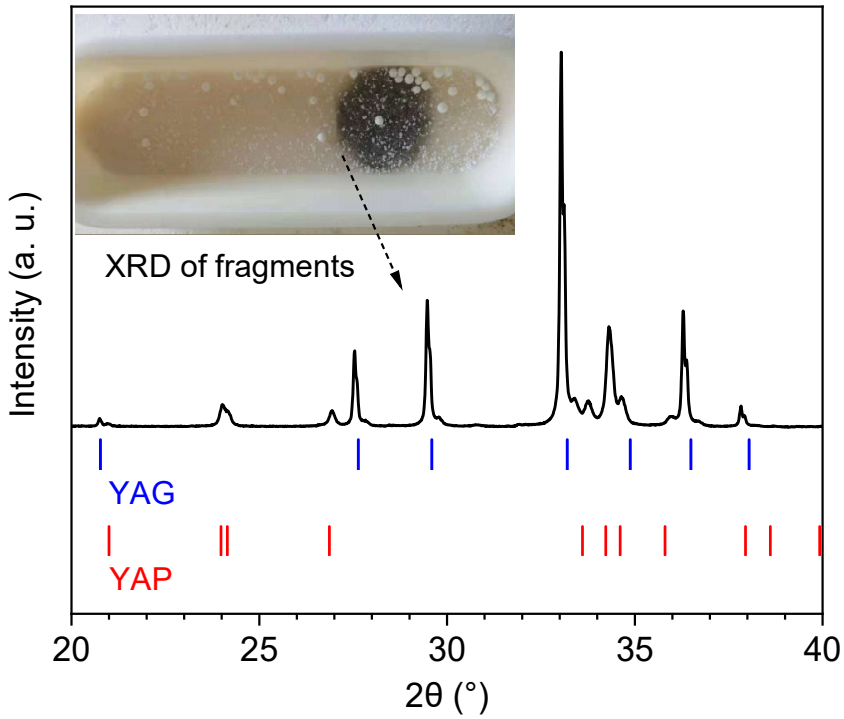

Figure 2.21. *XRD pattern of fractions peeled from the sample surface. The inserted photo was recorded after the crystallisation at 1100 ℃ for 5h in a furnace, there are many fragments peeled from the sample surface.*

2.3.7 SEM characterization of s− and ns−YAGs

Microstructure morphology of polished DC $Y_{3+x}Al_{5-x}O_{12}$ (x = 0 and 0.2) YAG beads (**figure 2.22**) were observed by SEM to see if the sample is free of impurities, and it shows there

are many comet−like pores which formed during rapid cooling and heading towards the same direction. For higher nonstoichiometry samples, *i.e*. in the *x* = 0.4 YAG, no such comet−like pores can be observed in the crystalline sample. This is owing to the fact that this latter sample was crystallized from glass. The whole polished section shows a solid color indicating a single phase. Under greater magnification, grains in *x* = 0 and 0.2 look tightly packed, thus microstructure cannot be seen except thin grain boundaries. Boundaries in *x* = 0.4 look not as solid as in *x* = 0 and 0.2 but formed by accumulated small pores. The two different boundaries resulted from different crystallisation way between direct crystallisation from melt and glass crystallisation.

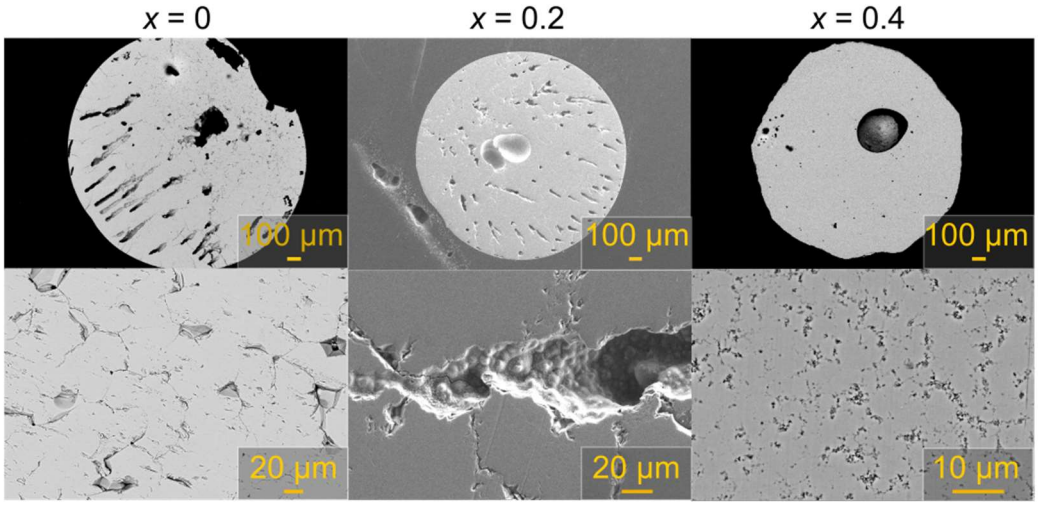

Figure 2.22. *Microstructure of polished x = 0, 0.2 and 0.4 YAG beads observed by SEM. The x = 0 and 0.2 YAGs were synthesized by direct crystallisation from melt in argon, and the x = 0.4 YAG was prepared by crystallizing the glass precursor prepared by ADL in oxygen. The images below magnify their respective crystal morphologies.*

2.3.8 Compositional analysis by electron microprobe

Figure 2.23 shows Y atom percent of $Y_{3+x}Al_{5-x}O_{12}$ (x = 0, 0.2 and 0.4 YAGs) measured by electron microprobe analysis (introduced in appendix) with sampling points across chosen across diameter of the sample. Since oxygen atomic percentage was fixed as 60% and Al atomic percentage is complementary to Y, they are not displayed in the figure. It shows, for x = 0 and 0.2, the measured Y contents are close to their nominal values. While the measured Y content for x = 0.4 has an obvious deviation from its nominal content, this needs to be confirmed with another x = 0.4 YAG sample.

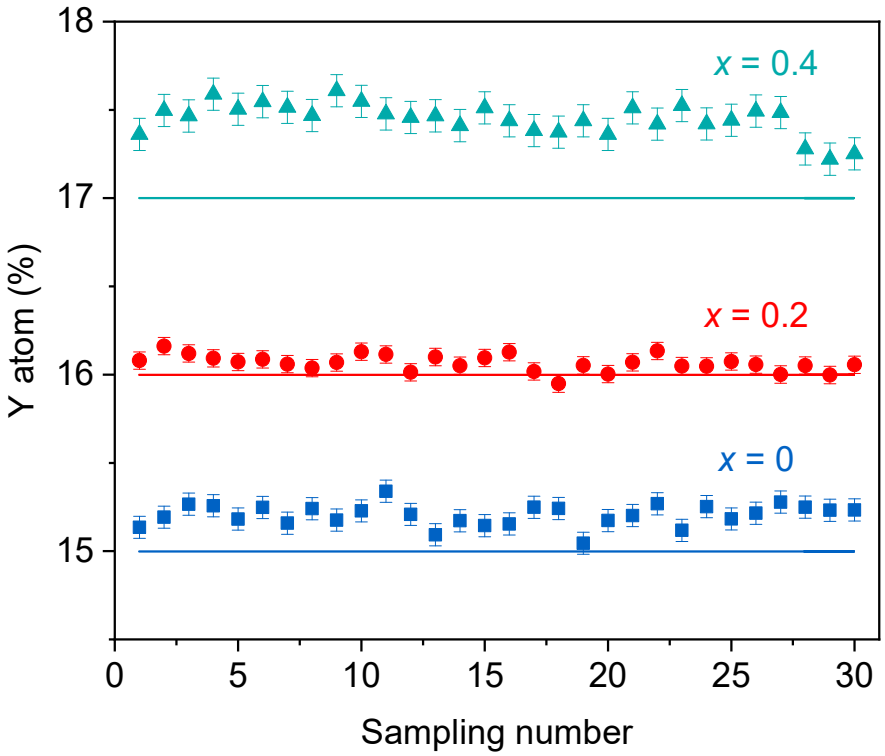

Figure 2.23. *Y atomic percent in $Y_{3+x}Al_{5-x}O_{12}$ (x = 0 (blue), 0.1 (purple), 0.2 (red), 0.3 (orange) and 0.4(green)). The solid lines indicate nominal Y atom percent in each composition. The measured volume of each sampling point is at μm^3 level.*

2.3.9 Average structure of s− and ns−YAGs

SPD patterns of $Y_{3+x}Al_{5-x}O_{12}$ ($-0.1 \leq x \leq 0.4$) are shown in **figure 2.24**, only YAG diffraction peaks are seen in this exhibition mode, indicating these samples contain high content of YAG. The diffraction peaks shift to lower angle as x increases, implying that larger Y^{3+} could successfully substitute Al^{3+} in the garnet structure lattice.

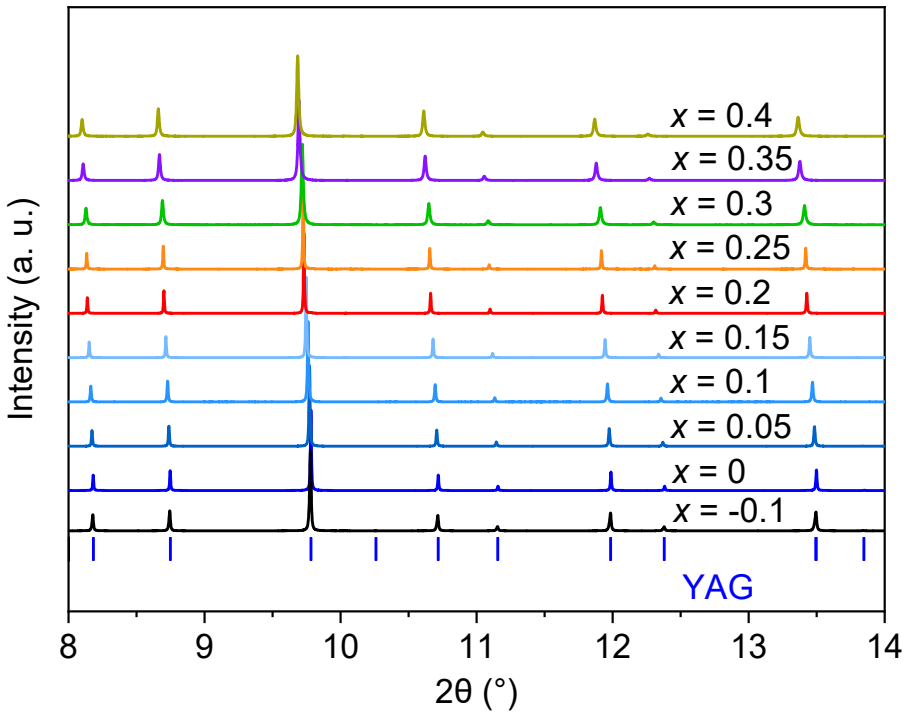

Figure 2.24. *SPD patterns of $Y_{3+x}Al_{5-x}O_{12}$ (-0.1 ≤ x ≤ 0.4) samples. -0.1 ≤ x ≤ 0.35 were prepared by direct crystallisation method by ADL and 0.3 ≤ x ≤ 0.4 by glass crystallisation.*

2.3.9.1 Rietveld structural refinement process

The average structure of $Y_{3+x}Al_{5-x}O_{12}$ (-0.1 ≤ *x* ≤ 0.4) YAGs was studied by Rietveld structural refinement on synchrotron powder diffraction (SPD) data using *TOPAS V6*[96]. The excess Y^{3+} occupation over the crystal structure was determined by Rietveld FFPF (fundamental parameters profile fitting) refinement, starting from $Y_3Al_5O_{12}$ structure model[97], on SPD data of $Y_{3+x}Al_{5-x}O_{12}$ (-0.1 ≤ *x* ≤ 0.4). The refinement was performed over 2−50° 2θ of the data with a wavelength of 0.458 Å and a step size of 0.001°, with considering all diffraction peaks in this range and without missing diffraction peaks before 2° 2θ. As too many parameters may deteriorate profile fitting, not all the parameters were refined simultaneously. Background function, sample displacement, scale factor and simple axial divergence model were first refined[98]. Peak shape was refined with TCHZ_peak_type macros. Lattice parameter, atomic positions were refined before the careful refinement on atomic occupation. All the atomic sites (referring to **figure 2.25**) were assumed to be fully occupied (occupation is 1), although the occupation of excess Y^{3+} at 6-coordinate site is the most promising, the Y and Al occupations at each site were refined to have a fair refining process over the three non-oxygen sites and not to miss the unexpected possibilities. After

that, thermal parameters at different Wyckoff sites were independently refined. No constraint on overall composition was applied. After dealing with garnet structure analysis, YAP impurity phase was refined, scale factor was set as different from that of main garnet phase. When we have a close look at the synchrotron diffraction pattern of Y-rich compositions, low-intensity peaks are present as the right shoulders of the peaks of main garnet phase (shown in **figure 2.26**), therefore they were assumed to be secondary garnet phase with smaller lattice size. To verify it, the refinement block from the main garnet phase was copied and pasted in another block in this input file, the lattice parameters was refined with an initial value smaller than that of the main garnet phase. Weight percentages of the accounted phases were determined by the peak areas.

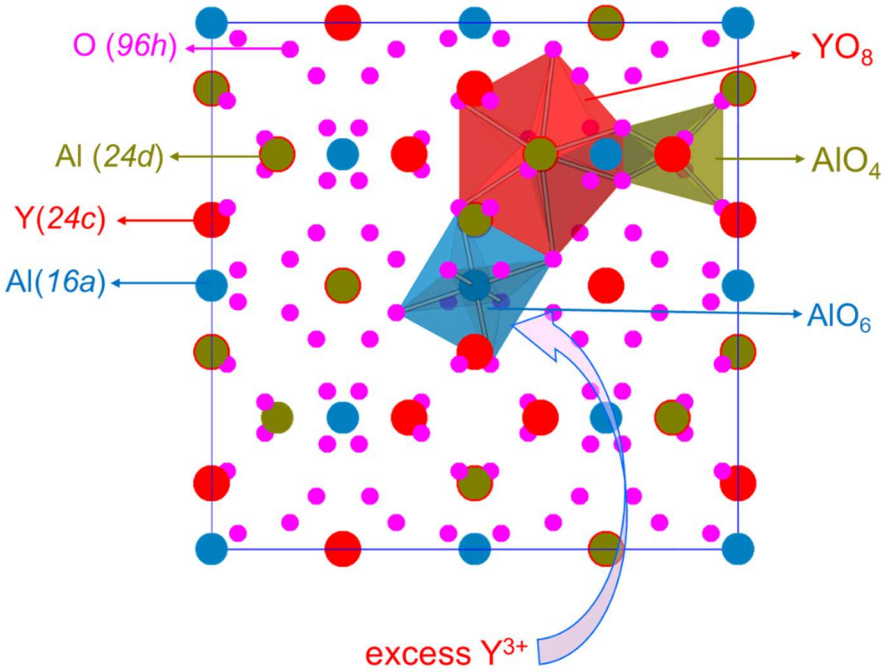

Figure 2.25. *The crystal structure of $Y_3Al_5O_{12}$ (space group: Ia-3d). Yttrium atoms occupy 24c sites, Al atoms occupy 16a and 24d sites and O atoms occupy 96h sites. The three polyhedra indicate the Y atoms are coordinated by eight oxygen atoms, the Al atoms are coordinated by four or six oxygen atoms. The excess Y atoms form $Y_{3+x}Al_{5-x}O_{12}$ ($x > 0$) are expected to enter the Y 24c sites.*

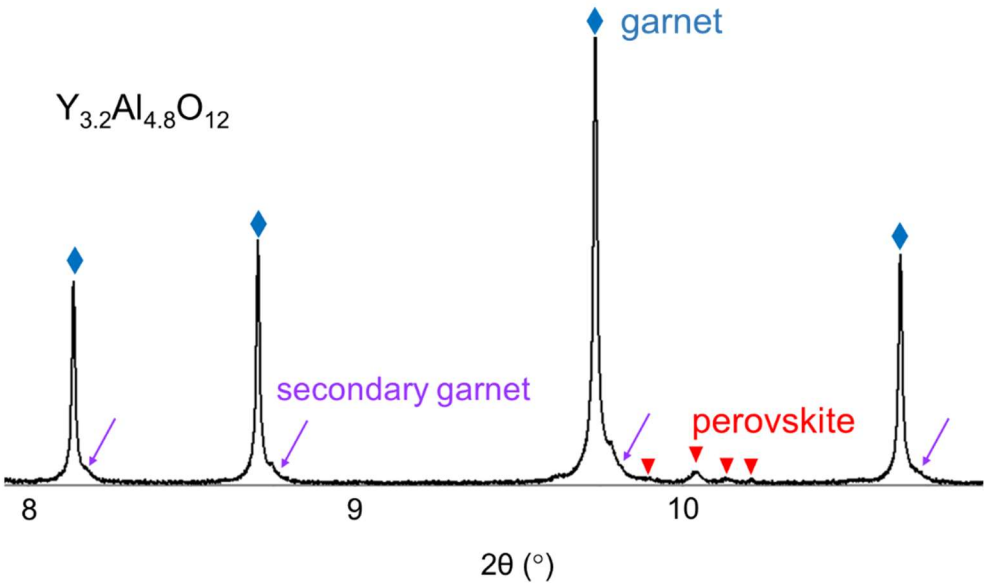

Figure 2.26. *Zoomed SPD pattern of $Y_{3.2}Al_{4.8}O_{12}$ as an example showing weak diffraction signal (labeled by purple arrows) from the possible secondary garnet phase.*

The following results indicate that high−resolution SPD data allows us see the crystalline minor impurities which actually exist but were missed by laboratory XRD data. The refined weight percent results (**figure 2.27**) indicate that the x = -0.1 ($Y_{2.9}Al_{5.1}O_{12}$) sample which was directly crystallized from melt by ADL is biphasic with 99.17(2) wt.% garnet and 0.82(2) wt.% Al_2O_3 , agreeing with the $Y_{2.9}Al_{5.1}O_{12} \rightarrow \frac{29}{30} Y_3Al_5O_{12} + \frac{4}{30} Al_2O_3$ reaction involving with 97.69 wt.% YAG and 2.31 wt.%, the difference between the experimental and the expected weight percentages is acceptable. The x = 0 ($Y_3Al_5O_{12}$) directly crystallized by ADL is monophasic with garnet phase. $0 < x \leq 0.25$ samples are dominated by garnet (G1), the garnet fraction decreases slightly from 99.900(5) to 97.38(1) wt.% as x increases in this range, and their impurities of perovskite (YAP) and secondary garnet (G2) are respectively less than 1 wt.% and 1.7 wt.% (magnified in insert). Glass crystallized (GC) $0.3 \leq x \leq 0.4$ compositions have ~99.7 wt.% garnet and ~0.3% YAP, the absence of secondary garnet phase in these compositions can be attributed to the synthesis difference compared to DC samples. x = 0.45 which was directly crystallized from melt in oxygen is a mixture of garnet, YAP, secondary garnet and Al_2O_3.

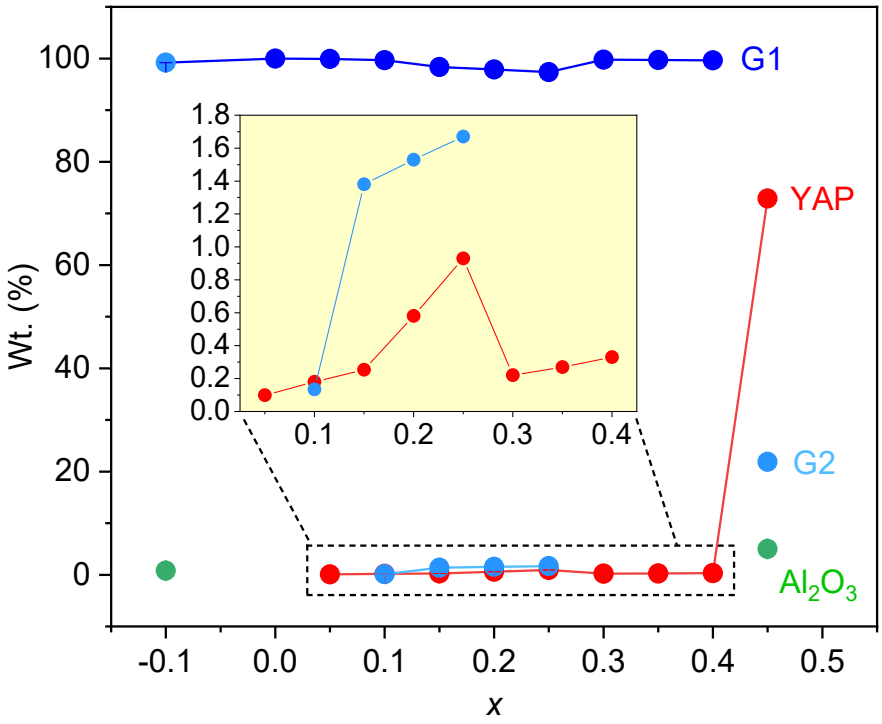

Figure 2.27. *Phase fraction of main garnet (G1), secondary garnet (G2), YAP and Al_2O_3 in $Y_{3+x}Al_{5-x}O_{12}$ ($-0.1 \leq x \leq 0.45$). $-0.1 \leq x \leq 0.25$ were synthesized by ADL in argon, $0.3 \leq x \leq 0.4$ were prepared by glass crystallisation (GC) method, the glass precursors were obtained by supercooling process by ADL in oxygen, 0.45 was directly crystallized from melt in oxygen as it could not be produced with glass. These data points were obtained from Rietveld structural refinement on $-0.1 \leq x \leq 0.4$ SPD data and $x = 0.45$ XRD data.*

Figure 2.28 a-c show the refinement plots of $Y_{3+x}Al_{5-x}O_{12}$ (x = -0.1, 0 and 0.2) samples, these compositions were chosen as the representatives of Al-rich, stoichiometric, and Y-rich YAG samples. The experimental SPD pattern of x = -0.1 was refined by YAG and Al_2O_3 models, x = 0 only by YAG structure model, and x = 0.2 by YAG, secondary garnet and YAP. The diffraction positions of the main garnet phase are indicated by the blues tick marks, although the garnet proportions for $x \neq 0$ compositions are almost 100%, the tiny diffraction peaks from the minor impurities were also refined, resulting in better refinement giving discrepancy values R_{wp} < 10% and goodness of fit (*gof*) ~ 1% (shown in corresponding refinement plots). Refinement plots of the other compositions are shown in figure B1 (a-g) in appendix.

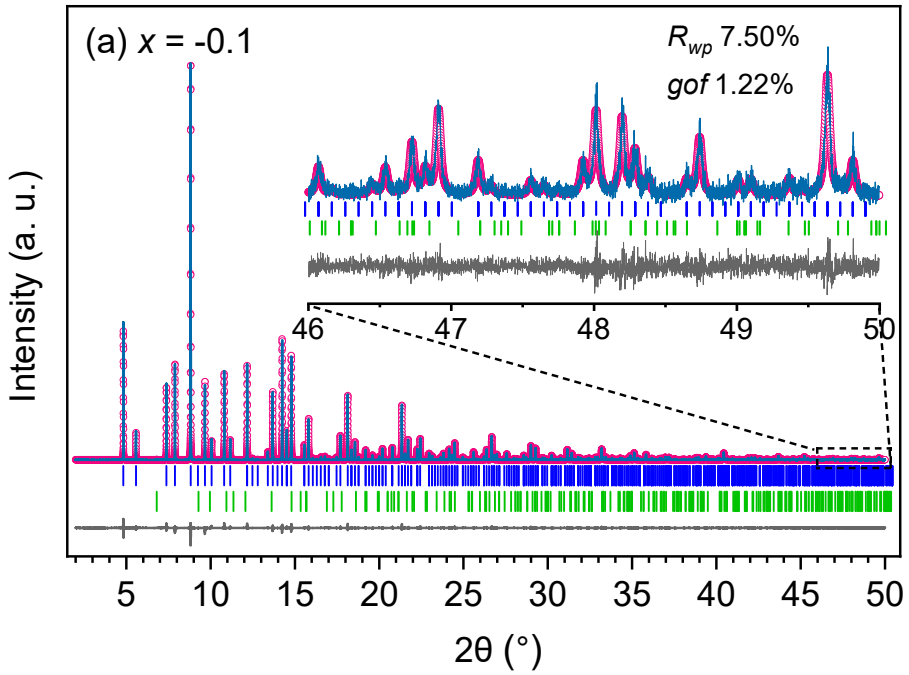
(a) x = -0.1
R_{wp} 7.50%
gof 1.22%
Intensity (a. u.)
46
47
48
49
50
5
10
15
20
25
30
35
40
45
50
2θ (°)

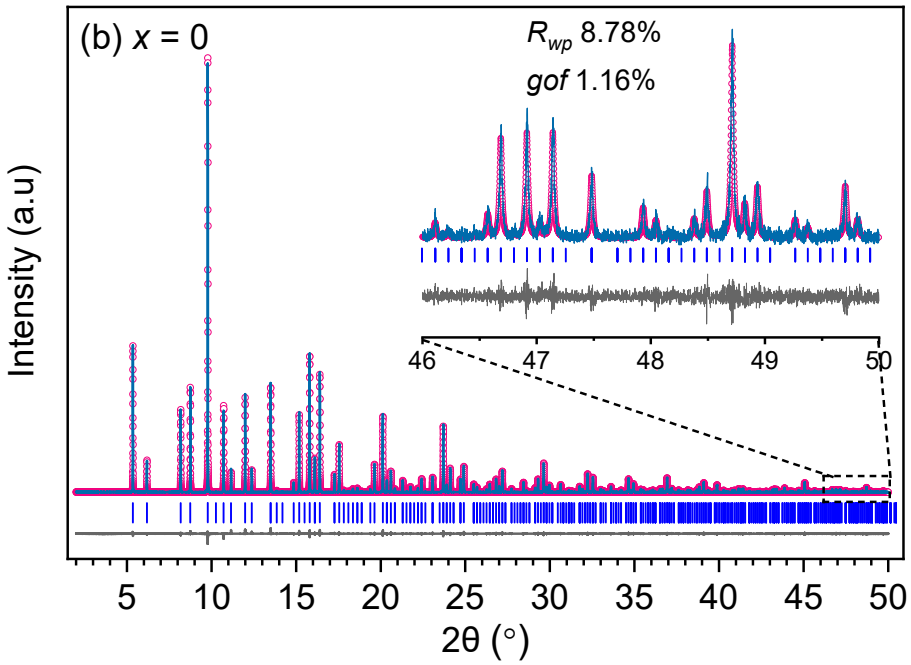
(b) x = 0
R_{wp} 8.78%
gof 1.16%
Intensity (a.u)
46
47
48
49
50
5
10
15
20
25
30
35
40
45
50
2θ (°)

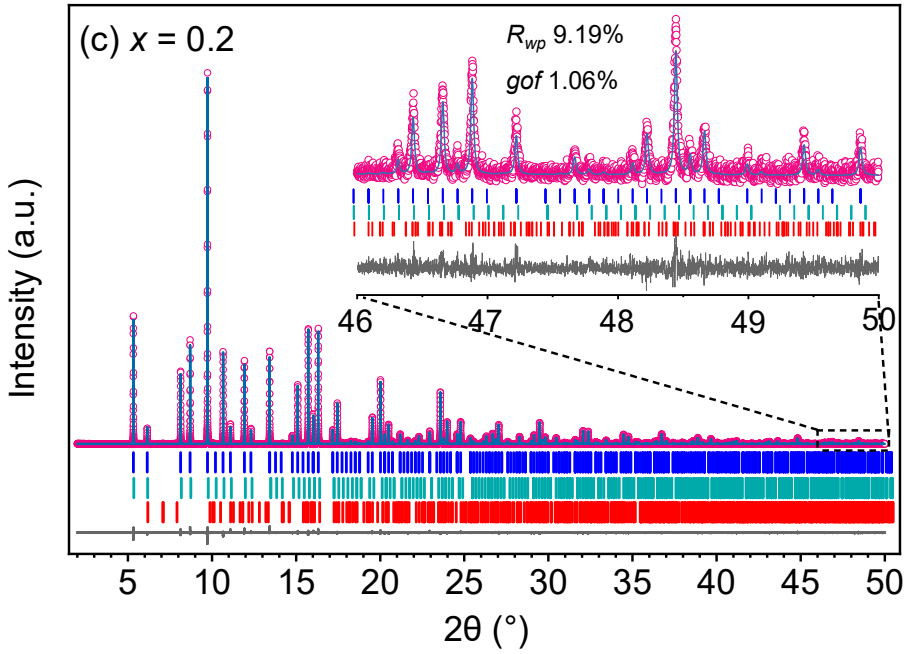

Figure 2.28. *Rietveld refinement plots of $Y_{3+x}Al_{5-x}O_{12}$ (x = -0.1, 0 and 0.2). The empty pink circle and blue line respectively represent observed and calculated data, the grey line at the bottom imply the difference between observed and calculated data, and the blue, cyan, green and red tick marks respectively indicate the Bragg diffraction positions of main garnet, secondary garnet, Al_2O_3 and YAP.*

Tables 2.3–2.12 show the structural parameters including atomic positions, lattice parameter (or volume), Y and Al occupations over *24c*, *16a* and *24d* Wyckoff sites, thermal parameters and occupancy values, *etc*. from structural refinement for $Y_{3+x}Al_{5-x}O_{12}$ (*x* = -0.1, 0 and 0.2) garnets, the structural information of *x* = .01, 0.3 and 0.4. The structure parameters of YAG in *x* = -0.1 composition are almost the same to that of stoichiometric YAG (*x* = 0), indicating that the YAG phase in *x* = -0.1 composition is stoichiometric, qualitatively and quantitatively agreeing with the resulted phase compositions. In the YAG structure of all x ≥ 0 compositions, the *24c* and *24d* Wyckoff sites are respectively fully occupied by Y and Al, when nonstoichiometry *x* increases from zero, the presence of Y starts to be detected, and its content is different from composition to the other, meanwhile lattice parameter also varies. The lattice parameter and Y concentration are plotted as function of nonstoichiometry in figure 2.29 and 2.30, they are discussed and compared with the published work in the following content.

Table 2.3 Rietveld structural parameters of $Y_{2.9}Al_{5.1}O_{12}$ with space group *Ia−3d* resulting from Rietveld refinement corresponding to the refinement plot in figure 2.28 a.						
atom	site	x	y	z	occupancy	Uiso×100
A	24c	0.125	0	0.25	1 Y	0.302(5)
B(VI)	16a	0	0	0	1 Al	0.330(7)
B(IV)	24d	0.375	0	0.25	1 Al	0.374(4)
O	96h	-0.036062(4)	0.05054(4)	0.14901(4)	1	0.244(7)
*a = 12.006046(8) Å, *V* = 1730.613(4) Å^3, *Z* = 8. R_{wp} ~ 7.50%, *gof* ~ 1.22%						

Table 2.4 Rietveld structural parameters of $Y_3Al_5O_{12}$ with space group *Ia−3d* resulting from Rietveld refinement corresponding to the refinement plot in figure 2.28 b.						
atom	site	x	y	z	occupancy	Uiso×100
A	24c	0.125	0	0.25	1 Y	0.230(1)
B(VI)	16a	0	0	0	1 Al	0.24(1)
B(IV)	24d	0.375	0	0.25	1 Al	0.238(8)
O	96h	-0.03049(4)	0.05026(5)	0.14913(4)	1	0.13(1)
*a = 12.007044(5) Å, *V* = 1731.045(2) Å^3, *Z* = 8. R_{wp} ~ 8.78%, *gof* ~ 1.16%						

Table 2.5 Rietveld structural parameters of $Y_{3.05}Al_{4.95}O_{12}$ with space group *Ia−3d* resulted from Rietveld refinement..						
atom	site	x	y	z	occupancy	Uiso×100
A	24c	0.125	0	0.25	1	0.226(1)
B(VI)	16a	0	0	0	0.9750(9)Al/ 0.0250(9)Y	0.189(5)
B(IV)	24d	0.375	0	0.25	1	0.246(2)
O	96h	-0.03035(4)	0.05058(4)	0.14949(4)	1	0.339(2)
*a = 12.019394(6)Å, *V* = 1736.392(2)Å^3, *Z* = 8. R_{wp} ~ 8.14%, *gof* ~ 1.04%						

Table 2.6 Rietveld structural parameters of $Y_{3.1}Al_{4.9}O_{12}$ with space group *Ia−3d* resulted from Rietveld refinement.						
atom	site	x	y	z	occupancy	Uiso×100
A	24c	0.125	0	0.25	1	0.404(1)
B(VI)	16a	0	0	0	0.9500(3) Al/ 0.0500(3)Y	0.355(6)
B(IV)	24d	0.375	0	0.25	1	0.436(2)
O	96h	-0.03060(4)	0.05085(4)	0.14958(4)	1	0.45(1)
*a = 12.045388(5) Å, *V* = 1747.682(2) Å^3, *Z* = 8. R_{wp} ~ 7.95%, *gof* ~ 0.99%						

Table 2.7 Rietveld structural parameters of $Y_{3.15}Al_{4.85}O_{12}$ with space group *Ia−3d* resulted from Rietveld refinement.

atom	site	x	y	z	occupancy	Uiso×100
A	24c	0.125	0	0.25	1	0.357(2)
B(VI)	16a	0	0	0	0.9250(6) Al/ 0.0750(6)Y	0.29(1)
B(IV)	24d	0.375	0	0.25	1	0.319(7)
O	96h	-0.03061(5)	0.05136(5)	0.14981(5)	1	0.44(1)
*a = 12.049939(6) Å, V = 1749.664(3) Å^3, Z = 8.R_{wp} ~ 9.26%, *gof* ~ 1.13%						

Table 2.8 Rietveld structural parameters of $Y_{3.2}Al_{4.8}O_{12}$ with space group *Ia−3d* resulted from Rietveld refinement corresponding to the refinement plot in figure 3.28 c).

atom	site	x	y	z	occupancy	Uiso×100
A	24c	0.125	0	0.25	1	0.620(2)
B(VI)	16a	0	0	0	0.9040(6)Al /0.0959(6)Y	0.37(1)
B(IV)	24d	0.375	0	0.25	1	0.581(7)
O	96h	-0.03049(6)	0.05147(5)	0.15006(5)	1	0.37(1)
*a = 12.06988(5) Å, V = 1758.368(2)Å^3, Z = 8. R_{wp} ~ 9.19%, *gof* ~ 1.06%						

Table 2.9 Rietveld structural parameters of $Y_{3.25}Al_{4.75}O_{12}$ with space group *Ia−3d* resulted from Rietveld refinement.

atom	site	x	y	z	occupancy	Uiso×100
A	24c	0.125	0	0.25	1	0.639(2)
B(VI)	16a	0	0	0	0.8750(4)Al /0.1250(4) Y	0.53(1)
B(IV)	24d	0.375	0	0.25	1	0.582(5)
O	96h	-0.03085(4)	0.05171(5)	0.15049(5)	1	0.78(1)
*a = 12.076947(5)Å, V = 1761.455(2)Å^3, Z = 8. R_{wp} ~ 8.67%, *gof* ~ 1.06%						

Table 2.10 Rietveld structural parameters of $Y_{3.3}Al_{4.7}O_{12}$ with space group *Ia−3d* resulted from Rietveld refinement.

atom	site	x	y	z	occupancy	Uiso×100
A	24c	0.125	0	0.25	1	0.607(3)
B(VI)	16a	0	0	0	0.8580(3)Al/ 0.1419(3)Y	0.36(1)
B(IV)	24d	0.375	0	0.25	1	0.519(8)
O	96h	-0.03092(5)	0.05176(6)	0.15033(6)	1	0.72(1)
*a = 12.09263(1) Å, V = 1768.327(8) Å^3, Z = 8. R_{wp} ~ 8.71%, *gof* ~1.14%						

Table 2.11 Rietveld structural parameters of $Y_{3.35}Al_{4.65}O_{12}$ with space group *Ia−3d* resulted from Rietveld refinement.						
atom	site	x	y	z	occupancy	Uiso×100
A	24c	0.125	0	0.25	1	0.768(5)
B(VI)	16a	0	0	0	0.8190(8)Al/ 0.1809(8)Y	0.33(1)
B(IV)	24d	0.375	0	0.25	1	0.667(8)
O	96h	-0.03122(5)	0.05320(6)	0.15133(5)	1	1.06(1)
*a = 12.12360(1) Å, V = 1781.948(8) Å^3, Z = 8. R_{wp} ~ 8.40%, *gof* ~1.15%						

Table 2.12 Rietveld structural parameters of $Y_{3.4}Al_{4.6}O_{12}$ with space group *Ia−3d* resulted from Rietveld refinement.						
atom	site	x	y	z	occupancy	Uiso×100
A	24c	0.125	0	0.25	1	0.732(3)
B(VI)	16a	0	0	0	0.7985(6)Al/ 0.2014(6)Y	0.31(1)
B(IV)	24d	0.375	0	0.25	1	0.633(8)
O	96h	-0.03130(5)	0.05343(6)	0.15147(6)	1	1.08(1)
*a = 12.13546(2) Å, V = 1787.185(9) Å^3, Z = 8. R_{wp} ~ 8.83%, *gof* ~1.16%						

2.3.9.2 Lattice parameter of s− and ns−YAGs

Structural analysis on SPD data of $Y_{3+x}Al_{5-x}O_{12}$ ($-0.1 \le x \le 0.4$) samples and XRD data of x = 0.45 sample confirmed that, as the Y^{3+} content (or x value) increases, the lattice parameter in the range $0 \le x \le 0.4$ (**figure 2.29**) systematically increases as expected form 12.0071 (1) Å to 12.13542(2) Å, as Y^{3+} (0.90 Å) is much larger than Al^{3+} (0.535 Å). When x = -0.1 and 0.45, it drops to the lattice parameter of x = 0 (s−YAG). For x = -0.1, Al_2O_3 forms and the garnet phase is stoichiometric[27], while for x = 0.45, it is out of the capability of the garnet lattice to incorporate 0.45 excess Y^{3+}, leading the sample to decompose into stoichiometric YAG, YAP and Al_2O_3. Combining with the shifting of Bragg diffraction positions towards lower angle, as excess Y^{3+} increases a $Y_{3+x}Al_{5-x}O_{12}$ solid solution is drawn in $0 \le x \le 0.4$.

In 1997, M. Gervais *et al*.[27] reported they synthesized monophasic yttrium aluminum garnet with 37.5-42.5 mol% Y_2O_3 (corresponding to $0 \le x \le 0.4$ compositions) through glass crystallisation method, the lattice parameter of the garnet phase in this range increased from 12.008 Å of the 37.5 mol% Y_2O_3 (x = 0) composition to 12.052 Å of the 42.5 mol%

Y_2O_3 (x = 0.4) composition, which could indicate that non-stoichiometric YAG was obtained in their work. However, the lattice parameter 12.052 Å of their x = 0.4 YAG is 0.083 Å lower than that in this work, this may indicate in their work the YAG solid solution actually could be $0 \leq x \leq 0.15$. In the work of L. Zhu *et al*. [29], the authors reported a YAG solid solution range in $0 \leq x \leq 0.13$ with lattice parameter varied from 12.0253 (4) Å to 12.0565 (9) Å, in which the 12.0253 (4) Å for $Y_3Al_5O_{12}$ is not normal to see. The mismatch of the lattice parameter of garnet phase between the two published work and our work could be ascribed to that for some reasons the phase characterizations in their work were not sufficient or rigorous, resulting in the neglect of possible impurities like secondary garnet and perovskite, or that additional Y is incorporated in non-crystalline secondary phases. And the reason for them not having a deeper evolving trend of lattice parameter of garnet phase could be the difficulty in forming non−stoichiometric YAG due to the nature of the reaction in Y_2O_3-Al_2O_3 system. Al_{Y24c} defect reaction consumes higher energy than Y_{Al} defect reaction, leading to no Al−rich non−stoichiometric YAG has been produced[28].

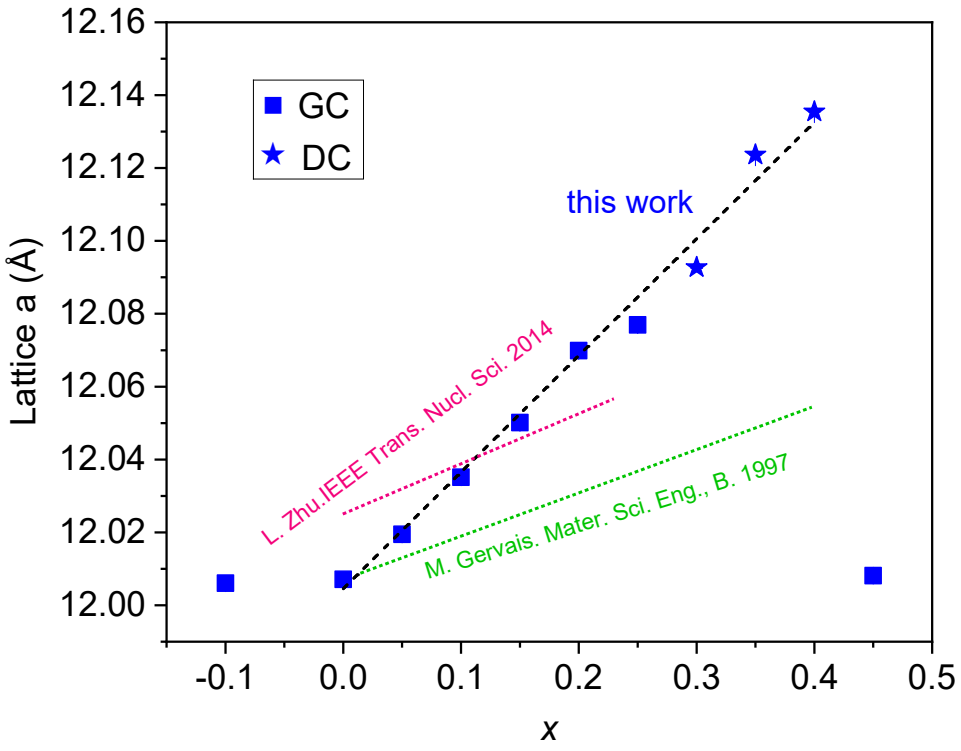

Figure 2.29. *Lattice parameter of YAG in -0.1 ≤ x ≤ 0.45 compositions. Lattice parameter of YAGs in -0.1 ≤ x ≤ 0.4 and x = 0.45 were respectively obtained from Rietveld refinement on SPD and XRD data. The green and pink dashed lines respectively modulate lattice evolution of the yttrium−aluminum garnet compounds from the work of S. Gervais Mater. Sci. Eng., B (1997)[27] and L. Zhu. IEEE Trans. Nucl. Sci (2014)[29].*

2.3.9.3 Quantification of excess Y^{3+}

The x value in the formula $Y_{3+x}Al_{5-x}O_{12}$ was originally determined by adjusting the Y/Al ratio in the mixture of Y_2O_3 and Al_2O_3 starting materials, in the YAG structure, it denotes the concentration of Y^{3+} at 16a sites. **Figure 2.30** shows as *x* value increases from 0 to 0.25, the percentage of Y at 16a site (Y_{Al16a}) obtained from the refinement increases linearly from 0 to 12.5%, it continues until 20% for *x* = 0.4. The experimental Y_{Al16a} data points lie on the dashed line which simulates the theoretical Y_{Al16a} percentage, proving the successful incorporation of Y at octahedral sites.

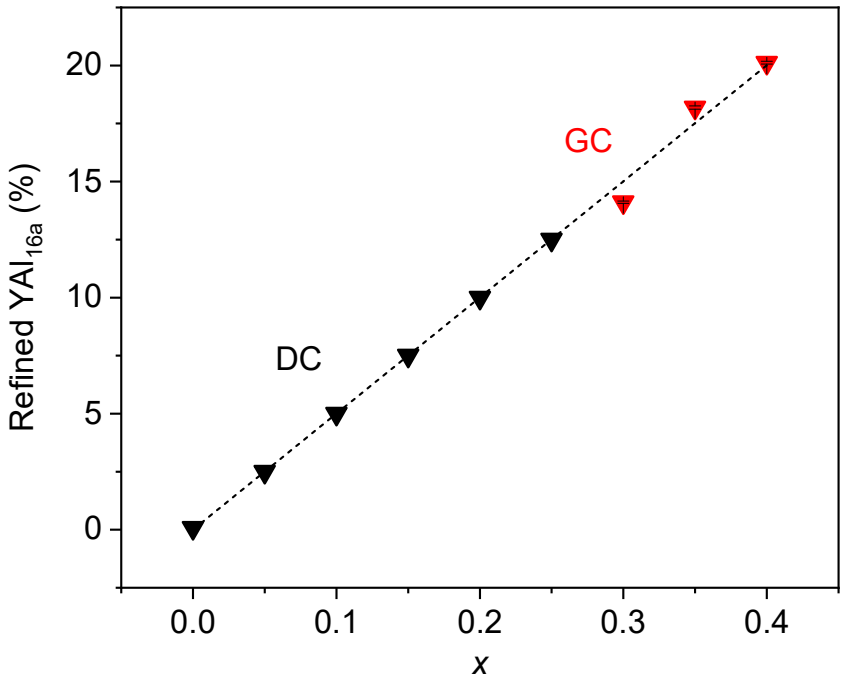

Figure 2.30. *Refined percentage of Y^{3+} at 6−coordinate site from Rietveld structural refinement on SPD data. The black line models, along the Y^{3+} substitution for Al^{3+}, the nominal percentage of excess Y^{3+} at 6−*coordinate site.

2.3.9.4 Influence of nonstoichiometry on bond lengths

As implied by **figure 2.29** (lattice parameter), one of the results of the incorporation of excess Y^{3+} in the cubic garnet structure is the expansion of lattice parameter. This is ascribed to the increase of bond lengths. **Figure 2.31** shows how excess Y^{3+} (or *x*) influences bond lengths of tetrahedra, octahedra and dodecahedra of $Y_{3+x}Al_{5-x}O_{12}$ ($0 \leq x \leq 0.4$) YAGs. Both tetrahedron and octahedron have unique Y/Al−O bond length, and dodecahedra has two Y/Al−O bond lengths. As excess Y^{3+} (or *x*) increases, bond lengths

of tetrahedra and octahedra grow longer, four bonds of dodecahedra grow and the other four contract slightly. It is implied that bond length of octahedra changes the most, from 1.9244(5) Å to 1.9858(7) Å, which is attributed to the location of excess Y^{3+} at 6−coordinate sites.

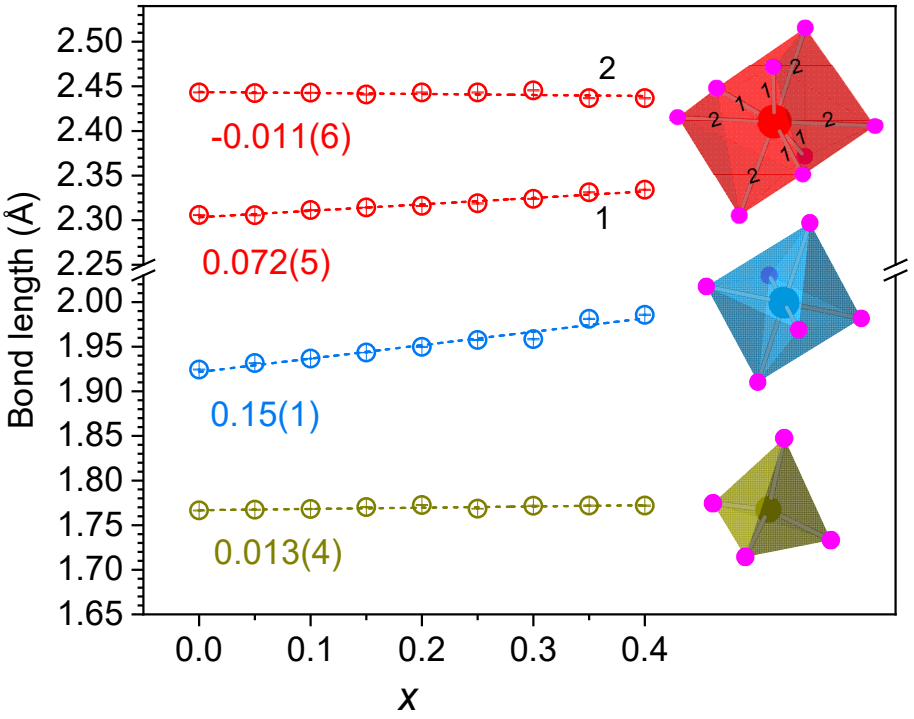

Figure 2.31. *Bond lengths of tetrahedra (dark yellow), octahedra (blue) and dodecahedra (red) derived by Rietveld refinement versus composition x in* $Y_{3+x}Al_{5-x}O_{12}$*. Dodecahedra has bonds with two lengths (green and brown). The dashed lines fit the bond lengths of the three polyhedrons in YAG structure. Numbers under each dashed line indicate the slope of the dashed lines and imply the evolution of bond lengths.*

2.3.10 Local structure of s− and ns−YAGs under STEM observation

2.3.10.1 Crystal grain of s- and ns-YAGs under HRTEM

Figure 2.32 shows HRTEM images of $Y_{3+x}Al_{5-x}O_{12}$ (x = 0, 0.2 and 0.4) YAGs, the samples were observed in the thinnest areas close to the hole (at the upper left corner of the images) produced by ion polishing. At the grain scale, no sub-grain or disorientation were observed, nor a second phase, indicating that the samples consist of a single crystalline phase. The occasional darkness change in the imaging area was caused by the thickness variation captured by HRTEM.

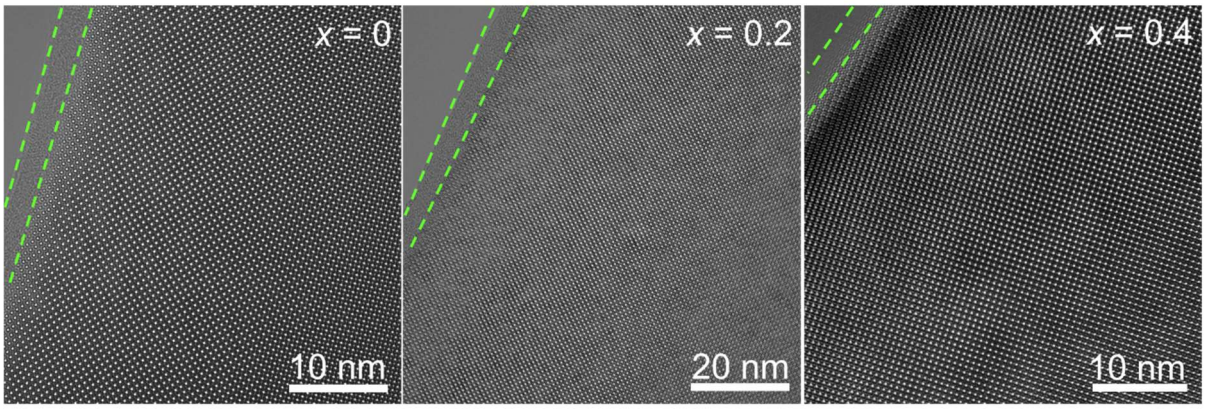

Figure 2.32. *HRTEM images of x = 0, 0.2 and 0.4 YAGs. Thin lamellae were obtained by ion milling which induce a nanometer amorphous layer at the surface (between the two green dashed lines). On the upper left corner, the hole formed during the ion milling can be observed.*

2.3.10.2 SAED characterization for a suitable direction to trace the excess Y^{3+}

Figure 2.33 **(a)** shows the SAED pattern of $Y_3Al_5O_{12}$ orientated along the [100] direction. The diffraction spots in the image (a) satisfies the diffraction conditions from cubic YAG structure with *Ia-3d* space group and lattice parameter of 12.008 Å.

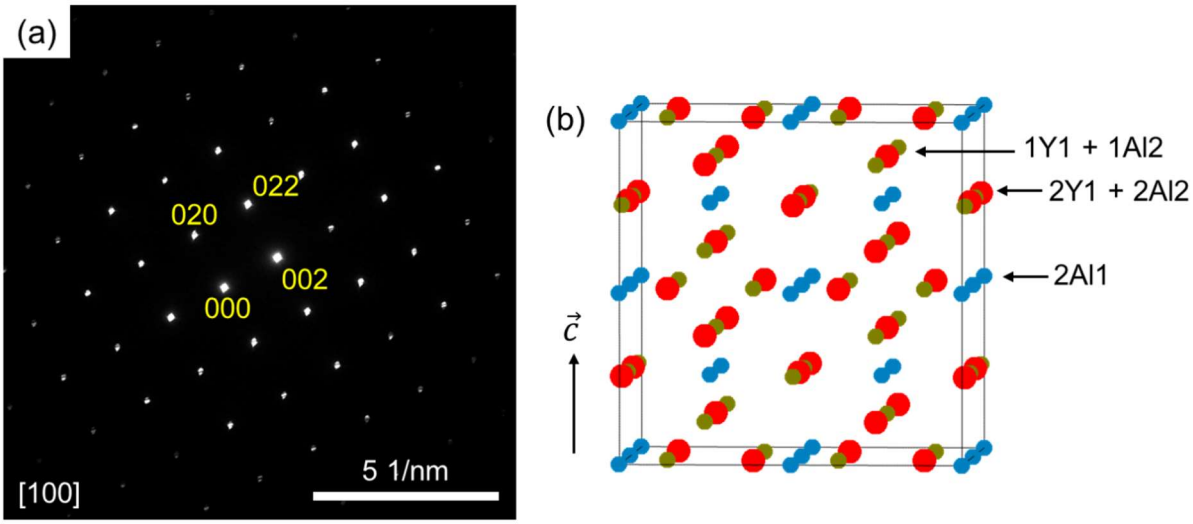

Figure 2.33. *(a) SAED along the [100] axis performed on $Y_3Al_5O_{12}$ sample and (b) Y and Al atoms distribution observed along the [100] axis. The red, blue and olive dots respectively represent Y1, Al1 and Al2 atoms.*

2.3.10.3 STEM−HAADF characterization of excess Y^{3+}

In STEM-HAADF mode, the signal is essentially dominated by Rutherford scattering, resulting in a Z-contrast imaging[99-101]. For thin objects (several tens of nanometers), the image intensity can be approximated by the following formula, $I \propto e\rho Z^n$ with e the thickness, ρ the density, Z the average atomic number and n the exponential coefficient comprised between 1.6-2. At the atomic scale, the imaged area measures around several nm by several nm, so it is reasonable to estimate that the thickness of the sample is the same from one side to the other of the image. At this scale, each point in the image is the 2-D projection of an atomic column and the intensity is proportional to the chemical composition (average atomic number Z) of this column and to the number of atoms (density ρ). Heavier is the column, brighter it appears. Along the [100] direction, it is possible to stack the pure octahedral Al atoms which are interpreted in **figure 2.33 (b)** as 2Al1 columns in the unit cell. This Al1 site is expected to incorporate excess Y^{3+} from ns-YAG as determined by Rietveld structural analysis. With the exception of the 2Al1 atomic columns, the structure model also involves the 1Y1 + 1Al2 and the 2Y1 + 2Al2 atomic columns. These three types of atomic columns are distinguishable from each other because they do not have the same average atomic number or the same density. Therefore, their intensity in STEM-HAADF mode is different. After introducing excess Y^{3+} into the YAG structure, the 2Al atomic columns in the unit cell of non−stoichiometric YAG become (2-*x*)Al + *x*Y (*x* is the content of the added Y in an unit cell). The brightness of the three typical atomic columns in a (s− or ns−) YAG can be ordered as 2Al + 2Y > 1Al + 1Y > (2−*x*)Al + *x*Y, with Y heavier than Al. Consequently, the addition of Y in the 2Al1 site will lead to an increase of the brightness. All the (2−*x*)Al + *x*Y (*x* = 0, 0.2 and 0.4) atomic columns in the following results actually include multiple (2-*x*)Al + *x*Y units depending on the thickness of the measured area.

Figure 2.34 shows the simulated STEM-HAADF image extracted from the $Y_3Al_5O_{12}$ (*x* = 0) cif file using JEMS software[102]. The spots in the image are classified into three brightness degrees which correspond to the three typical atomic columns. The brightest spots (red dot) in the center of the octagons reflect the signal from the 2Y1 + 2Al2 atomic columns, the spots (dark yellow dot) that have secondary brightness show the signal from the 1Y1 + 1Al2 atomic columns. Finally, the least bright spots (blue dot) have the signal from the 2Al1 atomic columns. The brightness of the 2Al1 atomic columns is constant although it is weak.

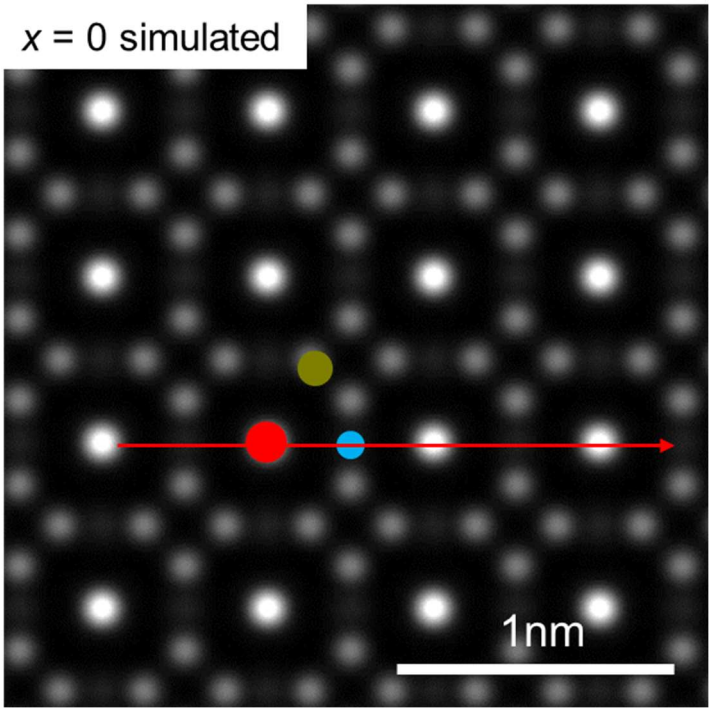

Figure 2.34. *Simulated $Y_3Al_5O_{12}$ (x = 0) STEM-HAADF image extracted form cif file using JEMS software[102]. The red, dark yellow and blue dots respectively represent the 2Y1 + 2Al2, 1Y1 + 1Al2 and 2Al1 atomic columns.*

In the experimental STEM-HAADF image of $Y_3Al_5O_{12}$ (**figure 2.35**), there are also three brightness levels for the signal spots corresponding to the three typical atomic columns. There is no obvious variation in the intensity of the 2Al1 atomic columns (position 3), this indicates that the 2Al1 sites only have Al atoms incorporated, agreeing with the simulated STEM-HAADF image.

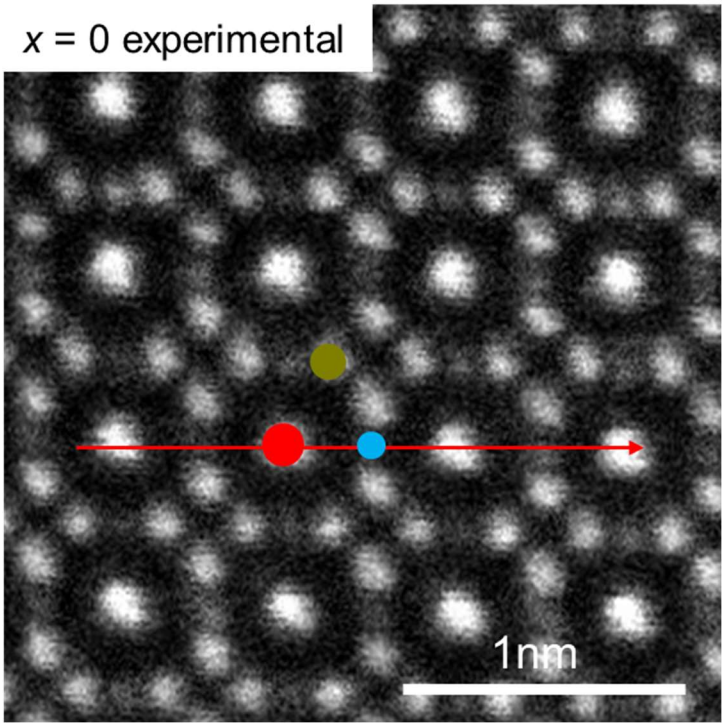

Figure 2.35. *STEM-HAADF image of x = 0 ($Y_3Al_5O_{12}$). The red, dark yellow and blue dots respectively locate the 2Y1 + 2Al2, 1Y1 + 1Al2 and 2Al1 atomic columns.*

In STEM-HAADF mode, the intensity can be affected by the sample thickness, the level of noise and channeling effect. To minimize the variation of these factors, the intensity profile was recorded from a 5 nm × 5 nm image, where the thickness of the sample and the other factors can be considered constant. The exact thicknesses of the measured area of the $Y_3Al_5O_{12}$ sample was determined by Electron Energy Loss Spectroscopy (EELS) and was found to be around 13.5 nm which corresponds to a stack of around 10-11 cells. Intensity profiles of $Y_3Al_5O_{12}$ (**Figure 2.36**) were extracted from the atomic columns along the long red arrow, as an example, in the experimental STEM-HAADF image figure 2.37. They result in a succession of high-intensity and low-intensity peaks respectively linked to the atomic columns 2Al2 + 2Y1 and 2Al1. The signal of each atomic column 2Al1 and 2Y1 + 2Al2 can be fitted by a constant background signal and Gaussian functions. The intensities of the 2Al1 atomic columns stay quite constant, in agreement with an unchanged composition. Some variations in intensity can be visible, in particular for the 2Y1 + 2Al2 atomic columns, this can be attributed to that the sample is not a good conductor for the scanning process by electron probe. Knowing that the compositions of the sites 2Al1 and 2Y1 + 2Al2 are homogeneous, these variations allow us to establish an error bar for the determination of the compositions for each type of site.

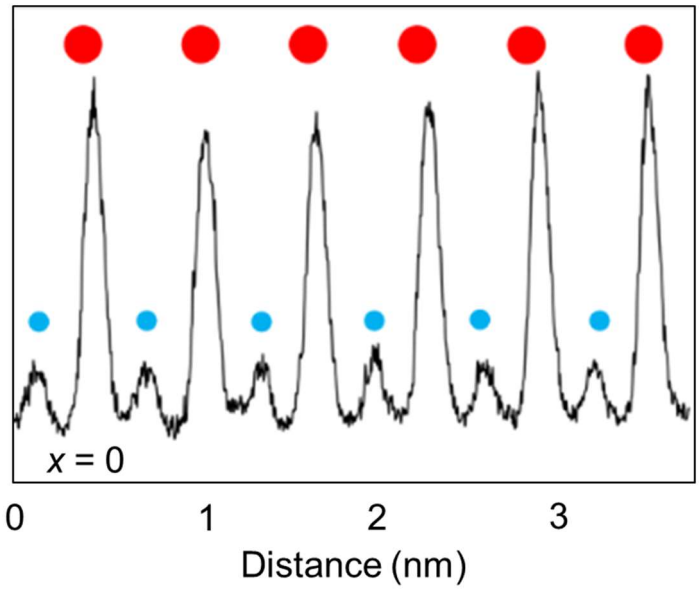

Figure 2.36. *An example of experimental intensity profile considering a succession of atomic columns of 2Y1 + 2Al2 (red dots) and 2Al1 (blue dots) for x = 0 YAG.*

For non-stoichiometric $Y_{3+x}Al_{5-x}O_{12}$ (x = 0.2 and 0.4) garnets, the 2Al1 site becomes 0.2Y + 1.8Al1 and 0.4Y + 1.6Al1, respectively. On the simulated STEM-HAADF images (**figure 2.37**), the signal of the 0.2Y + 1.8Al1 atomic columns of $Y_{3.2}Al_{4.8}O_{12}$ are brighter than that of 2Al1 of $Y_3Al_5O_{12}$, and they become even brighter for the 0.4Y + 1.6Al1 atomic columns of $Y_{3.4}Al_{4.6}O_{12}$, in consistence with the reality that Y is heavier than Al.

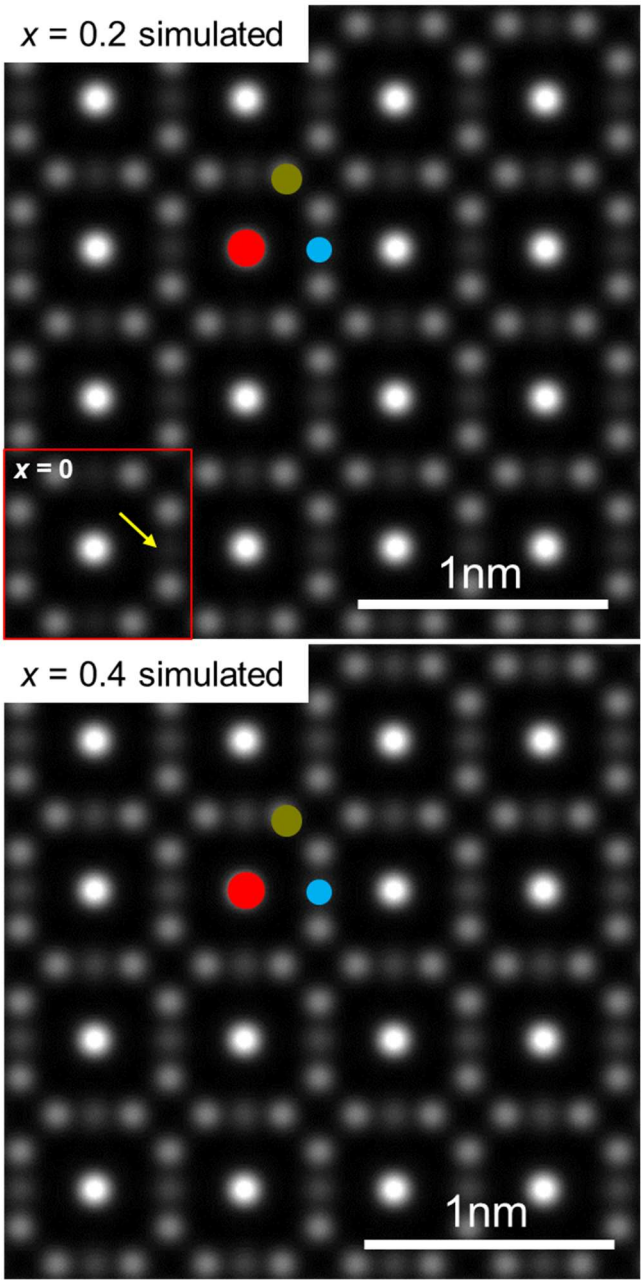

Figure 2.37. *Simulated STEM-HAADF images of x = 0.2 ($Y_{3.2}Al_{4.8}O_{12}$, above) and x = 0.4 ($Y_{3.4}Al_{4.6}O_{12}$, below). The red, dark yellow and blue dots indicate the three typical atomic columns. The insert at the left bottom corner of the simulated STEM-HAADF image of x =0.2 is a cropped simulated STEM-HAADF image of x = 0 ($Y_3Al_5O_{12}$), the yellow arrow indicates the 2Al1 atomic column.*

The thicknesses of the observed areas of the samples *x* = 0.2 and 0.4 are respectively 8 nm and 14.5 nm, corresponding to a stack of 6−7 and 12 cells, respectively, they are quite close to that of *x* = 0 (13.5 nm), allowing the comparison among them. As for the simulated images (**figure 2.38**), the signal of the atomic columns 0.2Y+1.8Al1 and 0.4Y+1.6Al1,

respectively for x = 0.2 and 0.4, is brighter than for the atomic columns 2Al1 of x = 0. Unlike x = 0, for the samples x = 0.2 and x = 0.4, the intensity varies from one atomic column $\underline{xY + (1\text{-}x)Al}$ to another, indicating that the excess Y^{3+} disorderly distribute in the crystal structure of the two non-stoichiometric YAGs. This phenomenon is clearly visible on the intensity profiles (**figure 2.39**).

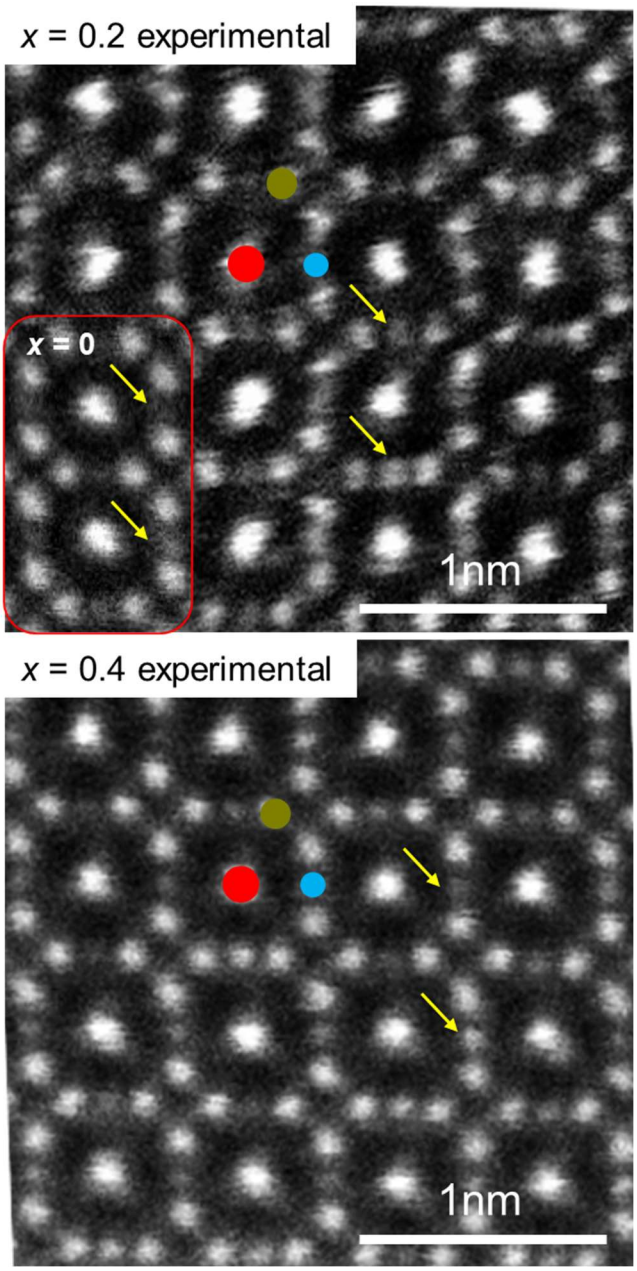

Figure 2.38. *Experimental STEM-HAADF images of x = 0.2 ($Y_{3.2}Al_{4.8}O_{12}$, above) and x = 0.4 ($Y_{3.4}Al_{4.6}O_{12}$, below). The red, dark yellow and blue dots indicate the three typical atomic columns. The insert at the left bottom corner of the experimental STEM-HAADF image of x =0.2 is a cropped experimental STEM-HAADF image of x = 0 ($Y_3Al_5O_{12}$). The two yellow arrows in each image point out the brightness of the two signal spots deviate from each other.*

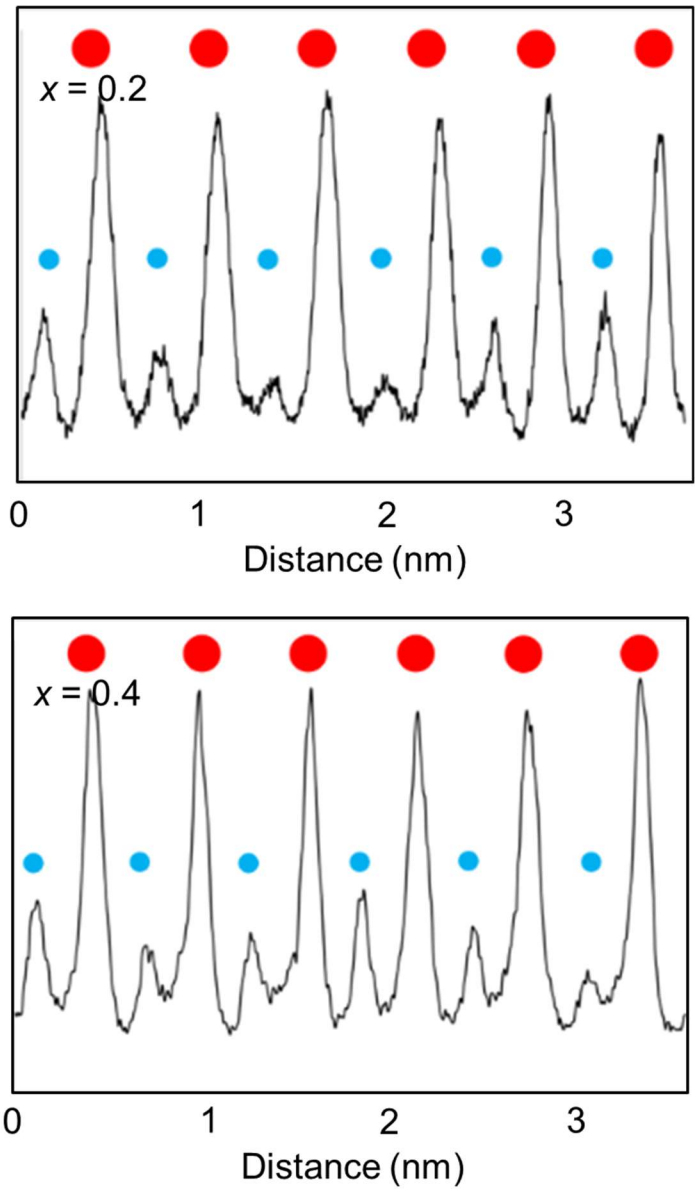

Figure 2.39. *An examples of experimental intensity profiles corresponding to a succession of atomic columns of 2Y1 + 2Al2 (red dots) and 0.2Y+1.8Al1 for x = 0.2 YAG, 0.4Y+1.6Al1 for x = 0.4 YAG (blue dots).*

2.3.10.4 STEM−EDS elemental mapping

Atomic−scale STEM−EDS elemental maps (**figure 2.40 a**, **b** and **c**) and the corresponding STEM−HAADF image (d) of $Y_{3.4}Al_{4.6}O_{12}$ garnet are shown in figure 2.40. Each dot corresponds to an atom column, the Y and Al atoms are respectively represented in red and blue. In the combined elemental map, columns 2Y1 + 2Al2 and 1Y1 + 1Al2 are displayed in pink, the columns 0.4Y + 1.6Al are in blue. The brightest and least bright dots in the STEM−HAADF image respectively correspond to the centered pink 2Y1 + 2Al2

columns and to the blue 0.4Y + 1.6Al columns. The intensity profiles e−f were plotted for the positions pointed out by yellow arrows in the EDS maps. These yellow arrows locate the position of the 0.4Y + 1.6Al atomic columns, where the presence of Al and Y is detected (black arrows on the profiles e and f). In the HAADF intensity profile (g), it can be seen that the intensity of the 0.4Y + 1.6Al columns, marked by black arrows, varies, which reflects a variation in composition. Closely looking the profile of Y (f), we can see that the columns the most intense are richer in Y.

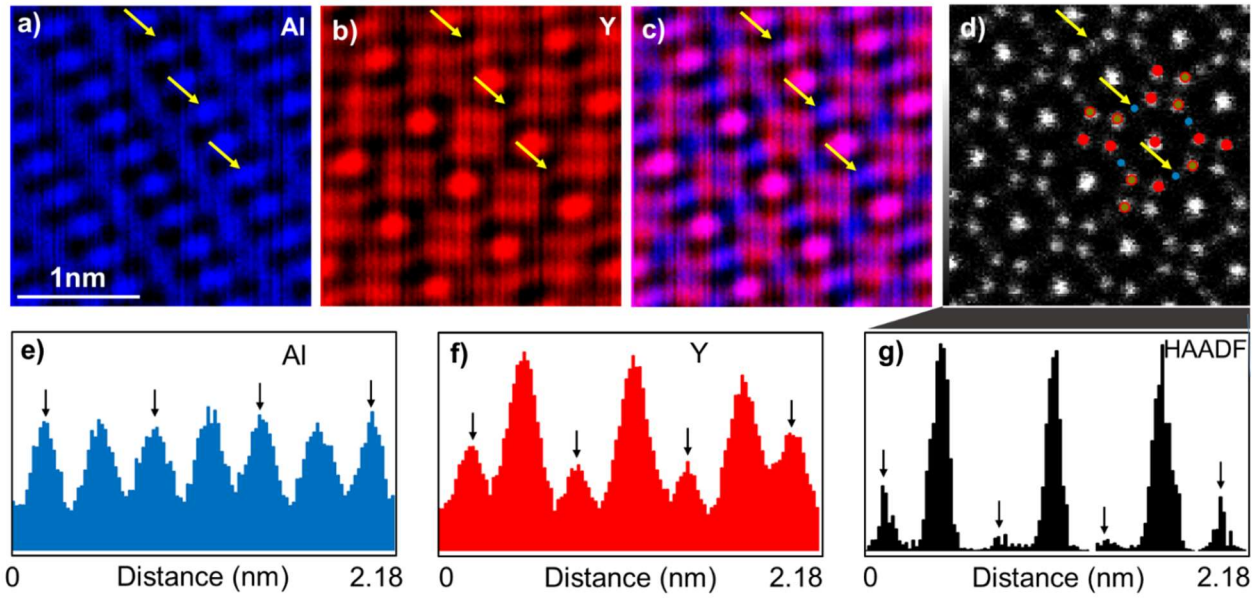

Figure 2.40. *Atomic−scale elemental maps of* ***(a)*** *Al,* ***(b)*** *Y cations and* ***(c)*** *the combined EDS map.* ***(d)*** *Corresponding STEM−HAADF image which was recorded along the [100] axis. The yellow arrows in* ***(a−d)*** *point out the location of the 0.4Y + 1.6Al atomic columns at the original 2Al1 sites, and the black arrows in intensity profiles, corresponding to* ***(e−f)*** *EDS maps and to (g) HAADF image, indicate the intensities of the sites pointed out by yellow arrows above.*

2.3.10.5 Experimental and simulated excess Y^{3+} concentration

The Y^{3+} concentration in the Al1 sites of the three compositions were determined as 0%, 9.59(6) % and 20.14(6)% by Rietveld refinement, which are equal to or quite close to the nominal values 0%, 10% and 20%. From the intensity profiles extracted from the STEM-HAADF images, it is possible to determine the composition of the Al1 sites, and thus the Y occupancy, via the formula $V \approx \sum_i (m_i Z_i^n)$, [103, 104] in which the volume (V) is the total signal intensity under the peak and *Z* the average atomic number of the site. The n values for each composition are respectively 2.36, 2.15 and 2.08 as deduced from the formula just

mentioned, which are close to the n value 2 predicted in the literature. The experimentally observed distribution of Y in each Al1 atom column was calculated by taking n and Z into account. It was found there is a variation of the probability for different observed Y occupancy at Al1 sites, but the Y occupancies of 10% for x = 0.2 and 20% for x = 0.4 have the greatest probabilities in each case (~35% for x = 0.2 and ~28% for x = 0.4). As a comparison, the probability of Y occupancy at Al1 sites in x = 0 is zero (probability is ~96%) (**figure 2.41**).

To calculate the probability of Y at Al1 sites for x =0.2 and 0.4 YAGs, it can be realized by the Bernoulli Distribution formula:

$$p[x = k]=(n!/(k!(n-k)!))\times(p\text{^}k)\times[(1-p)\text{^}(n-k)]$$

Where p is the probability of Y at Al1 sites, n is the number of atoms at Al1 sites, and k is the number of Y atoms at Al1 sites. The p values for x =0.2 and 0.4 are respectively 0.1 and 0.2 which are corresponding to theoretical Y_{Al} occupancy ratio. When taking 120 columns into account, the n values for the two compositions are respectively 12 (0.1×120) and 24 (0.2×120). Over all the cases, the sum of p[k] confines to 1 (*i. e.* Σp[k] = 1), therefore k value is an integer varying in 0-7 for x =0 .2 and in 0-14 for x = 0.4. The probability of expected Y atoms at Al1 sites is shown in figure 2.41 as a function of Y occupancy ratio at Al1 sites, the global maximum of the probability for x = 0.2 and 0.4 are respectively around 10% and 20%, agreeing with the experimentally observed Y distribution from a statistical point of view.

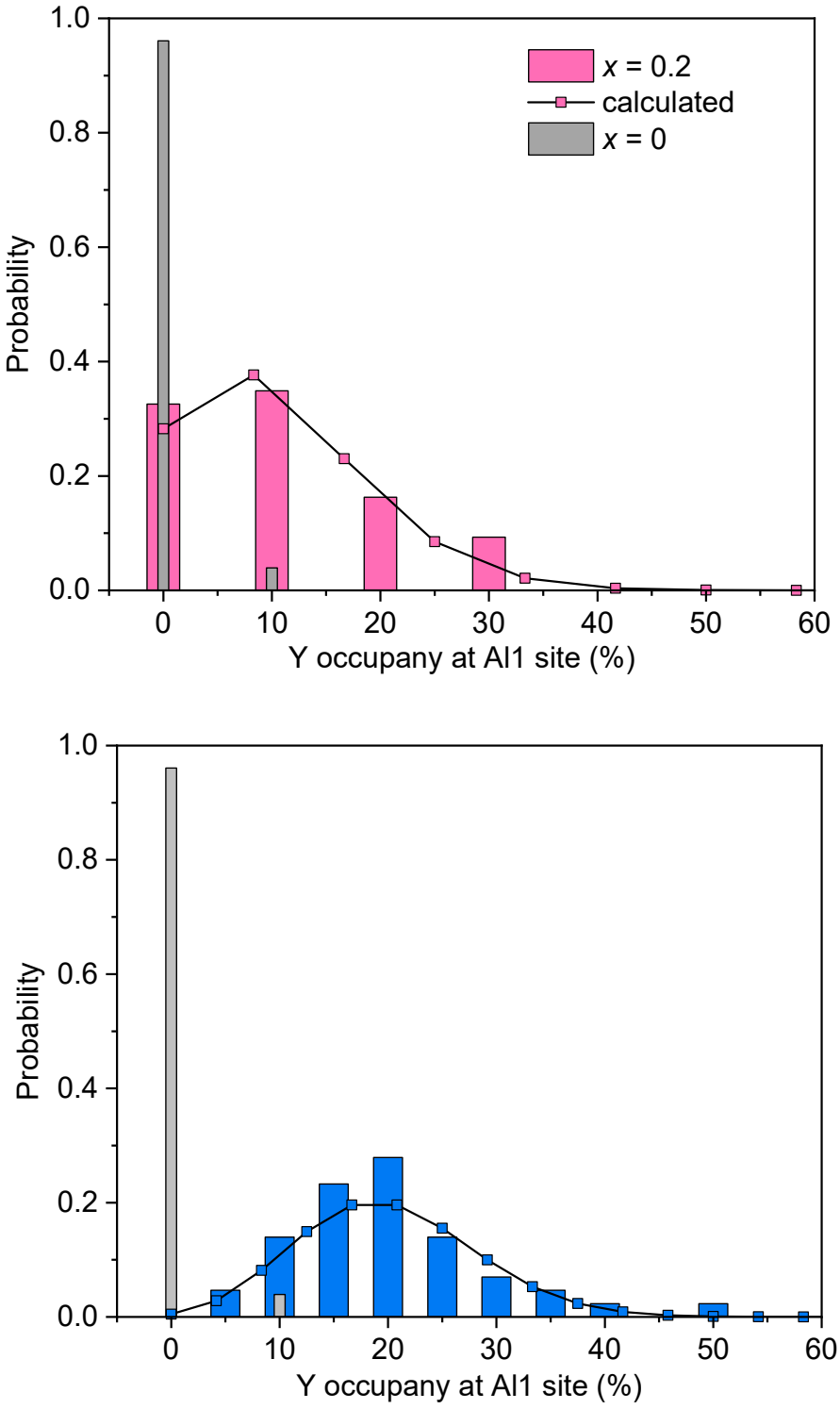

Figure 2.41. (a−b) *Experimentally observed probabilities (bars) of Y occupancy at Al1 site, , for $Y_{3+x}Al_{5-x}O_{12}$ (x = 0, 0.2 and 0.4) garnets. The black curves in (a) and (b) figures show the evolution of the expected Y occupancy in x = 0.2 and 0.4.*

2.3.11 DFT computation on ns−YAGs

Since the GIPAW method used planes waves with periodic boundary conditions, it is convenient to choose a crystalline compound with known structure and experimental isotropic chemical shift (δ_{iso}^{exp}) to obtain the σ_{ref} value (calculated isotropic shielding of a reference compound, the information on obtaining the σ_{ref} are given in table A1 in appendix), so that the calculated and experimental chemical shift for the compound are equal.

Using a series of reference compounds, a linear relationship δ_{iso}^{exp} = - 1.0(2) x σ_{iso}^{calc} – 2720 (480) describing the ^{89}Y isotropic shielding as a function of the ^{89}Y experimental isotropic chemical shift was obtained and shown in **figure 2.42**. The slope is close to the theoretical value but the correlation coefficient is relatively small (R^2 = 0.81) and this leads to relatively large uncertainties on the σ_{ref} value. In this case, using $Y_3Al_5O_{12}$ as a single reference compound was found more suitable and the relationship δ_{iso}^{exp} = - 1.0 x σ_{iso}^{calc} – 2601 was therefore applied.

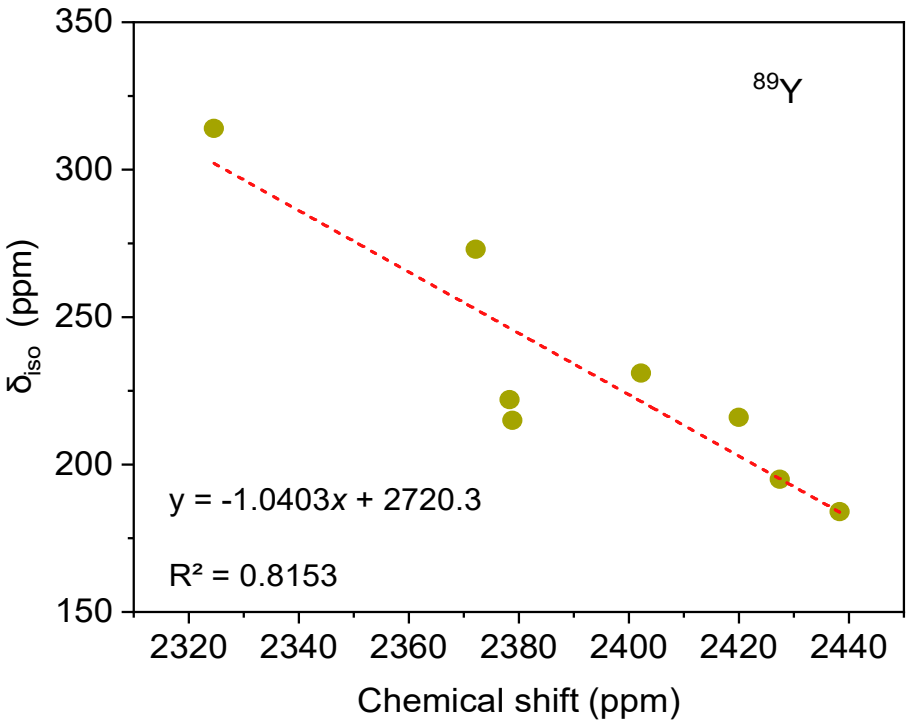

Figure 2.42 *GIPAW-calculated ^{89}Y isotropic shielding as a function of the ^{89}Y experimental isotropic chemical shifts for a series of reference compounds.*

The $Y_{3+x}Al_{5-x}O_{12}$ structural models were built with the 1x1x1 unit cell of YAG with P1 symmetry, in which additional Y atoms substitute for Al in octahedral sites. The selected

$Y_{3+x}Al_{5-x}O_{12}$ compositions correspond to x = 0.125, 0.25 and 0.375, for which the extra Y atoms occupy a single, two or three octahedral site of the 1x1x1 unit cell. For each composition, all possible configurations were generated using the Supercell code[105] and the configurations equivalent by symmetry were merged together. **Table 2.13** show the number of the possible configurations and the number of models after the merging process for the three compositions. The 16 possible configurations of x = 0.125 were merged into a single model, the 120 possible configurations of x = 0.25 were merged into five models and the 560 possible configurations of x = 3.375 into nine models.

Table 2.13. Number of possible configurations and the number of models with respective weight.

	num of possible configuration	num of model	weight
x = 0.125	16	1	————
x = 0.25	120	5	8, 24, 24,48, 16
x = 0.375	560	9	48, 48, 96, 96, 16, 96, 96, 16, 48

The total energies and structural features of the various models are summarized in **table 2.14**. **Figure 2.43** shows the only defect in the model of x =0.125. The defects in x = 0.25 and 0.375 are characterized by the distance between every two defects. For x = 0.25, the distance between the two defects are 5.121-10.459 Å for the 5 models. For x = 0.375, the distance from one defect to another is determined by the principle “shortest distance”, therefore the model has three distances forming a triangle as shown in the figure of the models. **Figure 2.44** shows the two examples form the 5 models for x = 0.25 **and figure 2.45** shows the two examples form the 9 models for x = 0.375. For the sake of layout art of the thesis, the rest models for the two compositions are shown **figure B2** in appendix.

Table 2.14. Total energies of the structural models used for GIPAW computations.

composition	cell parameter (Å)	Y at octahedral site	structure name	weight	total energy (eV)
x = 0.125	12.0426	1	Y3.125_i00_w16	16/16	
x = 0.250	12.0769	2	Y3.250_i000_w8	8/120	-74638.42
			Y3.250_i001_w24	24/120	-74638.42
			Y3.250_i002_w48	48/120	-74638.32
			Y3.250_i003_w48	48/120	-74638.66
			Y3.250_i004_w16	16/120	-74638.09
x = 0.375	12.1240	3	Y3.375_i000_w48	48/560	-75600.55
			Y3.375_i001_w48	48/560	-75601.10
			Y3.375_i002_w96	96/560	-75601.11
			Y3.375_i003_w96	96/560	-75601.03
			Y3.375_i004_w16	16/560	-75599.98
			Y3.375_i005_w96	96/560	-75600.56
			Y3.375_i006_w96	96/560	-75600.47
			Y3.375_i007_w16	16/560	-75600.65
			Y3.375_i008_w48	48/560	-75600.44

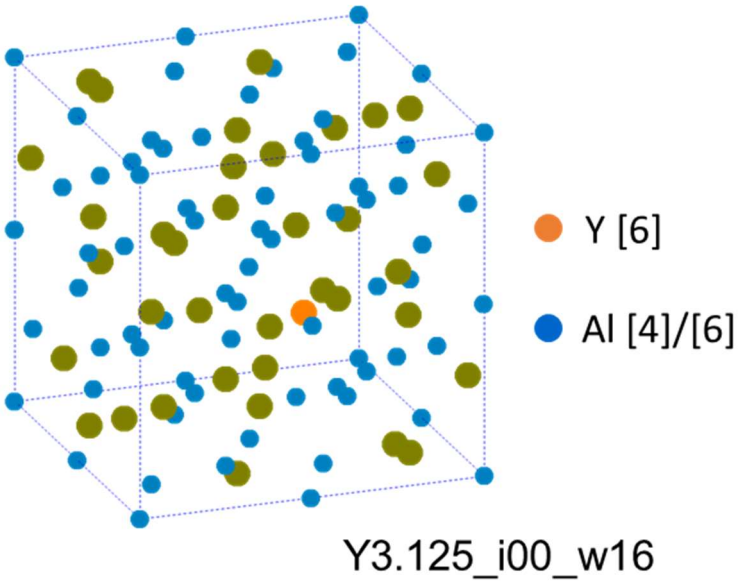

Figure 2.43. *The $Y_{3.125}Al_{4.875}O_{12}$ model showing the unique Y defect inside. Y defects (6-coordinate) are labelled as closed orange circles and Al (4- and 6- coordinate) atoms are labelled as closed blue circles. Oxygen atoms are not shown in these models for the sake of clarity.*

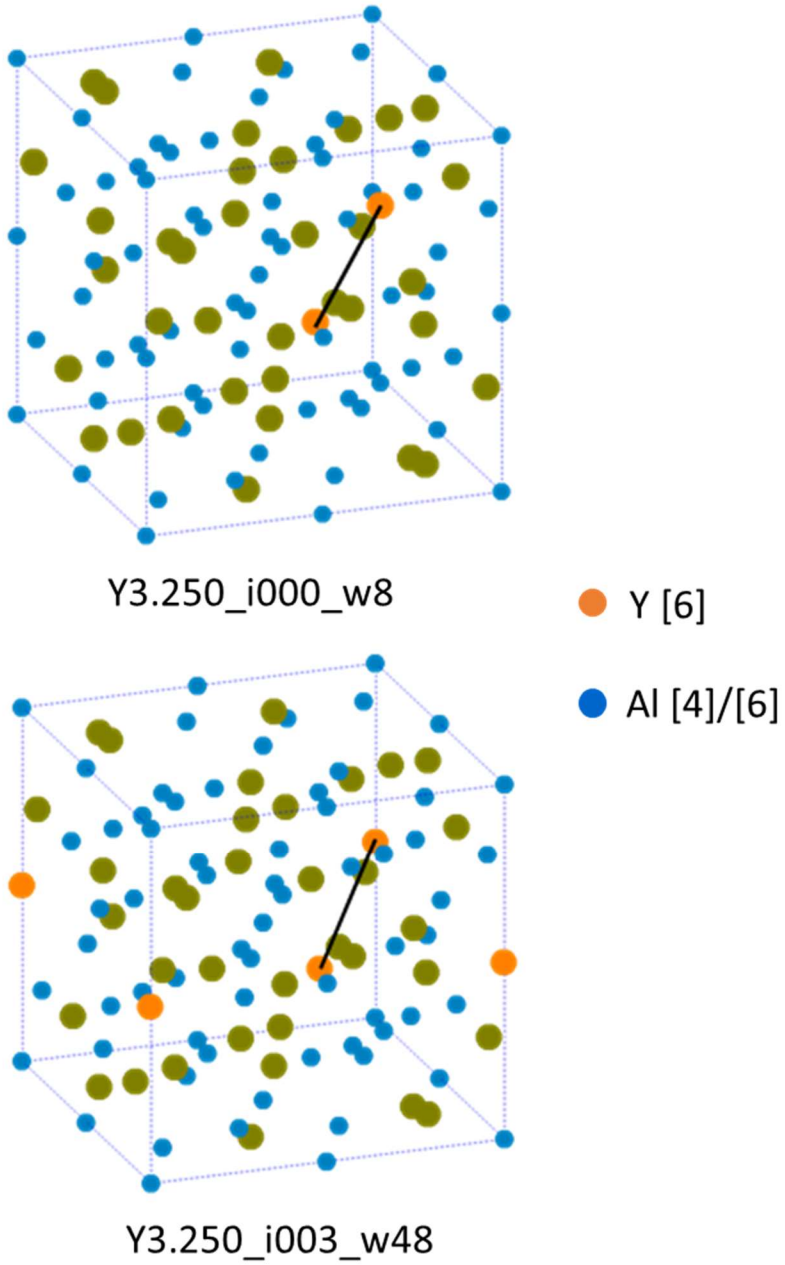

Figure 2. 44. *Two examples of $Y_{3.25}Al_{4.75}O_{12}$ model with two Y defects. The black line connects the involved Y defects in the two models. Y defects (6-coordiante) are labelled as closed orange circles and Al (4- and 6- coordinate) atoms are labelled as closed blue circles. Oxygen atoms are not shown in these models for the sake of clarity.*

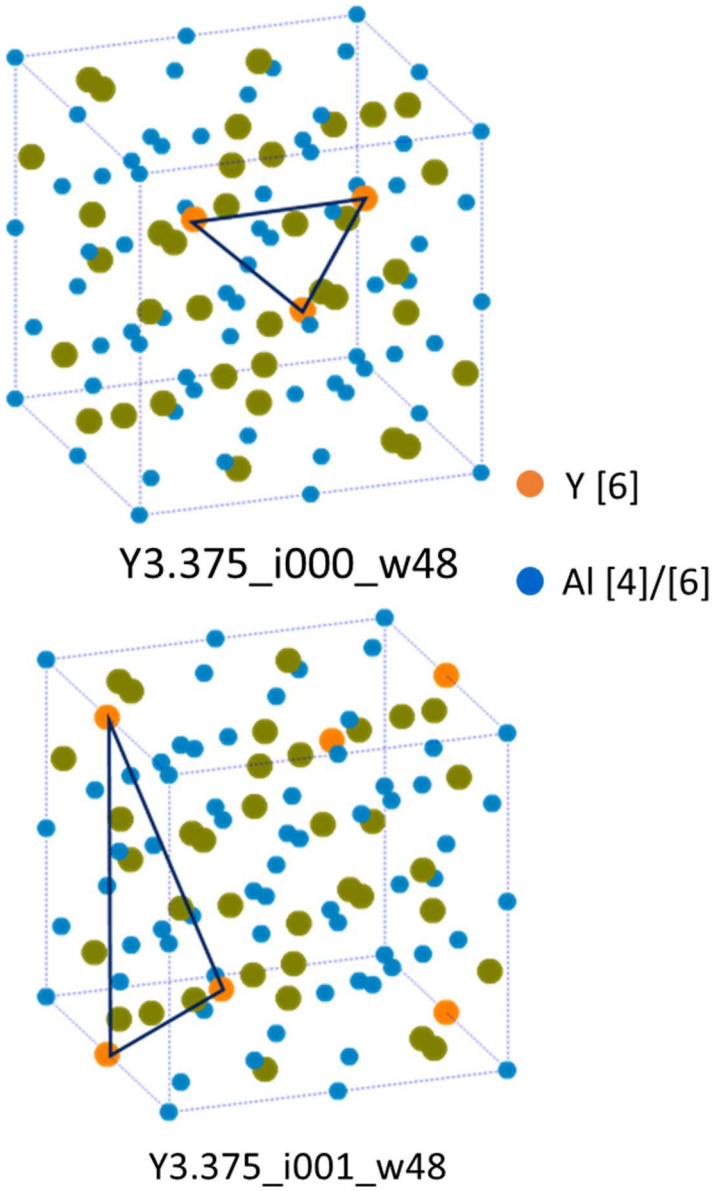

Figure 2.45. *Two examples of $Y_{3.375}Al_{4.625}O_{12}$ model with three Y defects. The vertex of the black triangle connects the involved Y defects in the models. Y defects (6-coordiante) are labelled as closed orange circles and Al (4- and 6- coordinate) atoms are labelled as closed blue circles. Oxygen atoms are not shown in these models for the sake of clarity.*

To set out the structural information of the models, all atomic positions in each model were optimized by DFT using P1 symmetry and cell parameters were fixed to experimental values which were obtained from the Rietveld structural refinement for $Y_{3+x}Al_{5-x}O_{12}$ ($0 \leq x \leq 0.4$). This allows reflecting the realistic interatomic Y-O distances for YO_6. After geometry optimizations, the average Y-O bond length for YO_6 octahedra is around 2.18 Å, significantly larger than the average Al-O bond length for AlO_6 octahedra (*i. e.* 1.9 Å), agreeing with the principle that the radius of Y^{3+} (0.9 Å) is larger than that of Al^{3+} (0.535 Å). The Y-O bond lengths are in 2.29-2.55 Å, resulting in an average bond length of 2.38 Å which is quite close to that obtained from Rietveld refinement (2.37 Å). The Al-O bond lengths of AlO_4 tetrahedra are in 1.75-1.77 Å, with an average value of 1.77 Å which is equal to the average AlO_4 bond length 1.77 Å from 1.768-1.772 Å from Rietveld refinement.

The DFT calculation results of the structural models of $Y_{3.125}Al_{4.875}O_{12}$, $Y_{3.25}Al_{4.75}O_{12}$ and $Y_{3.375}Al_{4.625}O_{12}$ indicate that in the structure of these three non-stoichiometric YAG compounds, the number of oxygen atoms as the first neighbors of Y atom can be 8 and 6 (**figure 2.46**). The chemical shift of 8- and 6-coordinate Y atoms are respectively at 180-230 ppm and 360-440 ppm ranges. The YO_8 chemical shift was found comprised of different components with their weights vary in different chemical shift range. The insert of **figure 2.47** reveals that the secondary neighboring environment of YO_6 in 360-440 ppm is unchanged. while in 210-226 ppm the YO_8 is comprised of three components corresponding to three types of secondary neighboring environments, they are: YO_8 surrounded by one YO_6 and five AlO_6 (first component, black circle); YO_8 surrounded by two YO_6 and four AlO_6 (second component, red circle); YO_8 surrounded by three YO_6 and three AlO_6 (third component, blue circle). In 195-213 ppm range, the weight of the first component is lower than that of in 210-226 ppm, and it does not exist at 182-208 ppm. It is also indicated that in the theoretical point of view, it is possible to have three defects in the structure with whose chemical shift locates at 191 ppm, although the probability is not that high.

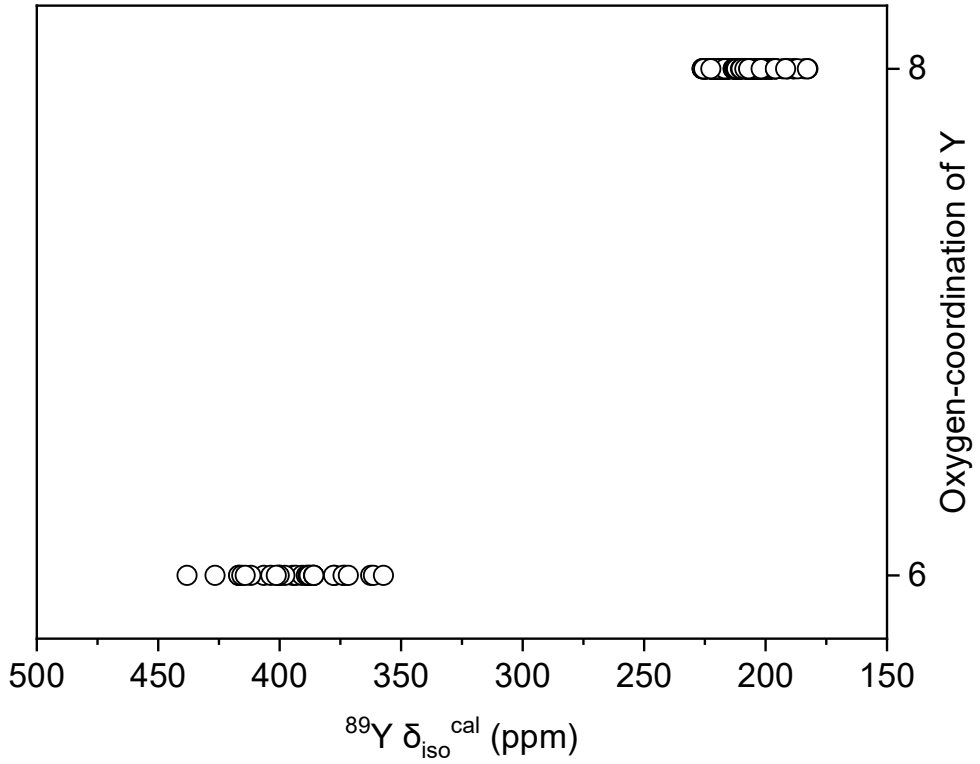

Figure 2.46. *Plot of $^{89}Y\ \delta_{iso}^{cal}$ as a function of oxygen coordination of Y.*

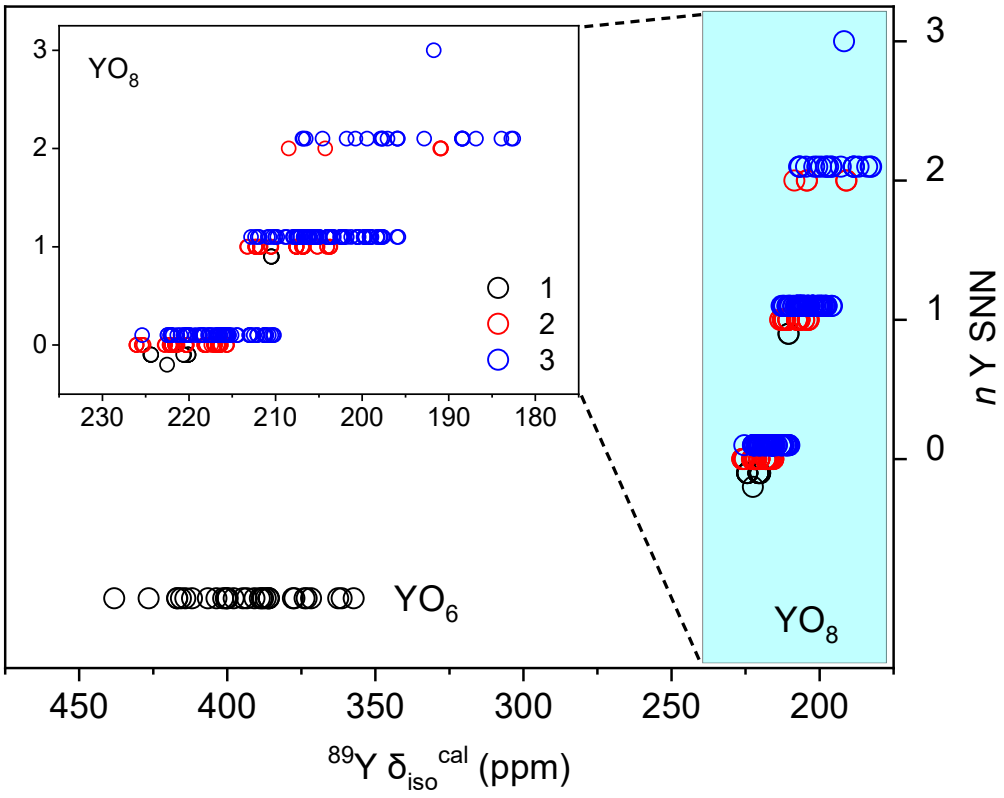

Figure 2.47. *Plot of ^{89}Y as a function of the number (n) of the secondary nearest neighbor (SNN) of Y.*

2.3.12 ^{89}Y NMR of s− and ns−YAGs

Figure 2.48 (a) shows the ^{89}Y MAS NMR spectra of 0.1% Gd-doped $Y_{3+x}Al_{5-x}O_{12}$ (x = 0, 0.1, 0.2, 0.25, 0.3 and 0.4) ceramic powders and of single crystal as a reference as well. The typical YO_8 chemical shift of x = 0 ($Y_3Al_5O_{12}$) appears at 215 ppm[106], the same to that of YAG single crystal. As x = increases, the peak of YO_8 chemical shift become more and more broad, as a shoulder on its right at lower chemical shift appears, its gets more and more intensive as x increases, this could be caused by the YAl_{16a} effect, it can be explained by the simulation on the YO_8 peak in the following text and figures.

The eye-catching point in **figure 2.48 (a)** is that a new chemical shift appears at around 410 ppm, its peak intensity gets more and more intensive as well, as for the shoulder of YO_8 peak. This new peak is magnified in the 300–500 ppm chemical shift range in **figure 4.48 (b)**, its presence is clearly observed and firmly confirmed, it is assigned to be the YO_6 signal. Furthermore, the new peak is found to shift to lower chemical shifts and finally drops at around 400 ppm for x = 0.4 YAG, this is also caused by the existence of Y_{Al16a}. **Table 2.15** lists ^{89}Y isotropic chemical shift (δ_{iso}), full-width at half maximum (fwhm) and relative intensities (I) of the different Y local environments in $Y_{3+x}Al_{5-x}O_{12}$ compounds.

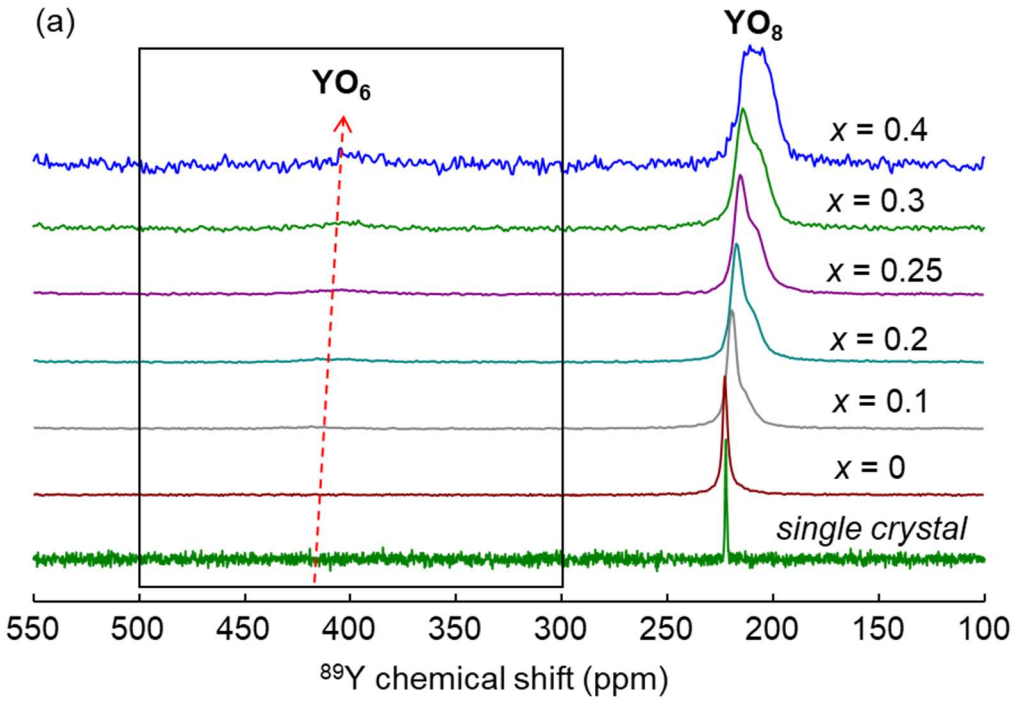

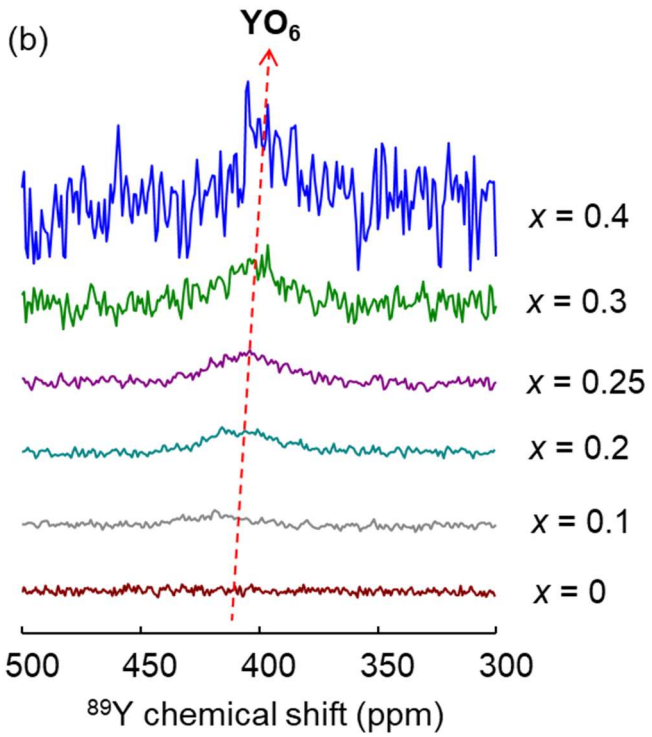

Figure 2.48. (a) *^{89}Y MAS NMR spectra of single crystal (as a reference) and $Y_{3+x}Al_{5-x}O_{12}$ (x = 0, 0.1, 0.2, 0.25, 0.3 and 0.4) from this work.* ***(b)*** *the magnified ^{89}Y MAS NMR spectra of $Y_{3+x}Al_{5-x}O_{12}$ (x = 0, 0.1, 0.2, 0.25, 0.3 and 0.4) garnets in 500-300 ppm. The long red dashed arrow indicates the gradually increased YO_6 chemical shift signal.*

Table 2.15. ^{89}Y isotropic chemical shift (δ_{iso}), full-width at half maximum (fwhm) and relative intensities (I) of the different Y local environments in $Y_{3+x}Al_{5-x}O_{12}$ compounds.

composition	site	δ_{iso} (ppm)	fwhm (ppm)	I (%)
$Y_3Al_5O_{12}$ (single crystal)	YO_8	222.5	0.8	100
$Y_3Al_5O_{12}$:0.1% Gd	YO_8	222.7	2.8	100
0.1% Gd : $Y_{3.1}Al_{4.9}O_{12}$	YO_8	219.5	4.8	69
	YO_8	212.9	9.2	28
	YO_6	419	27.5	3
0.1% Gd: $Y_{3.2}Al_{4.8}O_{12}$	YO_8	217.3	5.9	48
	YO_8	210.4	11.0	46
	YO_6	408	33.0	6
0.1% Gd : $Y_{3.25}Al_{4.75}O_{12}$	YO_8	216	6.0	40
	YO_8	209	11.5	49.5
	YO_8	202	11.0	2.2
	YO_6	405	38.0	8.3
0.1% Gd : $Y_{3.3}Al_{4.7}O_{12}$	YO_8	215	7.0	41
	YO_8	207	11.5	48
	YO_8	202	11.5	3
	YO_6	403	34.0	8
0.1% Gd : $Y_{3.4}Al_{4.6}O_{12}$	YO_8	213	7.5	27
	YO_8	206	11.5	46
	YO_8	201	11.5	17
	YO_6	396	34.0	10

The YO_6 (in 450-370 ppm) and YO_8 (in 250-170 ppm) peaks for non-stoichiometric YAGs ($x > 0$) were simulated using the DMFit software[107]. **Figure 2.49** shows the YO_6 peak in all the YAG samples were fitted by only one component (orange curve). While YO_8 peak cannot be fitted with only one components, but two or three components according to the composition, illustrating the sensitivity of NMR spectra to the specific local environment[87, 88]. From higher to lower chemical shift, the three components are respectively represented by the purple, dark cyan and light blue curves, for the sake of clarity and convenience, in this work they are called the first, second and third component. The three components imply different second coordination around YO_8, the first component indicates that YO_8 has pure AlO_6 second coordination effect, the second component involves five AlO_6 and one YO_6 second coordination effect, and the third component with four AlO_6 and two YO_6. The variation of the intensity of the component indicates the proportion change of a specific component.

For $x = 0.1$, the YO_8 peak was fitted by the first and the second components, it is the similar situation for $x = 0.2$ YAG, the difference is that the intensity of the second component get

more intensive while that of the first component becomes weaker, implying that from x = 0.1 YAG to x = 0.2, there are contribution from the second component (five AlO_6 and one YO_6). Further increasing x to 0.25, the contribution of the third component was observed, and it exists further in x = 0.3 and 0.4 YAGs. Generally, as x increases the intensity of the first component decreases, and the intensity of the second and third components increases, this leads to the broadening the YO_8 peak.

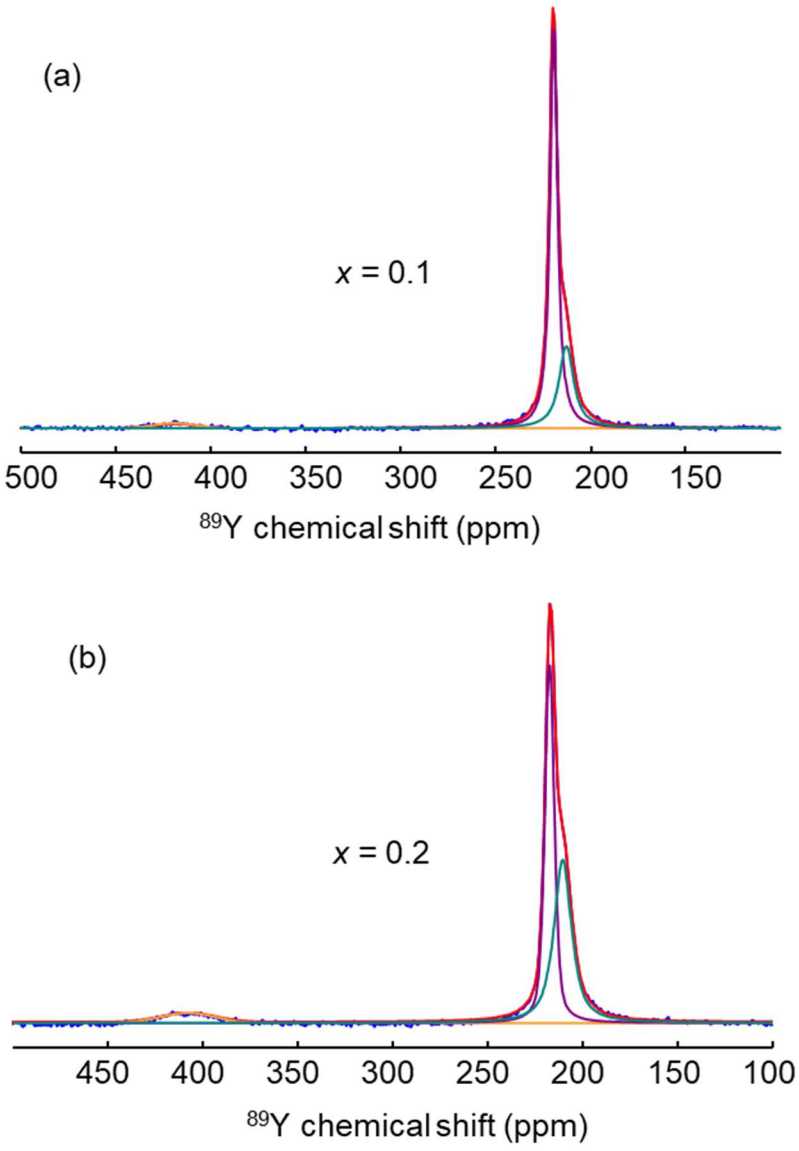

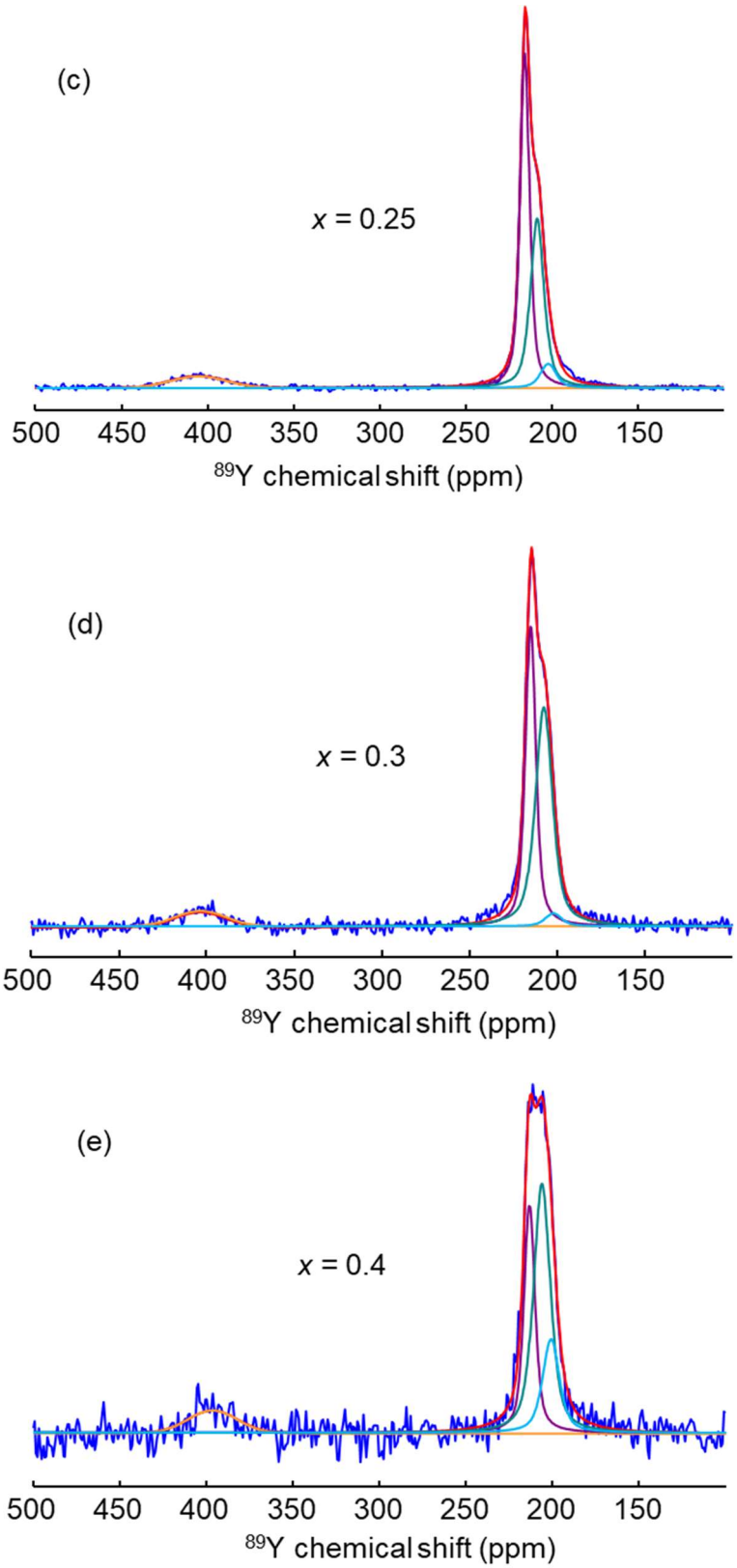

Figure 2.49. *Simulation of the ^{89}Y NMR spectra of $Y_{3+x}Al_{5-x}O_{12}$ (x = 0.1* ***(a)****, 0.2****(b)****, 0.25****(c)****, 0.3****(d)*** *and 0.4****(e)****) garnets. In each, there The blue and red lines are respectively experimental and simulated spectra, the orange line peaking at round 400 ppm shows the simulation of ^{89}Y signal of 6-coordinate Y. The purple, green and light blue lines respectively represent the three types of coordination effect from the secondary nearest neighbor (SNN).*

2.3.13 EXAFS results of s− and ns−YAGs

EXAFS data were collected from the DIFFABS beamline at the SOLEIL synchrotron at the Y K absorption edge. EXAFS oscillations ($k^2 \cdot \chi(k)$) (**figure 2.50**) was extracted from the linear absorption coefficient above yttrium absorption threshold using Athena software[108], it shows the oscillation shifts slightly towards lower k and its amplitude decreases as yttrium atoms in the garnet structure increases, this phenomenon becomes pronounced after the EXAFS signal is processed by Fourier transform (**figure 2.51**), especially for the two peaks labeled with asterisk in 1-2 and 3-4 Å R value ranges. The decrease in amplitude of the peak is ascribed to the local disorder caused by the importation of 6-coordiante Y^{3+} and its concentration in ns-YAG.

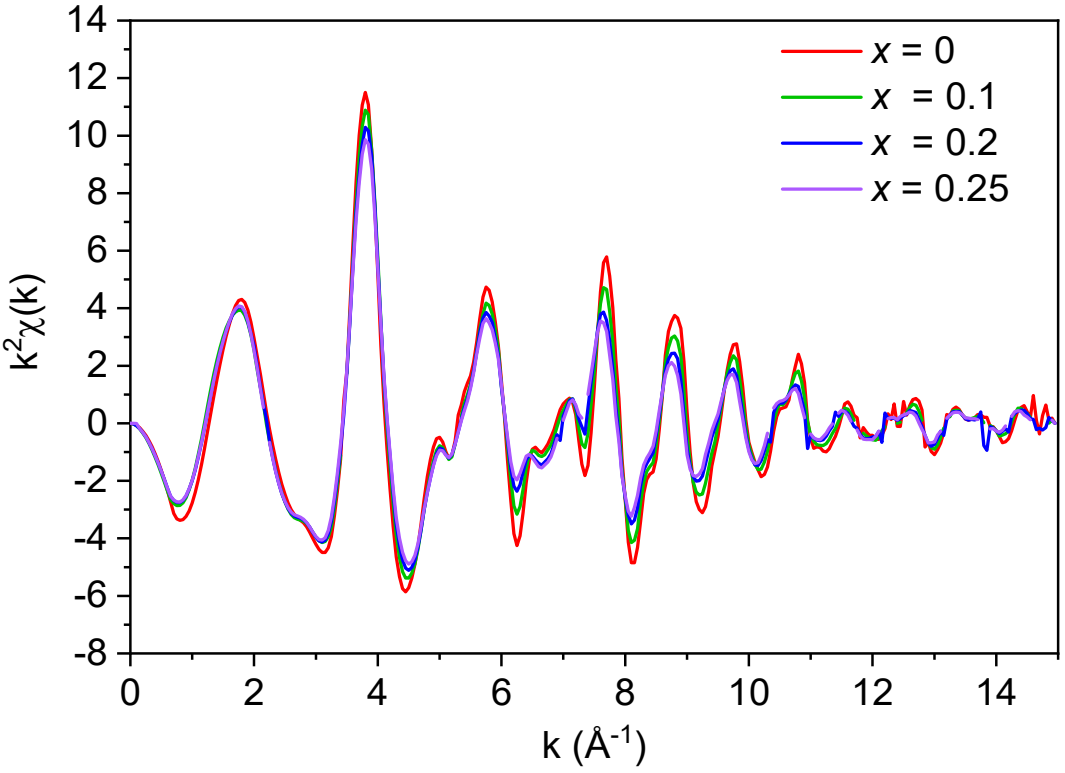

Figure 2.50. *EXAFS oscillations ($K^2 \cdot \chi$ (k)) of $Y_{3+x}Al_{5-x}O_{12}$ (x = 0. 0.1, 0.2 and 0.25), they are extracted from the linear absorption coefficient measured in transmission mode at the K edge of yttrium (17038 eV).*

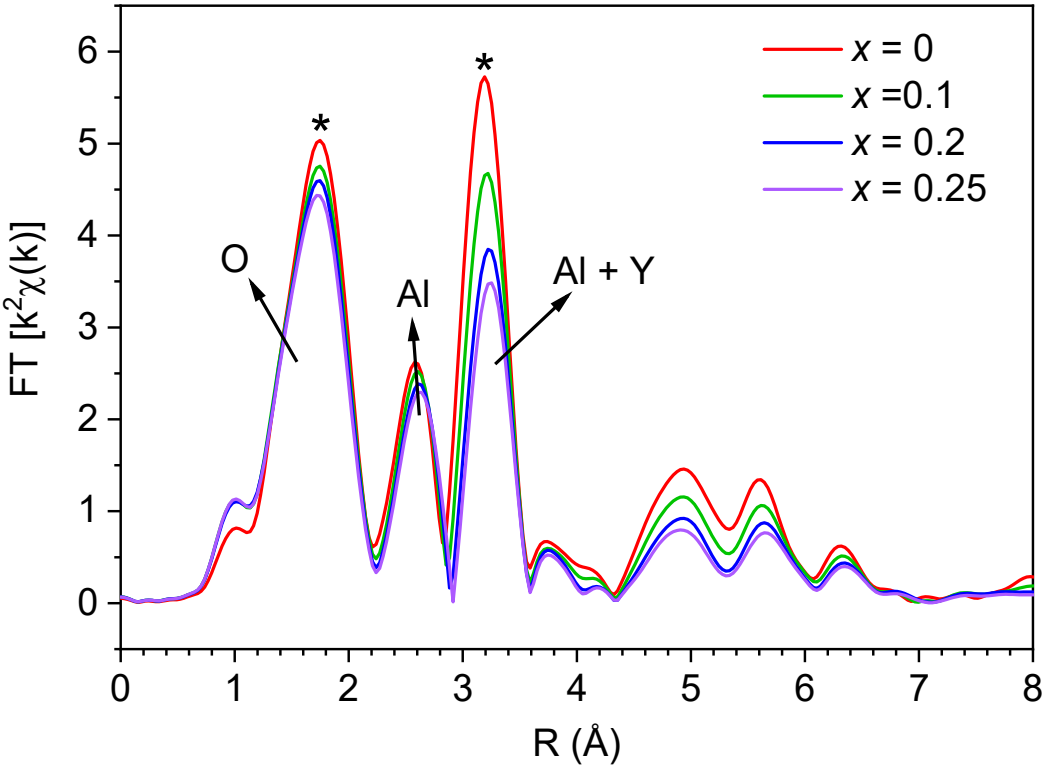

Figure 2.51. *Fourier transform of EXAFS oscillations for $Y_{3+x}Al_{5-x}O_{12}$ (x = 0. 0.1, 0.2 and 0.25).*

Simulation of the EXAFS oscillations was performed by Didier ZANGHI (CEMHTI), with FFF8 calculation code[109]. The input file for the simulation was obtained by relaxing the structure at 0 K by CASTEP code[90] using a cubic box with 12.0426 Å lattice parameter and 160 atoms (16 octahedral Al, 24 tetrahedral Al, 24 dodecahedral Y and 96 O). The total EXAFS signal of Y atoms is represented as a linear combination of two signal components: the signal from 8- and 6-coordinate Y atoms. The weight (w_i) of each contribution is decided by the Y_{Al} substitution rate (*x* in the equation) and the multiplicity of octahedral sites, thus the total EXAFS signal can be represented as:

$$\chi_{tot} = \sum_i w_i \,.\, [x.\chi_1 + (1-x).\chi_2]$$

The calculated weight w_i of inequivalent octahedral Al sites as a function of the number of Y_{Al} defect are listed in **table 2.16**, and distances corresponding to the 8 single scattering paths around an absorbing Y atom are in table 2.16.

Table 2.16. Calculated weight w_i of inequivalent octahedral Al sites as a function of the number of Y_{Al} defect.

substitution Al/Y	*x*	multiplicity site Al1	w_i (%)
1	0.04166667	-	100
2	0.08	8	6.67
		24	20.00
		24	20.00
		48	40.00
		16	13.33

The structural relaxation was performed by Density Function Theory (DFT) to minimize the inter-atomic forces and optimize the lattice geometry in non-stoichiometric YAG structure, which is necessary when atomic substitution takes place between two different atoms. In the DFT calculation, the defect number of yttrium atom, rather than the number of excess Y in a structure unit, was concerned. In the $Y_3Al_5O_{12}$ structure, there is no Y_{Al} defect, but there exist, respectively, 1 and 2 defects in $Y_{3.125}Al_{4.875}O_{12}$ and $Y_{3.25}Al_{4.75}O_{12}$. When the structure is not relaxed (**figure 2.52**), the Fourier transform of EXAFS oscillations of the samples with 0, 1 and 2 defects are overlapped despite of the different number of Y defect, which is ascribed to the neglect of the inter-atomic forces introduced by the Y substitution. While with structural relaxation, the Fourier transform of EXAFS oscillations deduced from the linear combination are shown as in **figure 2.53**. The amplitude of the peaks decreases as the number of Y_{Al} defect increases, whilst peaks shift towards larger R values, agreeing with the experimental EXAFS oscillations which were directly extracted from the original linear absorption coefficient.

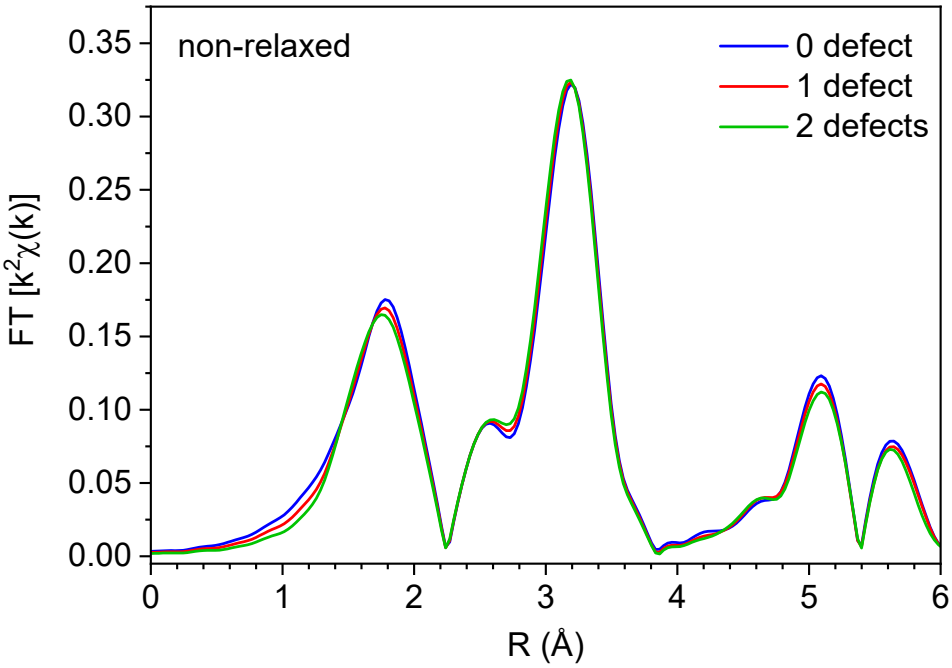

Figure 2.52. *Fourier transform of EXAFS oscillations calculated by FEFF on non-relaxed structures after substitution of Al1 (octahedral) atoms by Y.*

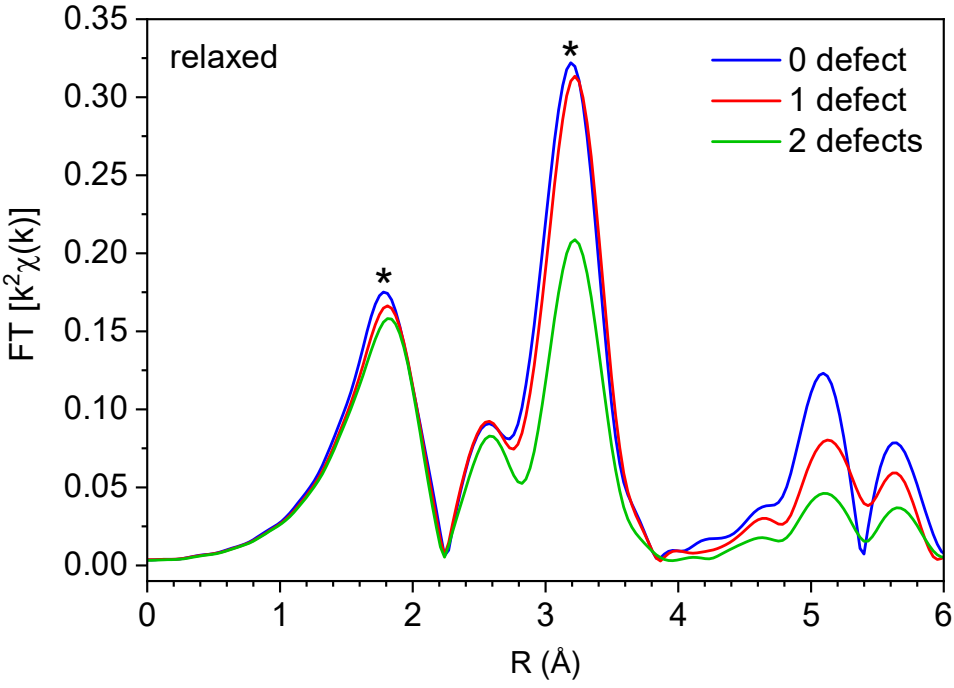

Figure 2.53. *Fourier transform of EXAFS oscillations calculated by FEFF8 on relaxed structures after substitution of Al1 (octahedral) atoms by Y.*

The X-ray absorption spectroscopy was not only sensitive to the Y_{Al} defect even it was at a low level, but also can distinguish different coordinating contributions together with their corresponding bonging length between the central and ligand atoms. Contributions from all the atomic coordinating components in $Y_3Al_5O_{12}$ are resolved from the total Fourier transform signal (**figure 2.54**). It determines the peak in 0-2.25 Å R range composes of oxygen neighbors and the two peaks in 2.25-3.8 Å R range involve aluminum and yttrium neighbors and multiple scattering as well. **Table 2.17** lists the distances between involved atoms concerned by the two peaks in 2.25-3.8 Å R range. Since the atoms are close to each other, the different contribution components under the two peaks are not 100% distinguishable. So our focus on the Fourier transform is set on the single peak in 0-2.25 Å R range.

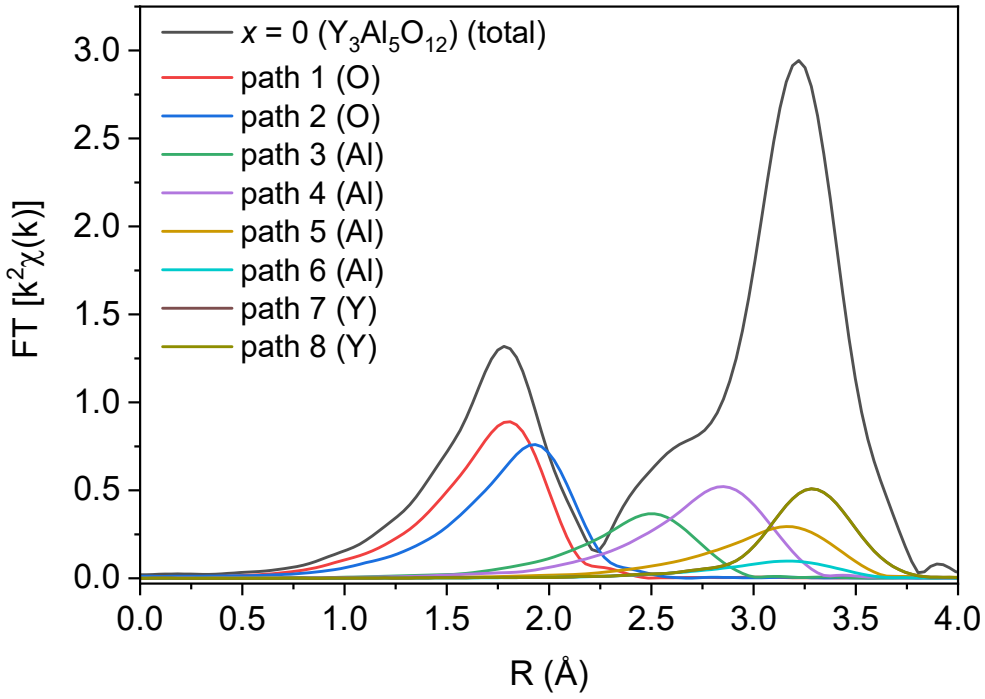

Figure 2.54. *Resolved contributions, in 0-4 Å R range, of Fourier transform on relaxed structure for $Y_3Al_5O_{12}$.*

Table 2.17. 8 single backscattering paths around an absorbing Y atom.

paths	pairs	coordination number	distance (Å)
path1	Y-O	4	2.3033
path2	Y-O	4	2.4377
path3	Y-Al2	2	3.0015
path4	Y-Al1	4	3.3561
path5	Y-Al2	3	3.6763
path6	Y-Al2	1	3.6766
path7	Y-Y2	2	3.6764
path8	Y-Y2	2	3.6766

Figure 2.55 shows the experimental Fourier transform of EXAFS oscillations of $Y_{3.25}Al_{4.75}O_{12}$ whose structure contains 2 Y_{Al} defects, its first peak in 0-2.25 Å R range was simulated with the all the contributions. The simulation was carried out for single wave backscattering by applying the sample composition and the amplitude functions of Y(absorber)-O(backscattered) atomic pair determined by FEFF[110] for $Y_3Al_5O_{12}$ to the standard EXAFS formula. The simulated peak matches well with the corresponding experimental result. This simulation was extended to other non-stoichiometric YAGs.

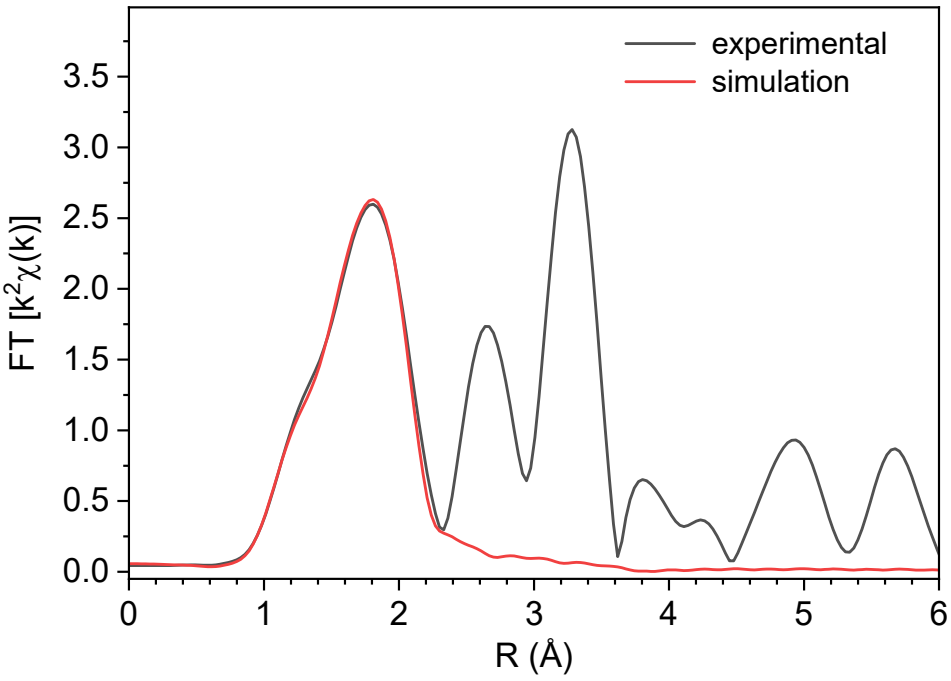

Figure 2.55. *Simulation of the Fourier Transform of EXAFS oscillations on the peak in 0-2.25 Å for* $Y_{3.25}Al_{4.75}O_{12}$.

Table 2.18 shows the simulation results of $Y_{3+x}Al_{5-x}O_{12}$ (x = 0, 0.1, 0.2, and 0.25), S_0^2 and E_0 are involved parameters in the standard EXAFS formula[110]. It indicates as Y substitution for Al increases, a slight decrease in peak position and a decrease in the average yttrium coordination appear. Whilst, the Debye-Waller term at around 0.10 $Å^{-1}$ was also found to increase slightly, indicating a significant structural disorder.

Table 2.18. Simulated result of the Fourier Transform of EXAFS oscillations for the single peak in 0-0.25 Å of the Fourier Transform of EXAFS oscillations on the peak in 0-2.25 Å for $Y_{3.25}Al_{4.75}O_1$.

sample	N (Y-O)	ΔN	σ^2 ($Å^{-2}$)	$\sigma(Å^{-1})$	R(Å)	S_O^2	ΔE_0(eV)
Y3	8.0000000	0.4000000	0.011387	0.10670989	2.347948	1.288677	-0.10944
Y3.1	7.5304450	0.3765223	0.011413	0.10683164	2.344769	1.288677	-0.10944
Y3.2	7.3616930	0.3680847	0.011556	0.10749884	2.341898	1.288677	-0.10944
Y3.25	7.1940770	0.3597039	0.011643	0.10790273	2.339202	1.288677	-0.10944

It has been determined that the decrease of the amplitude of the EXAFS oscillation peak is ascribed to the decreases in yttrium coordination. Therefore, the substitution x can be deduced by the formula below:

$$x = (1-\frac{N}{8}) \times 100$$

where N is calculated average yttrium coordination, substitution rates x for each composition are given in **table 2.19**.

Table 2.19. Y_{atomic} deduced from the number of coordination of Y determined by simulating the peak in 0-2.25 Å of Fourier Transform of EXAFS oscillations.

coordination (fit)	ratio N/8	Substitution rate x	Y_{atomic} (EXAFS)	1/2errorYat(EXAFS)	Y_{atomic} initial
8.00	1	0	2.995	0.084	3
7.53	0.94130563	0.05869438	3.193	0.079	3.1
7.36	0.92021163	0.07978838	3.264	0.078	3.2
7.19	0.89925963	0.10074038	3.335	0.076	3.25

The theoretical number of yttrium atom and the substitution rate *x* is in a linear relationship (**figure 2.56**). The experimental Y_{atomic} as a function of initial (or theoretical) Y_{atomic} are compared with the theoretical Y_{atomic} (**figure 2.57**), it indicated that the experimental Y_{atomic} values also increases, they deviate from the theoretical trend but fall within in the error bar.

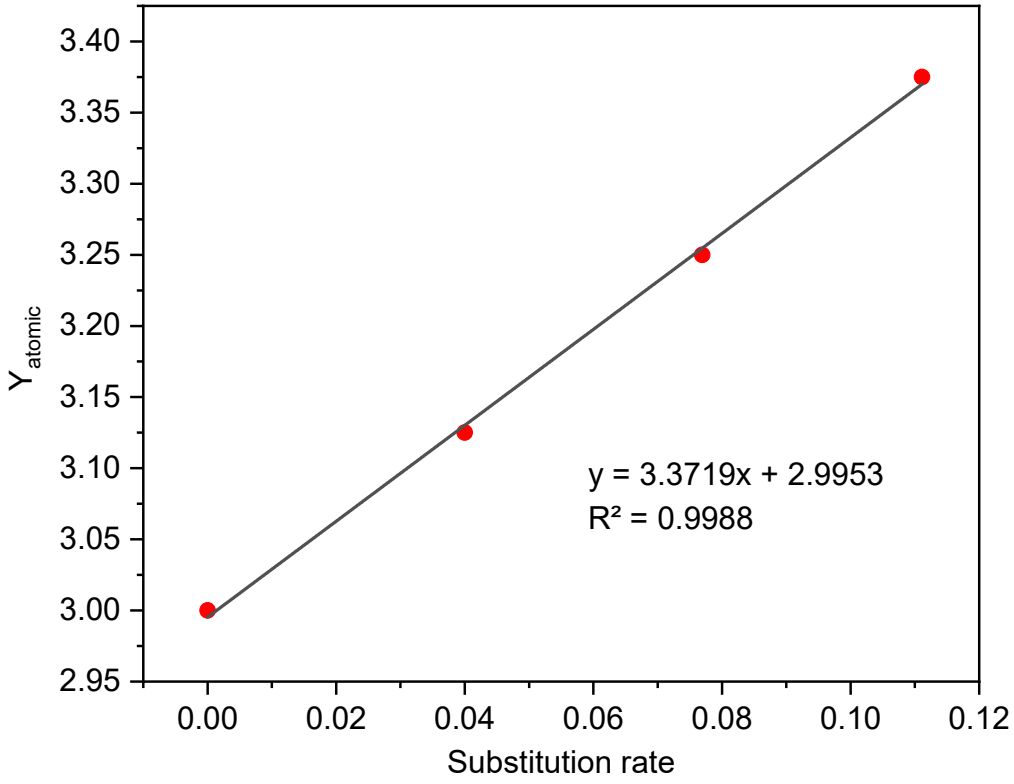

Figure 2.56. *Relationship between 'theoretical' Y_{atomic} and the substitution rate x.*

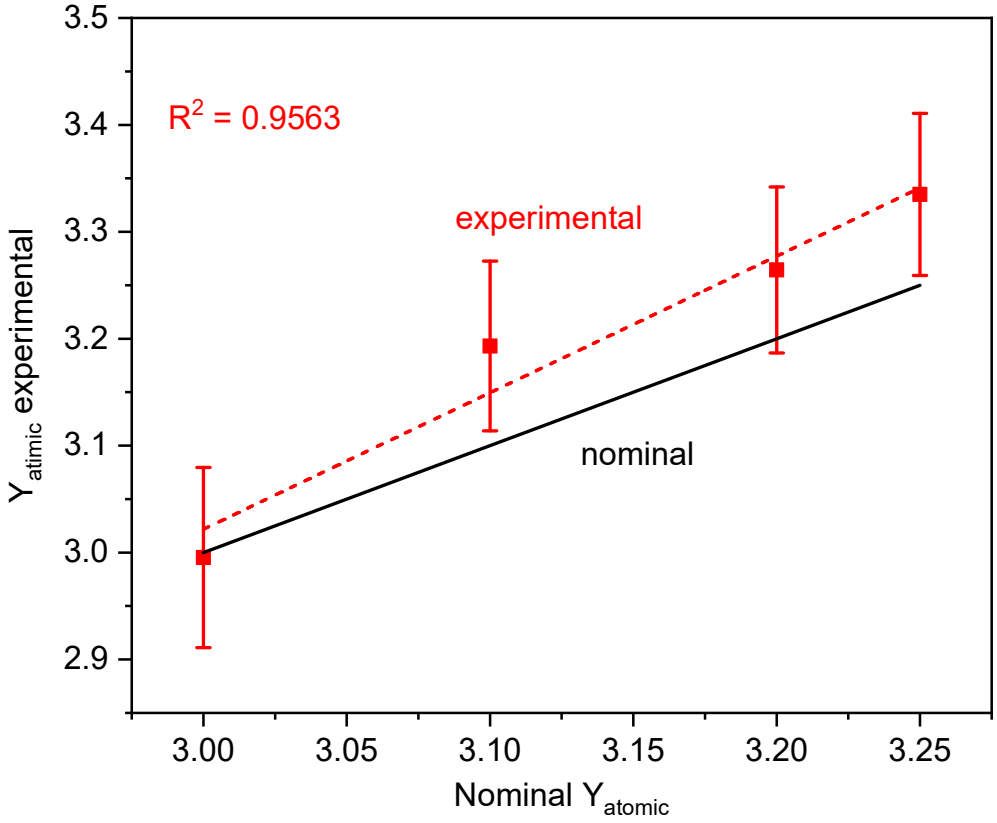

Figure 2. 57. *Comparison between the Y_{atomic} deduced from EXAFS and the experimental Yatomic which was confirmed by Rietveld refined in good agreement with theoretical Y_{atomic} values.*

Chapter 3

Luminescence properties of rare−earth doped s− and ns−YAGs

3 Luminescence properties of rare−earth and transition metal doped s− and ns−YAGs

3.1 Introduction

Luminescence properties of $A_3B_5O_{12}$ garnet arise from luminescence centers under excitation. The luminescence centers are created by two ways: (1) substitution of foreign isoelectronic cations which are not originally in the host compound or (2) defects caused by the substitution of excess cations for one of the other, where both cations originally exist in garnet lattice. In the $A_3B_5O_{12}$ garnet crystal structure, A cations occupy the 8−folded dodecahedral and B cations occupy the 6−folded octahedral (40%) and 4−folded tetrahedral (60%) sites. The luminescence performance in YAG is usually caused by the incorporation of lanthanides, *e.g*. Nd^{3+}, Yb^{3+}, Er^{3+} and so on. These lanthanides are usually after the seventh group period in the periodic table, their radii are around 1 Å, therefore favored by dodecahedral sites in stoichiometric YAG and become luminescence centers, *Ln*: YAG (*Ln* = Yb^{3+} [26], Nd^{3+} [24] and Ce^{3+} [111]). The successful synthesis of non−stoichiometric YAG ($Y_{3+x}Al_{5-x}O_{12}$) which intrinsically possesses site defect Y_{Al16a} may bring the possibility of inducing lanthanide doping into octahedral sites, therefore new environments for lanthanide dopants would be created. This may result in different luminescence performance of non−stoichiometric YAG. Approaches of increasing the concentration and changing the site coordination of luminescence centers is one of the ways to change emission frequency therefore the color, thus the importance of creating high−content nonstoichiometry is addressed. Luminescence properties study in this work is based on our successful synthesis of highly non−stoichiometric YAG ($Y_{3+x}Al_{5-x}O_{12}$, $0 < x \leq 0.2$) synthesized by ADL in argon. As the synthesis method is one the factors that affect the emission properties[31, 112], luminescence properties of other $Y_{3+x}Al_{5-x}O_{12}$ ($0.3 \leq x < 0.4$) non−stoichiometric garnets were not studied, as they were prepared by glass crystallisation method rather than same method of direct crystallisation. It has been known that different synthesis methods or detailed synthesis conditions (mostly for the temperature) would introduce different defects or different concentration of defect in the YAG structure[32, 113-115], which have important affect in luminescence properties of the YAG ceramics materials. Furthermore, the nonstoichiometry of the crystallized YAG are also different, this makes the comparison of the luminescence properties between directly crystallized YAG and glass crystallized YAG complicated and even incomparable in some way. But it would be interesting in the future to study the effect of different synthesis methods (direct

crystallisation by ADL and glass crystallisation in our case) on lattice defect concentration or distribution in the YAG structure thereby on the luminescence properties.Ln^{3+}−doped YAG crystalline compounds have been broadly studied due to their applications as phosphors, the related Ln^{3+} can be elements with atomic numbers in 58 (Ce)–70 (Lu), from this range we choose the large Ce^{3+}, mediumDy^{3+} and small Yb^{3+} (plus Er^{3+} for co-doping). The Yb^{3+}−Er^{3+} co−doped and Dy^{3+} or Ce^{3+} single doped YAG phosphors are commonly in the form of powders, by integrating the phosphors powders into carrier materials and coating them on carriers, LED components with high luminous efficiency then are manufactured. In this work, we especially analyze stoichiometric (s−) and non−stoichiometric (ns−) YAGs which are Yb^{3+}−Er^{3+} co−doped and Ce^{3+} single doped, because these two doping relate to the smallest and the biggest radius of lanthanide ions that induced in this work. The effect of ionic radius on cationic distribution and thus on luminescence property will be discussed in the result part of this chapter. Ce^{3+}−YAG yellow phosphor is popular for its combination with blue LED to manufacture white LED[84, 116]. Yb^{3+}, Er^{3+} YAG works in a mechanism of energy transfer upconversion (ETU), where Yb^{3+} sensitizer ions firstly absorb pump energy at broad 900−1000 nm range compared to Er^{3+} [25], and later partially transfer energy in a non−radiative process to Er^{3+} activator ions leading Er^{3+} ions to reach an excited state. The Er^{3+} ion is then again promoted by Yb^{3+}ion to an even higher excited state. The following Er^{3+} emission from its excited state to ground state typically leads to green and red emission.

It is commonly known that lanthanides doping levels in YAG structure is very important to emission intensity. It has been reported that Yb^{3+} and Er^{3+} doping levels vary respectively in 0.5−30 at % and 0.5−10 at %, while 15−20 at % Yb^{3+} [25, 117] and 2 mol % Er^{3+} [118] are optimal concentration for emission intensity rather than 30 at % for Yb^{3+} and 10 at % for Er^{3+}. By referring to these work, in our work, Yb^{3+} concentration was fixed at 20 at % and Er^{3+} concentration varied at 0.5 at. %, 1 at. % and 2 at. %. Emission intensity and lifetime and were studied. Most importantly, average structure of 20 at.% Yb^{3+}−2 at.% Er^{3+} co−doped stoichiometric and non−stoichiometric YAGs was analyzed by Rietveld refinement, and luminescence mechanism of Yb^{3+} − Er^{3+} co−doped YAG non−stoichiometric YAG was discussed combing with structural analysis.

As stated in the previous chapter, although non−stoichiometric (ns−) YAG has been studied since around half an century[39], a YAG compound with its Y_{Al16a} defects up to 20 at. % has never been reported. However, this topic is still interesting as the existence of Y_{Al16a} defect is one the most important factors influencing luminescence properties[30]. Y. Zorenko *et al*.[31]

reported that the native Y_{Al16a} defects in $Y_3Al_5O_{12}$ form as analogs of isoelectronic impurities and work as luminescent and trap centers[30], therefore influenced luminescence properties. This implies that if Y_{Al16a} defects are produced with high concentration, the effect of Y_{Al16a} defects on luminescence properties could be magnified and it is possible by this way to improve the obtained luminescence properties.

3.2 Methods

Synthesis of rare−earth (*RE* = Yb, Er, Dy and Ce) and transition metal Mn doped YAG (stoichiometric and non−stoichiometric) and other non−YAG garnets were tried in this chapter. The synthesized doped garnets listed in **table 3.1** and starting materials are listed in **table 3.2**. The synthesis work was mainly performed by aerodynamic levitation method, the as-synthesized samples were ground into powders and measured by XRD over 15−80° 2θ whit a 0.01° step size for phase indexation.

SPD measurements were performed on 20 at.% Yb−2 at.% Er doped $Y_3Al_5O_{12}$, $Y_{3.2}Al_{4.8}O_{12}$ and $Y_{3.3}Al_{4.8}O_{12}$ (not for $Y_{3.1}Al_{4.8}O_{12}$ for the sake of due), their average structures were analysed by Rietveld refinement and the refinements were evaluated by the rationality of structural parameters and Rietveld discrepancy values R_{wp} and *goodness-of-fit* (*gof*).

Luminescence properties measurement for these rare−earth doped YAG samples were conducted by Dr. Isabel Becerro (ICMS laboratory, Seville, Spain) on sample powders which have been measured by XRD and indexed with single garnet phase. Before the measurement, sample powders were manually pressed using glass slide. The pressed sample was exposed to laser beam with a diameter of ~1 mm. To confirm if the pressing process on the sample powders have influence on luminescence performance and to check homogeneity inside the sample, Yb^{3+}−Er^{3+} co−doped YAG sample beads were polished on two opposite sides, and processed into ceramic disks. Diameters of the two polished sides are around 1−1.2 mm.

Table 3.1. *RE*s (*RE* = Yb, Er, Dy and Ce) and Mn doped s−YAG and ns−YAG.

dopant	host
20 at.% Yb−0.5 at.% Er	$Y_3Al_5O_{12}$
	$Y_{3.1}Al_{4.9}O_{12}$
	$Y_{3.2}Al_{4.8}O_{12}$
20 at.% Yb−1 at.% Er	$Y_3Al_5O_{12}$
	$Y_{3.1}Al_{4.9}O_{12}$
	$Y_{3.2}Al_{4.8}O_{12}$
20 at.% Yb−2 at.% Er	$Y_3Al_5O_{12}$
	$Y_{3.1}Al_{4.9}O_{12}$
	$Y_{3.2}Al_{4.8}O_{12}$
1 at.% Dy	$Y3Al5O_{12}$
	$Y_{3.2}Al_{4.8}O_{12}$
0.5 at.% Mn	$Y_3Al_5O_{12}$
	$Y_{3.2}Al_{4.8}O_{12}$
5 at.% Ce	$Y_3Al_5O_{12}$
	$Y_{3.2}Al_{4.8}O_{12}$

Table 3.2. Information on starting materials.

starting materials	molar mass	purity	production company
Y_2O_3	225.8099	99.9%	STREM CHEMICALS
Al_2O_3	101.9613	99.999%	STREM CHEMICALS
MnO_2	86.9368	99.9%	STREM CHEMICALS
Fe_2O_3	159.6882	99.5%	Alfa Aesar
Ga_2O_3	187.4442	99.998%	STREM CHEMICALS
Sc_2O_3	137.91	99.9%	Alfa Aesar
CeO_2	172.1148	99.99%	STREM CHEMICALS
Nd_2O_3	336.4782	99.99+%	STREM CHEMICALS
Sm_2O_3	348.7182	99.9%	STREM CHEMICALS
Gd_2O_3	362.4982	99.99%	STREM CHEMICALS
Er2O3	382.5162	99.99%	STREM CHEMICALS
Yb_2O_3	394.0782	99.9%	STREM CHEMICALS

Emission spectra were performed, under room temperature, by FLS1000 photoluminescence spectrometer (Edinburgh instrument) equipped with a 2W 980 nm laser as the excitation source. Fluorescence lifetimes were obtained by fluorescence decay curves. The decay curves were collected in an extended pulse range tuned by a control box installed in the same instrument. Peak intensity of the green and red luminescence was recorded by changing the pumping power of the 980 nm laser using an iris filter.

3.3 Results

3.3.1 Synthesis of Yb, Er co−doped s− and ns−YAGs

Figure 3.1 show XRD patterns of 20 at.% Yb−*n* at.% Er (*n* = 0.5, 1) doped $Y_3Al_5O_{12}$ and $Y_{3.2}Al_{4.8}O_{12}$, and 20 at.% Y−2 at.% Er doped $Y_3Al_5O_{12}$, $Y_{3.1}Al_{4.9}O_{12}$, $Y_{3.2}Al_{4.8}O_{12}$ and $Y_{3.3}Al_{4.7}O_{12}$, all the diffraction peaks belong to YAG phase, indicating that all these samples have been synthesized as single garnet phase.

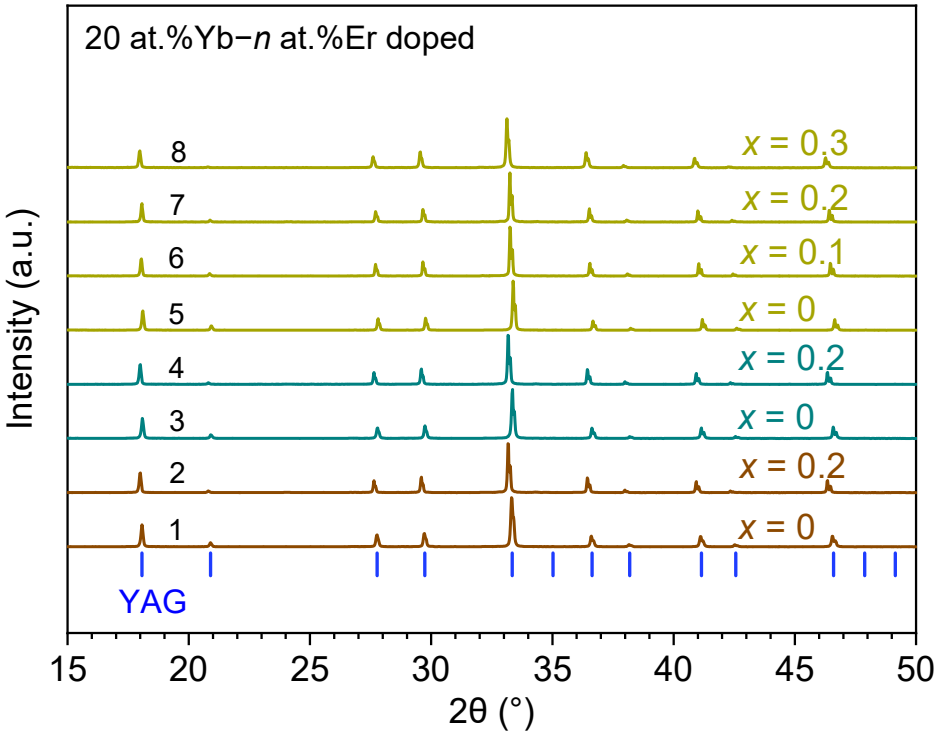

Figure 3.1. *XRD patterns of 20 at. % Yb−n at.% Er (n = 0.5 (with number 1 and 2), 1 (with number 3 and 4)) doped $Y_{3+x}Al_{5-x}O_{12}$ (x = 0 and 0.2) and 20 at. % Yb−2 at.% Er doped $Y_{3+x}Al_{5-x}O_{12}$ (x = 0, 0.1, 0.2 and 0.3 with number 5-8) which were synthesized by ADL in argon (except that x = 0.3 was synthesized by glass crystallisation method). The ticks indicate Bragg diffraction positions of YAG.*

3.3.1.2 Average structure of 20 at.% Yb–2 at.% Er co−doped YAGs

To detect the occupation of Yb and Er in the YAG structure, samples with Er doping level at 2 at.% was measured by SPD for Rietveld structural analysis, as 0.5 at.% and 1 at. % Er doping could be too low to be correctly characterized. 20 at.% Yb-2 at.% Er doped $Y_{3+x}Al_{5-x}O_{12}$ (x = 0, 0.1, 0.2 and 0.3) YAG powders from single beads were prepared for SPD measurement, the powders were loaded into a capillary with a 0.8 mm diameter, their

data were collected under diffraction wavelength of ~0.457 Å and over 0.5-50° 2θ with a step size 0.001°, the diffraction patterns are shown in **figure 3.2**, due to the poor quality, the SPD pattern of Yb, Er-doped $Y_{3.1}Al_{4.9}O_{12}$ is not concluded.

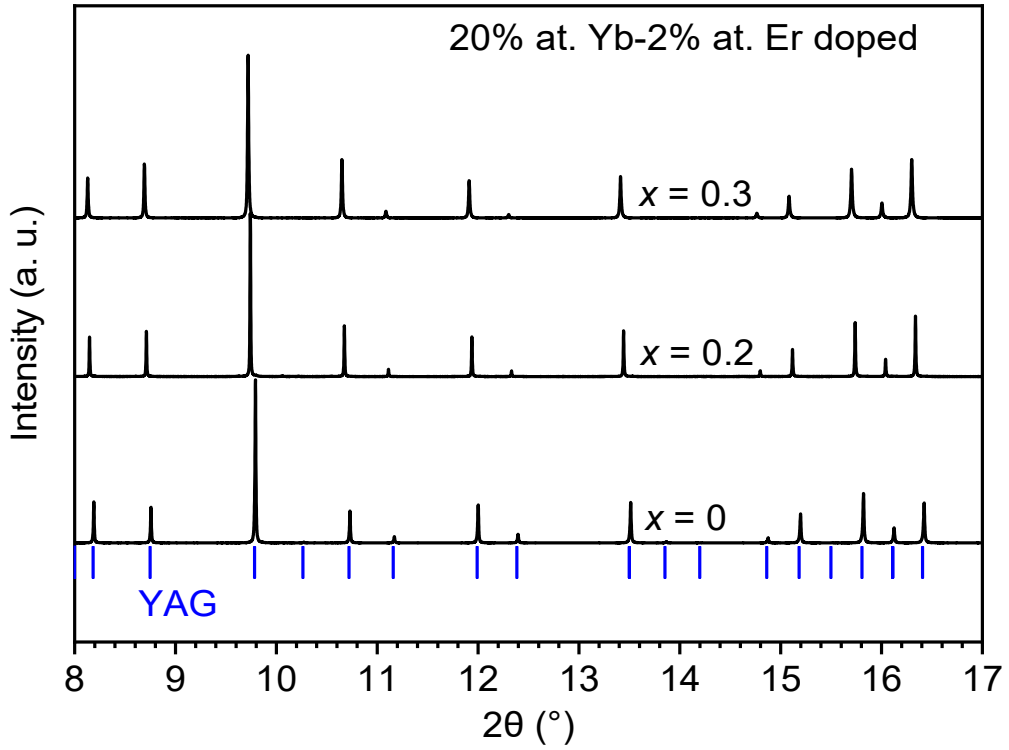

Figure 3.2. *SPD patterns of 20 at.Yb–2 at.% Er doped $Y_{3+x}Al_{5-}O_{12}$ (x = 0, 0.2 and 0.3). The blue tick marks indicate the Bragg positions of YAG structure.*

■ Rietveld refinement process

Cubic $Y_3Al_5O_{12}$ with space group *Ia−3d* was used as structural refinement model. To determine the influence of Yb and Er doping ions on host lattice structure, structural refinement was performed on high−resolution SPD data of 20 at.% Yb−2 at.% Er co−doped $Y_{3+x}Al_{5-x}O_{12}$ (x = 0, 0.2 and 0.3) compositions using *TOPAS Academic V6* software. Lattice parameter, atomic positions, peak profile were successively refined. Yb/Er occupation was refined not only at dodecahedral (8−coordinate, Wyckoff site 24c) but octahedral (6−coordinate, Wyckoff site 16a) sites. As Er (atomic number 68) and Yb (atomic number 70) are close to each other and Er fraction in the whole composition is quite low, Yb and Er occupations were coupled during the refinement: the Er occupancies were set as one−tenth of Yb occupations at these two sites. As excess Y^{3+} has been confirmed, by

characterization on average structure and local structure, to locate at octahedral sites in ns-YAG, therefore in the refinement process, Y was also refined at this site for Yb, Er doped x > 0 YAG. All Wyckoff sites were considered to be fully occupied (occupancy is 1). Compositional constraints were applied to have the occupancy of each atom at every Wyckoff site as close as possible to the expected value. Finally, thermal parameters at each Wyckoff site were independently refined. After confirming that the structural information of main garnet phase is reasonable, lattice parameters, atomic positions and peak function of the impurities were refined.

Refined average structure

R_{wp} ~ 10% and goodness of fit (*gof*) ~ 1% were obtained from the structural refinement The refinement results (table 3.3–3.5) show Yb, Er doping leads to the decrease of lattice parameter when compared to the corresponding non−doped YAGs, this is because both Yb^{3+}(0.868 Å) and Er^{3+}(0.89) Å ions are smaller than Y^{3+}(0.90 Å). While the lattice parameter is still expanded in a linear trend as *x* increases (**figure 3.3**). For the atomic occupancy, in *x* = 0 composition, Yb and Er ions only occupy 8−coordinate sites, while in *x* = 0.2 and 0.3 compositions, Yb^{3+} and Er^{3+} occupy 8−coordinate sites and 6-coordinate sites as well. Interestingly, as non-stoichiometry *x* increases, the concentration of Yb/Er at 8-coordinate site decreases and meanwhile it increases at 6-coordinate site (**figure 3.4**), this determines that in YAG structure lanthanides Yb/Er can be introduced to octahedral sites by Y_{Al16a} defects. Compared to stoichiometric YAG, new environments for luminescence centers are created in non−stoichiometric YAG and would supply new energy transfer path.

Table 3.3 Rietveld structural parameters of 20 at.% Yb-2 at.% Er: $Y_3Al_5O_{12}$ with space group *Ia−3d* resulted from Rietveld refinement of SPD data

atom	Wyck symbol	x	y	z	occupancy	Uiso×100
Y	24c	0.125	0	0.25	0.7841(2)	0.222 (2)
Yb	**24c**	**0.125**	**0**	**0.25**	**0.1961(1)**	**0.222 (2)**
Er	**24c**	**0.125**	**0**	**0.25**	**0.0196(1)**	**0.222 (2)**
Al	16a	0	0	0	1	0.02(9)
Al	24d	0.375	0	0.25	1	0.146(5)
O	96h	-0.03039 (4)	0.05107(5)	0.14921 (5)	1	0.183(9)
a = 11.995060(7) Å, *V* = 1725.867(3) $Å^3$, *Z* = 8. R_{wp} ~ 7.64%, *gof* ~ 1.02%						

Table 3.4 Rietveld structural parameters of 20 at.% Yb-2 at.% Er: $Y_{3.2}Al_{4.8}O_{12}$ with space group *Ia−3d* resulted from Rietveld refinement of SPD data						
atom	Wyck symbol	x	y	z	occupancy	Uiso×100
Y	24c	0.125	0	0.25	0.8214(3)	0.5112 (2)
Yb	**24c**	**0.125**	**0**	**0.25**	**0.1623(3)**	**0.5112 (2)**
Er	**24c**	**0.125**	**0**	**0.25**	**0.01624(3)**	**0.5112 (2)**
Al	16a	0	0	0	0.9	0.246(7)
Y	16a	0	0	0	0.0159(5)	0.246(7)
Yb	**16a**	**0**	**0**	**0**	**0.0764(4)**	**0.246(7)**
Er	**16a**	**0**	**0**	**0**	**0.00765(5)**	**0.246(7)**
Al	24d	0.375	0	0.25	1	0.505(6)
O	96h	-0.03081 (5)	0.05287(6)	0.15060 (5)	1	0.75(1)
a = 12.064114(7) Å, V = 1755.845(2) Å^3, Z = 8. R_{wp} ~ 7.60%, *gof* ~ 1.09%						

Table 3.5 Rietveld structural parameters of 20 at.% Yb-2 at.% Er: $Y_{3.3}Al_{4.7}O_{12}$ with space group *Ia−3d* resulted from Rietveld refinement of SPD data						
atom	Wyck symbol	x	y	z	occupancy	Uiso×100
Y	24c	0.125	0	0.25	0.8394(4)	0.552(2)
Yb	**24c**	**0.125**	**0**	**0.25**	**0.1459(3)**	**0.552(2)**
Er	**24c**	**0.125**	**0**	**0.25**	**0.01459(4)**	**0.552(2)**
Al	16a	0	0	0	0.85	0.207(8)
Y	16a	0	0	0	0.0278(6)	0.207(8)
Yb	**16a**	**0**	**0**	**0**	**0.1110(5)**	**0.207(8)**
Er	**16a**	**0**	**0**	**0**	**0.01111(6)**	**0.207(8)**
Al	24d	0.375	0	0.25	1	0.486(8)
O	96h	-0.03114(6)	0.05323(7)	0.15113(7)	1	0.75(1)
a = 12.09119(1) Å, V = 1767.695(6) Å^3, Z = 8. R_{wp} ~ 9.05%, *gof* ~ 1.31%						

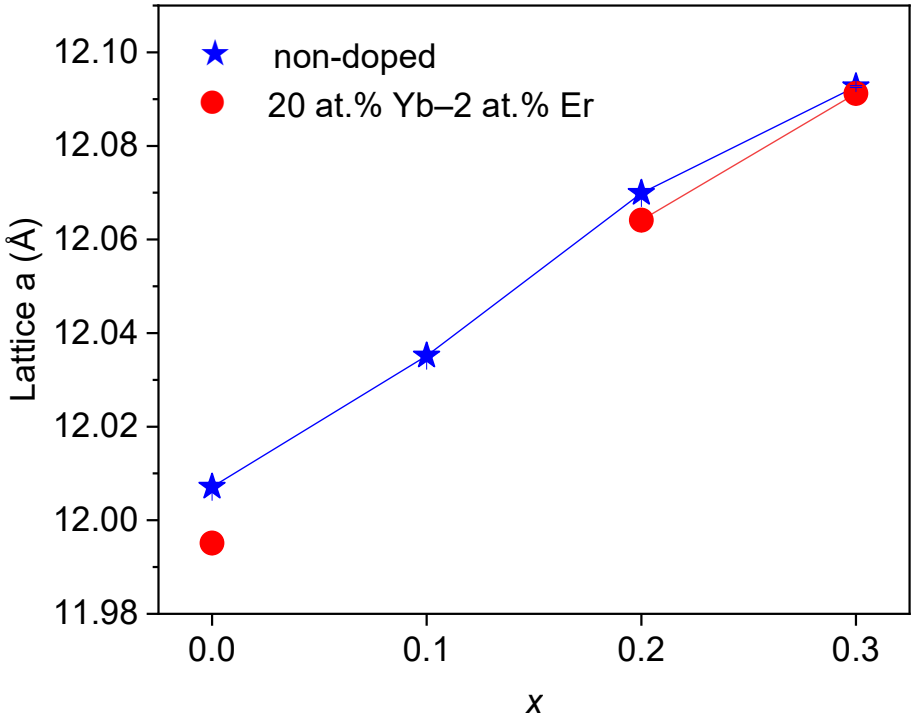

Figure 3.3. *Lattice parameter of non−dopes and 20 at.% Yb−2 at.% Er doped $Y_{3+x}Al_{5-x}O_{12}$ (x = 0, 0.2 and 0.3) garnets. It implies after being co−doped with Yb and Er, the lattice of garnet structure shrinks a little.*

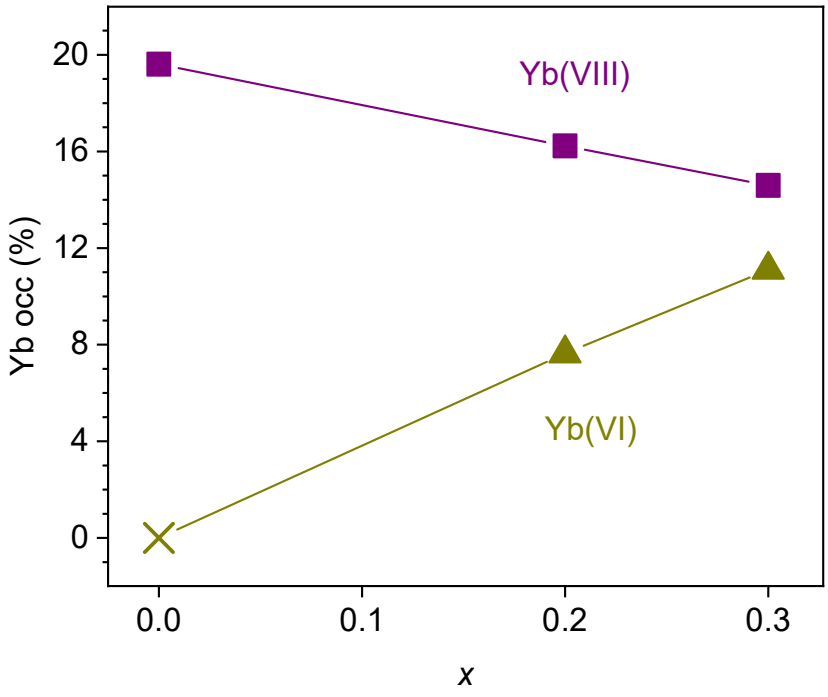

Figure 3.4. *Calculated Yb occupancy at 6−coordinate (triangle) and 8−coordinate (square) sites for 20 at.% Yb−2 at.% Er doped $Y_{3+x}Al_{5-x}O_{12}$ (x = 0, 0.2 and 0.3) garnets. The olive cross indicates there is no Yb at 6−coordinate sites in x = 0 composition.*

Rietveld refinements plots of 20 at.% Yb and 2 at.% Er: $Y_{3+x}Al_{5-x}O_{12}$ (x = 0, 0.2 and 0.3) are shown in **figure 3.5 (a−c)**. In each case the structural parameters fit well with XRD data of synthesized samples, R_{wp} and *gof* values of each refinement are labeled in the plot, they are respectively lower than 10% and about 1%. Phase quantification on these samples indicate that there are 99.848(9) wt.% YAG and 0.152(9) wt.% YAP in (Yb, Er) $Y_3Al_5O_{12}$, 96.31 (5) wt.% YAG, 0.66(1) wt.% YAP, 1.92 (3) wt.% G2 (secondary YAG), 1.09(3) wt.% G3 (third garnet) in (Yb, Er) $Y_{3.2}Al_{4.8}O_{12}$, and 99.89(2) wt.% YAG and 0.10 (2) wt.% YAP in (Yb, Er) $Y_{3.3}Al_{4.8}O_{12}$. The Bragg positions of these phase are shown as tick marks with different colors in the figure.

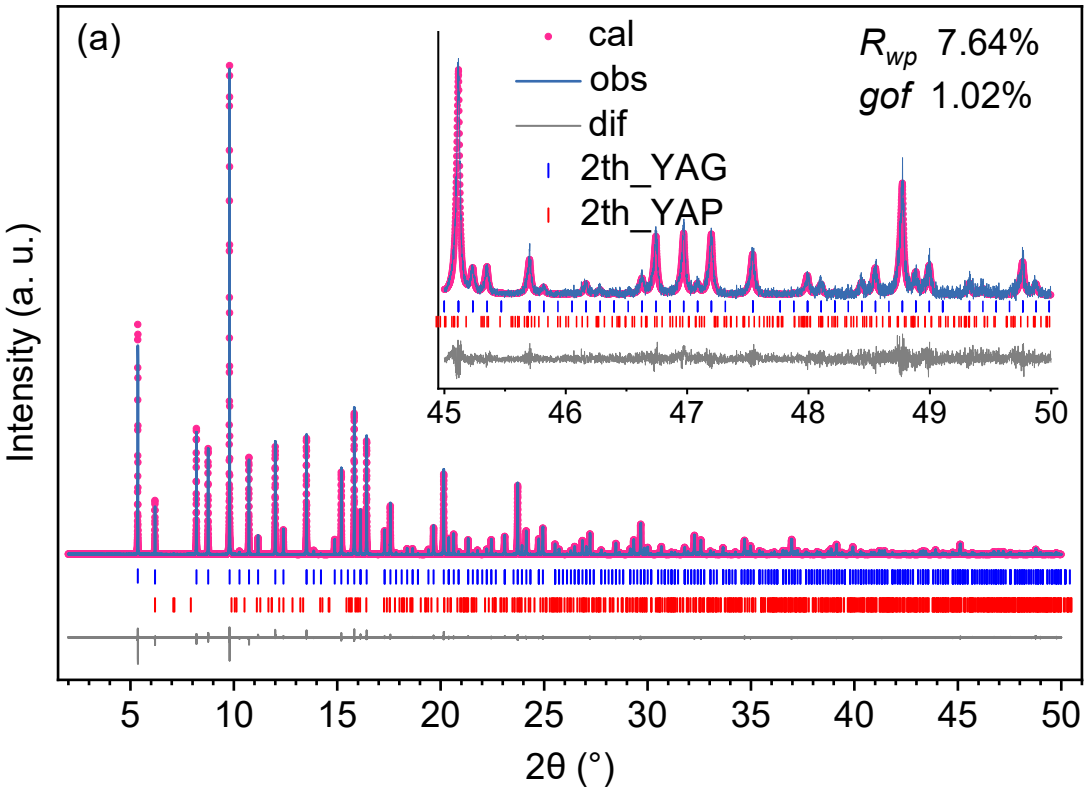

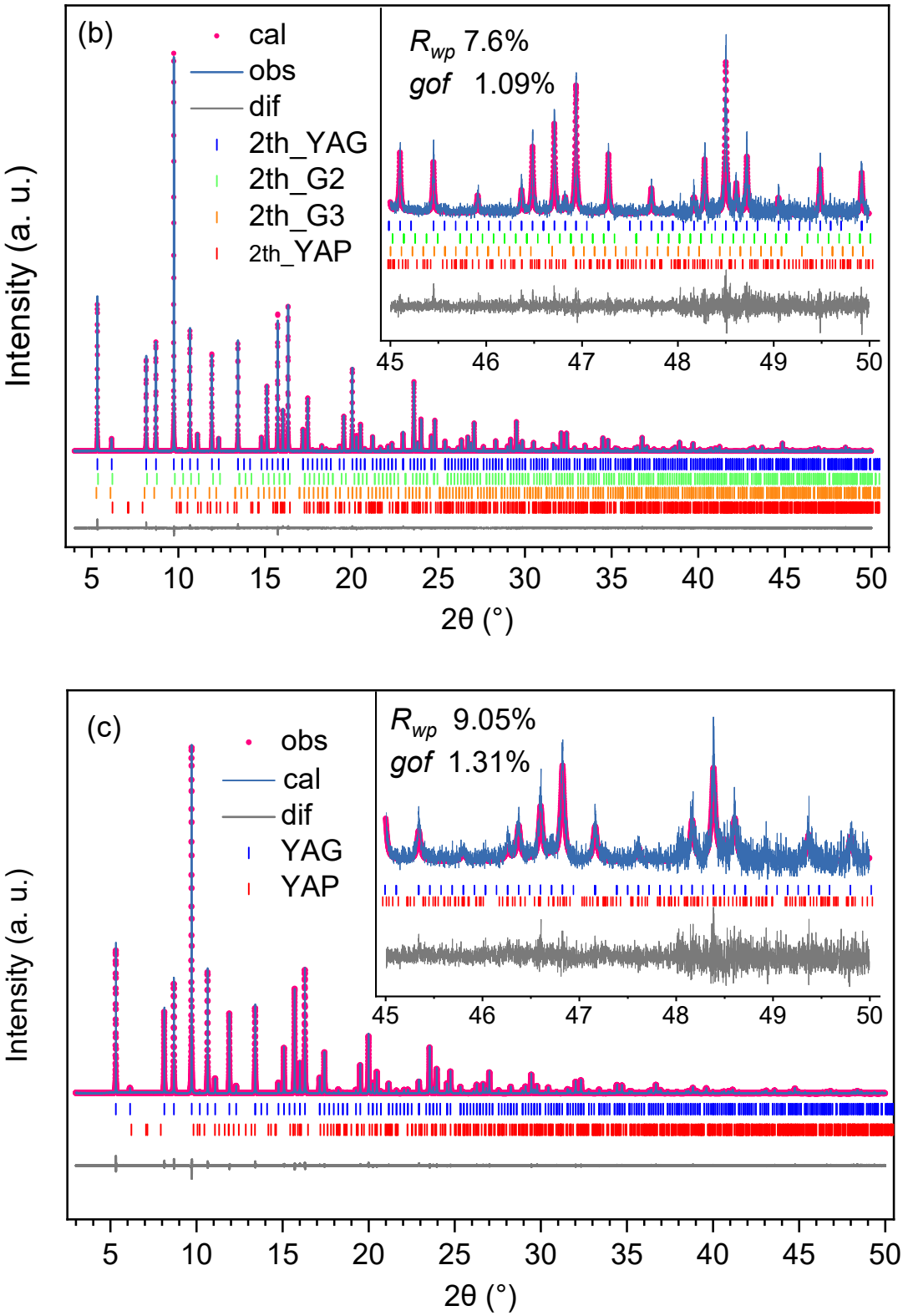

Figure 3.5. *Rietveld refinement plot of 20 at.% Yb−2 at.% Er: $Y_{3+x}Al_{5-x}O_{12}$ (x = 0* ***(a)****, 0,2****(b)*** *and 0.3****(c)*** *) garnets. The light blue line and pink dots respectively represent observed and calculated data. Dark blue and red ticks indicate Bragg positions of YAG and YAP phases. Green and orange ticks in (****c****) indicate second and third minor garnets, The grey curve is the difference between observed and calculated data. R_{wp} and gof values are labeled in each plot in the final refinement.*

3.3.1.3 Emission properties of Yb, Er co−doped s− and ns− YAG

The Er single doped YAG has can be used as 1.5−1.65 μm laser medium operating in eye−safe region, however it has a drawback that Er upconversion competes with radiative process from $^4I_{13/2}$ level and resulting in low absorption coefficient of the material[25, 119, 120]. Therefore, Yb^{3+} ions working as sensitizer are introduced to enhance the efficiency of energy transfer by absorbing excitation radiation and transferring the energy to Er^{3+} ions[25]. Under this premise, suitable dopant concentration of Yb^{3+} was explored to obtain optical emission performance of the Yb, Er co−doped YAG.

Varying the dopant concentration is one of the solutions to tune absorption or emission efficiency of Yb, Er doped YAG. According to the reported work in which Er^{3+} concentration was fixed as 1 at.% and Yb^{3+} concentration varies in 0.5−30 at.%, the Yb^{3+} concentration at 20 at.% exhibits the highest energy transfer efficiency to Er^{3+}. Therefore, in this work Yb^{3+} concentration was fixed as 20 at.% and Er^{3+} concentration varies at 0.5, 1 and 2 at%. **Figure 3.6 (a−c)** show emission spectra of 20 at.% Yb, (0.5, 1 and 2) at.% Er doped $Y_3Al_5O_{12}$ and $Y_{3.2}Al_{4.8}O_{12}$ collected under 980 nm laser excitation. It is indicated whatever the Er^{3+} doping level is, upconversion emission spectra of $Y_3Al_5O_{12}$ show emission bands centered at 520−570 nm and 640−700 nm, which are respectively corresponding to green and red emission[117, 118, 121]. The two color emission respectively result from $^4S_{3/2}$, $^2H_{11/2}\rightarrow{}^4I_{15/2}$ and $^4I_{9/2}\rightarrow{}^4I_{15/2}$ transitions of Er^{3+} ions. Similarly, emission spectra of $Y_{3.2}Al_{4.8}O_{12}$ also show emission bands in the green and red regions. The common but striking point of these a−c emission spectra is that $Y_{3.2}Al_{4.8}O_{12}$ always has much stronger emission intensity.

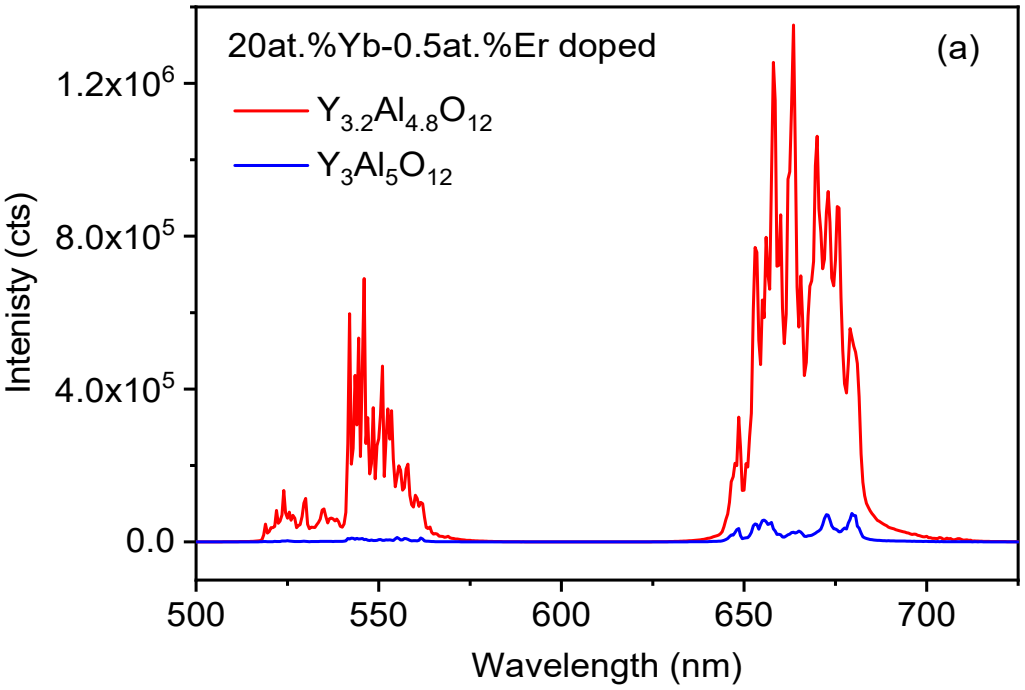
20at.%Yb-0.5at.%Er doped
(a)
$Y_{3.2}Al_{4.8}O_{12}$
$Y_3Al_5O_{12}$
Intenisty (cts)
1.2x10^6
8.0x10^5
4.0x10^5
0.0
500
550
600
650
700
Wavelength (nm)

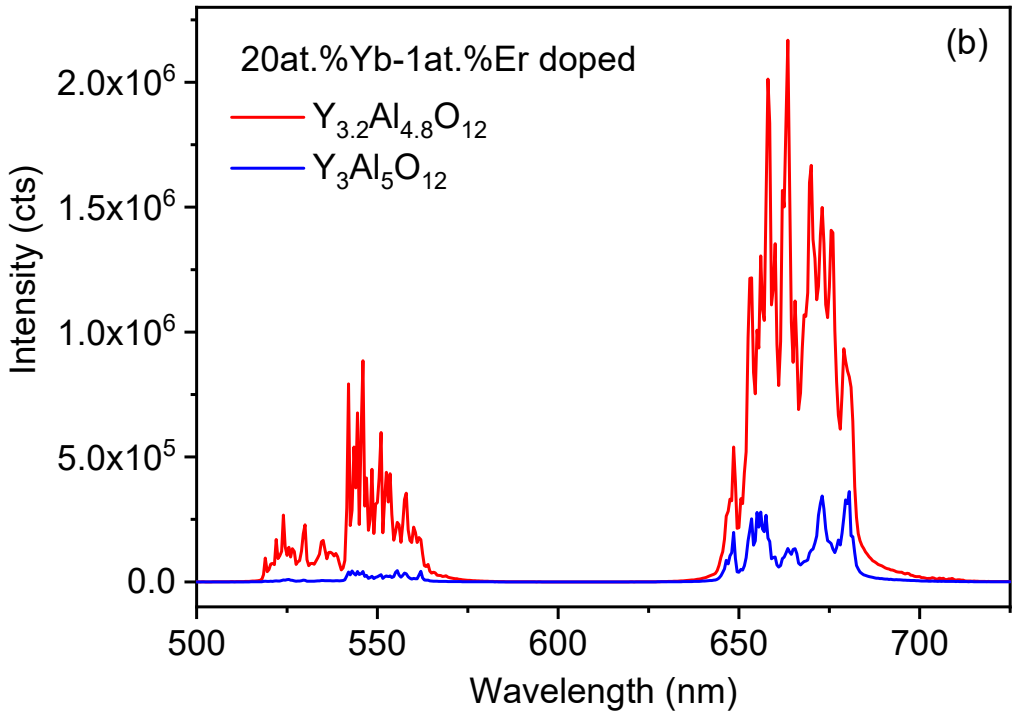
20at.%Yb-1at.%Er doped
(b)
$Y_{3.2}Al_{4.8}O_{12}$
$Y_3Al_5O_{12}$
Intensity (cts)
2.0x10^6
1.5x10^6
1.0x10^6
5.0x10^5
0.0
500
550
600
650
700
Wavelength (nm)

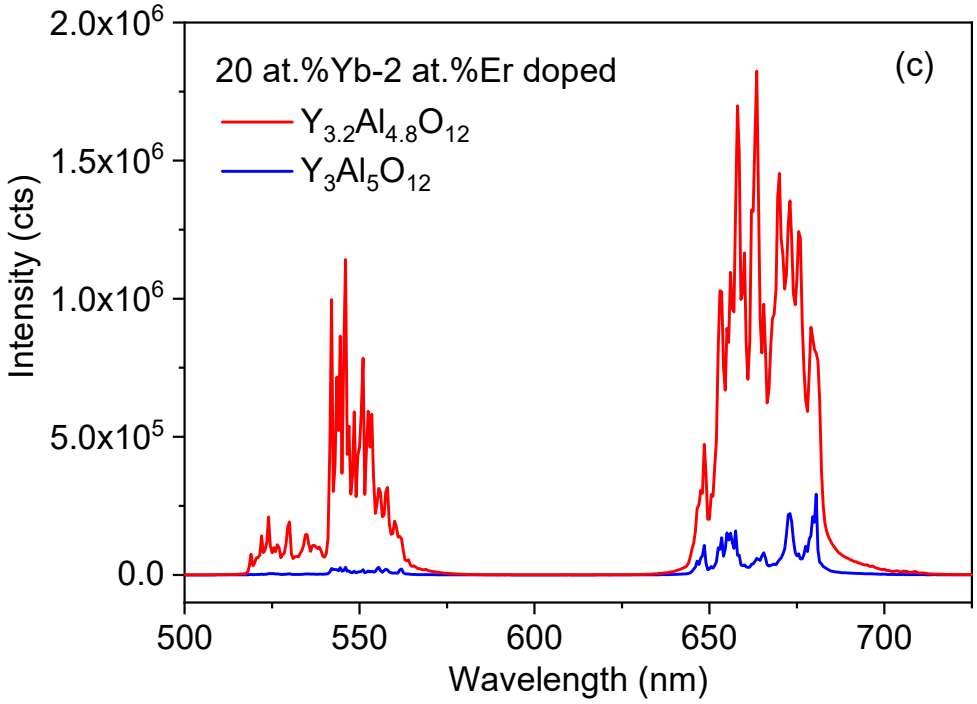

Figure 3.6. *Raw UC emission spectra of $Y_3Al_5O_{12}$ (blue) and $Y_{3.2}Al_{4.8}O_{12}$(red) garnets co−doped with 20 at.% Yb, 0.5* ***(a)****, 1****(b)*** *and 2 at.%* ***(c)*** *Er recorded under 980nm laser excitation.*

The influence of Er^{3+} doping levels on emission efficiencies of $Y_3Al_5O_{12}$ and $Y_{3.2}Al_{4.8}O_{12}$ garnets is discussed based on integrated area covered by emission bands in 500−725 nm (**figure 3.7**). Combined with emission spectra, it implies, for both $Y_3Al_5O_{12}$ and $Y_{3.2}Al_{4.8}O_{12}$, by increasing the number of Er^{3+} emission centers from 0.5 at.% to 1 at.%, emission intensity is enhanced. Further increasing Er^{3+} concentration to 2 at.%, however, decreases the emission intensity. This phenomenon is ascribed to concentration quenching effect which occurs when the emitting centers are in close proximity to each other, allowing energy transfer processes to take place between them. While the energy transfer could increase the probability that photons may encounter deactivation centers (impurities, grain boundaries, *etc*.) when travelling through the crystal lattice. Therefore, 1 at.% is the optimal doping level for the emission performance of stoichiometric and non−stoichiometric YAG host.

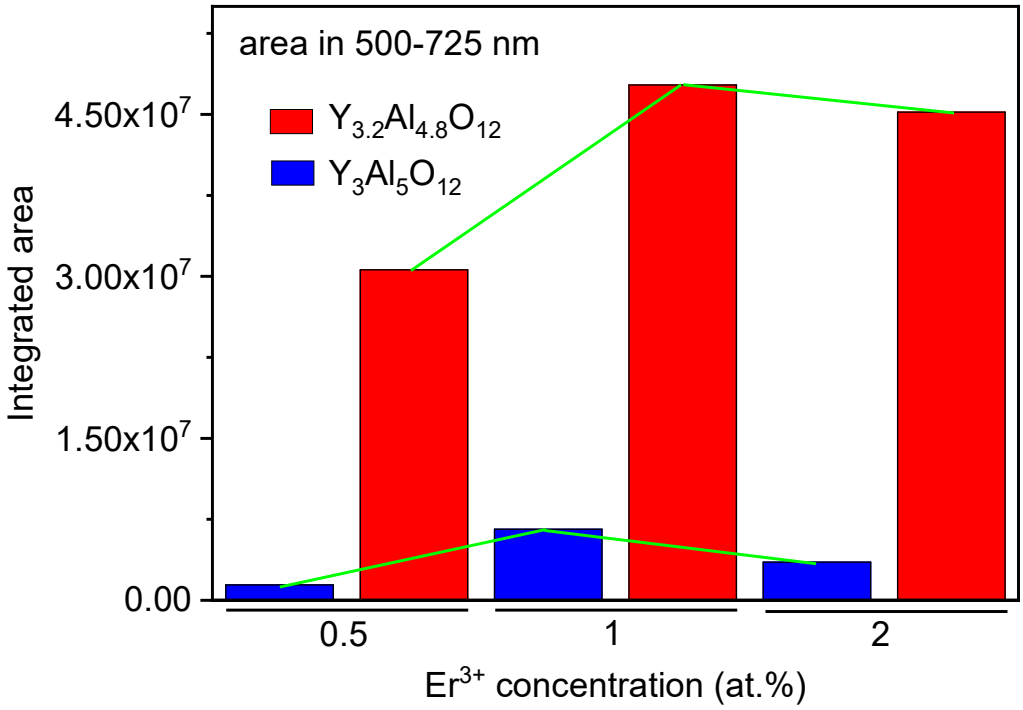

Figure 3.7. *Integrated area (in 500−725 nm range) of 0.5, 1 and 2 at.% Er^{3+}−20at.% Yb^{3+} doped $Y_3Al_5O_{12}$ (blue box) and $Y_{3.2}Al_{4.8}O_{12}$ (red box), the green solid lines point out the change of integrated area.*

3.3.1.4 CIE chromaticity coordination of s− and ns−YAGs

Figure 3.8 (a-c) show the normalized emission spectra of 20 at.% Yb−*n* at.% Er (*n* = 0.5, 1 and 2) doped $Y_3Al_5O_{12}$ and $Y_{3.2}Al_{4.8}O_{12}$, the fine structures of the two hosts with the three doping types are qualitatively similar. Whatever the doping levels, the fine structures of both green and red bands of $Y_{3.2}Al_{4.8}O_{12}$ are significantly different from that of $Y_3Al_5O_{12}$, this led the two YAGs to have different emission colors. The chromaticity coordinates of $Y_3A_5O_{12}$ and $Y_{3.2}Al_{4.8}O_{12}$ with different Er^{3+} doping levels are listed in table 3.4 and demonstrated in CIE chromaticity triangle (**figure 3.9**). It is implied the emission color of $Y_3Al_5O_{12}$ samples does not alter when changing Er^{3+} concentration, it is always yellowish. By contrast, $Y_{3.2}Al_{4.8}O_{12}$ has green emission with chromaticity changes slightly. The difference in emission intensity and emission color between the two YAGs can be ascribed to the appearance of Yb and Er not only at dodecahedral sites (which is the case of doped $Y_3Al_5O_{12}$) but at octahedral sites, as proved by structural refinement results.

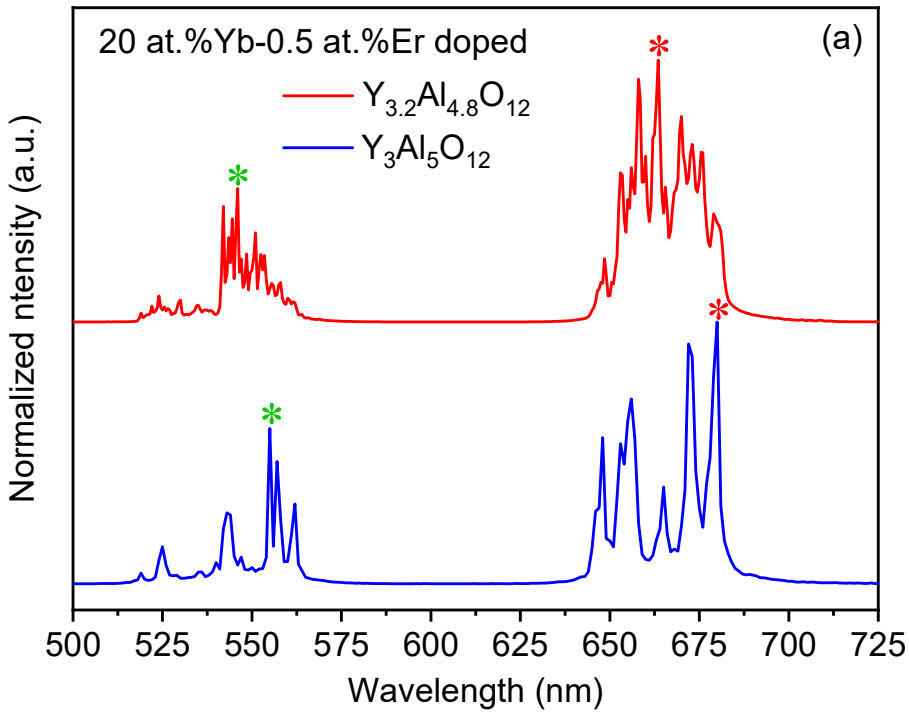
20 at.%Yb-0.5 at.%Er doped
(a)
$Y_{3.2}Al_{4.8}O_{12}$
$Y_3Al_5O_{12}$
Normalized ntensity (a.u.)
500 525 550 575 600 625 650 675 700 725
Wavelength (nm)

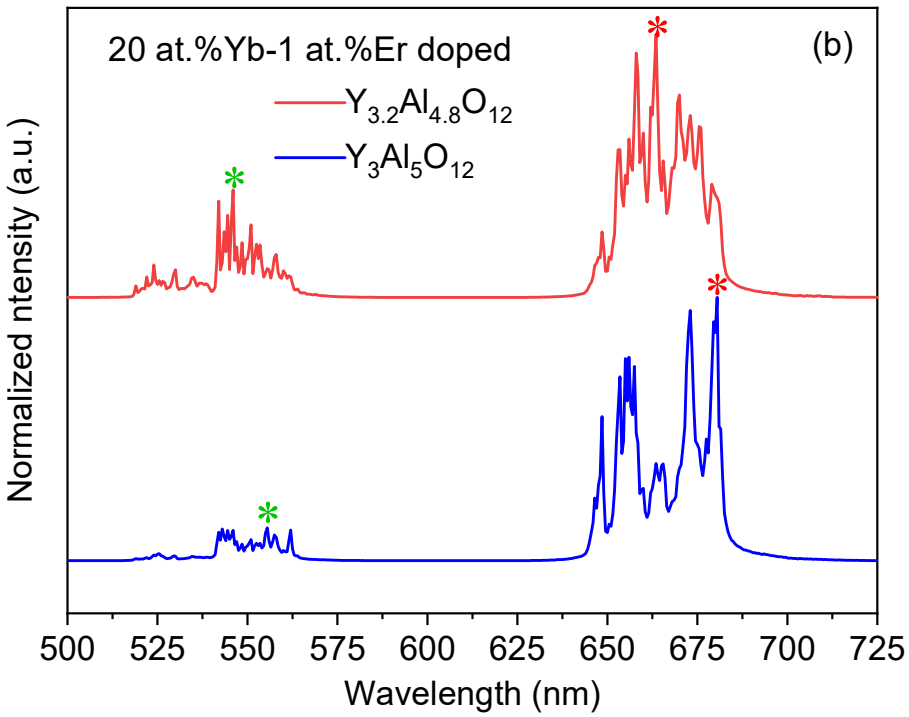
20 at.%Yb-1 at.%Er doped
(b)
$Y_{3.2}Al_{4.8}O_{12}$
$Y_3Al_5O_{12}$
Normalized ntensity (a.u.)
500 525 550 575 600 625 650 675 700 725
Wavelength (nm)

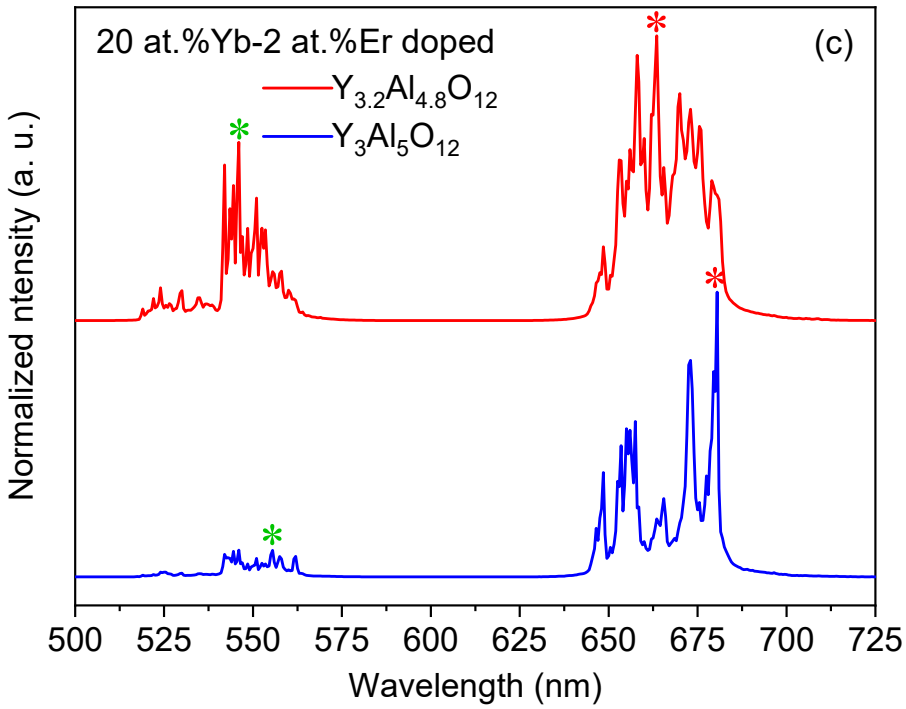

Figure 3.8. *Normalized emission spectra of 20 at.% Yb−n at.% Er (n = 0.5* ***(a)****, 1* ***(b)*** *and 2* ***(c)****) doped* $Y_3Al_5O_{12}$ *and* $Y_{3.2}Al_{4.8}O_{12}$ *under laser excitation at 980 nm. The stars in each figure indicate the most intensive peaks in green and red bands of the emission spectra.*

Table 3.6 Chromaticity coordinates of Yb, Er co−doped $Y_3Al_5O_{12}$ (Y_3) and $Y_{3.2}Al_{4.8}O_{12}$ ($Y_{3.2}$), Yb concentration is fixed as 20 at.% and Er concentrations are 0.5, 1 and 2 at.%.

	0.5 at.% Er	1 at.% Er	2 at.% Er
$Y_3Al_5O_{12}$	(0.50, 0.49)	(0.51, 0.49)	(0.50, 0.49)
$Y_{3.2}Al_{4.8}O_{12}$	(0.41, 0.59)	(0.41, 0.57)	(0.39, 0.60)

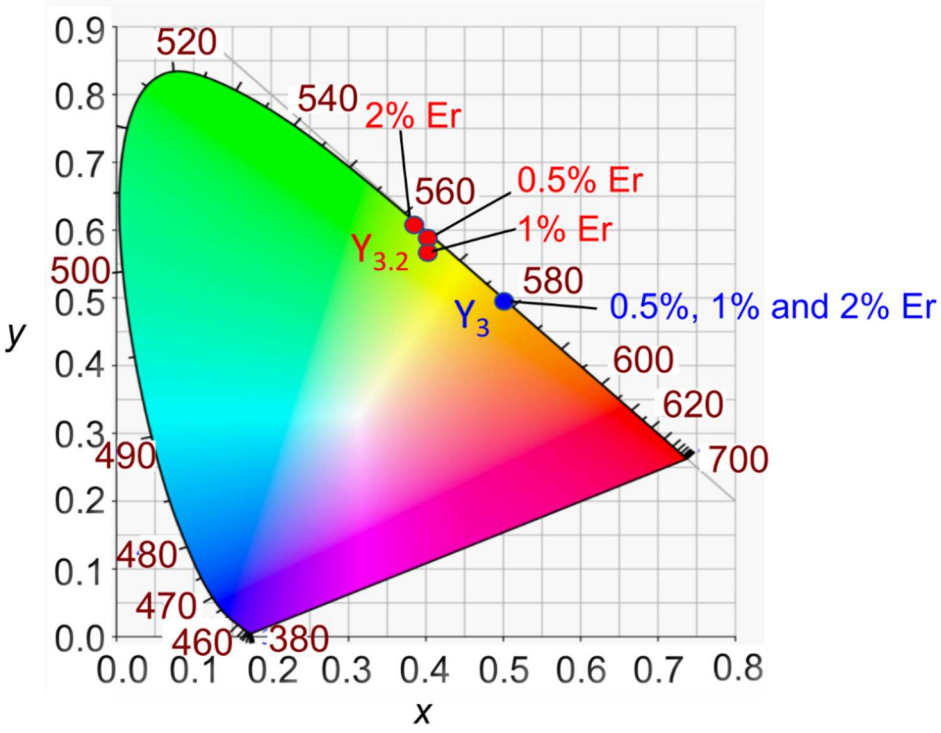

Figure 3.9. *CIE chromaticity coordinates for characterizing the emission color of $Y_3Al_5O_{12}$ (Y_3, blue) and $Y_{3.2}Al_{4.8}O_{12}$ ($Y_{3.2}$, red) with different Er^{3+} concentrations. The three blue dots are overlapped.*

3.3.1.5 Two photon absorption process in Yb, Er co−doped s− and ns−YAGs

UC emission intensity (I_{em}) is proportional to a certain power (n) put into pumping power intensity (Ip) coming from infrared (IR) excitation, the process confines the formula: $I_{em} = A \cdot I_p^n$, where n is the number of absorbed IR photons[122, 123]. Considering in this work 1 at.% Er concentration in the two YAG hosts exhibits optimal emission performance. Green and red UC emission intensities of 20 at.% Yb−1 at.% Er doped $Y_3Al_5O_{12}$ (**figure 3.10 a**) and $Y_{3.2}Al_{4.8}O_{12}$ (**figure 3.10 b**) are displayed as function of pumping power in log−log plot mode, linear fitting for these emission intensities gives n value (slope). The n values of green and red emission for 20 at.% Yb−1 at.% Er doped $Y_3Al_5O_{12}$ are respectively 1.92 and 2.04 and they are respectively 2.08 and 2.13 for 20 at.% Yb-1 at.%Er doped $Y_{3.2}Al_{4.8}O_{12}$. They all are close to 2, determining that the upconversion mechanism of the two host matrices is promoted by the two−photon absorption process[123]. The nonstoichiometry influences luminescence emission performance but does not alter the luminescence mechanism in yttrium aluminum garnet.

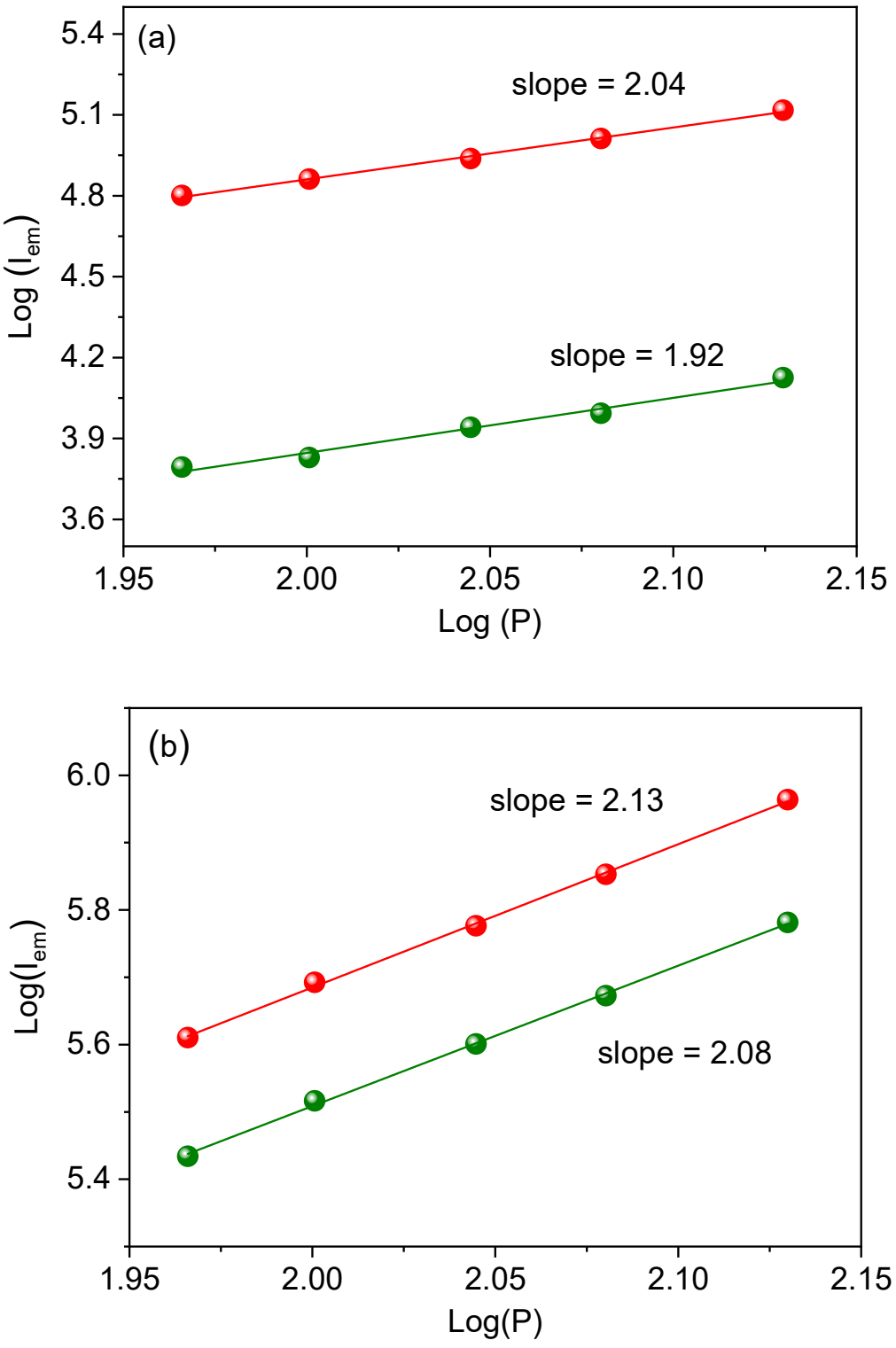

Figure 3.10. *Logarithm dependence of emission intensity as a function of pump power of 980 nm laser excitation of green and red emission for 20 at.% Yb−1 at.% Er doped* ***(a)*** $Y_3Al_5O_{12}$ *and* ***(b)*** $Y_{3.2}Al_{4.8}O_{12}$.

3.3.1.6 Common luminescence mechanism of Yb, Er co−doped s− and ns−YAGs

The upconversion mechanism of Yb, Er co−doped YAG is depicted in **figure 3.11**, in the excitation process, Yb^{3+} undergoes a successive energy transfer process. the Yb^{3+} sensitizer ions at the ground state absorbs the NIR photons (980 nm laser) and is excited to $^2F_{5/2}$ state, then they transfer energy to Er^{3+} ions (activator) and promote them to their excited state $^4I_{11/2}$. Later the Er^{3+} ion is further promoted to higher $^4F_{7/2}$ excited state by a second energy transfer from Yb^{3+} ions. This two−step energy transfer process from Yb^{3+} sensitizers to Er^{3+} activators is called “successive energy transfer”[122]. The Er^{3+} ion which is at $^4F_{7/2}$ energy state has a small energy drop to land on the $^2H_{11/2}$, $^4S_{3/2}$ and $^4F_{9/2}$ energy states, the following $^2H_{11/2}$, $^4S_{3/2}$ $\rightarrow$$^4I_{15/2}$ and $^4I_{9/2}$$\rightarrow$$^4I_{15/2}$ transitions respectively yield green and red emission.

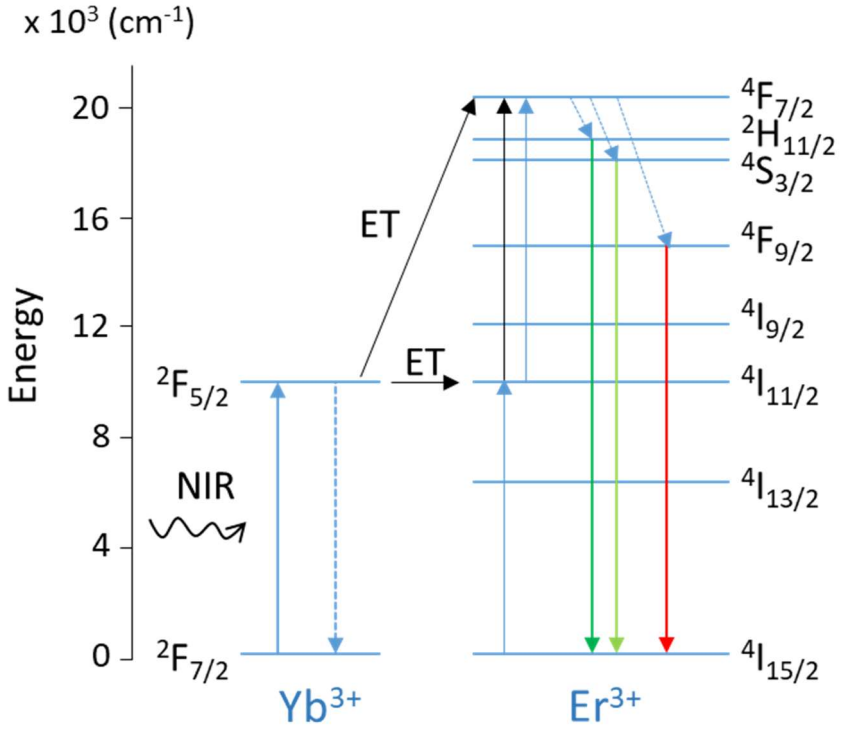

Figure 3.11. *Scheme of the excitation and emission process in Yb, Er co−doped YAG. The successive energy transfer process from Yb^{3+} to Er^{3+} enables Er^{3+} to reach higher energy levels and produce green and red emission.*

3.3.1.7 Luminescence mechanism in relation to crystal structure

The general excitation and emission in Yb, Er co−doped s−YAG ($Y_3Al_5O_{12}$) and ns−YAG ($Y_{3.2}Al_{4.8}O_{12}$) are the same, the reason for the different emission properties between the

YAGs can be explained from a structure point of view (**figure 3.12**). In s−YAG, Yb^{3+}/Er^{3+} only locate at 8−coordinate sites, all the A−A bond lengths are 3.6727 Å, thus the distance between Yb^{3+} sensitizer and Er^{3+} activator are the same. While in ns−YAG, the two doping ions are present not only at 8−coordinate sites but also at 6−coordinate sites, this helps to create, besides A−A (3.372(1) Å) bonding, A−B (3.694(1) Å) bonding for Yb^{3+} and Er^{3+}. The A−B bonds in ns−YAG are shorter than A−A bonds, thus the involved ions can be closer to each other and get the energy transfer more efficient. Meanwhile, the 6−cordinate Yb^{3+} and Er^{3+} ions build, besides Yb(VIII)→Er(VIII), three new transfer paths: Yb(VIII)→Er (VI), Yb(VI)→Er (VI) and Yb (VI)→Er (VIII), this makes full use of the probability of the transfer. These two reasons lead to the improved emission performance of ns−YAG than s−YAG.

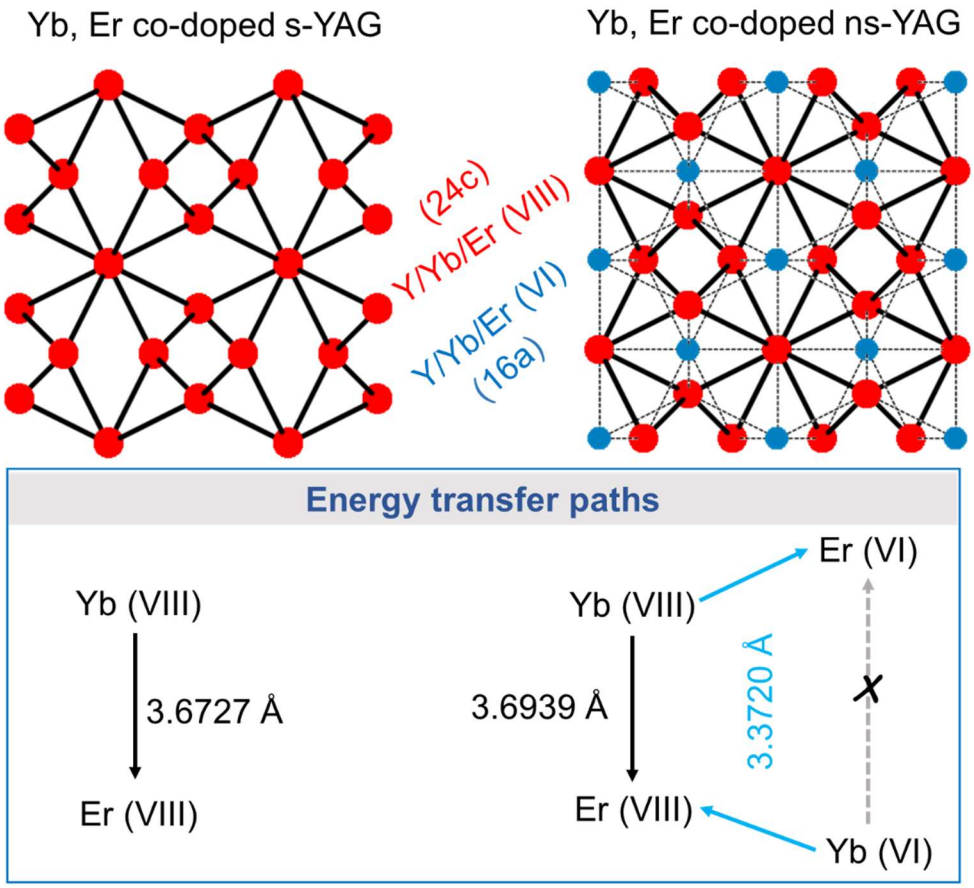

Figure 3.12. *Atomic bonding in 20 at.% Yb−2 at.% Er doped s−YAG and ns−YAG. The possible energy transfer paths in the two compositions are shown in the box below.*

3.3.1.8 Luminescence decay of Yb, Er co−doped s− and ns−YAGs

Luminescence decay curves (**figure 3.13**) of green and red emissions have been recorded for $Y_3Al_5O_{12}$ and $Y_{3.2}Al_{4.8}O_{12}$ doped with 20 at.% Yb−*n* at.% Er (*n* = 0.5, 1 and 2). Lifetimes of the excited state of Er^{3+} ions were obtained by analyzing these decay curves. They are shown in **table 3.6 a-b**. The influence of nonstoichiometry on the lifetime is discussed according to the fitting process and result of the curves. The curves were recorded according to the respective green and red emission bands of each sample. For $Y_3Al_5O_{12}$, the curves of both green and red emission could be fitted to a single exponential decay of:

$$I(t) = I\ exp(-t/\tau)$$

where *I(t)* is luminescence intensity, *t* is the time after excitation, and τ is the decay time. While the suitable fitting of decay curves of green and red emission for $Y_{3.2}Al_{4.8}O_{12}$ was realized by a bi−exponential decay function:

$$I(t) = I_1\ exp(-t/\tau_1) + I_2\ exp(-t/\tau_2)$$

where *I(t)* is luminescence intensity, t is the time after excitation, and τ_1 *and* τ_2 are decay time of two different components with their respective I_1 and I_2. The fitting parameters and resulted average decay time are listed in table 3.7, the average decay time is defined as:

$$\langle \tau \rangle = \frac{\int_{t_0}^{t_f} tI(t)dt}{\int_{t_0}^{t_f} I(t)dt} = \left(\tau_1^2 I_1 + \tau_2^2 I_2\right) / \left(\tau_1 I_1 + \tau_2 I_2\right)$$

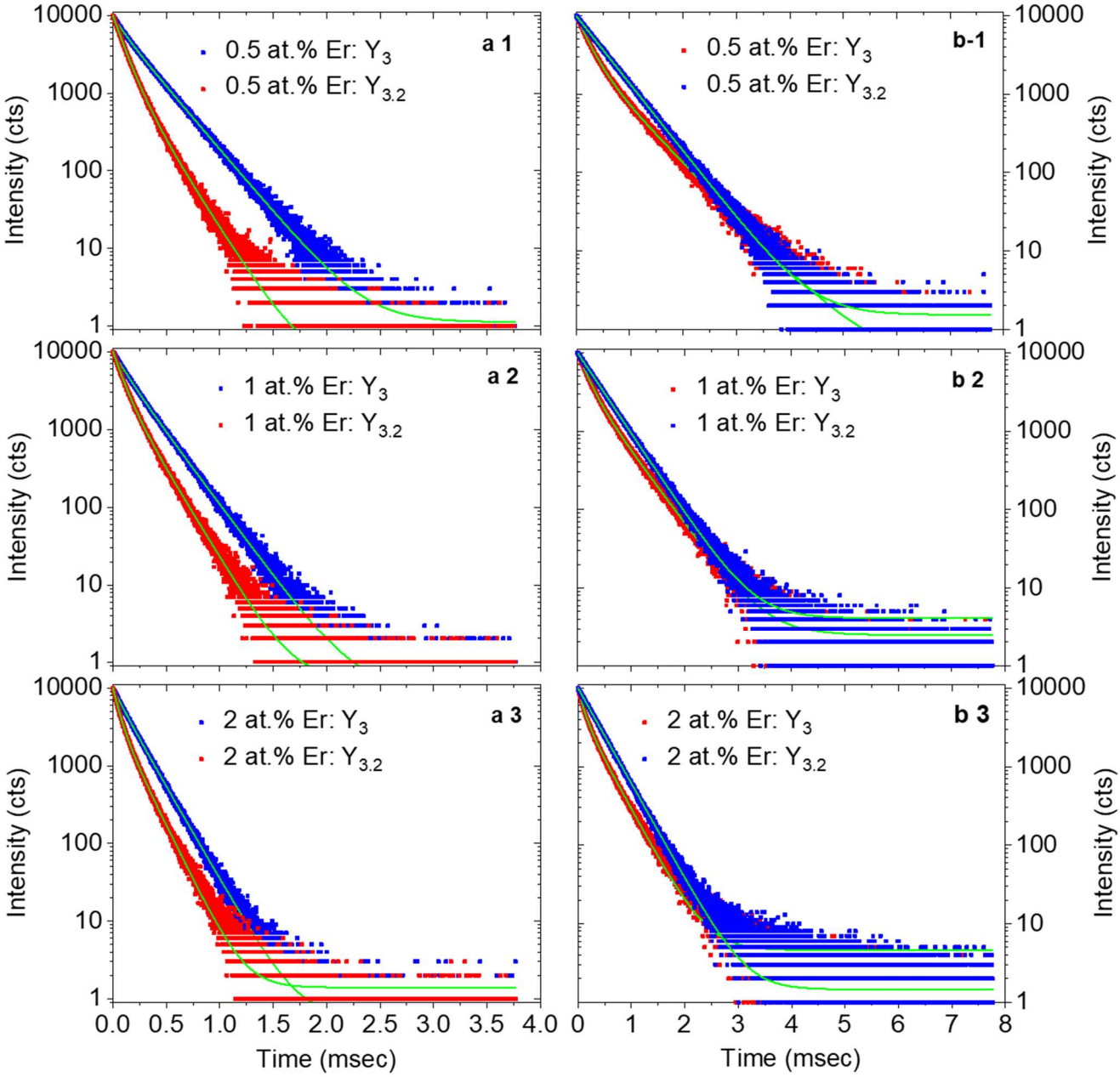

Figure 3.13. *Luminescence decay curves green* ***(a 1−3)*** *and red* ***(b 1−3)*** *emission of 20 at.% Yb−n at.% Er (n = 0.5, 1 and 2) doped* $Y_3Al_5O_{12}$ *(blue) and* $Y_{3.2}Al_{4.8}O_{12}$ *(red).*

Table 3.7. a−b Lifetimes of green ($^4S_{3/2}\rightarrow{}^4I_{15/2}$) and red ($^4I_{9/2}\rightarrow{}^4I_{15/2}$) emission under 980 nm laser excitation for 20 at.% Yb−*n* at.% Er (*n* = 0.5, 1 and 2) doped $Y_3Al_5O_{12}$ (a) and $Y_{3.2}Al_{4.8}O_{12}$ (b).

a

sample	transition	emission (nm)	τ_1 (msec)	I_1 (%)	τ_2 (msec)	I_2 (%)	τ avg (msec)
0.5 at.% Er	$^4S_{3/2}\rightarrow{}^4I_{15/2}$	555	233	100			233
1 at.% Er	$^4S_{3/2}\rightarrow{}^4I_{15/2}$	555	206	100			206
2 at.% Er	$^4S_{3/2}\rightarrow{}^4I_{15/2}$	555	168	100			168
0.5 at.% Er	$^4F_{9/2}\rightarrow{}^4I_{15/2}$	655	505	100			505
1 at.% Er	$^4F_{9/2}\rightarrow{}^4I_{15/2}$	655	426	100			426
2 at.% Er	$^4F_{9/2}\rightarrow{}^4I_{15/2}$	655	357	100			357

b

sample	transition	emission (nm)	τ_1 (msec)	I_1 (%)	τ_2 (msec)	I_2 (%)	τ avg (msec)
0.5 at.% Er	$^4S_{3/2}\rightarrow{}^4I_{15/2}$	546	202	25	96	75	140
1 at.% Er	$^4S_{3/2}\rightarrow{}^4I_{15/2}$	546	158	37	62	63	120
2 at.% Er	$^4S_{3/2}\rightarrow{}^4I_{15/2}$	546	155	42	57	58	122
0.5 at.% Er	$^4F_{9/2}\rightarrow{}^4I_{15/2}$	658	617	33	220	67	451
1 at.% Er	$^4F_{9/2}\rightarrow{}^4I_{15/2}$	658	411	38	128	62	316
2 at.% Er	$^4F_{9/2}\rightarrow{}^4I_{15/2}$	658	346	49	103	51	289

The single exponential decay curve and the single lifetime for $Y_3Al_5O_{12}$ may indicate that Er^{3+} ions are located at one lattice site which was determined as dodecahedral site by Rietveld structural refinement. By contrast, $Y_{3.2}Al_{4.8}O_{12}$ has bi−exponential decay curve resulting in two lifetimes τ_1 *and* τ_2 as shown in table 3.6 b. The values of τ_1 for green and red emission are close to that of $Y_3Al_5O_{12}$, therefore it can be related to the Er^{3+} ions at dodecahedral sites. The shorter lifetimes τ_2 are assigned to the Er^{3+} ions at octahedral site, agreeing with structural refinement results.

3.3.1.9 Local inhomogeneity in Yb, Er co−doped s− and ns−YAGs

In the repeated luminescence measurements of 20 at.% Yb−2 at.% Er doped $Y_{3.2}Al_{4.8}O_{12}$, the newly recorded raw emission spectra is different from the one recorded before (**figure 3.14 a**), regarding not only the change of emission intensity but also the fine structure of two emission spectra. To distinguish the previously and lately measured (Yb, Er) $Y_3Al_5O_{12}$ and $Y_{3.2}Al_{4.8}O_{12}$ in the following text and figure, labels P3, L3, P32 and L32 are given before each composition. Compared to the normalized emission spectra (**figure 3.14 b**) of P3 (Yb, Er) $Y_3Al_5O_{12}$ and P32 (Yb, Er) $Y_{3.2}Al_{4.8}O_{12}$, the fine structure of normalized emission spectra of L32 Yb, Er doped $Y_{3.2}Al_{4.8}O_{12}$ shows two extra peaks respectively on the two edges of

the red emission band, as labeled by two dark dots, these two emerging peaks peak at the same wavelengths as for P3 (Yb, Er,) doped $Y_3Al_5O_{12}$, but they do not appear at the spectra of P32 (Yb, Er) $Y_{3.2}Al_{4.8}O_{12}$. This may imply that the lattice structure of L32 (Yb, Er) $Y_{3.2}Al_{4.8}O_{12}$ has a slight difference from that of the P32 (Yb, Er) $Y_{3.2}Al_{4.8}O_{12}$, which could be explained as that the dopant ions distribute differently in the sample, leading to the local inhomogeneity at micro region[124].

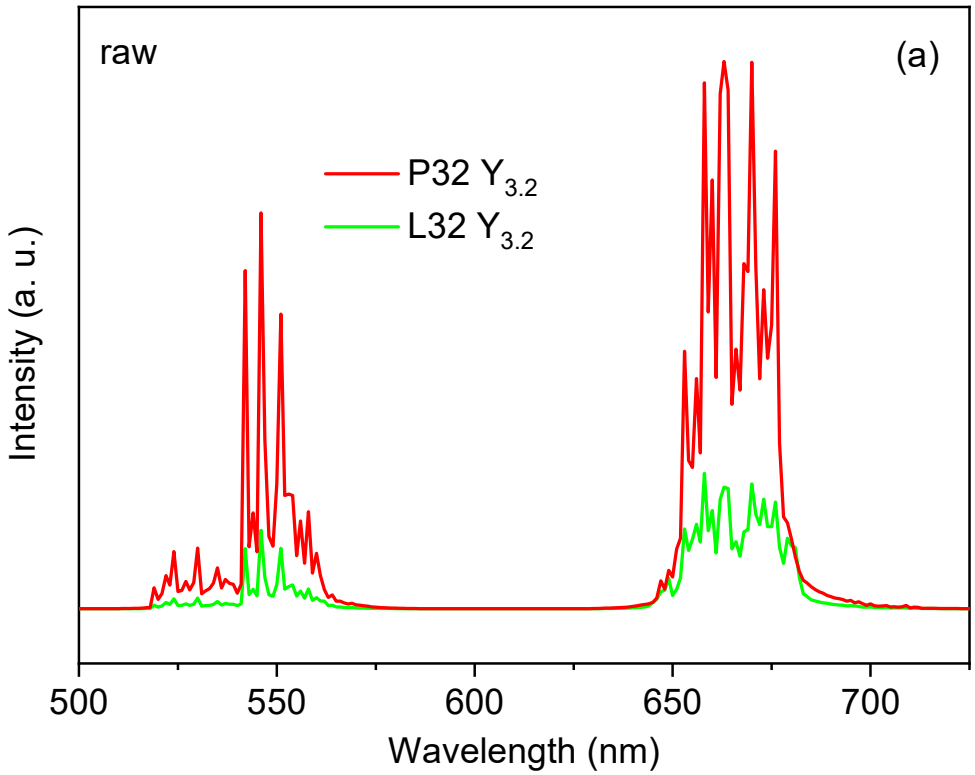

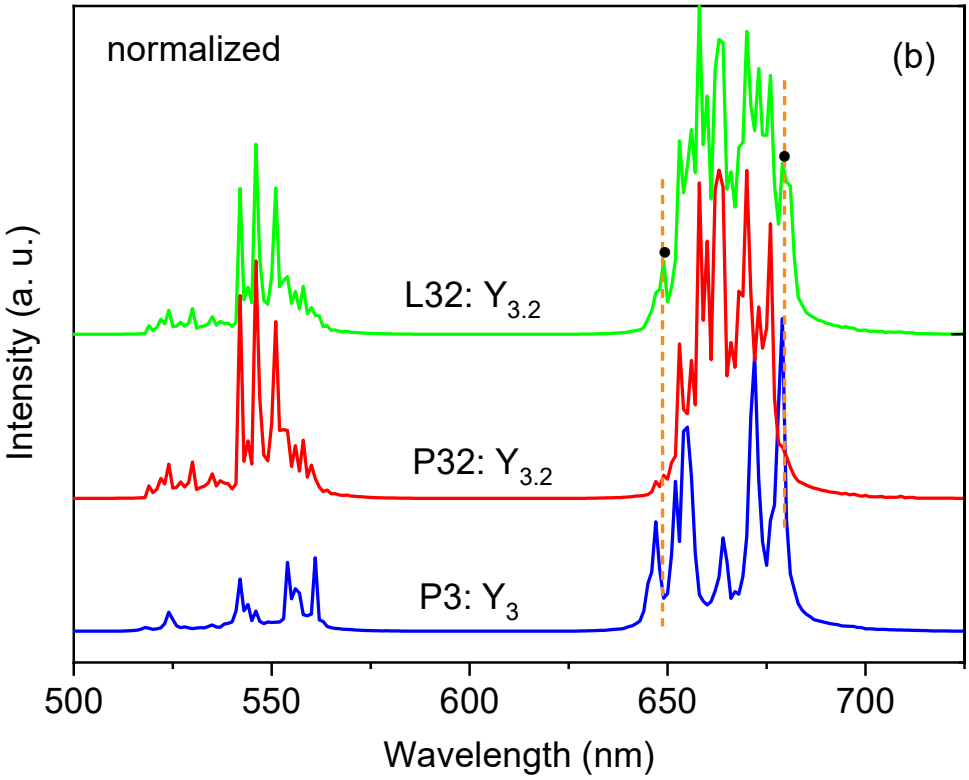

Figure 3.14. *Raw (a) and normalized (b) emission spectra of the previous and latest 20 at.% Yb−2 at.% Er doped $Y_{3.2}Al_{4.8}O_{12}$ samples. The normalized emission spectra of previous 20 at.% Yb−2 at.% Er doped $Y_3Al_5O_{12}$ (P3) works as reference for discussing the difference in fine structure.*

3.3.1.10 Possible sources of error responsible for the emission results

It is necessary to question whether it is possible that the inconsistent emission performance of $Y_{3.2}Al_{4.8}O_{12}$ resulted from systematic error of sample preparation. The samples for the luminescence measurement above are in the form of powders, sample powders were pressed before the measurement. A new batch of samples therefore were prepared as disks by polishing the opposite sides of sample bead which were synthesized by ADL. The appearance of the final sample disks, as well as the moment the sample disk exposed to laser radiation are depicted in figure 3.15. The two sides of the sample disk are different in diameter due to unpredicted the thickness removed by polishing, the smaller side has a diameter around 1.3 mm and the larger one 1.5 mm. The area covered by laser radiation is around 1 mm in diameter. It is known that $Y_{3.2}Al_{4.8}O_{12}$ garnet bead could not be made as big as wanted, its cooling rate is related to sample mass, therefore related to the size of the bead. Also on the polished side, many pores, generated in the undercooling process, are presented. Herein, it risks losing partial pumped laser power apart from the part

reached the sample. While anyway, disks of 20 at.% Yb−*x* at.% Er (*x* = 0.5, 1 and 2) co−doped $Y_3Al_5O_{12}$ and $Y_{3.2}Al_{4.8}O_{12}$ samples were finally measured with luminescence measurement with aim to detect, in microscale, the micro−scale homogeneity of the samples.

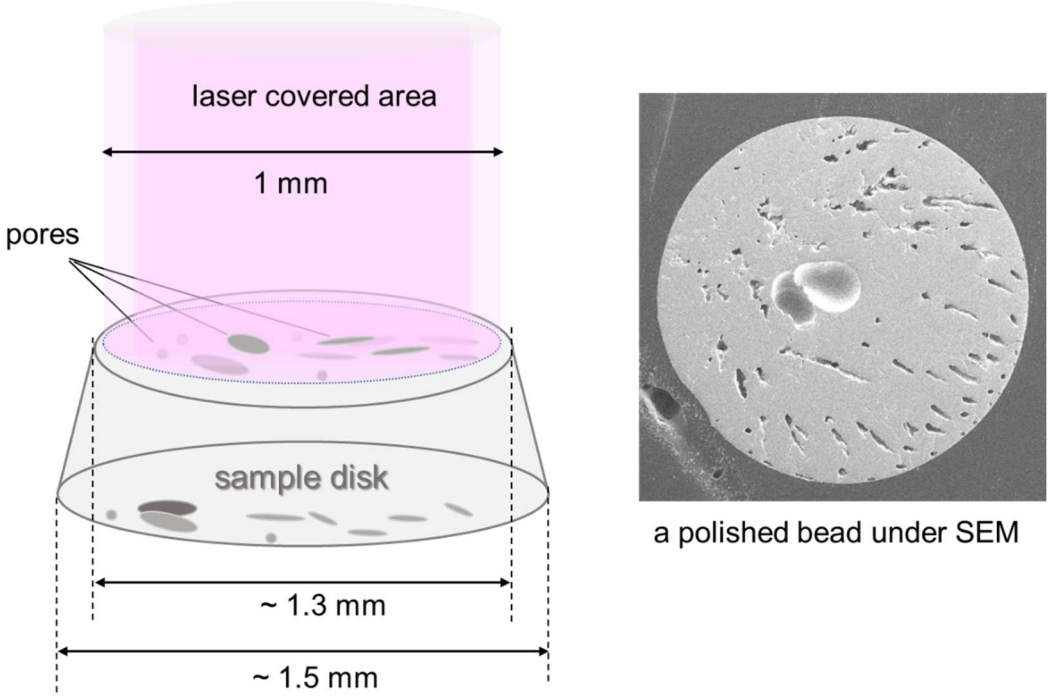

Figure 3.15. *schematic diagram of the contact between the sample and laser radiation during the luminescence measurement. The sample in the upper right corner shows the morphology of the polished bead observed by SEM, many pores are present on the sample.*

3.3.1.11 Luminescence spectra of polished sections of sample bead

Luminescence spectra were recorded from the four positions shown in the schematic diagram (**figure 3.16**). The measurement was first performed on the two polished sides, since the diameter of one side does not deviate much, in this round the two sides were not distinguished from each other in labeling. The measurement process was the same as for powdered sample, targeted sample was excited by 980 nm laser source. **Figure 3.17** shows emission spectra of 20 at.% Yb−*x* at.%Er doped $Y_3Al_5O_{12}$ and $Y_{3.2}Al_{4.8}O_{12}$, with *x* = 0.5, 1 and 2, it is implied all the emission spectra have the same green and red emission bands as existing in powdered sample. The shape and the intensity of the emission spectra of $Y_3Al_5O_{12}$ are similar for both sides, whatever the doping is. While for $Y_{3.2}Al_{4.8}O_{12}$, the emission intensity of the sized deviate from each other, the highest intensity of the peak

deviation happens to be in 0.5 at.% Er−$Y_{3.2}Al_{4.8}O_{12}$ sample. Thus the luminescence measurement on disk sample also implies the micro−region inhomogeneity in Yb, Er doped $Y_{3.2}Al_{4.8}O_{12}$.

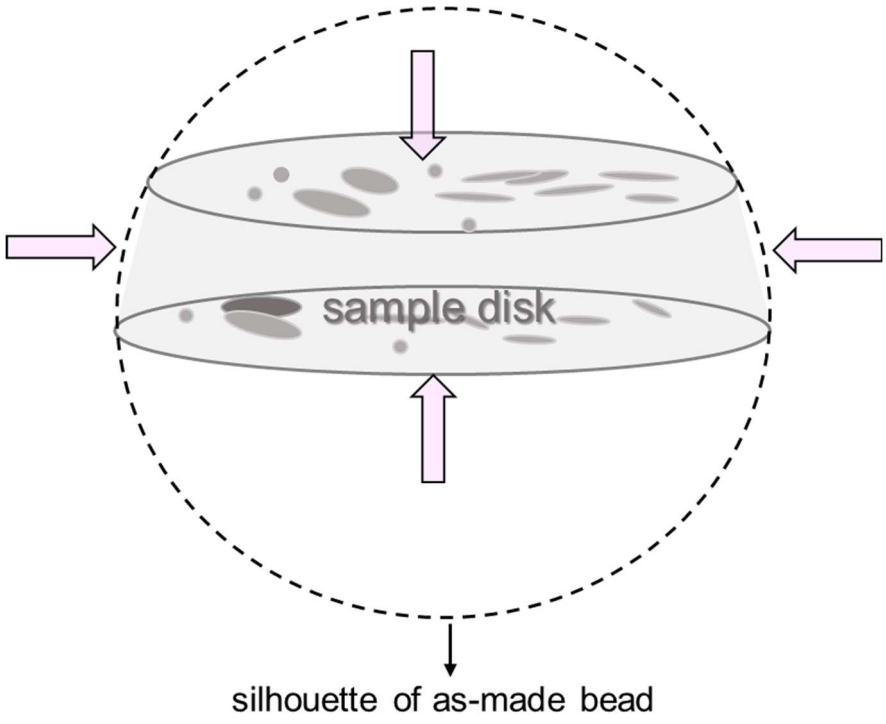

Figure 3.16. *A schematic diagram showing the positions (labeled by light pink arrows) where emission spectra were recorded.*

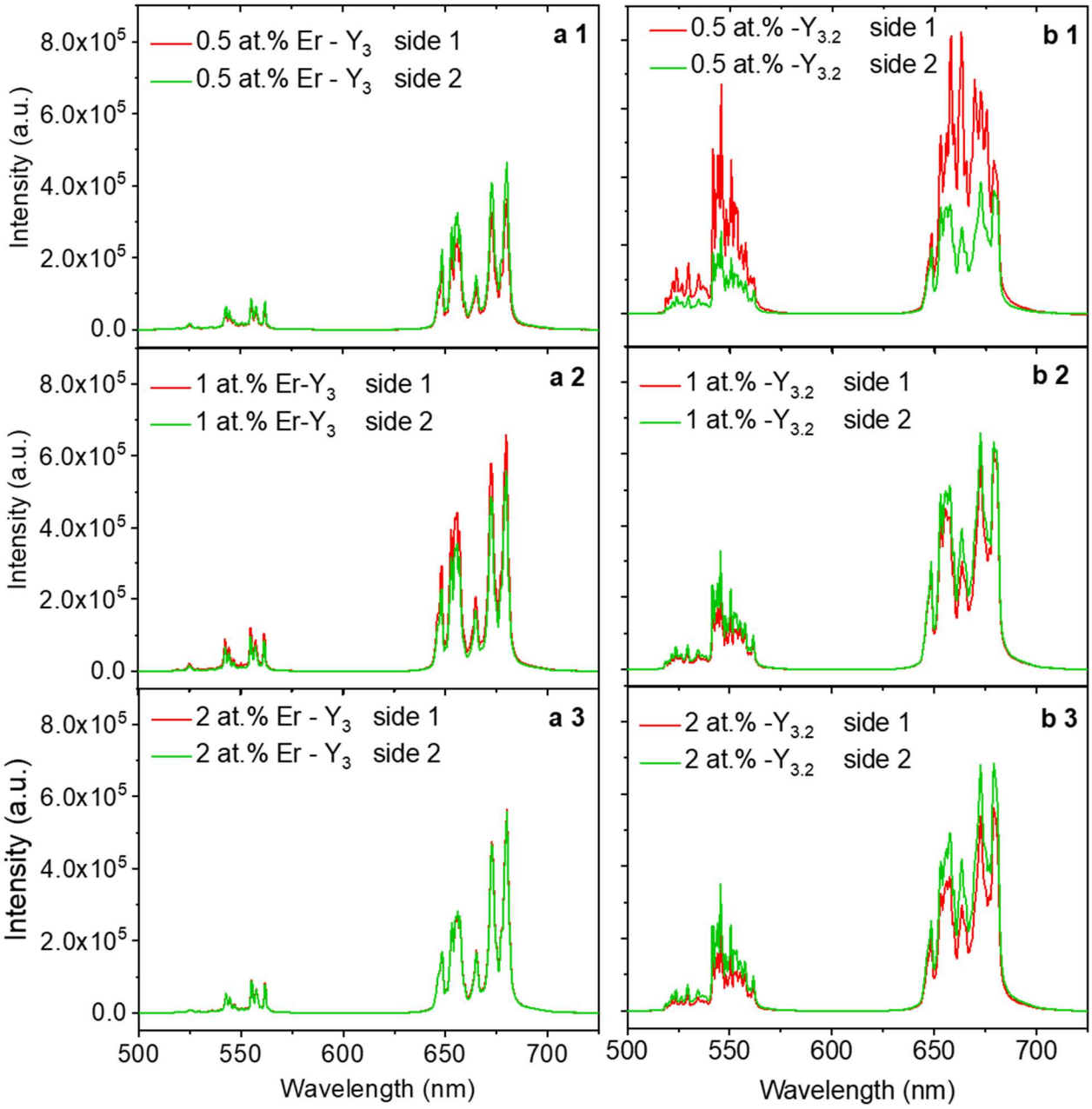

Figure 3.17. *Emission spectra of polished sections of 20 at.% Yb−x at.% Er (x = 0.5, 1 and 2) doped* $Y_3Al_5O_{12}$ (***a1−a3***) *and* $Y_{3.2}Al_{4.8}O_{12}$ (***b1−b3***).

For further confirming the homogeneity of Yb, Er doped $Y_{3.2}Al_{4.8}O_{12}$, the 20 at.% Yb−0.5 at.% Er doped $Y_{3.2}Al_{4.8}O_{12}$ sample was chosen as research target. The two sides this time were distinguished by area size (small or large) to investigate if the position along the surface−volume axis can have influence on luminescence performance. Also the two edges (labeled by two horizontal arrows in the **figure 3.16**) were also measured. When measuring the two edges, the disk was fixed perpendicular to the sample holder. Since the area could be smaller than the area exposed to the laser, some of the laser radiation could be missed,

therefore weaken the emission intensity. Fortunately, the emission intensities are comparable for the two measured edges, as their size of area are very similar. The emission spectra (**figure 3.18**) of small and large sides of the sample indicate the small side has more intensive emission intensity, especially for red emission band. CIE chromaticity coordinates (insert of **figure 3.18**) of the emission spectra of the small and large sides are respectively (0.41, 058) and (0.37, 0.62), both are in green area, but the green emission of the former is more intensive. By comparing the emission spectra of the two edges and the large side (**figure 3.19**), it was found their emission intensities are very different, the large side has the most intensive emission peaks, one edge has more intensive emission than the other. Their chromaticity coordinates in CIE chromaticity diagram (**insert**) indicate the edge 2 show most intense green color, then successively comes that of large side and edge 1. These luminescence measurements performed on different positions of the sample implies the inhomogeneity is all over the sample, which could be caused by the variation in cooling rates from the edge to the center of the disk.

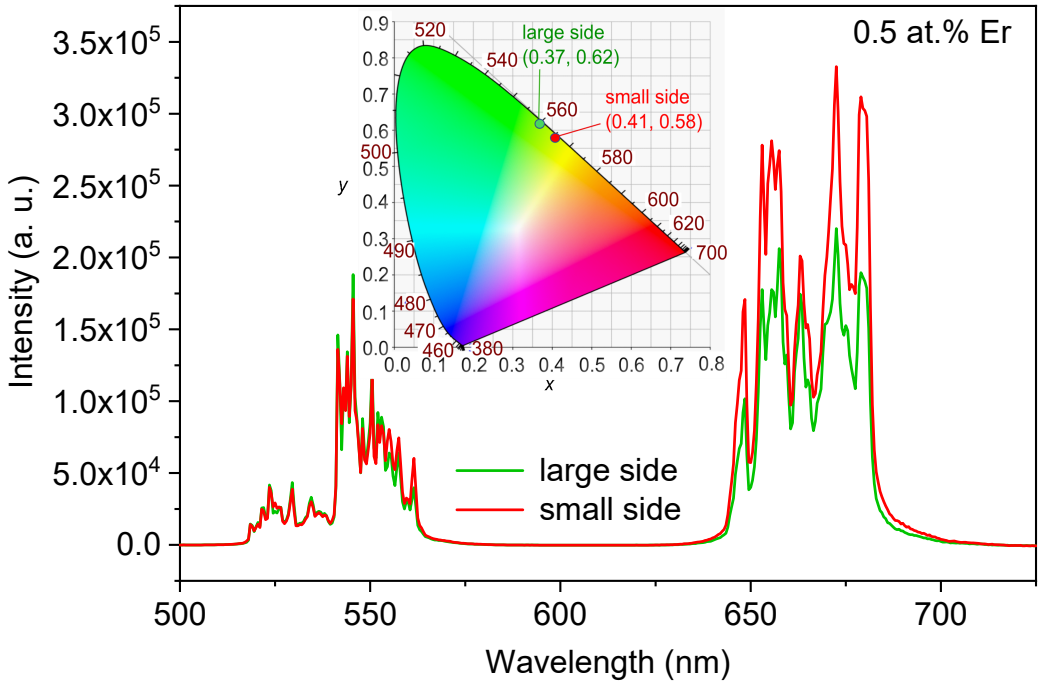

Figure 3.18. *Emission spectra recorded from the small and large sides of 20 at.% Yb−0.5 at.% Er doped* $Y_{3.2}Al_{4.8}O_{12}$ *disk. The insert shows the chromaticity coordinates indicating the emission color of the two side of the sample.*

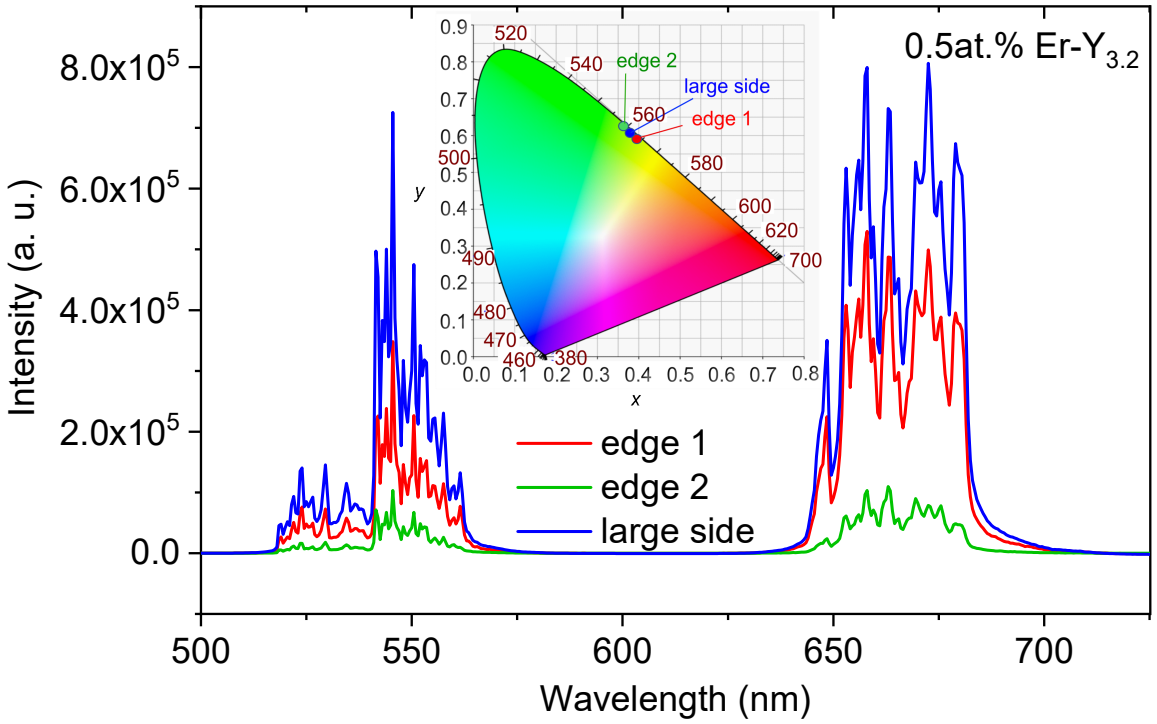

Figure 3.19. *Emission spectra of two edges and the large side of 20 at.% Yb−0.5 at.% Er doped* $Y_{3.2}Al_{4.8}O_{12}$ *disk. The insert indicates the chromaticity coordinates of the three measured positions.*

3.3.2 Ce single doped s− and ns− YAGs

5 at.% Ce^{3+} single doped $Y_3Al_5O_{12}$ and $Y_{3.2}Al_{4.8}O_{12}$ (respectively corresponding to $Ce_{0.15}Y_{2.85}Al_5O_{12}$ and $Ce_{0.16}Y_{3.04}Al_{4.8}O_{12}$) were synthesized as pure garnet phase (**figure 3.20**). Rietveld structural refinement was performed on long−scan XRD data. The structural refinement process is similar to that of non−doped YAGs, in which lattice parameter, atomic positions, thermal parameters, peak function and atomic occupation were refined. The occupation of Ce was refined on both dodecahedral (*24c*) and octahedral (*16a*) sites as they the possible position that Ce^{3+} could enter.

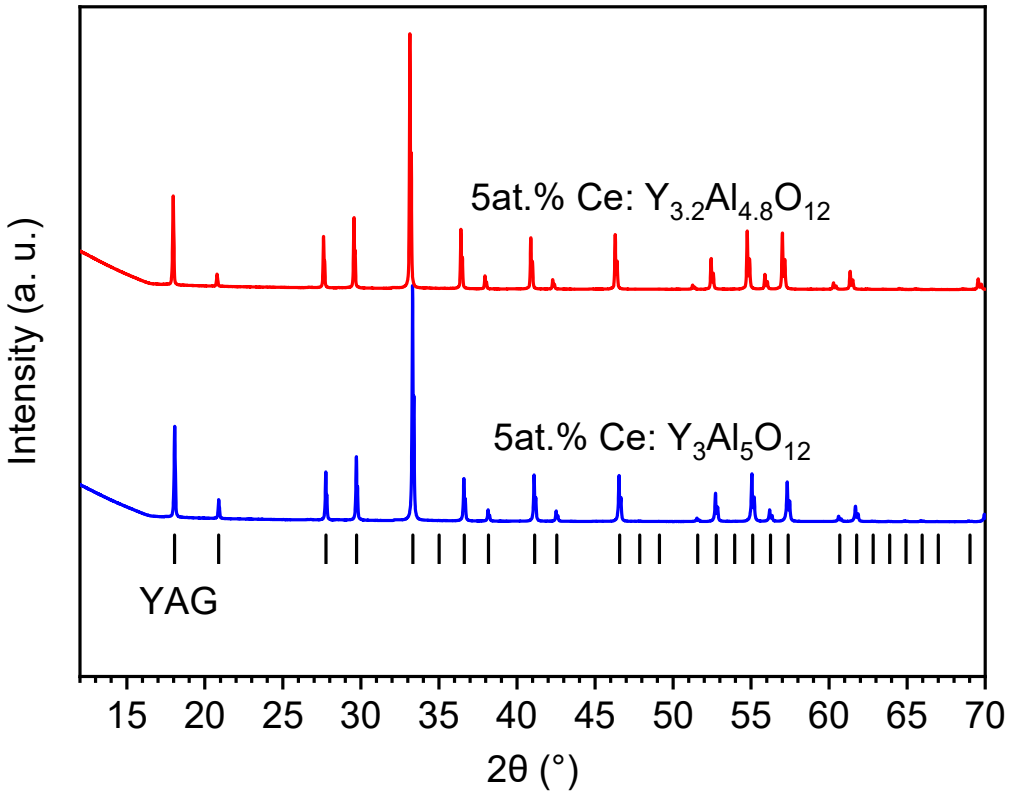

Figure 3.20. *XRD patterns of 2 at.% Ce (a) and 5 at.% Ce (b) doped $Y_3Al_5O_{12}$ and $Y_{3.2}Al_{4.8}O_{12}$ which were prepared ADL method in argon. The ticks indicate Bragg diffraction positions of YAG.*

Although the XRD data is not as high−resolution as SPD data, its Rietveld refinement still allows to get the understandable structural information of the two garnet structures, including the occupation preference of Ce^{3+} ions in the structural lattice, these information are shown in **table 3.8** and **3.9**. It shows the lattice parameter of $Ce_{0.15}Y_{2.85}Al_5O_{12}$ and $Ce_{0.16}Y_{3.04}Al_{4.8}O_{12}$ are respectively 12.02110(3) Å and 12.08139(3) Å, which are larger than that of their non−doped hosts (12.007 Å for $Y_3Al_5O_{12}$ and 12.070 Å for $Y_{3.2}Al_{4.8}O_{12}$ Å) due to the larger radius of Ce^{3+} (1.02 Å) than that of Y^{3+} (0.9 Å). Like what has been reported[115], in $Ce_{0.15}Y_{2.85}Al_5O_{12}$ structure, Ce^{3+} ions only occupy the dodecahedral site with an occupation of 0.068(3)%. In $Ce_{0.16}Y_{3.04}Al_{4.8}O_{12}$ (i. e. Ce doped $Y_{3.2}Al_{4.8}O_{12}$), Ce^{3+} also only occupy the dodecahedral site with an occupation of 0.051(3)%, which is not higher than that in stoichiometric YAG as expected, this could be attributed to the indecent data quality. The discrepancy values R_{wp} of the final refinements for $Ce_{0.15}Y_{2.85}Al_5O_{12}$ and $Ce_{0.16}Y_{3.04}Al_{4.8}O_{12}$ are respectively ~ 4.82% and ~ 4.97%. The final refined structural informatioo are plotted in **figure 3.21 (a)** and **(b)**.

Table 3.8. Rietveld structural parameters of $Ce_{0.15}Y_{2.85}Al_5O_{12}$ with space group *Ia−3d* resulted from Rietveld refinement of XRD data						
atom	Wyck symbol	x	y	z	occupancy	Uiso
Y	24c	0.125	0	0.25	0.931(3)	0.018 (3)
Ce	**24c**	**0.125**	**0**	**0.25**	**0.068(3)**	0.018 (3)
Al	16a	0	0	0	1	0.01(2)
Al	24d	0.375	0	0.25	1	0.02(1)
O	96h	-0.03027(6)	0.04909(8)	0.1495197)	1	0.01(2)
a = 12.02110(3)Å, V = 1737.13(1)Å^3, Z = 8. R_{wp} ~ 4.82%, *gof* ~ 2.88%.						

Table 3.9. Rietveld structural parameters of $Ce_{0.16}Y_{3.04}Al_{4.8}O_{12}$ space group *Ia−3d* resulted from Rietveld refinement of XRD data						
atom	Wyck symbol	x	y	z	occupancy	Uiso
Y	24c	0.125	0	0.25	0.948(3)	0.014(7)
Ce	**24c**	**0.125**	**0**	**0.25**	**0.051(3)**	**0.014(7)**
Al	16a	0	0	0	0.9	0.01(2)
Y	16a	0	0	0	0.1	0.012(2)
Al	24d	0.375	0	0.25	1	0.01(1)
O	96h	-0.03161 (6)	0.05063(8)	0.15014(8)	1	0.01(2)
a = 12.08139(3) Å, V = 1763.40(1) Å^3, Z = 8. R_{wp} ~ 4.97%, *gof* ~ 3.07%.						

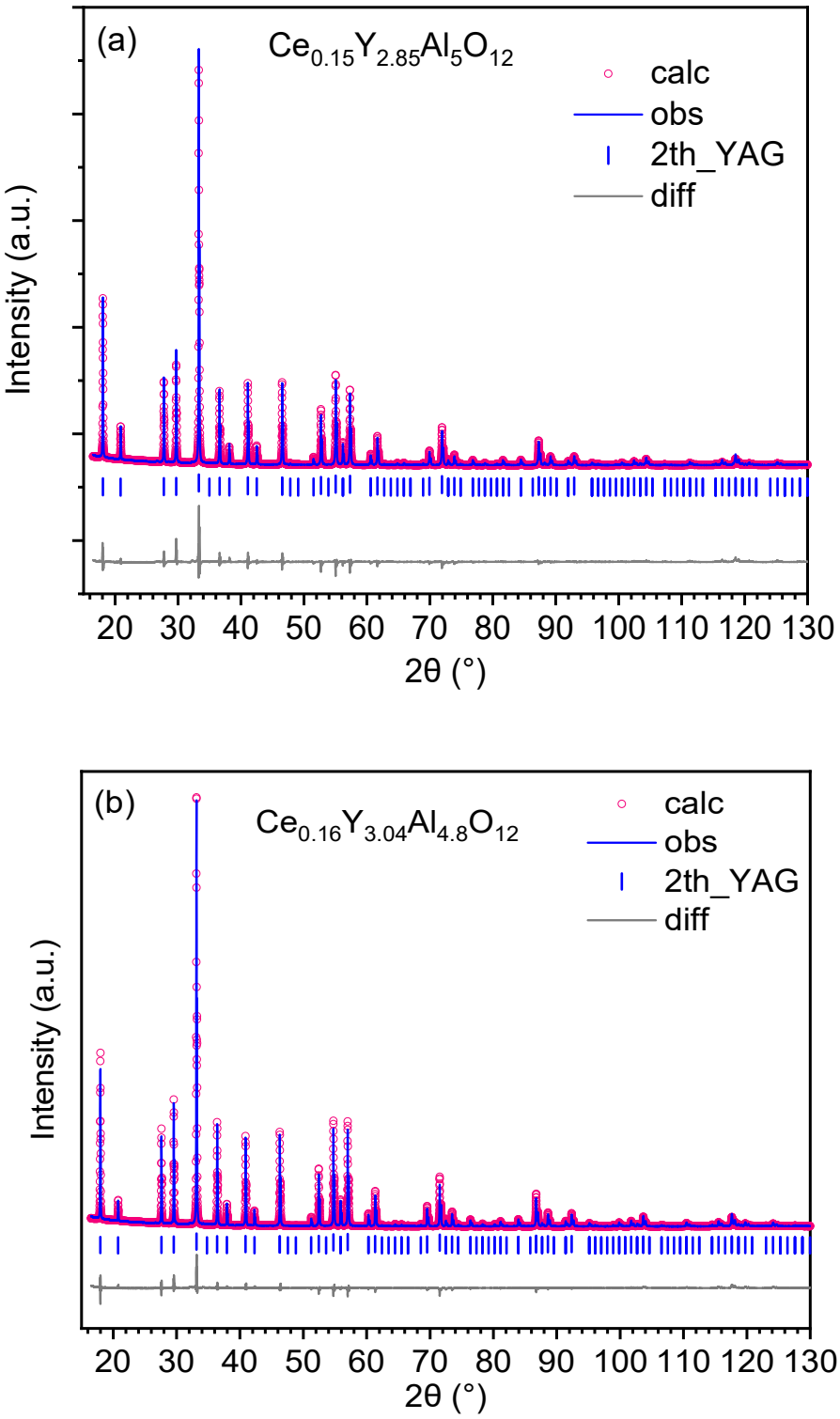

Figure 3.21. *Rietveld refinement plot of $Ce_{0.15}Y_{2.85}Al_5O_{12}$* ***(a)*** *and $Ce_{0.16}Y_{3.04}Al_{4.8}O_{12}$* ***(b)****. The blue line and red circle respectively represent observed and calculated data, the blue tick marks represent Bragg positions of YAG phase, and the grey line represent difference between observed and calculated data. The resulted discrepancy values of the two plot (a) and (b) R_{wp} ~4.82% and 4.97%.*

Figure 3.22 shows the excitation spectra of the $Ce_{0.15}Y_{2.85}Al_5O_{12}$ (5 at.% Ce: $Y_3Al_5O_{12}$) and $Ce_{0.16}Y_{3.04}Al_{4.8}O_{12}$ (5 at.% Ce: $Y_{3.2}Al_{4.8}O_{12}$) samples are qualitatively similar. They have two excitation bands respectively in UV region (340 nm) and blue region (460 nm), agreeing with the reported Ce: YAG [34]. Emission spectra of $Ce_{0.15}Y_{2.85}Al_5O_{12}$ and $Ce_{0.16}Y_{3.04}Al_{4.8}O_{12}$ under 340 nm (**figure 3.23 a**) and 460 nm (figure 3.23 b) excitation show single broad band peaking at 565 nm, the emission intensity of $Ce_{0.15}Y_{2.85}Al_5O_{12}$ is much higher than that of $Ce_{0.16}Y_{3.04}Al_{4.8}O_{12}$.

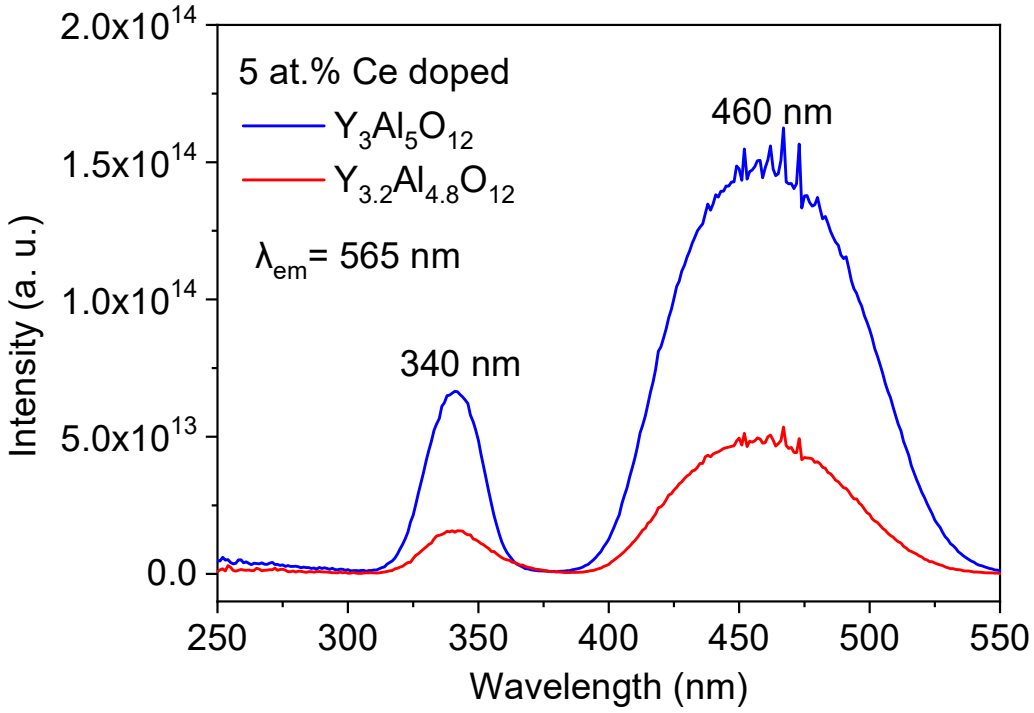

Figure 3.22. *Raw excitation spectra at λ_{em} = 565 nm of 5 at.% Ce doped $Y_3Al_5O_{12}$ and $Y_{3.2}Al_{4.8}O_{12}$ garnets.*

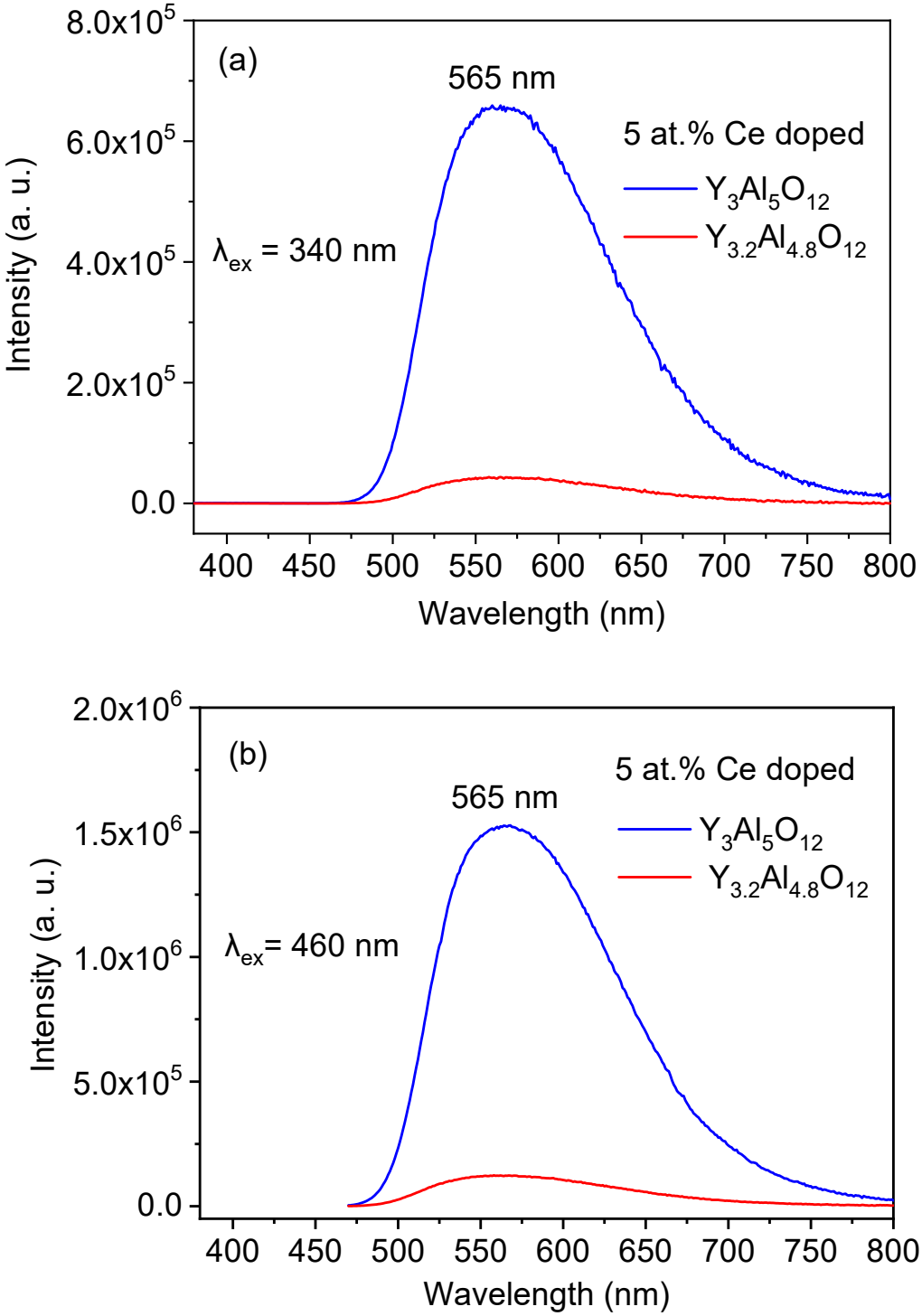

Figure 3.23. *Emission spectra of 5 at.% Ce doped $Y_3Al_5O_{12}$ and $Y_{3.2}Al_{4.8}O_{12}$ under 340 nm (a) and 460 nm (b) excitation.*

Compared to Yb, Er doped $Y_3Al_5O_{12}$ and $Y_{3.2}Al_{4.8}O_{12}$, Ce^{3+} incorporation also does not change the crystal structure. The fine structure of normalized emission spectra for 340 nm and 460 nm excitation are respectively shown in **figure 3.24 a** and **b**, it indicates that Ce:

$Y_{3.2}Al_{4.8}O_{12}$ has no difference to that of Ce: $Y_3Al_5O_{12}$, it can be attributed to the unique 8−coordinate environment of Ce^{3+} in both two hosts. Moreover, emission performance of Ce: $Y_{3.2}Al_{4.8}O_{12}$ is poorer than that Ce: $Y_3Al_5O_{12}$, this could be attributed to the random error caused atomic disorder in the structure, which happens often to non-stoichiometric YAG samples, *e.g*. the (Yb, Er) $Y_{3.2}Al_{4.8}O_{12}$. While fortunately, nonstoichiometry was found to be efficient solution to introduce Yb and Er to octahedral sites of the yttrium aluminum garnet structure and therefore improve the luminescence properties. The luminescence measurement is a good way to detect crystallinity change in non−stoichiometric YAG.

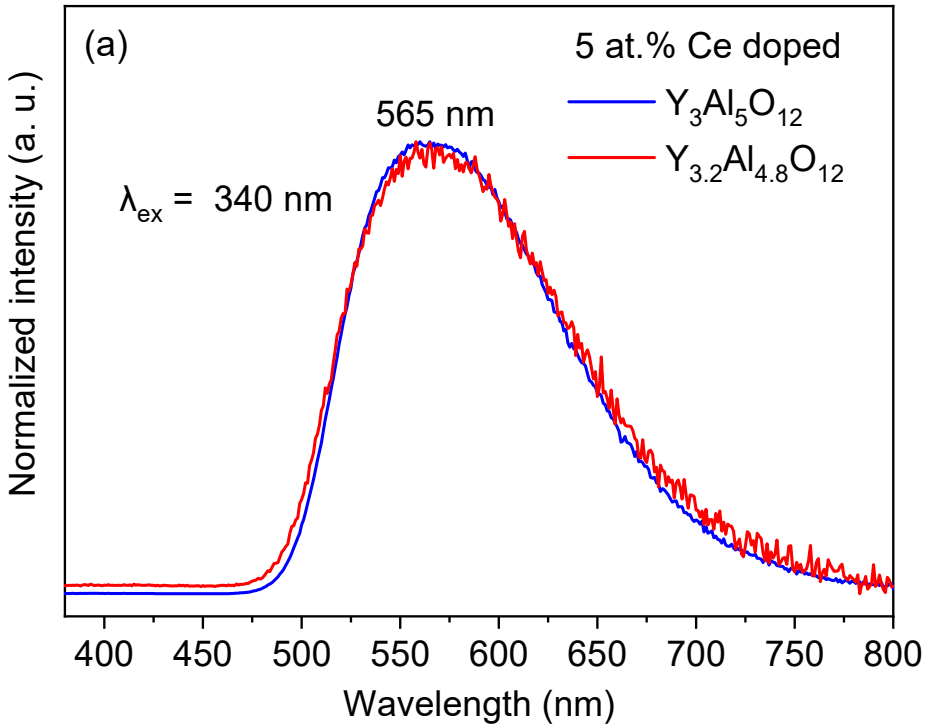

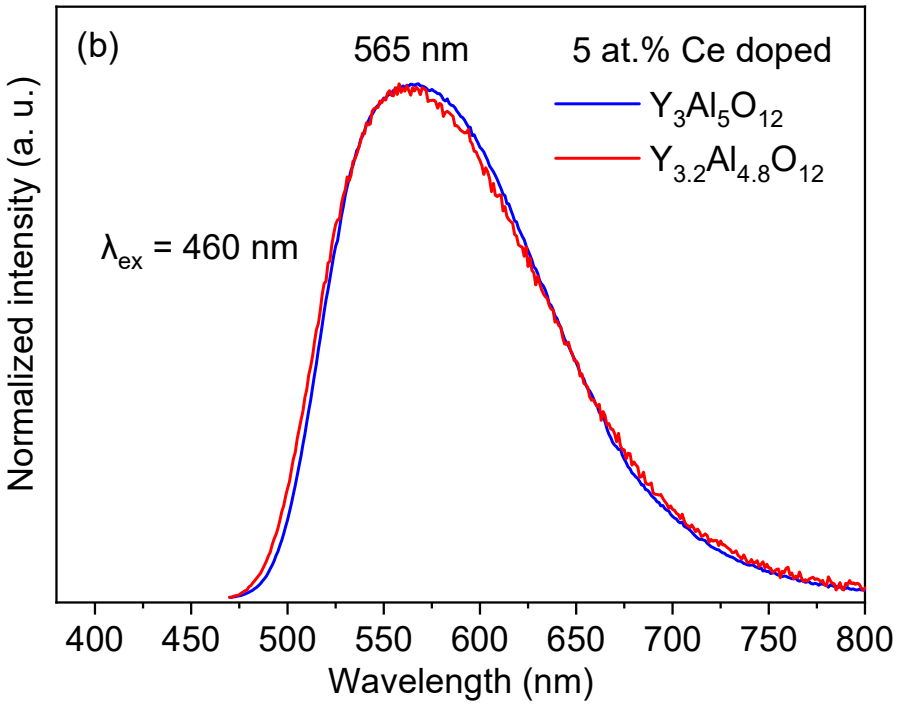

Figure 3.24. *Normalized emission spectra of 5 at.% Ce doped $Y_3Al_5O_{12}$ and $Y_{3.2}Al_{4.8}O_{12}$ under laser excitation at 340 nm (a) and 460 nm (b).*

3.3.3 Mn and Dy doped s− and ns−YAGs

Synthesis of 0.5 at.% Mn and 1 at.% Dy doped s- and ns-YAGs

In addition to Yb/Er and Ce dopants, we were also interested in red emission Mn^{4+}: YAG phosphor and Dy^{3+}: YAG thermographic phosphor, and wonder how are the optical properties of the ns-YAG with the two dopants. The 0.5 at.% Mn (**figure 3.25**) and 1 at.% Dy single doped (**figure 3.26**) $Y_3Al_5O_{12}$ and $Y_{3.2}Al_{4.8}O_{12}$ were isolated with single YAG phase as shown by the XRD patterns. The Mn doped $Y_3Al_5O_{12}$ and $Y_{3.2}Al_{4.8}O_{12}$ were synthesized by ADL in argon, the oxidation state of Mn is expected to be 4+. The dopants in both s-YAG ($Y_3Al_5O_{12}$) and ns-YAG ($Y_{3.2}Al_{4.8}O_{12}$) does not change the crystal structure.

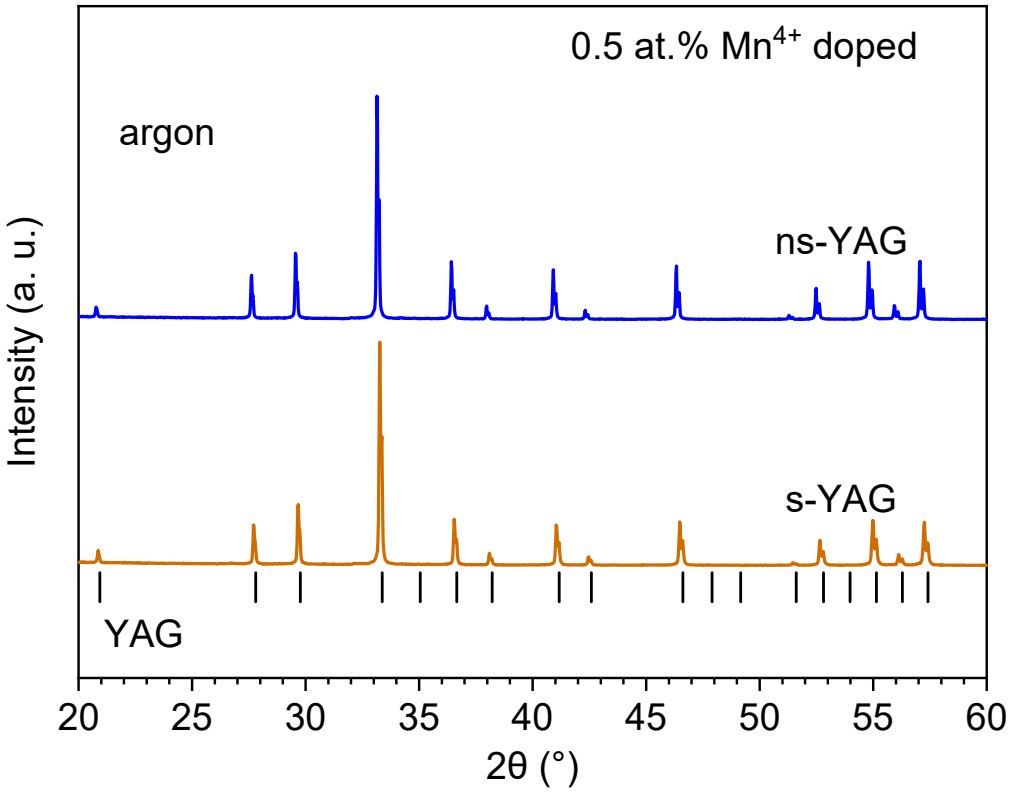

Figure 3.25. *XRD patterns of 0.5 at% Mn doped s- and ns-YAGs prepared in argon.*

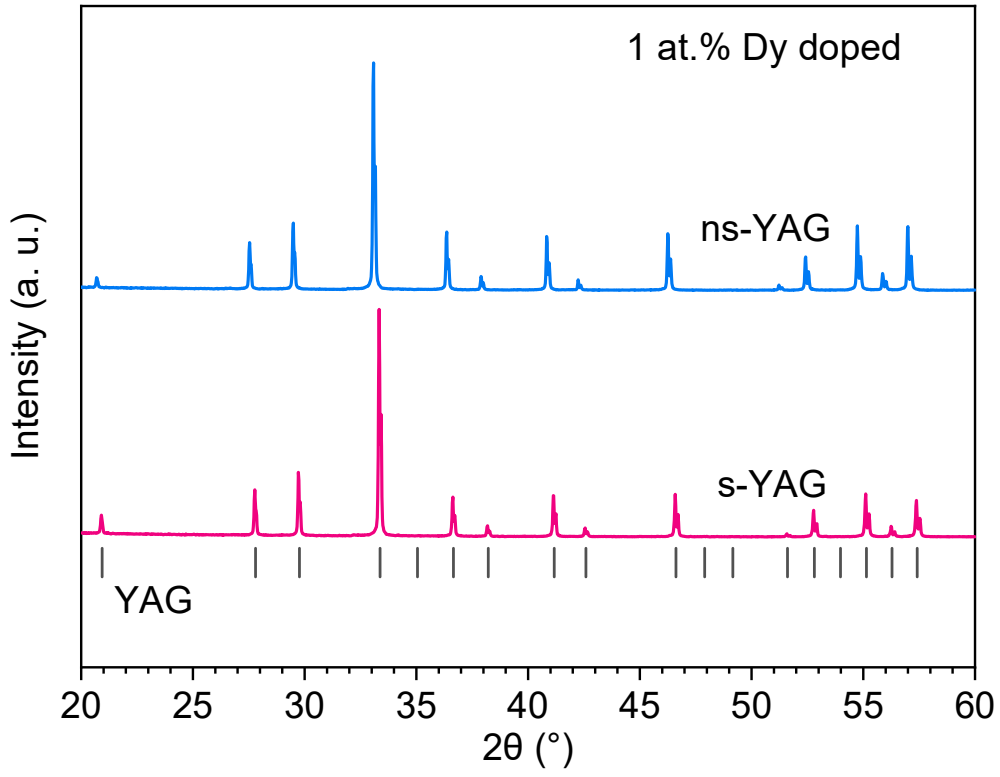

Figure 3.26. *XRD patterns of 1 at.% Dy doped s- and ns-YAGs synthesized.*

Luminescence properties of 0.5 at.% Mn doped s- and ns-YAGs

Figure 3.27 shows the excitation spectra of 0.5 at.% Mn^{4+} doped s- and ns-YAGs recorded at an emission wavelength of 673 nm, characteristic of Mn^{4+}. Both samples have an excitation band in 240-425 nm corresponding to the $^4A_2 \rightarrow {}^4T_1$ excitation (**figure 3.27**). It is shown under 310 nm excitation (**figure 3.28**), both samples have emission spectra in 625-700 nm with similar spectra shape, the main peak centers at 672 nm comes from the $2E \rightarrow {}^4A_2$ energy transition, giving out red emission. This agrees well with that of reported 0.1 at. % Mn^{4+} doped $Y_3Al_5O_{12}$ (s-YAG)[125] (**figure 3.29**). Combing with XRD data, the incorporation of Mn^{4+} in the structure lattice does not change the crystal structure. Emission intensity of 0.5 at.% Mn: ns-YAG are higher than that of 0.5 at. % Mn: s-YAG, but the fine structure shown by the normalized spectra (**figure 3.30**) of the two samples appear quite similar., indicating the nonstoichiometry has little influence on their emission frequency.

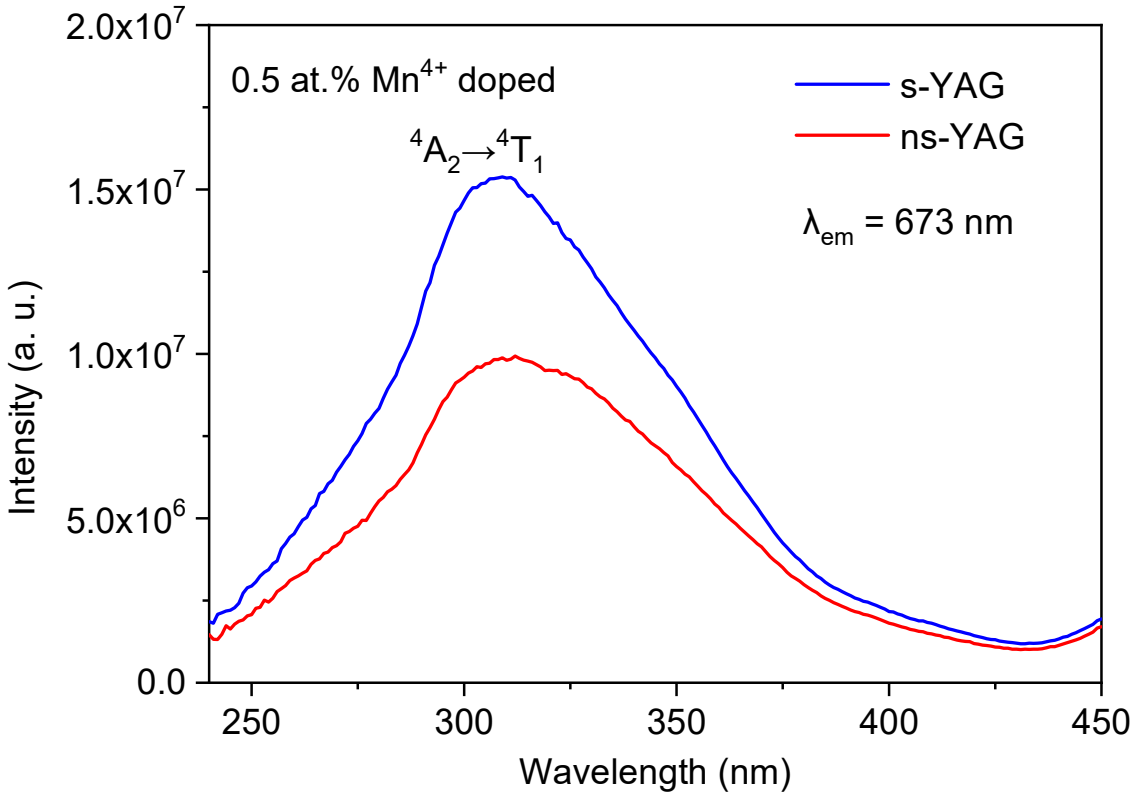

Figure 3.27. *Excitation spectra (λ_{em} = 673 nm) of 0.5 at.% Mn^{4+} doped s- and ns-YAGs.*

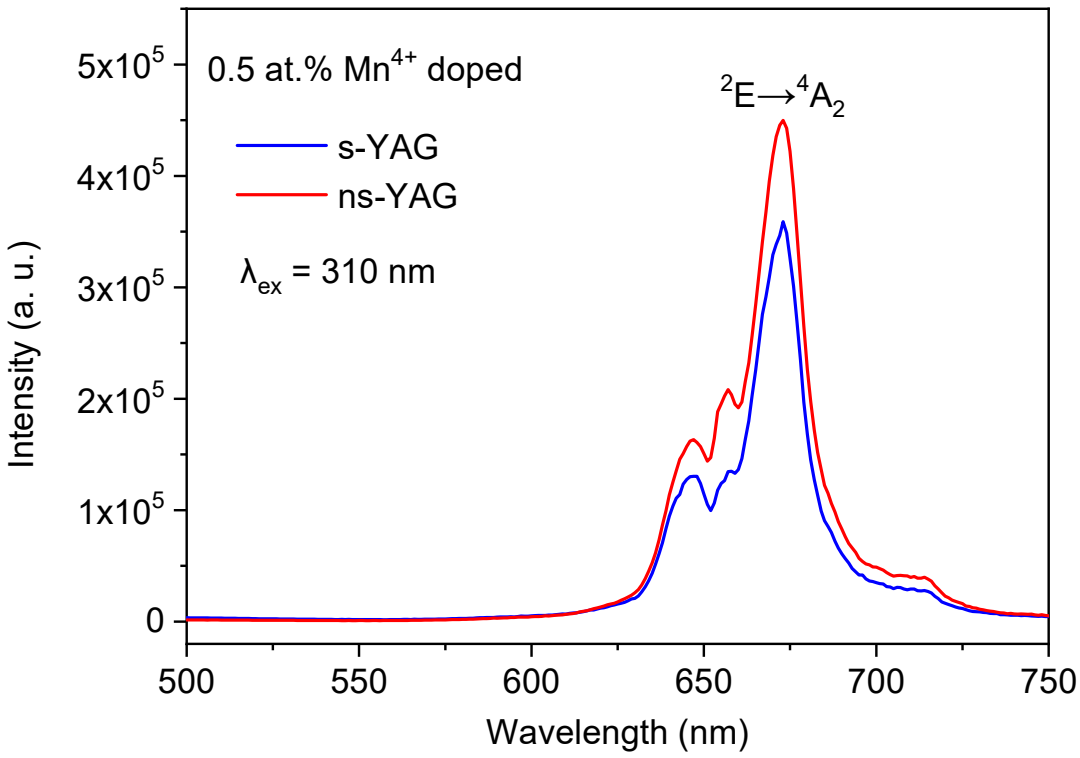

Figure 3.28. *Emission spectra (λ_{ex} = 310 nm) of 0.5 at.% Mn^{4+} doped s- and ns-YAGs.*

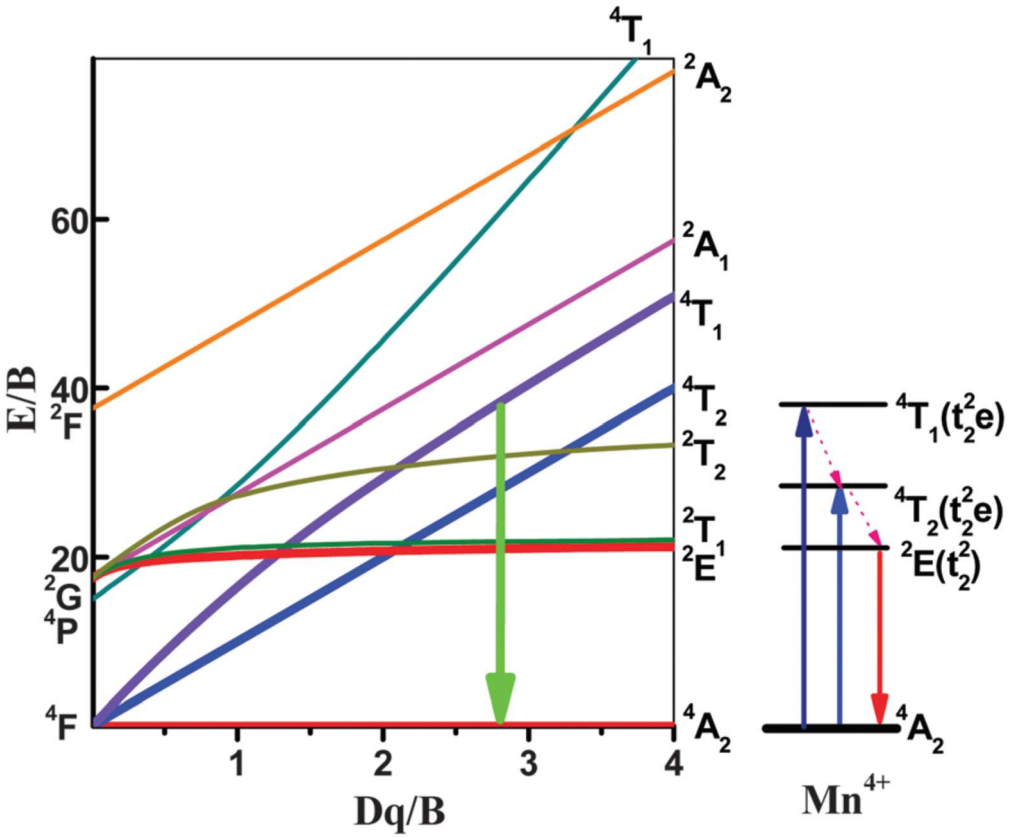

Figure 3.29. *Tanabe-Sugano energy-level diagram of 6-coordinate Mn^{4+} in YAG host, referred from the work of D. Chen, et al.[125].*

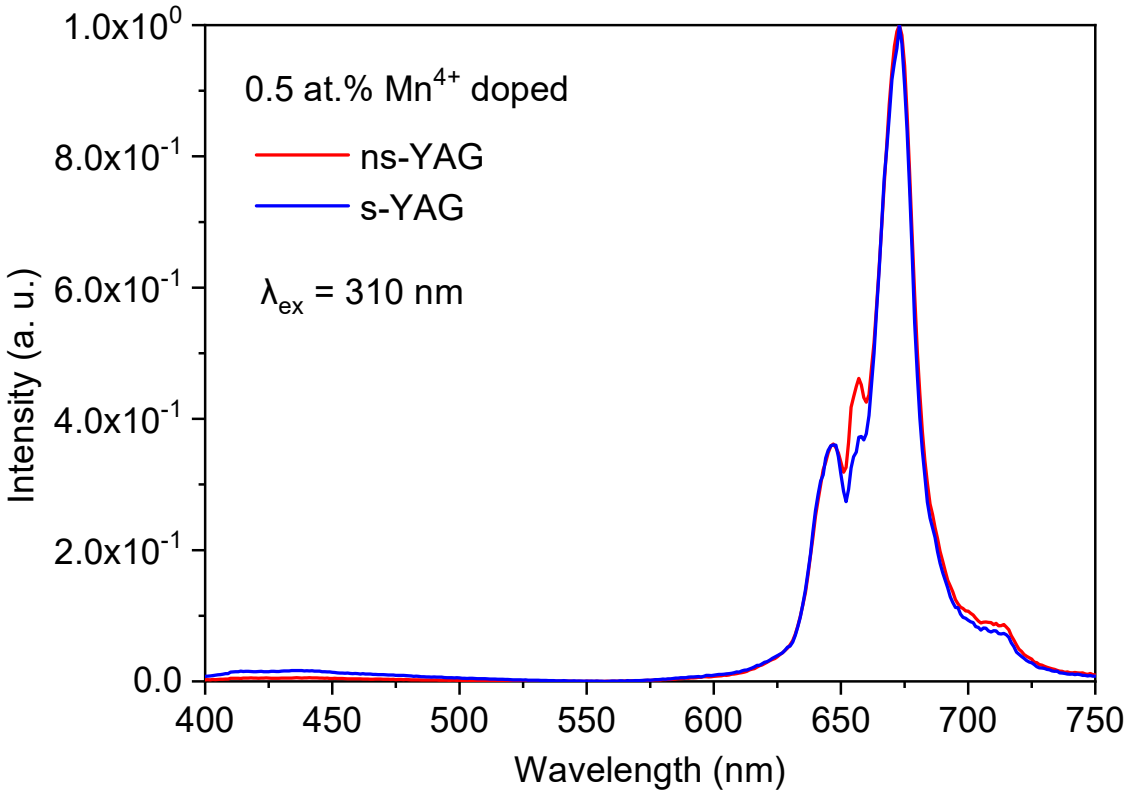

Figure 3.30. *Normalized emission spectra under 310 nm excitation of 0.5 at.% Mn^{4+} doped s- and ns-YAGs.*

The decay curves (**figure 3.31**) of the two samples are similar and imply they have close lifetimes of ~ 0.8 ms. Since Mn^{4+} (0.53 Å) and Al^{3+} (0.535Å, CN = 6) have similar ionic radii, Mn^{4+} cations enter the octahedral site and lead to red emission color[125, 126]. Compared to large Y^{3+} (0.9 Å, CN = 6; 1.019 Å, CN = 8) cations, Mn^{4+} has stronger preference for octahedral sites[125-127]. As the concentration of Mn^{4+} was calculated as the numerator of Y^{3+} denominator, the exact theoretical compositions of the two samples are $Mn_{0.015}Y_{2.985}Al_5O_{12}$ (Mn: s-YAG) and $Mn_{0.016}Y_{3.184}Al_{4.8}O_{12}$ (Mn: ns-YAG). Therefore, probably Mn: s-YAG is biphasic of main garnet phase and small amount of residual Al_2O_3 which could not be determined by XRD, whilst the Mn^{4+} concentration in the garnet lattice gets higher than expected, increasing the O^{2-} quenching centers and decreasing the emission intensity. In contrast, Mn^{4+} in ns-YAG could easily go 6-coordinate sites without pushing Al^{3+} out of the garnet lattice. The Al_2O_3 impurity and higher concentration of O^{2-} quenching centers are responsible for the poorer emission intensity of Mn: s-YAG, however because of their low contents, no big difference in emission performance between s-YAG and ns-YAG was produced.

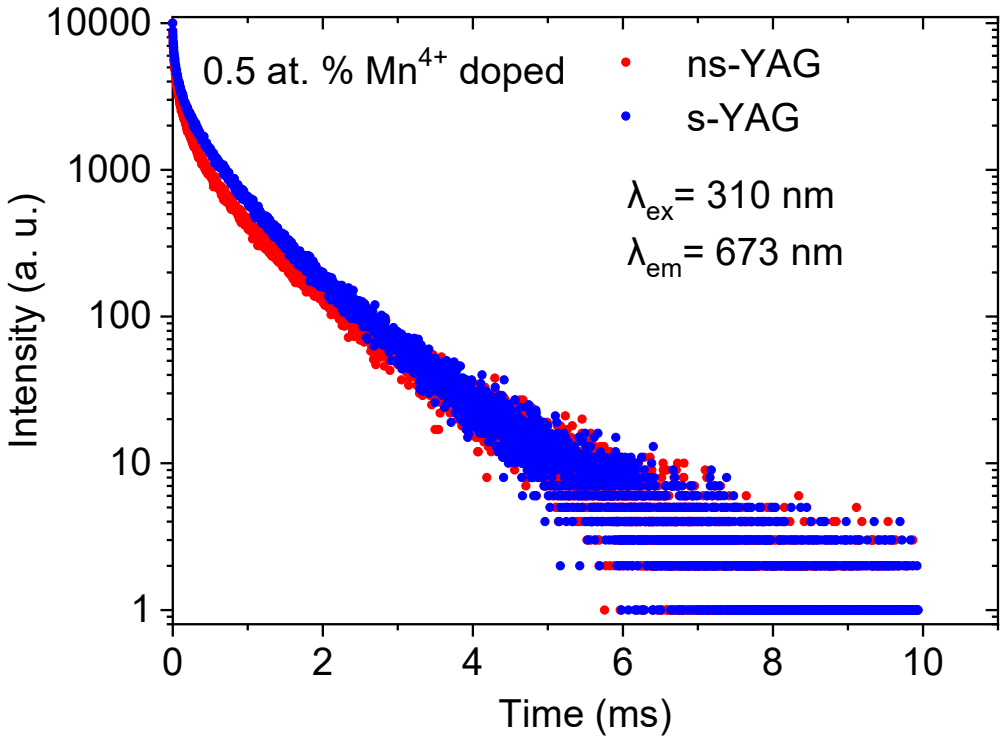

Figure 3.31. *Decay curves (λ_{ex} = 310 nm) of 0.5 at.% Mn^{4+} doped s- and ns-YAGs.*

Luminescence properties of 1 at.% Dy doped s- and ns-YAGs

Figure 3.32 shows the excitation spectra of 1 at.% Dy doped s- and ns-YAGs recorded at an emission wavelength of 582 nm, typically for Dy^{3+} ions, they are similar in shape but deviate in intensity, the spectra of s-YAG is more intensive than that of ns-YAG. The excitation signals are over the 250-450 nm range. The emission spectra (**figure 3.33**) under 352 nm excitation for the s- and ns-YAG samples show emission bands in 450-515 nm, 550-615 nm and 650-685 nm, the two emission spectra are qualitatively identical. Their similarity can be explained by the nature of Dy^{3+} cation, the 5s electrons shield the 4f orbitals from where the optical characteristics arise[128]. Therefore, the emission performance is independent of crystal field.

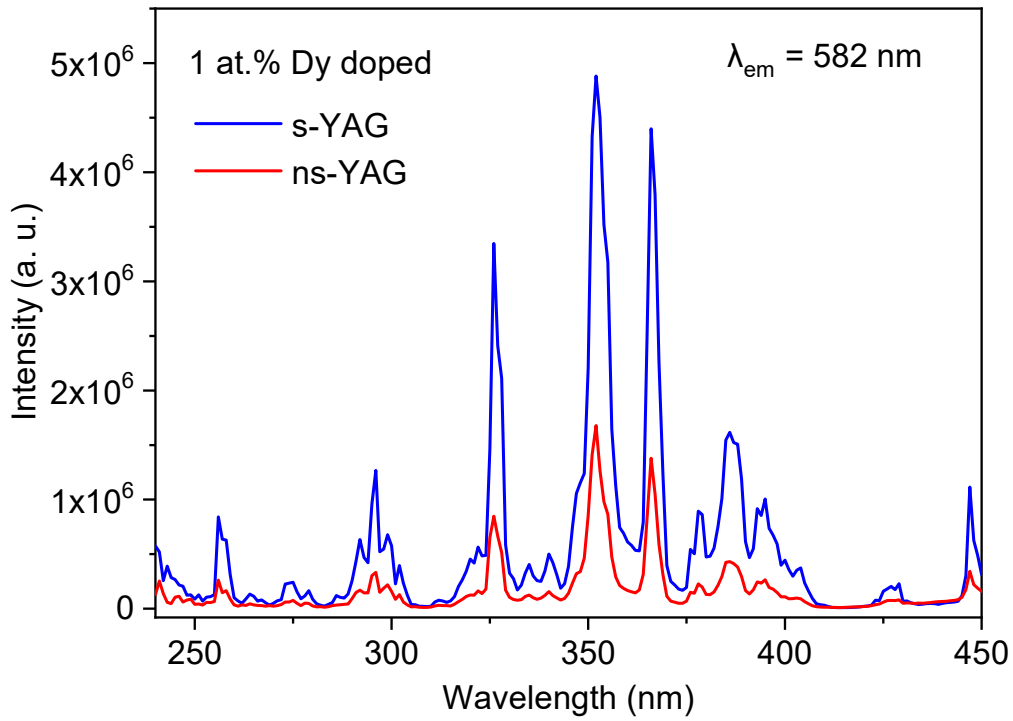

Figure 3.32. *Excitation spectra (λ_{em} = 582 nm) of 1 at.% Dy^{3+} doped s- and ns-YAGs.*

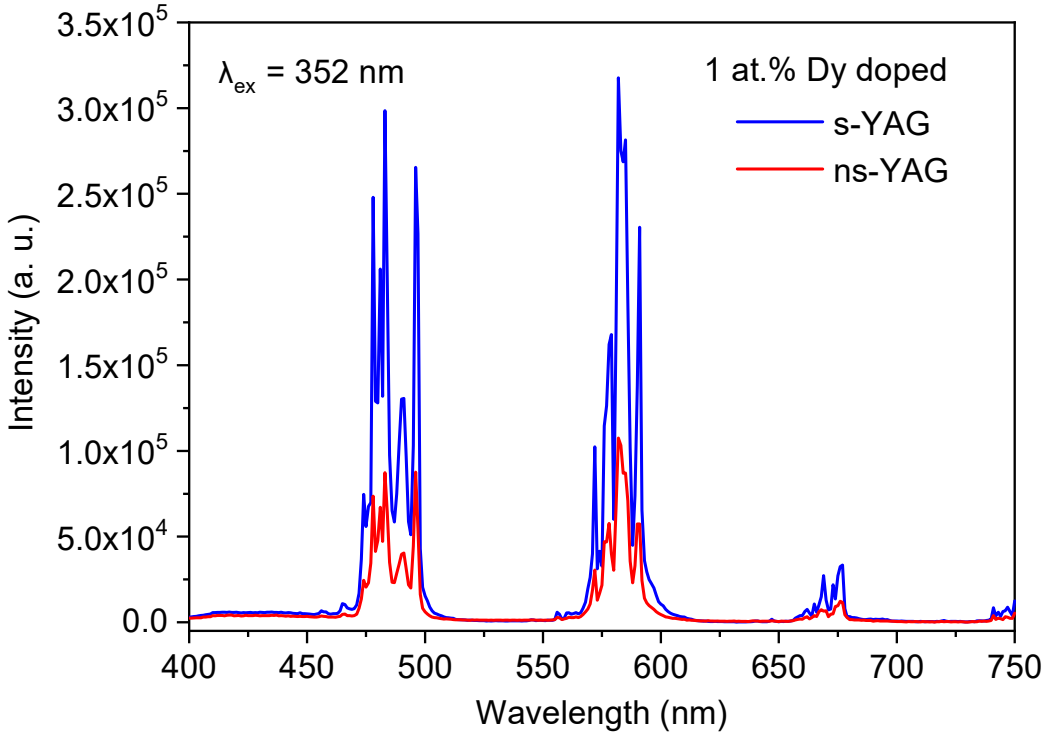

Figure 3.33. *Emission spectra (λ_{ex} = 352 nm) of 1 at.% Dy^{3+} doped s- and ns-YAG.*

The luminescence of Dy^{3+} doped YAG leads to the thermal effect, allowing for the application as thermographic phosphors. The involved mechanism follows the Boltzmann's law, the ratio between the two intensities of corresponding transition lines can determine the temperature of the sample[69, 129]. The normalized emission spectra in **figure 3.34** indicate the two garnet samples almost have the same fine structure, the nonstoichiometry has little effect on changing frequency, thus could little effect on the ability of determining the temperature.

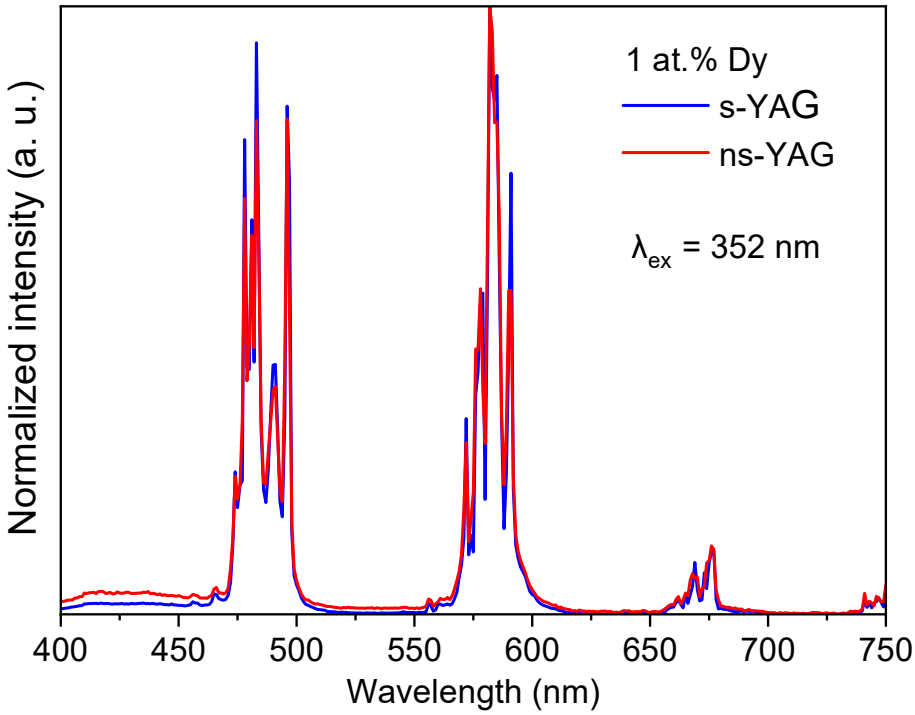

Figure 3.34. *Normalized emission spectra of 1 at.% Dy^{3+} Doped s-and ns-YAGs under λ_{ex} = 352 nm excitation .*

The decay curves (**figure 3.35**) of the two samples overlap and give the same lifetime 880 ms. In comparison with s-YAG, the new possible occupation of Dy^{3+} at octahedral sites for ns-YAG has little impact on luminescence properties.

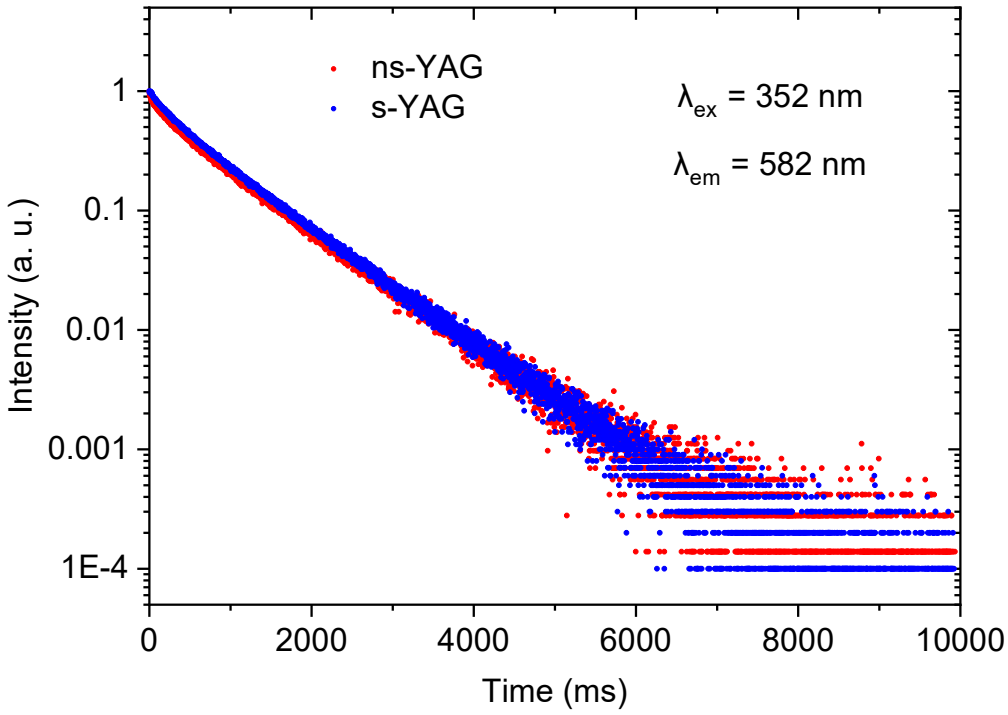

Figure 3.35. *Decay curves of 1 at.% Dy^{3+} doped s- and ns-YAG.*

3.3.4 Other s− and ns−garnets

3.3.4.1 Other ADL synthesized s− and ns−garnets

$A_3B_5O_{12}$ is a big family of garnets, in this part 34 compositions with A and B are respectively set as one element. A is Y, Yb, Er, Dy, Gd, Sm, Nd, and Ce and B is Al, Ga, Fe, Mn and Sc (indicated in the cropped element table below, **figure 3.36**). The synthesis of the composition aims to prepare other non−stoichiometric garnet, and study their potential properties, for example, optical or magnetic properties. These sample were synthesized only by ADL method.

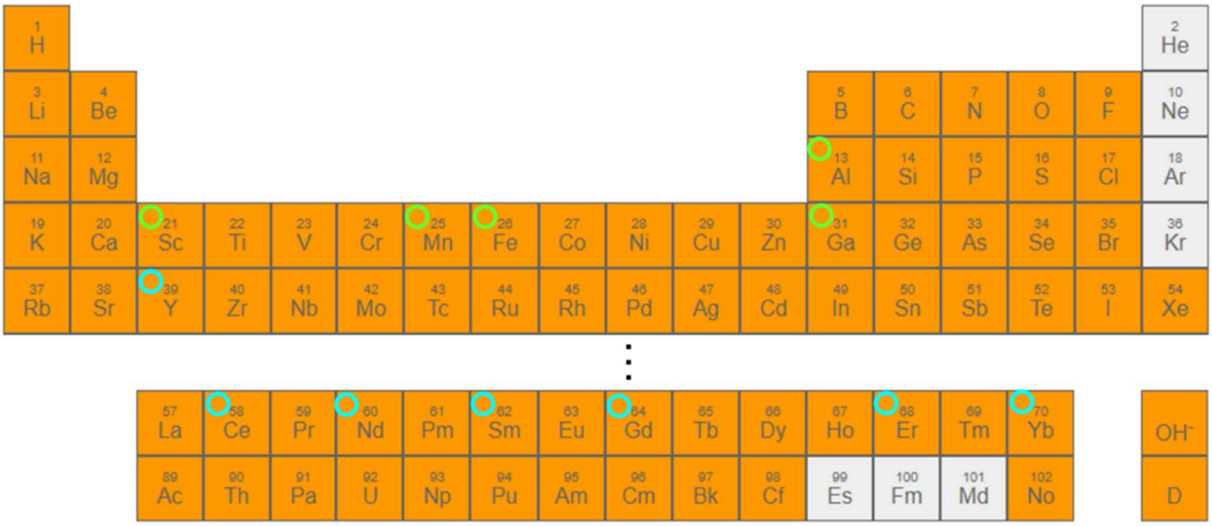

Figure 3.36. *A capture of periodic table, the cyan and green circles respectively indicate the A and B cations in $A_3B_5O_{12}$ garnet structure.*

All the samples were processed by the same method, powders mixture were first pressed into pellets. The pellets were crushed into fragments before being put into the nozzle for synthesis by ADL. Argon was used as levitation gas for these compositions, except Fe-containing samples were synthesized in oxygen to stabilize Fe^{3+}. Except that Ga−containing compositions were heated at around 1860 °C to prevent the Ga from evaporation, the others were heated at around 2000−2200 °C. In all the heating process, samples were heated for 5−10 seconds to ensure that the sample to be thoroughly melted before cooling. Cooling process was controlled by two ways, immediately switching off lasers or gradually decreasing laser power until zero. **Figure 3.37** shows the synthesizing solutions of these compositions using numbers 0 and 1 to indicate the two cooling process.

5 / 3	Y	Yb	Er	Gd	Sm	Nd	Ce
Sc	R	R	R	R	R	R	R
Fe	R	R	R	R	R	R	R
Mn	R	R	R	R	R	R	R
Ga	R	R	R	R	R/S	R/S	R
Al		R	R	R	R/S	R/S	R

Figure 3.37. *Compositions synthesized by ADL method. The letters R and S respectively indicate rapid and slow cooling process.*

XRD patterns of these compositions were recorded by fast scan for phase indexation, they are shown in **figure 3.38 a−g**, being classified into Y−, Yb−, Er-, Gd−, Sm−, Nd− and Ce−based groups. Among these $A_3B_5O_{12}$ compositions, single garnet phase was obtained from $Er_3Al_5O_{12}$, $Gd_3Al_5O_{12}$, $Sm_3Ga_5O_{12}$ and $Nd_3Ga_5O_{12}$. The resulted phasing situation of the other compositions which crystallized into mixture were not studied in details but simply exhibited in **figure 3.34**. Therefore, in the following work, new non−stoichiometric garnets were explored basing on these four stoichiometric garnets (**figure 3.39**). Although in the XRD pattern of $Gd_3Al_5O_{12}$ weak diffraction peaks of $GaAlO_3$ appear, the synthesis of non−stoichiometric gadolinium aluminum garnet was also attempted.

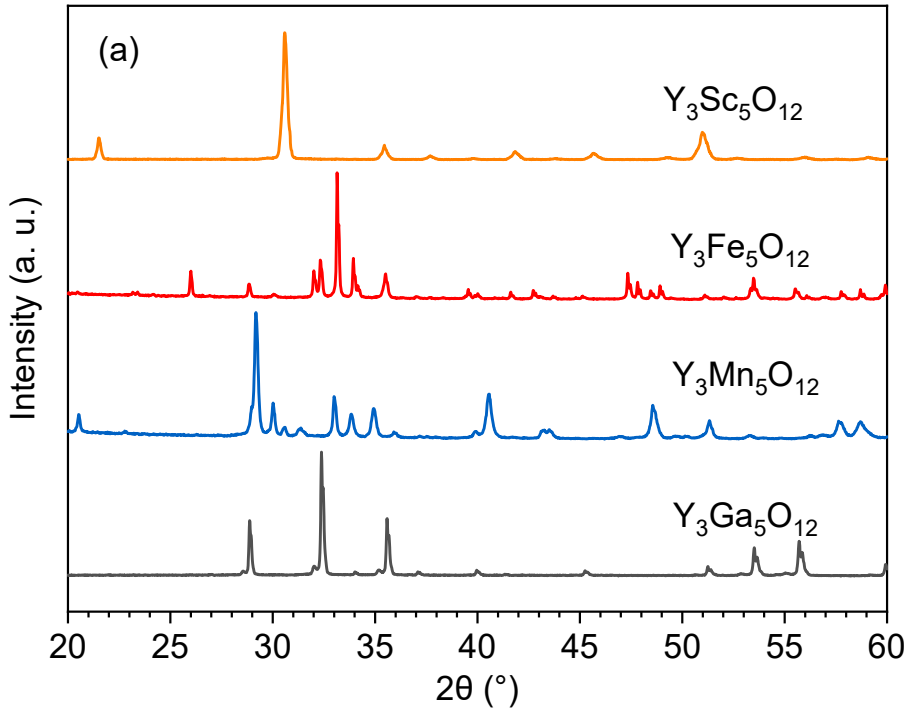

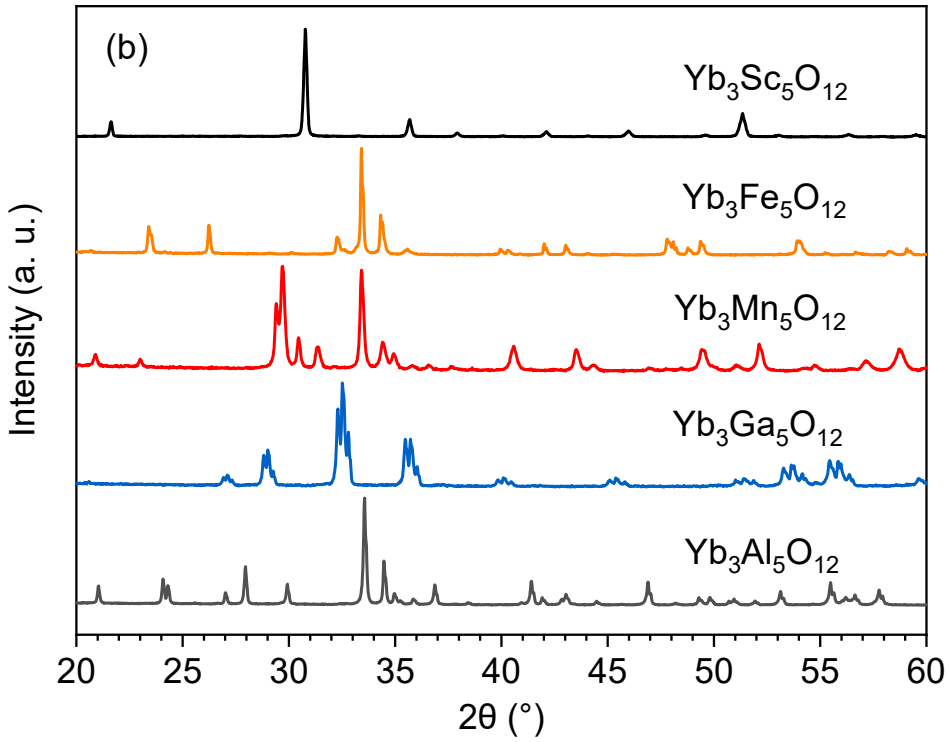
(b)
$Yb_3Sc_5O_{12}$
$Yb_3Fe_5O_{12}$
$Yb_3Mn_5O_{12}$
$Yb_3Ga_5O_{12}$
$Yb_3Al_5O_{12}$
Intensity (a. u.)
20 25 30 35 40 45 50 55 60
2θ (°)

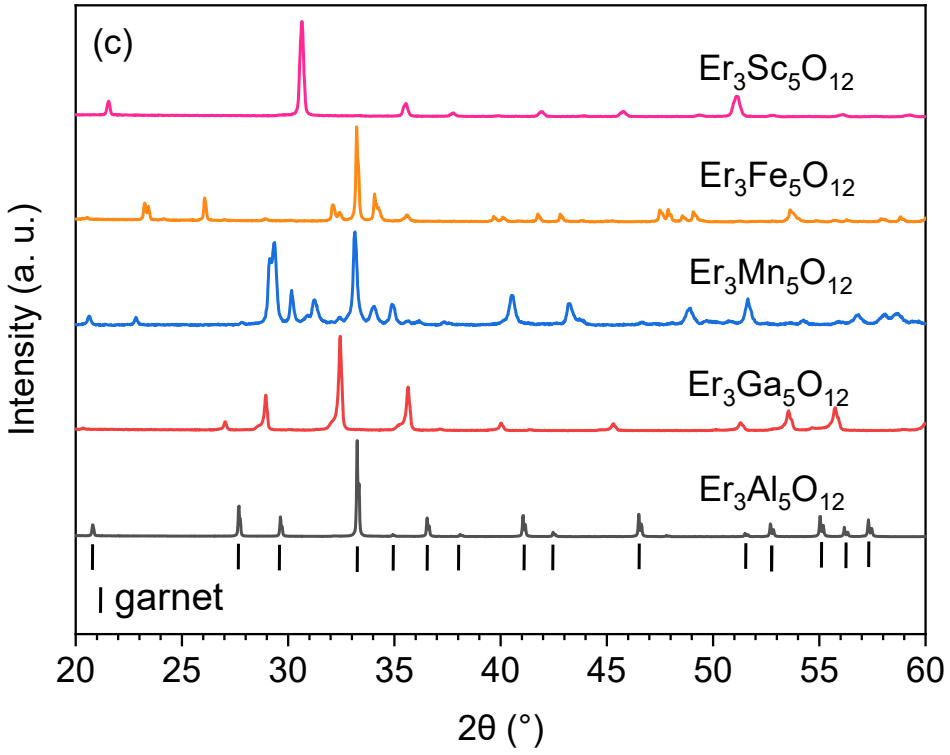
(c)
$Er_3Sc_5O_{12}$
$Er_3Fe_5O_{12}$
$Er_3Mn_5O_{12}$
$Er_3Ga_5O_{12}$
$Er_3Al_5O_{12}$
garnet
Intensity (a. u.)
20 25 30 35 40 45 50 55 60
2θ (°)

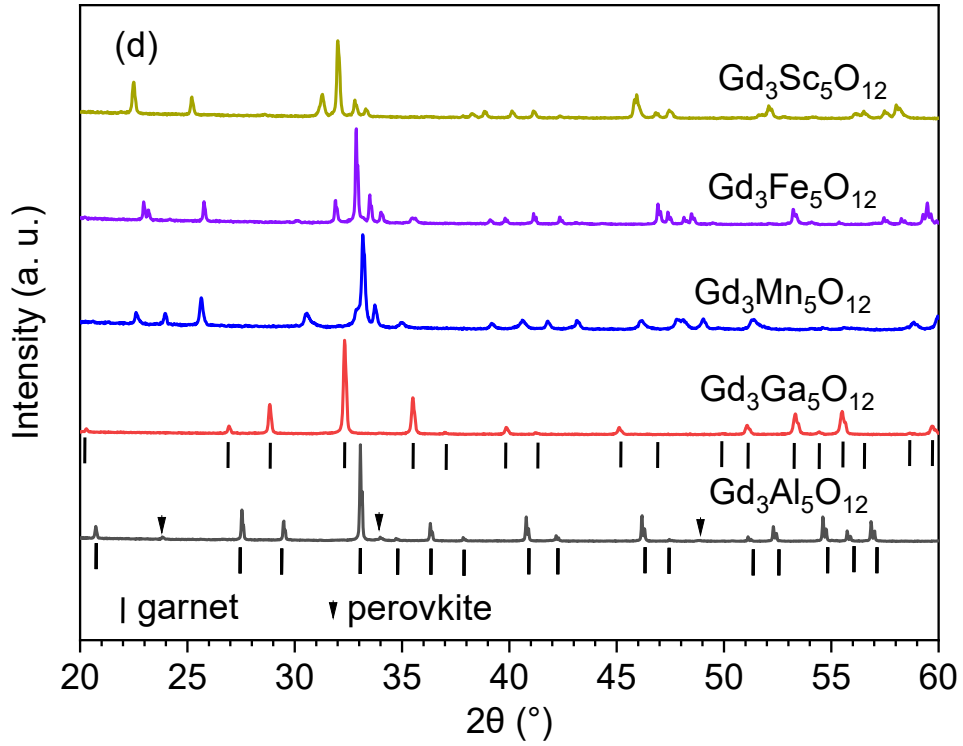
(d)
$Gd_3Sc_5O_{12}$
$Gd_3Fe_5O_{12}$
$Gd_3Mn_5O_{12}$
$Gd_3Ga_5O_{12}$
$Gd_3Al_5O_{12}$
garnet
perovkite
Intensity (a. u.)
20
25
30
35
40
45
50
55
60
2θ (°)

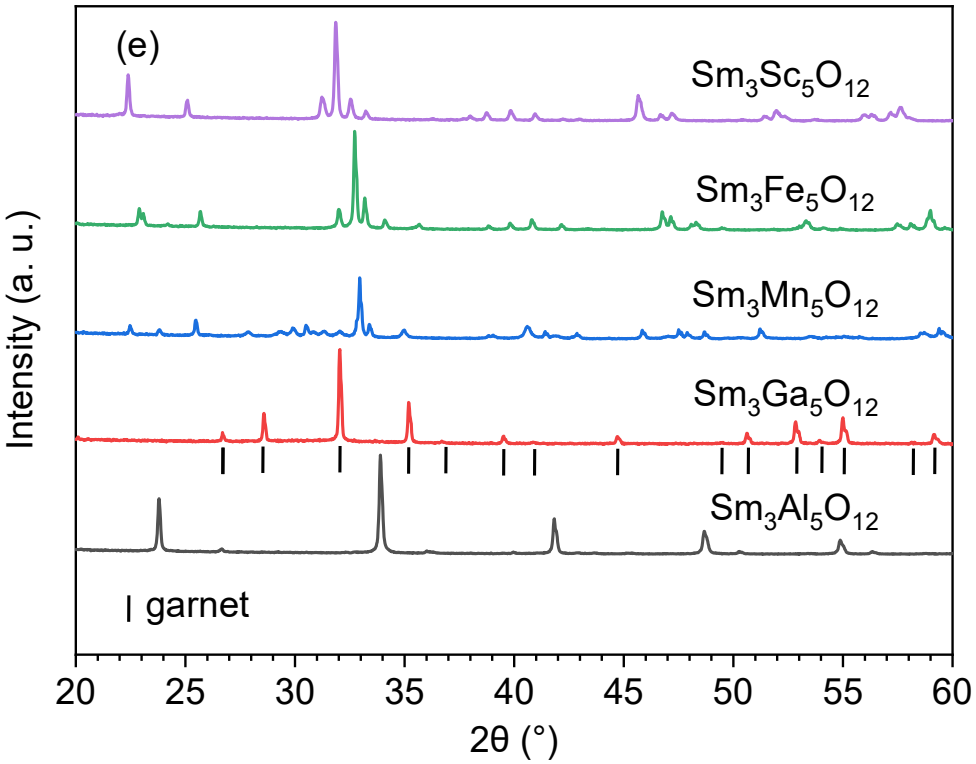
(e)
$Sm_3Sc_5O_{12}$
$Sm_3Fe_5O_{12}$
$Sm_3Mn_5O_{12}$
$Sm_3Ga_5O_{12}$
$Sm_3Al_5O_{12}$
garnet
Intensity (a. u.)
20
25
30
35
40
45
50
55
60
2θ (°)

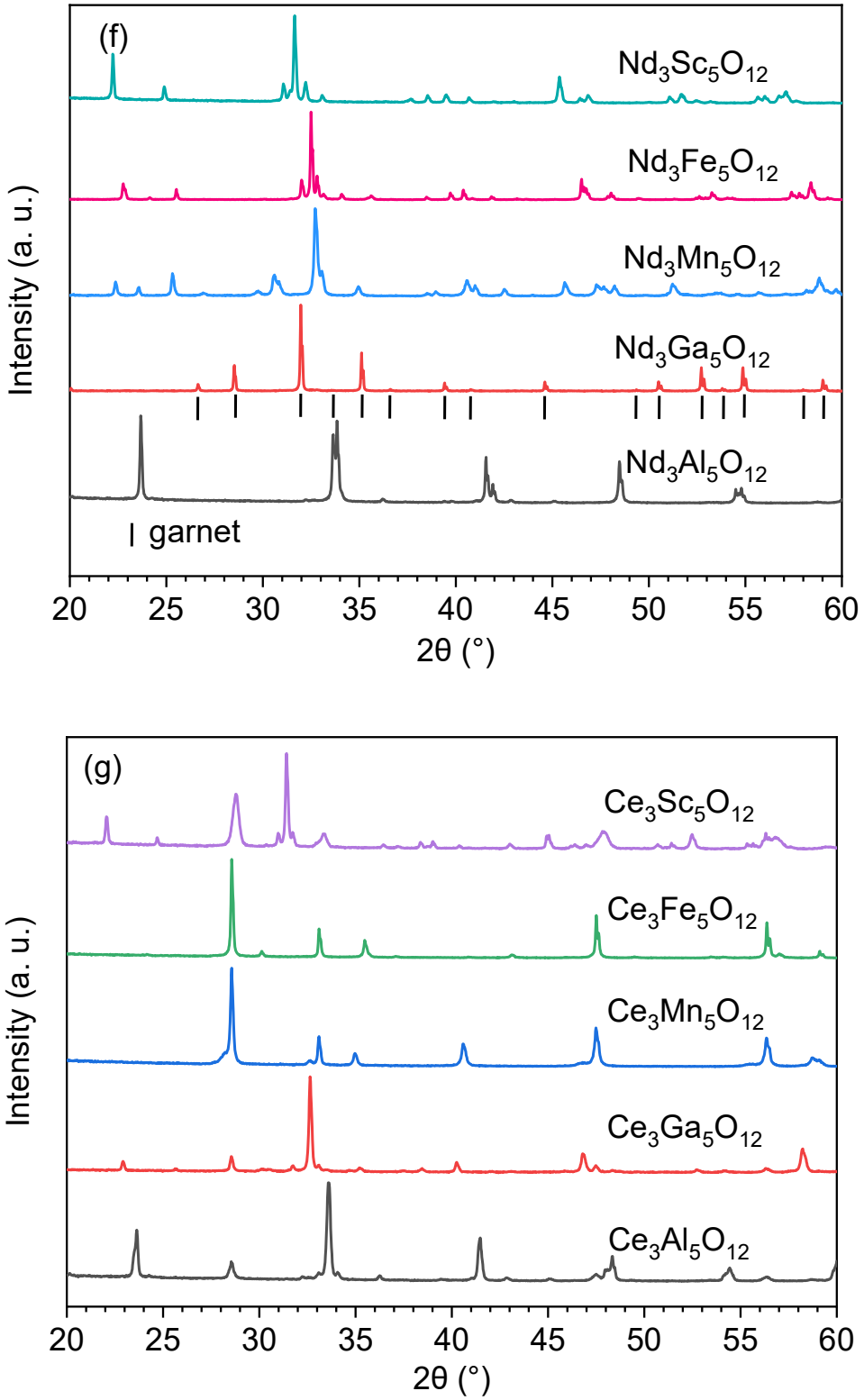

Figure 3.38. *XRD patterns of $A_3B_5O_{12}$ (A = Y, Yb, Er, Dy, Gd, Sm, Nd, and Ce; B = Al, Ga, Fe, Mn and Sc) samples synthesized by ADL method.*

5/3	Y	Yb	Er	Gd	Sm	Nd	Ce
Sc							
Fe							
Mn							
Ga				G	G	G	
Al			G	G			

Figure 3.39. *Garnets were obtained from $Er_3Al_5O_{12}$, $Gd_3Al_5O_{12}$, $Gd_3Ga_5O_{12}$, $Sm_3Ga_5O_{12}$ and $Nd_3Ga_5O_{12}$ composition. The grey "G" is added in the box as the $Gd_3Al_5O_{12}$ garnet is mixed with very small amount of $GdAlO_3$.*

3.3.4.2 ADL synthesis of other ns−garnets

Stoichiometry *x* in $A_{3+x}B_{5-x}O_{12}$ was set as 0.1 and 0.2 to synthesize the $Er_3Al_5O_{12}$, $Gd_3Ga_5O_{12}$, $Sm_3Ga_5O_{12}$, $Nd_3Ga_5O_{12}$ and $Gd_3Al_5O_{12}$ based non−stoichiometric garnets. The synthesis method was similar to that of their stoichiometric garnets. XRD patterns (**figure 3.40–3.43**) show that pure garnets were obtained for $Er_{3.1}Al_{4.9}O_{12}$, $Gd_{3.1}Ga_{4.9}O_{12}$, $Gd_{3.2}Ga_{4.8}O_{12}$, $Sm_{3.1}Ga_5O_{12}$, and $Sm_{3.2}Ga_{4.8}O_{12}$. Others are mixture of garnet and perovskite. These results open the way to further synthesis of highly non−stoichiometric gadolinium gallium garnet and samarium gallium garnet and to study their potential properties. One thing to be noticed is that, it is quite feasible to further broaden the solid solution of gadolinium gallium garnet and samarium gallium garnet by ADL method or by glass crystallisation method as what have done for ns-YAG. Other samples which can only be made into glass by ADL, for example $Nd_3Al_5O_{12}$, $Sm_3Al_5O_{12}$, $Nd_3Ga_5O_{12}$ glasses, could be synthesized as garnet phase by glass crystallisation method, and it is also possible to obtain their non-stoichiometric garnet by adjusting cationic ratio. Due to the time scale, the further synthesis and characterization work will be developed by Xue FANG also PhD student in our research group.

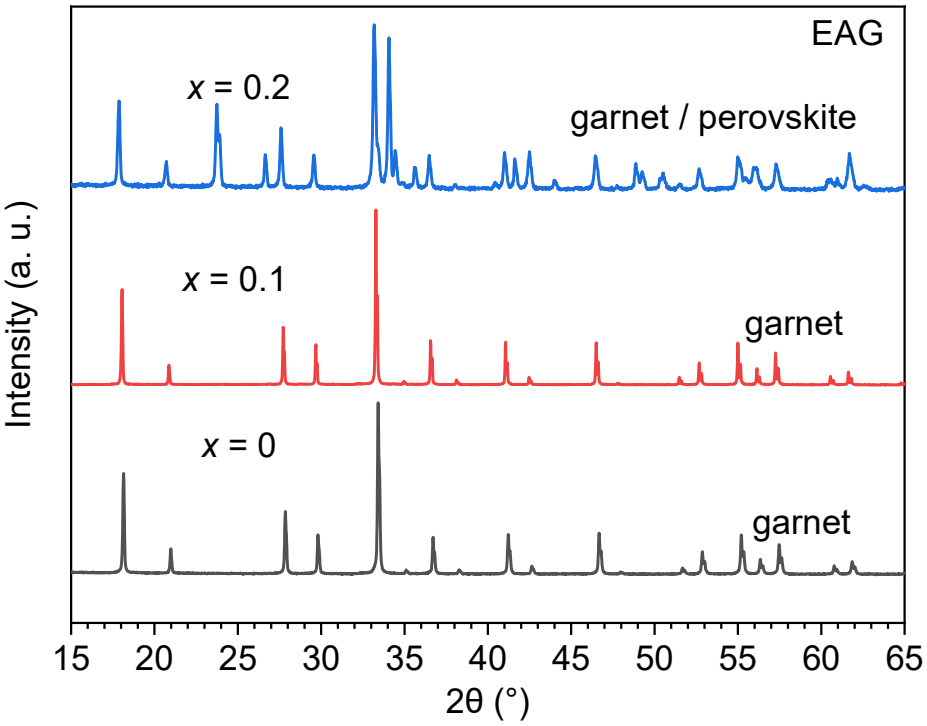

Figure 3.40. *XRD patterns of $Er_{3+x}Al_{5-x}O_{12}$ (x = 0, 0.1 and 0.2) synthesized by ADL.*

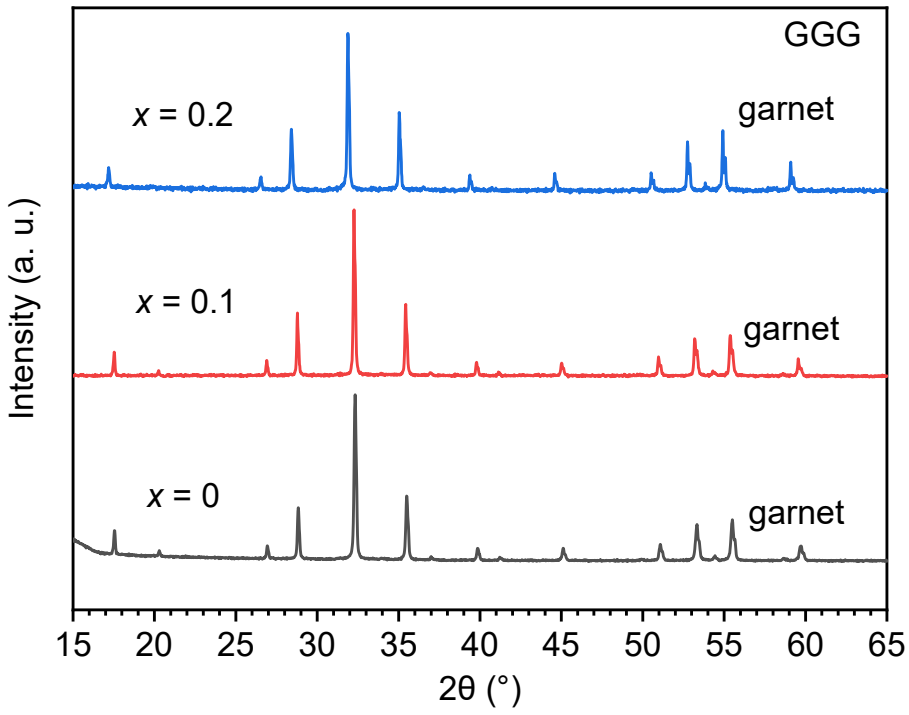

Figure 3.41. *XRD patterns of $Gd_{3+x}Ga_{5-x}O_{12}$ (x = 0, 0.1 and 0.2) synthesized by ADL.*

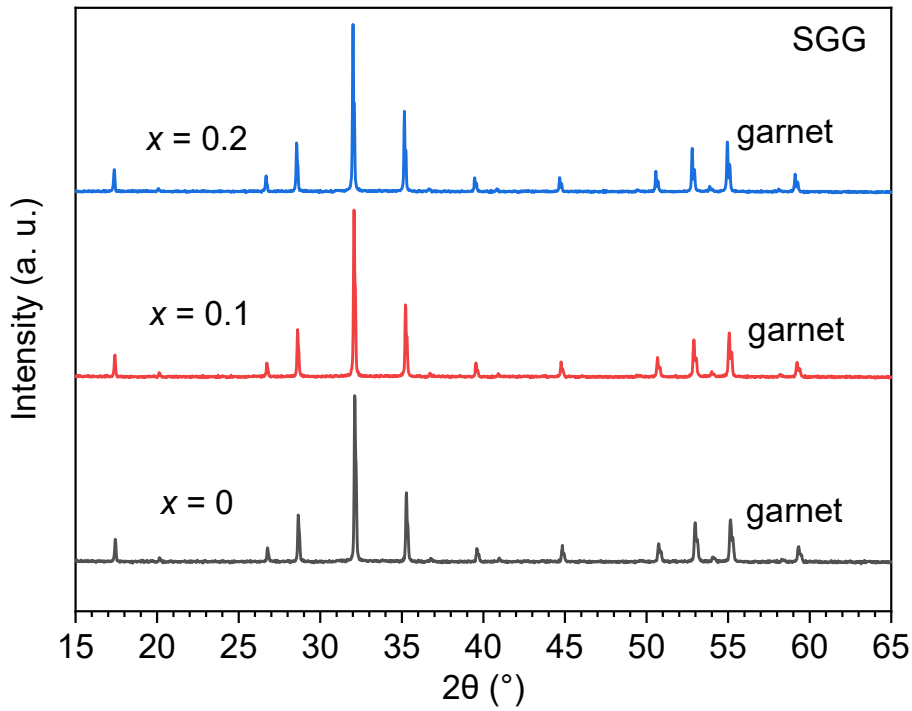

Figure 3.42. *XRD patterns of $Sm_{3+x}Ga_{5-x}O_{12}$ (x = 0, 0.1 and 0.2) synthesized by ADL.*

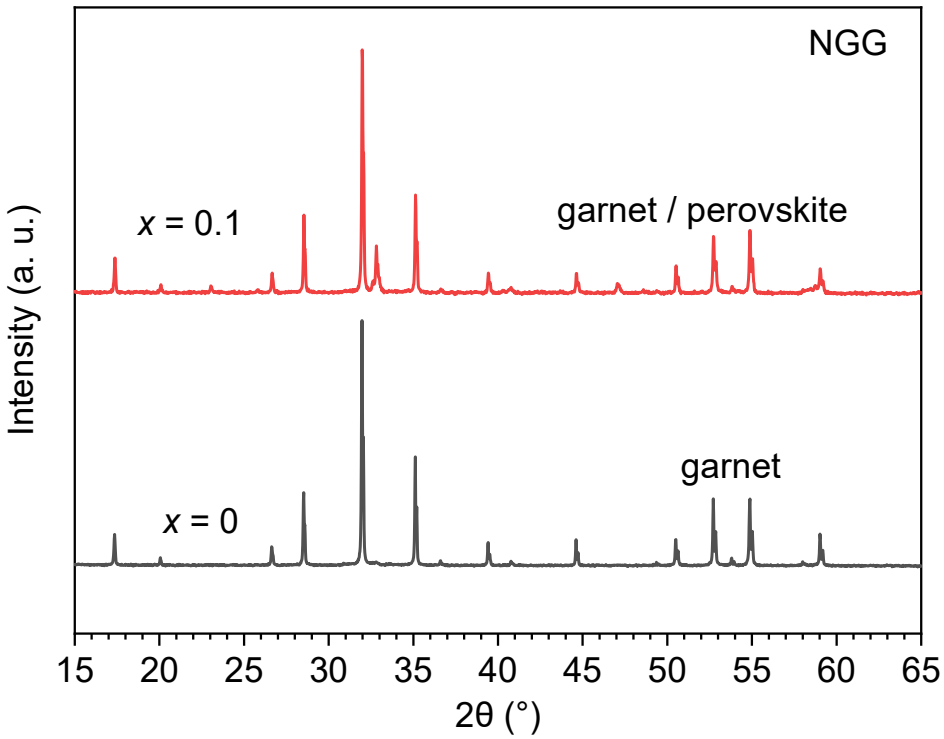

Figure 3.43. *XRD patterns of $Nd_{3+x}Ga_{5-x}O_{12}$ (x = 0 and 0.1) synthesized by ADL.*

Chapter 4

Attempts to synthesise pure YAG glasses

4 Attempts to synthesise pure YAG glasses

4.1 Short review on YAG-based glasses

As presented in the previous chapter, $Y_{3+x}Al_{5-x}O_{12}$ ($0.3 \leq x \leq 0.4$) garnet ceramics were synthesized by full glass crystallisation (GC) method. The glass precursors were prepared by cooling down the sample in oxygen which makes the cooling process faster than in argon. Up to now, $Y_3Al_5O_{12}$ glass without any glass inclusion has not been produced due to the inevitable internal liquid−liquid phase separation and surface crystallisation of eutectic YAP/Al_2O_3[19-21]. This phenomenon is an obstacle for preparing transparent YAG for phosphors, solid state laser and other optical applications. The yttrium aluminum garnet−based nanoceramics obtained by X. Ma *et al.*[10] were synthesized by glass crystallisation method. One of the essential factor for producing the glass precursor is that the Al_2O_3 content is higher than 62.5% (corresponding to $x < 0$) which is the case of $Y_3Al_5O_{12}$. The YAG crystals are embedded in Al_2O_3 crystalline phase with very thin grain boundary, resulting in the excellent transparency of the nanoceramic.

In this work, our yttrium aluminum “glasses” are based on the compositions of stoichiometric YAG and non−stoichiometric YAG. The glass beads were prepared by ADL method. The as-made glass beads look translucent as shown in **figure 4.1**, and their related XRD patterns imply that the glass constituent is dominant in the bead, and diffraction peaks are also present, indicating the existence of crystallized phase, which can be the reason for the translucence of the bead.

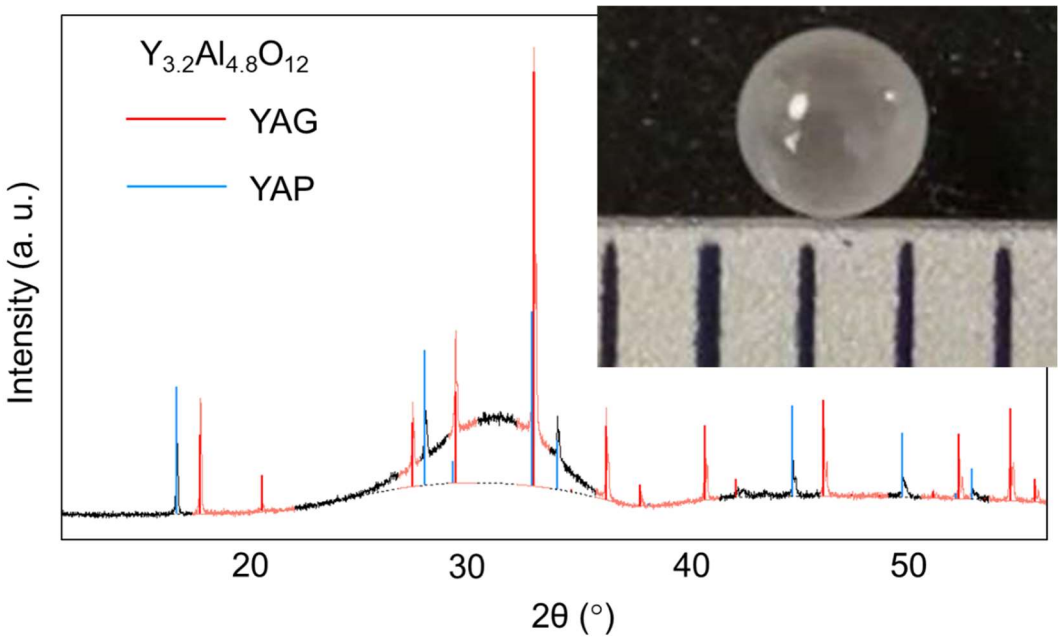

Figure 4.1. *Picture (upper right) and XRD pattern of yttrium aluminum "glass" bead with $Y_{3.2}Al_{4.8}O_{12}$ composition prepared by ADL in argon. The red and blue vertical lines indicate the Bragg position of YAG and YAP.*

4.2 Microstructure and composition of YAG glasses

SEM was conducted for mirror polished $Y_3Al_5O_{12}$ and $Y_{3.2}Al_{4.8}O_{12}$ as-synthesized "glass" beads to observe the spatial distribution of the crystalline phase. **Figure 4.2** shows that in the section across the volume of the glass beads, there are many rounded droplets embedded in the glass matrix with size distributed in the range 1-40 μm, their brightness was close to that of the glass matrix, which was confirmed by the EDS results indicating that the two components have the same composition (within EDS measurements error), as shown in **table 4.1**. This phenomenon may have been caused by liquid-liquid phase separation as reported in many papers[19-21, 57], and commonly called liquid-liquid phase separation.

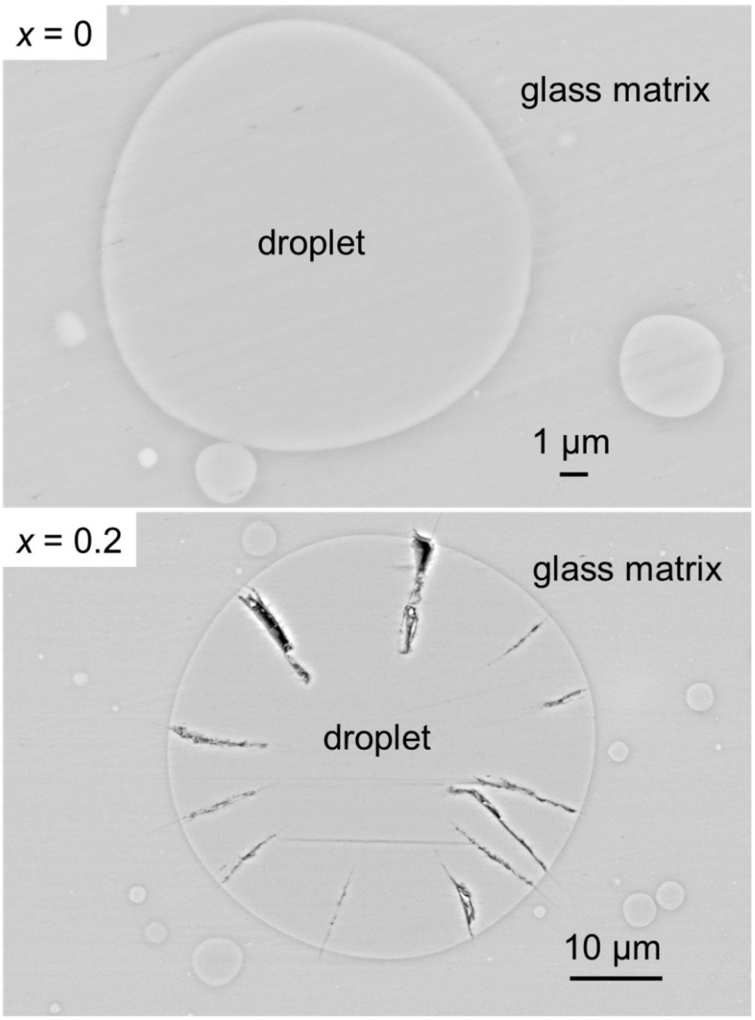

Figure 4.2. *SEM microstructure morphology of the volume section of $Y_3Al_5O_{12}$ (x = 0) and $Y_{3.2}Al_{4.8}O_{12}$ (x = 0.2) glass beads produced by levitation melting in argon.*

Table 4.1 Average atomic concentration from EDS measurement for the droplets and glass matrix of the glass beads with theoretical compositions of $Y_3Al_5O_{12}$ and $Y_{3.2}Al_{4.8}O_{12}$.

area	**$Y_3Al_5O_{12}$**		**$Y_{3.2}Al_{4.8}O_{12}$**	
	Y (at.%)	Al (at.%)	Y (at.%)	Al (at.%)
glass matrix	16.0	24.0	17.0	23.0
droplet	16.0	24.0	17.0	23.0

4.3 Crystallinity of droplets studied by Raman

In the work of S. Aasland and P. F. McMillan in 1994[21], a similar phenomenon in supercooled Y_2O_3−Al_2O_3 melt was observed. Their glass matrix and droplets showed the same composition and are both amorphous. This phenomenon was interpreted as density–driven and was called liquid−liquid phase separation or polyamorphism. Such phase separation is common in metallic liquids and also takes place in water[130], SiO_2[131] and GeO_2[132]. Later, in 2002, K. Nagashio *et al*[19]. published a work on Y_2O_3−Al_2O_3 glass and declared that the droplets in their YAG glass are crystallized and contain YAG nanocrystals. Further in 2008, L. B. Skinner *et al*[133], found that the droplets in their work were also crystallized by indexing the diffraction peaks of the glass sample with a pure YAG diffraction pattern. **Figure 4.3** shows a pattern recorded by optical microscopy of $Y_3Al_5O_{12}$ glass prepared by ADL from their work, showing a similar morphology as observed in this work.

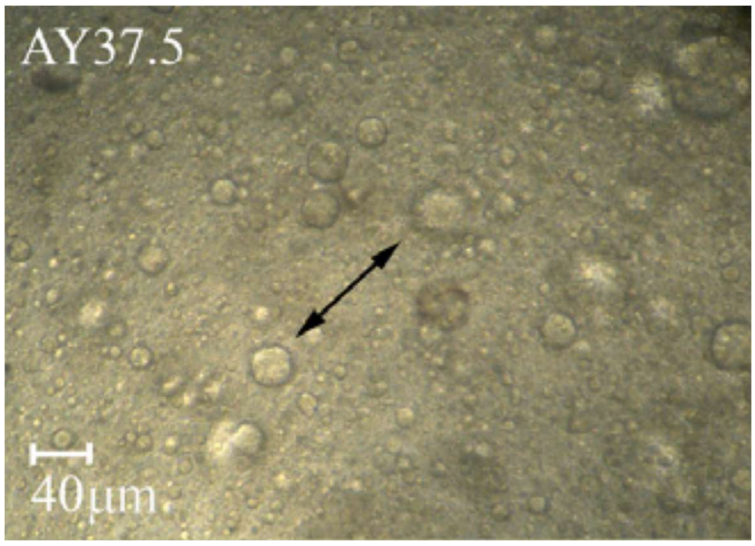

***Figure 4.3**. Optical microscopy pattern of sections of the spheres in the YAG composition (corresponding to x = 0), produced by L. B. Skinner, et al[133].*

As the crystallinity of the droplets in YAG glass is debatable, in our work, Raman mappings were performed to determine if they are amorphous or crystalline. The measurement was conducted under 514 nm green laser operating at 50 mW (the instrumental information is stated in Raman spectroscopy along with the redrawn depicted Raman principle diagram). The $Y_{3+x}Al_{5-x}O_{12}$ (x = 0 and 0.2) glass beads prepared by ADL in argon indicate that the glass matrix shows only broad Raman features (**figure 4.4**), which are assignable to a fully amorphous material. However, no evidence for the occurrence of two distinct amorphous phases (*i.e*. of polyamorphism) could be noticed. Instead, the droplets exhibit sharp Raman

features typical of crystalline YAG (compared to the reference spectra collected from beads of fully crystallized YAG), implying that the droplets could be YAG nanocrystals. These results are similar to previous report stating that the droplet has YAG crystallinity confirmed by convergent beam electron diffraction (CBED)[134].

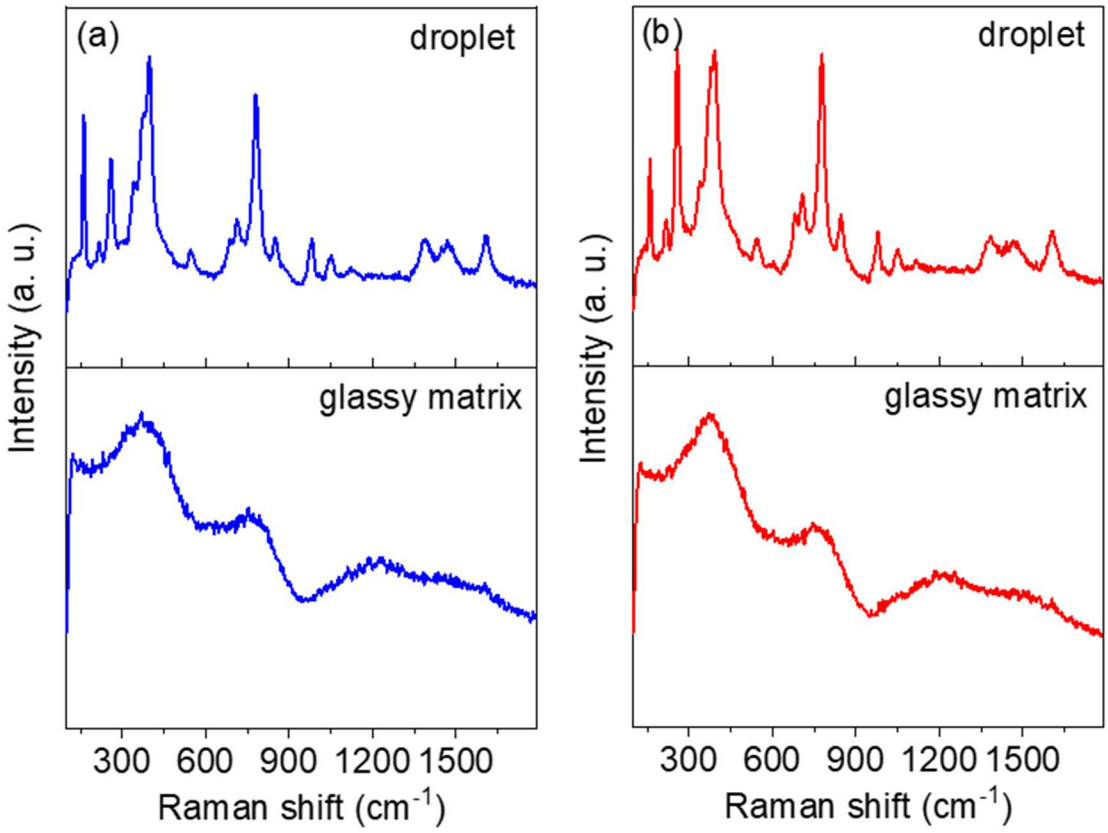

Figure 4.4. *Raman spectra of glassy matrix and droplets of 9 mg x = 0 (a) and 0.2 (b) glass beads quenched in Ar.*

Figure 4.5 shows that Raman peaks of pure x = 0.2 garnet are broader than that of pure x = 0 garnet, which may indicate that x = 0.2 garnet is more structurally disordered. In both x = 0 and 0.2 glasses, Raman peaks in the droplets are broader than those of their respective pure garnets, again possibly hinting at a higher disorder or the precipitation of this phase as nanocrystals. The big droplets in both x = 0 and 0.2 glass, shown in the Raman mapping image in **figure 4.6**, tend to be brighter than smaller ones in the Raman mappings; two possibilities can explain it: (1) smaller droplets have poorer crystallinity than bigger ones; (2) the Raman spectra collected in those regions consisted of a mixture of glass and droplet signals, due to the limited spatial resolution of the focused laser beam.

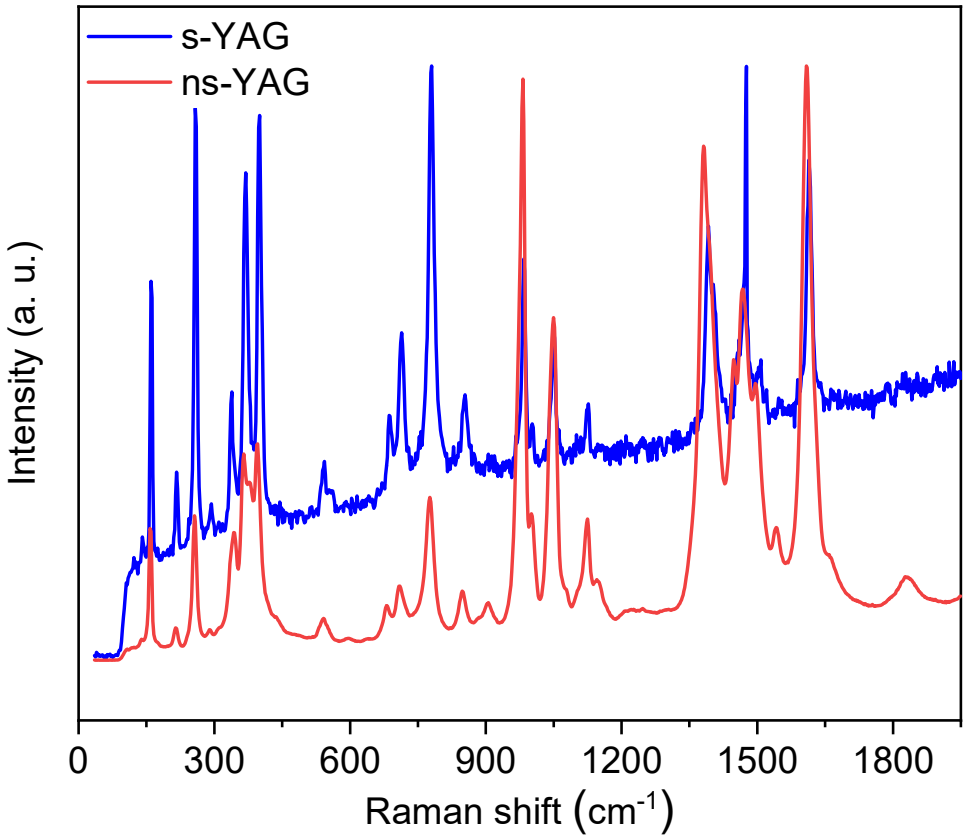

Figure 4.5. *Raman spectra of fully crystallized s- and ns-YAGs by ADL in argon.*

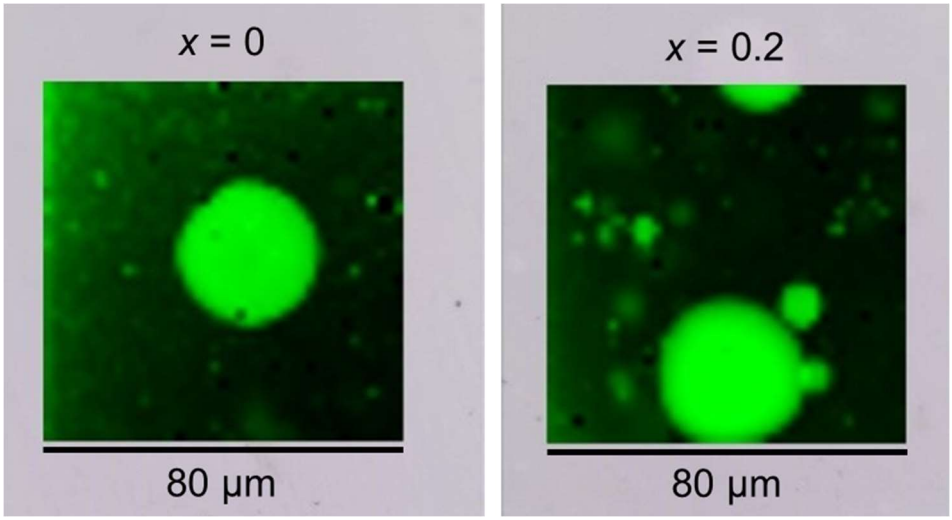

Figure 4.6. *Raman mapping of 9 mg x = 0 and 0.2 glass prepared by ADL in argon. The nearly round green spots correspond to the droplets under SEM observation and the grey background is a reflected-light microscope picture of a polished glass bead. A total of 1681 Raman spectra was recorded every 2 µm along the two dimensions of the 80 × 80 µm square (acquisition time at each point: 5 s); they were processed using the spectra shown in figure 4.5 as reference for the fully amorphous matrix and the crystallized droplets.*

4.4 Attempts to eliminate droplets from our YAG glass samples

The approach we used to eliminate the droplets in our YAG samples prepared by ADL was to synthesize pure YAG glass. In the previous section, cooling experiments of $Y_{3.2}Al_{4.8}O_{12}$ determined that glass, YAG and YAP/Al_2O_3 form respectively under different cooling rates, and that using less dense levitation gas can effectively enhance the cooling rate. Therefore we were interested to study the phase compositions of these $Y_3Al_5O_{12}$ and $Y_{3.2}Al_{4.8}O_{12}$ glasses levitation synthesized in argon, oxygen and helium, and look for the glass bead with least crystals. XRD patterns of these glasses prepared in different levitation gases are shown in **figure 4.7**, they indicate that as levitation gas was changed from argon to oxygen and finally helium, most of the diffraction peaks from the crystalline phase disappear or decrease in intensity, especially for that of YAG phase which are highlighted by the green triangles in the figure. Finally, only YAP phase exists in the glass bead, and obviously its content in $Y_3A_5O_{12}$ composition is lower than in $Y_{3.2}Al_{4.8}O_{12}$ composition. According to the order of cooling rate of different phase, it makes sense that YAG disappears before YAP when cooling rate was enhanced, the key to make a real YAG glass by ADL method could point to further increasing the cooling rate.

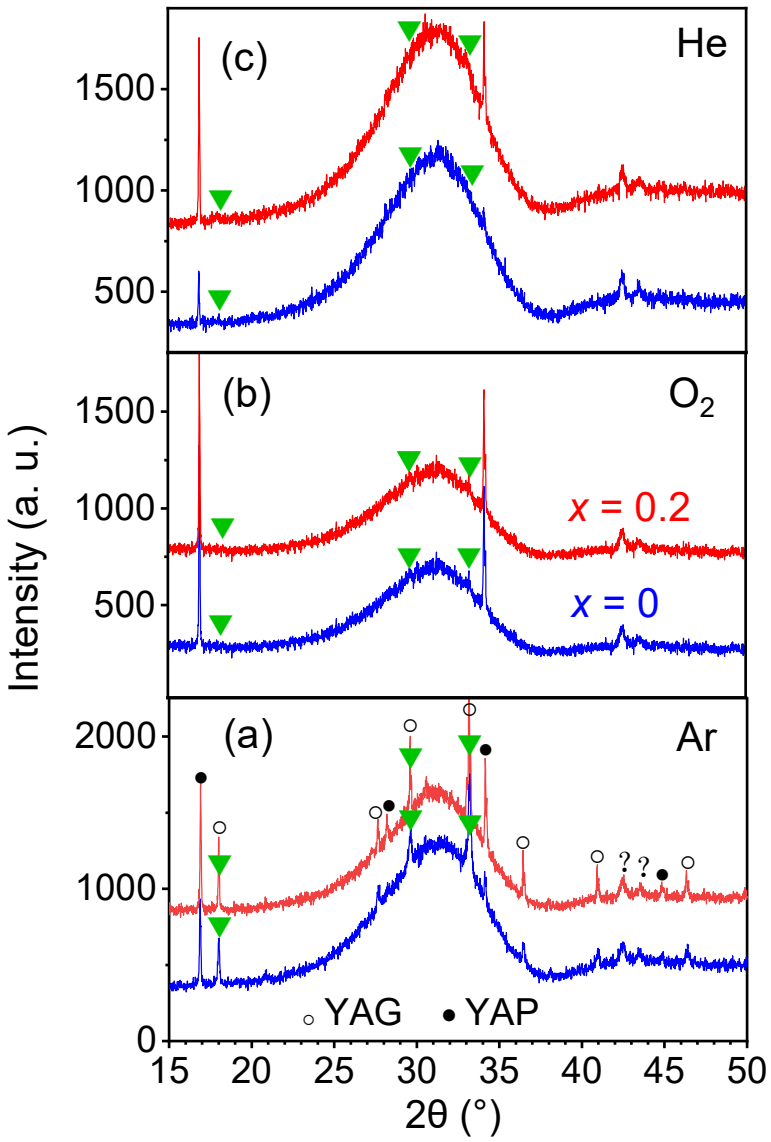

Figure 4.7. *XRD patterns of 9 mg x = 0 and 0.2 glass bead synthesized by ADL under Ar, O_2, and He. The green rectangles in each plot show the diminishing process of YAG phase. The two peaks labeled by question marks in 2θ 41-44° in (a) came from the knife installed in the diffractometer used to avoid unexpected X-ray scattering, they could belong to the blend fixed in the diffractometer for avoiding X-ray scattering during the XRD measurement.*

We were then interested to observed the morphology of the glass synthesized in helium, Fortunately. although the sample bead vibrated violently when it was levitated by helium and frequently touched with nozzle, leading to fully crystallisation, with many attempts, we were able to obtain $Y_3Al_5O_{12}$ glass, but not for $Y_{3.2}Al_{4.8}O_{12}$ glass as its vibration was more serious. The $Y_3Al_5O_{12}$ glass prepared in helium was mirror polished and observed by SEM (**figure 4.8**), one can clearly see in this glass sample, the droplets have been substantially

removed, and only one small (labeled by the green arrow) spot which could the residual droplet was observed, this implies high cooling rate makes YAG glass accessible.

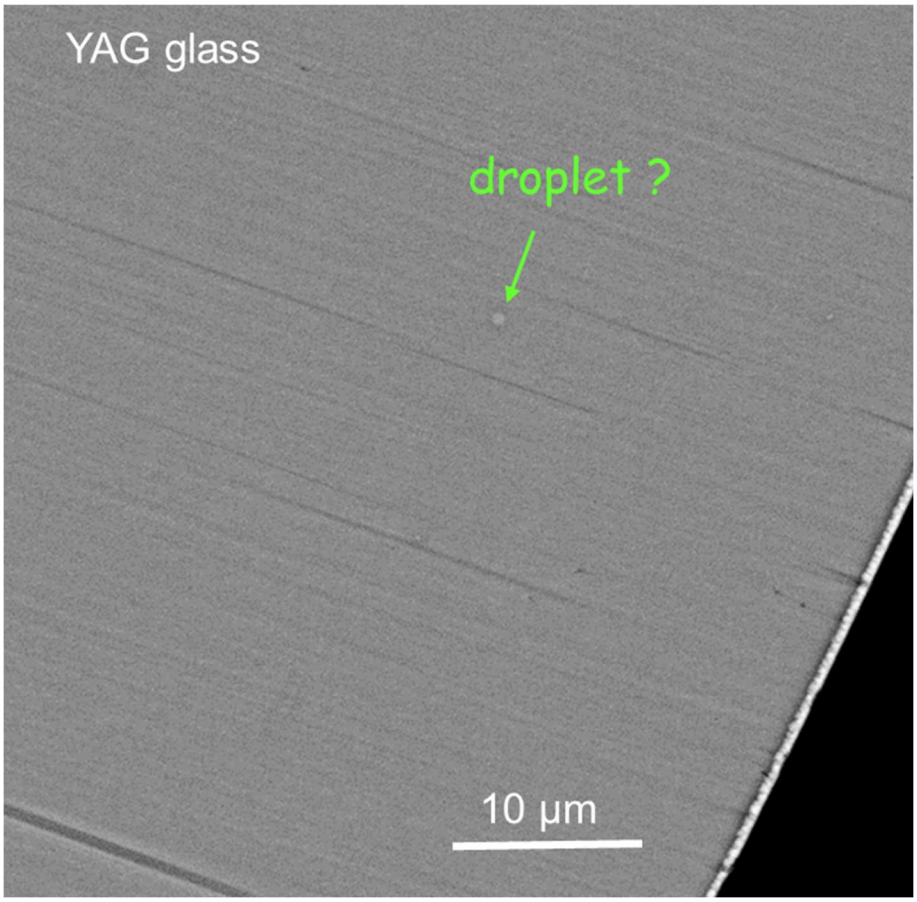

Figure 4.8. *SEM microstructure of 9 mg $Y_3Al_5O_{12}$ glass prepared by ADL in helium. The green arrow points out the doubtful droplet.*

General conclusion

General conclusion

The initial aim of this work was to explore the synthesis of new compounds by glass-crystallisation, starting with some hypothetical target compounds including $Y_2Al_3O_{7.5}$ as a possible melilite structure (as for $La_2Ga_3O_{7.5}$ whose work has been published by Fan *et al*. in 2020[14]). This led to the unexpected appearance of garnet phase with $Y_2Al_3O_{7.5}$ composition. Therefore, the following main objectives of this work was to (**1**) synthesize highly non-stoichiometric yttrium aluminum garnet (YAG) polycrystalline in $Y_{3+x}Al_{5-x}O_{12}$ (x > 0) system by introducing Y_{Al16a} defects into the garnet lattice; (**2**) make the solid solution range as broad as possible via two different synthesis approaches (direct crystallisation from the melt and full glass crystallisation); (**3**) study the effect of Y_{Al16a} defect on the luminescence properties of stoichiometric (s-) and non-stoichiometric (ns-) YAGs with different dopings.

SYNTHESIS and RESULTS

$Y_2Al_3O_{7.5}$ was first synthesized by aerodynamic levitation (ADL) approach, as its resulted phase was not the expected melilite, but the unexpected garnet ($Y_{3.2}Al_{4.8}O_{12}$), the attempt at synthesizing non-stoichiometric YAG was expanded to other compositions: $Y_{3+x}Al_{5-x}O_{12}$ ($0 \leq x < 0.3$). These samples were finally synthesized as garnet by direct crystallisation from melt using ADL, argon was used as carrier gas. The flaw was that $x = 0.3$ was not isolated as garnet, but was a mixture of $Y_3Al_5O_{12}$ (YAG), $YAlO_3$ perovskite (YAP) and α-Al_2O_3 corundum.

Synthesis conditions of $x = 0.2$ YAG were studied by a series of cooling experiments on sample beads with different masses. Samples beads were cooled down by directly shutting down the lasers after melting. The YAG phase was found accessible under 400-550 °C s^{-1} (in 2100-1300 °C range), cooling rate. Cooling rates higher than 550 °C s^{-1} and lower than 400 °C s^{-1} respectively led to the formation of glass and YAP/Al_2O_3 mixture.

The cooling experiments on $x = 0.2$ ($Y_{3.2}Al_{4.8}O_{12}$) gave us a hint that it is possible to synthesize $x \geq 0.3$ YAG compounds by other methods. For example, synthesizing glass, under higher cooling rate, as the precursor for glass-crystallisation, the higher cooling rate can be achieved by using levitation gas less dense than argon, for example oxygen or even helium. After several rounds of experiments, oxygen was found to be more suitable than helium to stabilize $0.3 \leq x \leq 0.4$ beads, preventing the sample from touching with nozzle and avoiding heterogeneous crystallisation. It was found that the $0.3 \leq x \leq 0.4$ samples

cannot be obtained as garnet by this non-equilibrium synthesis method, however they can be prepared as glass samples. These glass samples were subsequently heated at 1100 C in a furnace, and the resulting ceramics were determined as garnet by XRD. The x = 0.45 sample could neither be synthesized into garnet nor into glass

Although M. Gervais *et al*.[27] stated that they obtained $Y_{3+x}Al_{5-x}O_{12}$ garnet in the $0 \leq x \leq 0.4$ range, the lattice parameter a they obtained changed from 12.008 Å to 12.052 Å, behaving much gentler than the lattice change in this work (12.00710 (1) Å for x = 0 and 12.13542(1) Å for x = 0.4). L. Zhu *et al*.[29] reported that the composition x = 0.13 which hit the ceiling of the $Y_{3+3x}Al_5O_{12+4.5x}$ solid solution range has a lattice a of 12.0565 (9) Å. Something unexpected in their work is that x = 0 composition ($Y_3Al_5O_{12}$) has lattice a of 12.0253 (4) Å which is uncommonly large. The largest lattice a of the two respective previous work is approximately equal to the value 12.049939(6) Å of x = 0.15 composition in $Y_{3+x}Al_{5-x}O_{12}$ of our work. The following table makes the comparison between the two previous work and our study. The difference in the variation of lattice parameter of YAGs in these three works may indicate that in the two previously published works there was large compositional deviation from their actual to theoretical compositions.

comparison of lattice a evolution between this work and other two published works					
projects	***a_1 (Å)***	***x_1***	***a_2 (Å)***	***x_2***	***actual x_2***
M. Gervais *et al*. [27]	12.008	0	12.052	0.4	~ 0.15
L. Zhu *et al*. [29]	12.0253 (4)	0	12.0565 (9)	0.23	~ 0.15
This work	12.00710 (1)	0	12.13542 (1)	0.4	0.4

THERMAL STABILITY of NS-YAGs

Thermal stability of x =0.2 ($Y_{3.2}Al_{4.8}O_{12}$) and x = 0.4 ($Y_{3.4}Al_{4.6}O_{12}$) ns-YAGs was studied by VT-XRD with maximum heating temperature of 1600 °C. Both ns-YAGs started to decompose at 1350 °C. Indeed, at the next heating stage, *i.e*. at 1400 °C, the proportion of YAP impurity was higher than in x = 0.2, as implied by the much intensive diffraction peaks of YAP. The final diffraction data (1600 °C) indicated that x =0.2 finally decomposed into YAG, YAM and YAP, and x = 0.4 decomposed into YAG and YAP, these results agree with ex-situ thermal decomposition experiments where x = 0.2 and 0.4 ns-YAGs underwent

heating at 1600 °C for 12h. The ns-YAGs were determined as metastable phases, given that their decomposition temperature (1350°C) is lower than the typical YAG synthesis temperature (1400-1700 °C)[45], it is understandable for their early unachieved synthesis by solid-state reaction at 1500 °C in this work.

AVERAGE and LOCAL STRUCTURE of NS- YAG

Average structure

Rietveld structural refinements on high-resolution synchrotron X-ray diffraction data determined that the excess of Y^{3+} in ns-YAG enter the octahedral sites (Wyckoff site 16a) which are only occupied by Al^{3+} in s-YAG, enlarge the bond lengths of octahedra and causing the lattice parameter to increase in a linear trend within $0 \leq x \leq 0.4$. The Y_{Al16a} percentage in the garnet structure increases in a linear trend as expected from the nominal composition, confirming that Y_{Al16} is the only lattice defect formed in ns-YAG structure and agrees with the conclusion from the atomistic calculation of Patel *et al.*[28], that due to the lower defect energy, Y_{Al16a} rather than Y_{Al24d} defect is favored in ns-YAG structure. Impressively, the maximum nonstoichiometry concentration in our work reaches 20% of the octahedral sites occupied by Y^{3+} (for $x = 0.4$), with more than one order of magnitude larger than in their synthesis work.

Local structure

The local structure of $Y_{3+x}Al_{5-x}O_{12}$ ($x = 0$, 0.2 and 0.4) YAGs were first studied by observing a very thin area (with thickness comprising of 6-12 cells) of the ion polished sample foil at an atomic scale using STEM-HAADF. The presence of Y^{3+} at 16a sites was detected in $x = 0.2$ and 0.4 ns-YAGs, clearly indicated by an increase of the Z-contrast signal. This result agrees with simulated STEM-HAADF images. The peak intensities of the 16a atomic columns in peak profile, which was extracted from STEM-HAADF image, for $x = 0.2$ and 0.4 ns-YAGs, are not constant in comparison with that for $x = 0$ s-YAG, demonstrating that the Y^{3+} distribution at 16a sites is random.

^{89}Y solid state NMR was performed on 0.1 at.% Gd-doped $Y_{3+x}Al_{5-x}O_{12}$ ($x = 0$, 0.1, 0.2, 0.25, 0.3 and 0.4) ceramics. The typical YO_8 chemical shift was observed at around 215 ppm but most importantly a new chemical shift at around 410 ppm, which was attributed to 6-coordinate Y, was clearly observed as well. As x increases, the intensity of the YO_6 peak appeared more and more intense and the YO_8 peak broadened. Simulation of the YO_8 peak indicates that, for $x > 0$ ns-YAGs, the YO_8 is comprised of more than one component.

In x = 0.1 and 0.2 ns-YAGs, the YO_8 peak is composed of two components. These are the first component which involves pure AlO_6 second coordination effects, and the second component with five AlO_6 and one YO_6. The third component was introduced for x = 0.25, 0.3 and 0.4 ns-YAG which contains four AlO_6 and two YO_6 second coordination effects. Peak intensity of the first component decreases and that of the second and the third components intensities increase as x increases, the variation of the intensity of the component indicates the proportion change of a specific component. DFT calculation of models containing Y defects in the ns–YAG structure, were consistent with NMR results.

EXAFS determines the location of 6-coordinate Y by investigating its neighboring cations. NMR detected the chemical shift signal from 6-coordinate Y in $Y_{3+x}Al_{5-x}O_{12}$ ($0 < x \leq 0.4$) garnet, which is expected for non–stoichiometric YAG and has never been found in stoichiometric YAG.

RARE-EARTH DOPED NON-STOICHIOMETRIC YAGs

$Y_3Al_5O_{12}$ and $Y_{3.2}Al_{4.8}O_{12}$ were doped with 20 at.% Yb-n at.% Er (n = 0.5, 1, and 2) to: **(1)** find the optimal Er doping level for luminescence measurements; **(2)** study the difference in luminescence properties between $Y_3Al_5O_{12}$ and $Y_{3.2}Al_{4.8}O_{12}$; **(3)** determine how nonstoichiometry affects the luminescence performances when the same doping is introduced to s- and ns-YAG hosts.

LOCALISATION of Yb/Er DOPANTS

20 at.% Yb-2 at.% Er co-doped $Y_{3+x}Al_{5-x}O_{12}$ (x = 0, 0.2 and 0.3) (*i.e*. $Yb_{0.6}Er_{0.06}Y_{2.34}Al_5O_{12}$, $Yb_{0.64}Er_{0.064}Y_{2.496}Al_{4.8}O_{12}$ and $Yb_{0.66}Er_{0.066}Y_{2.574}Al_{4.7}O_{12}$) were synthesized by direct crystallisation (for x = 0 and 0.2, in argon) or glass crystallisation (for x = 0.3, glass precursor was prepared in oxygen) method. The presence of Yb^{3+} and Er^{3+} substitution ions did not change the crystal structure of s- and ns-YAGs, but caused the lattice parameter to decrease slightly in comparison with the corresponding non-doped YAGs. Via Rietveld refinements on synchrotron X-ray powder diffraction data, taking advantage of the good scattering contrast between Yb^{3+} and Y^{3+}, Yb^{3+} occupation is traceable in the refinement. Yb^{3+}/Er^{3+} ions in the $Y_3Al_5O_{12}$ crystal structure were found to substitute for Y^{3+} ions and sitting at the 8-coordinate sites, however the two rare-earth ions in $Y_{3.2}Al_{4.8}O_{12}$ and $Y_{3.3}Al_{4.7}O_{12}$ occupy not only the 8-coordinate but also 6-coordinate sites. As a function of nonstoichiometry x, the concentration of 6-coordinate Yb^{3+}/Er^{3+} ions linearly increase while the concentration of 8-coordinate Yb^{3+}/Er^{3+} decreases, this helps to create a new

bonding path between 6- and 8- coordinate ions in non-stoichiometric YAGs in comparison with stoichiometric YAG.

LUMINESCENCE PROPERTIES

The measured samples at this stage are powdered, and their luminescence properties were compared with that of ceramic disks of YAGs. The results indicated that increasing the Er doping level from 0.5 at.% to 1 at.% led to improved emission properties for both $Y_3Al_5O_{12}$ and $Y_{3.2}Al_{4.8}O_{12}$, the increasing concentration of emission centers make the energy transfer more efficient in some way. Further increasing Er doping to 2 at.% however caused the emission intensities to deteriorate, but still better than the case with 0.5 at.% Er. The drop of emission intensity, when Er^{3+} concentration increases from 1 at.% to 2 at.%, is ascribed to the concentration quenching caused by numerous Er^{3+} activators. Under the three doping levels, $Y_{3.2}Al_{4.8}O_{12}$ emission spectra showed different distribution of frequencies compared to s-YAG.

The newly created $Yb^{3+}\rightarrow Er^{3+}$ energy transfer paths from Yb(VIII) to Er(VI) and from Yb(VI) to Er(VIII) in ns-YAG produced a metastable lifetime τ_2 and also made the fine structure of emission spectra differ from that of s-YAG, leading to the green emission color of ns-YAG, differ from the yellowish color of s-YAG. Changing the Er^{3+} doping level did not alter the emission color of s-YAG, but altered slightly that of ns-YAG in the green region. The luminescence process was developed in a two-photon involved upconversion mechanism.

IMHOMOGENEITY OF Yb/Er DISTRIBUTION

Luminescence study on 20 at.% Yb–*n* at.% Er (*n* = 0.5, 1 and 2) doped s– and ns–YAG ceramic disks indicate that, when changing the laser focused area, the emission performance of s–YAG stays the same, while it varies much in ns–YAG. This could be attributed to the inhomogeneous distribution of Yb/Er the microscale area in the ns–YAG beads, this will be further confirmed by Raman, SEM and microprobe analysis.

OTHER RARE EARTH DOPINGS

The luminescence properties of Ce^{3+}, Dy^{3+} and Mn^{4+} single doped s- and ns-YAGs from single-cycle measurement also showed the two garnet have different frequencies distribution, implying the crystallinity change in the garnet structure caused by nonstoichiometry.

Rare earth (*RE*) ions can enter the B site (*16a*) of ns-YAGs, while when they are larger than Y^{3+}, they prefer the A site (*24c*). This opens the way to other garnet compounds.

OTHER NONSTOICHIOMETRIC GARNETS

Nonstoichiometry in the YAG structure has been expanded to other garnet compounds in this work. For example, $Er_{3.1}Al_{4.9}O_{12}$, $Gd_{3.1}Ga_{4.9}O_{12}$, $Gd_{3.2}Ga_{4.8}O_{12}$, $Sm_{3.1}Ga_5O_{12}$, and $Sm_{3.2}Ga_{4.8}O_{12}$, garnets have been synthesized by ADL. Their structural and optical properties, which deviate from the stoichiometric garnets, will be explored by Xue FANG who is studying these compositions in her PhD work.

Perspectives

Perspectives

If a solution is found to further enhance the cooling rate of $Y_3Al_5O_{12}$ composition, YAG glass, without involving liquid-liquid phase separation in the volume of the sample and without surface crystallisation, could be fabricated. Therefore possible nice optical and physical properties could be explored. This might also be applied to ns-YAG glass compositions (x>0.4) as well.

By taking advantage of direct–crystallisation and glass–crystallisation with the rapid melt quenching rates developed for the synthesis work of ns-YAG, the non-stoichiometric $Gd_{3+x}Ga_{5-x}O_{12}$ and $Sm_{3+x}Ga_{5-x}O_{12}$ garnets, whose nonstoichiometry has reached x = 0.2 by direct crystallisation, are supposed to be developed with even higher nonstoichiometry levels.

Non-stoichiometric $Nd_{3+x}Al_{5-x}O_{12}$, $Sm_{3+x}Al_{5-x}O_{12}$, $Nd_{3+x}Ga_{5-x}O_{12}$ garnets could be synthesized, starting from their glass precursors, by glass-crystallisation method. It may be possible to make these into transparent ceramics thanks to their good glass forming ability.

Furthermore, it is worth finding solutions to enhance the quenching rate of the samples with $A_3B_5O_{12}$ compositions which were neither garnet nor glass from ADL synthesis, *i. e*. $Y_3Al_5O_{12}$ (YIG), to synthesize them as glass, for example using oxygen or helium as carrier gas.

Recently Wisniewski *et al*.[135] proposed that it would be possible to synthesize single crystals by ADL if the conditions for flash crystallisation are supplied. Following this idea, which was demonstrated for the La_2O_3-Ga_2O_3 system, it may be possible to synthesize ns-YAG single crystals from ADL. By the same logic, it will facilitate single crystal synthesis for other garnets.

EXAFS local structure characterization has shown it sensitivity to the nonstoichiometry in YAGs, it could be used to analyze other garnet compositions, such as GGG ($Gd_3Ga_5O_{12}$) and GAG ($Gd_3Al_5O_{12}$) which are not possible to study by neutron diffraction or NMR spectroscopy.

Changes in emission spectra (emission color) have impact on optical applications, which may lead to new possibilities for other YAG-type hosts whose emission colors are usually controlled by dopant identity rather than host stoichiometry. Other persistent luminescent

compositions, such as $Y_3Al_2Ga_3O_{12}$ (YAGG) and $Gd_3Al_2Ga_3O_{12}$ (GAGG), could be developed into non-stoichiometric compounds, leading to interesting applications.

Garnets-like $Gd_{3+x}Ga_{5-x}O_{12}$ and $Sm_{3+x}Ga_{5-x}O_{12}$ can be developed with nonstoichiometry levels higher than $x = 0.2$ by direct crystallisation from the melt and glass crystallisation methods. Non-stoichiometric garnets starting from $Nd_3Al_5O_{12}$, $Sm_3Al_5O_{12}$ and $Nd_3Ga_5O_{12}$ glasses can be developed by glass crystallisation method, and may be made into transparent ceramics. Also, it appears worth enhancing the quenching rate of compositions which were neither garnet nor glass from ADL synthesis, for example using oxygen or helium as carrier gas.

Appendix

Appendix

A part – Techniques

Aerodynamic Levitation (ADL)

The ADL instrument works at the situation: the two vertical parallel CO_2 lasers heat the sample (0.7-3.5 mm in diameter) which is levitated by gas jet and floats above the nozzle. The temperature of the sample is detected by the pyrometer by sensing the radiation emitted from the sample. There are three main advantages of this technique: 1) the sample can be heated in a broad temperature range (up to 3000 °C); 2) the gas jet protects the sample from contamination or heterogeneous crystallisation and provide a suitable gaseous environment demanded for different compounds; 3) the synthesis is under real-time control and the deep cooling process is accessible to produce glass or other compounds under rapid cooling, *e.g.*, glass ceramic and metastable ceramic.

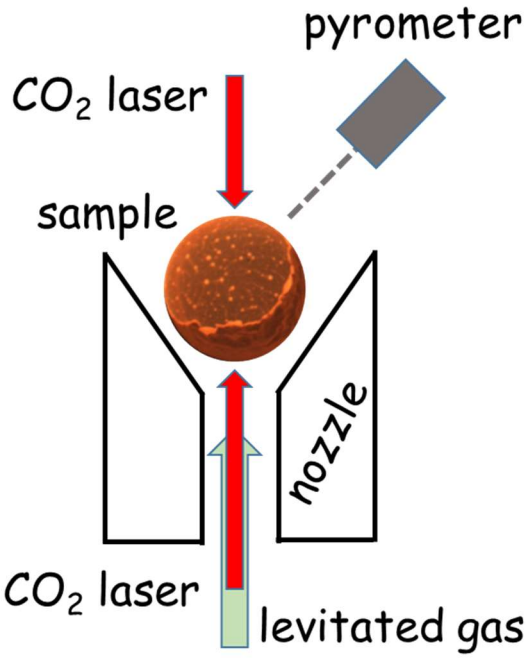

Figure A1. *Schematic diagram of the synthesis process by ADL.*

Cooling experiment conducted by ADL

The cooling experiment mainly depends on two parts of laser heating and cooling process recording, the corresponding process are shown below:

(1) Launch software **Manual Laser** and increasing laser power to heat the sample to aimed laser power/temperature;

(2) Launch software **3Voies** and connect it with **Manal Laser**;

(3) **3Voies** performs cooling process by;

(4) **3Voies** records time–temperature cooling curve and corresponding time–temperature data.

(5) Analysis of crystallisation temperature and cooling rate, *etc*.

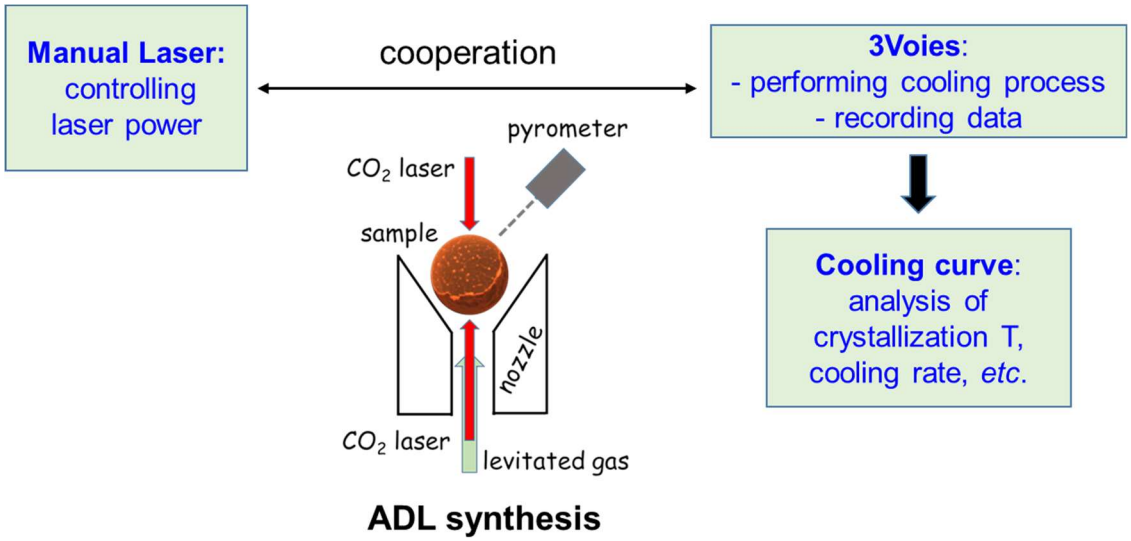

Figure A2. *Schematic diagram of cooling experiment by combining laser heating and data recording processes.*

Room-temperature X-ray Powder Diffraction (RT-XRPD or RT-XRD)

The RT-XRD measurement was performed by Bruker D8 Advance. Samples were ground into fine powers and dropped on the Silicon sample holder before the measurement. The recorded XRD data were used for phase checking.

In an X-ray diffraction experiment, the sample is placed at the center of the diffractometer and between the X-ray tube and detector. When diffraction takes place, the X-rays emitted from the X-ray tube interact with the electrons surrounding the atoms in the sample, its energy is absorbed by the electrons and re-emitted in an elastic scattering way. In a crystal, the atoms are arranged in repeating way on planes, the distance between every two planes are defined as the same. Since the wavelength of the beam is similar to the distance between

the atoms, the distance (*d*) between two atomic planes can be calculated. During the measurement, the X-ray tube and the detector move in a synchronized way, therefore the angle between the incident and the scattered beams is always twice that of diffraction angle (*theta, θ*), the side opposite to the theta angle is one half the length of wavelength λ. The distance between two atomic planes is the hypotenuse of the triangle, therefor the atomic distance d can be calculated through $sin\theta = \lambda/2d$ *or* $n\lambda = 2dsin\theta$, which is called Bragg's law. As the diffraction angle θ changes the, a XRD pattern is generated and provides structural information, *i.e.*, crystal size, lattice strain, chemical composition, state of ordering, *etc*.

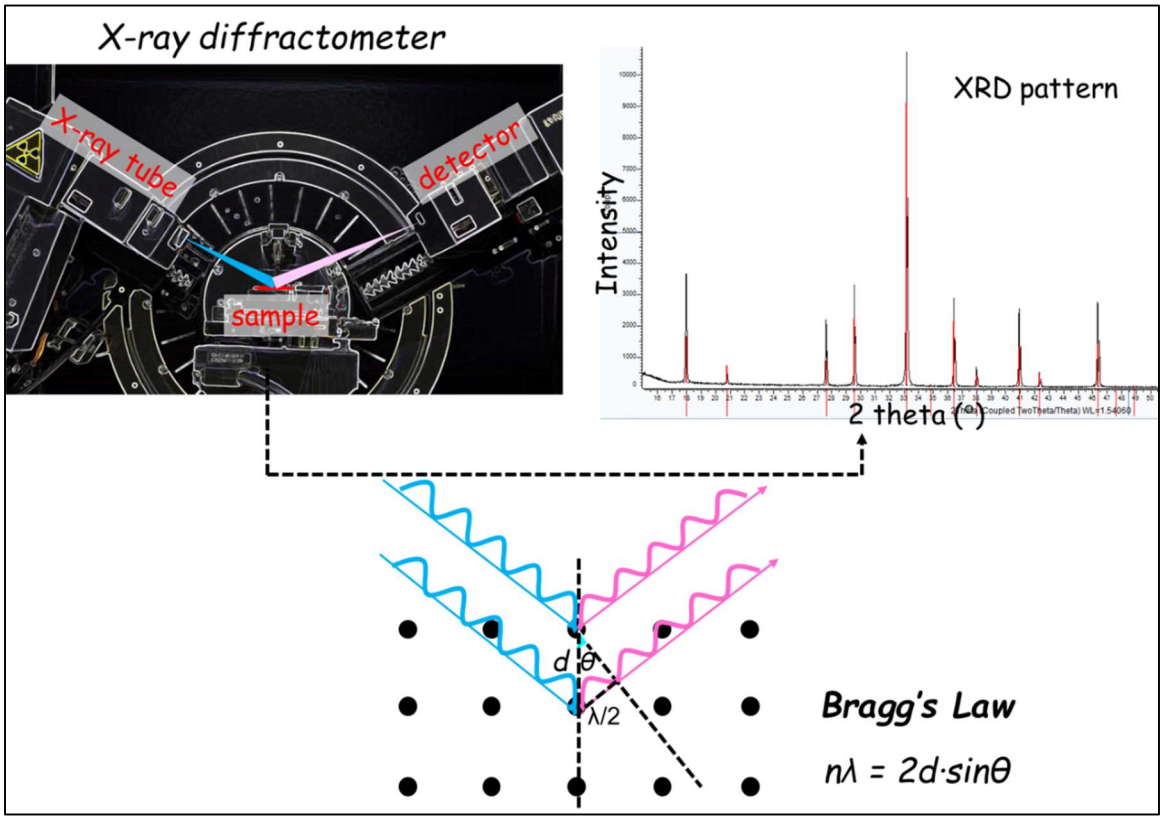

Figure A3. *Schematic of the geometry of the laboratory XRD diffractometer, it works under Bragg's law and recording an XRD pattern.*

Variable Temperature–X-ray powder diffraction (VT-XRD)

The HTK16 (Anton Paar) furnace was equipped with Bruker D8 Advance diffractometer, it allowed following the evolution the sample, for example crystallisation, phase transition, etc. Platinum sample holder without cavity was finally used for VT-XRD measurement for $Y_{3+x}Al_{5-x}O_{12}$ (x = 0.2 and 0.4) garnets, the platinum sample holder was connected two thermocouples with one of them directly connecting with the sample for reliable temperature measurement and control.

For the measurement, the temperature interval in RT–900 °C was 100 °C and that in 900-1600 °C was 50 °C. The heating rate between every adjacent temperatures was 10 °C/min and the data recording time at each temperature took 30 min.

Synchrotron X-ray Powder Diffraction (SXRRD or simply SPD)

The Beamline 11BM is a powder diffraction instrument at APS (Argonne laboratory, the USA), it has a resolution of $\Delta Q/Q \approx 1.4\times10^{-4}$ (min. 2θ step size = 0.0001°) which is not available by a lab oratory diffractometer. The recorded high-quality SPD data enable researchers to perform structural analysis for the lattice parameter, atomic occupation, crystal size and strain, *etc*. Figure A4 (from the website of 11BM) shows the resolution comparison between the XRD data collected by laboratory source and the SPD collected by 11BM, the resolution of the SPD is much higher, enabling to detect the diffraction peaks which appear quite weak on XRD data. This enable us to detect the occupation of excess Y in the structure of non-stoichiometric YAG.

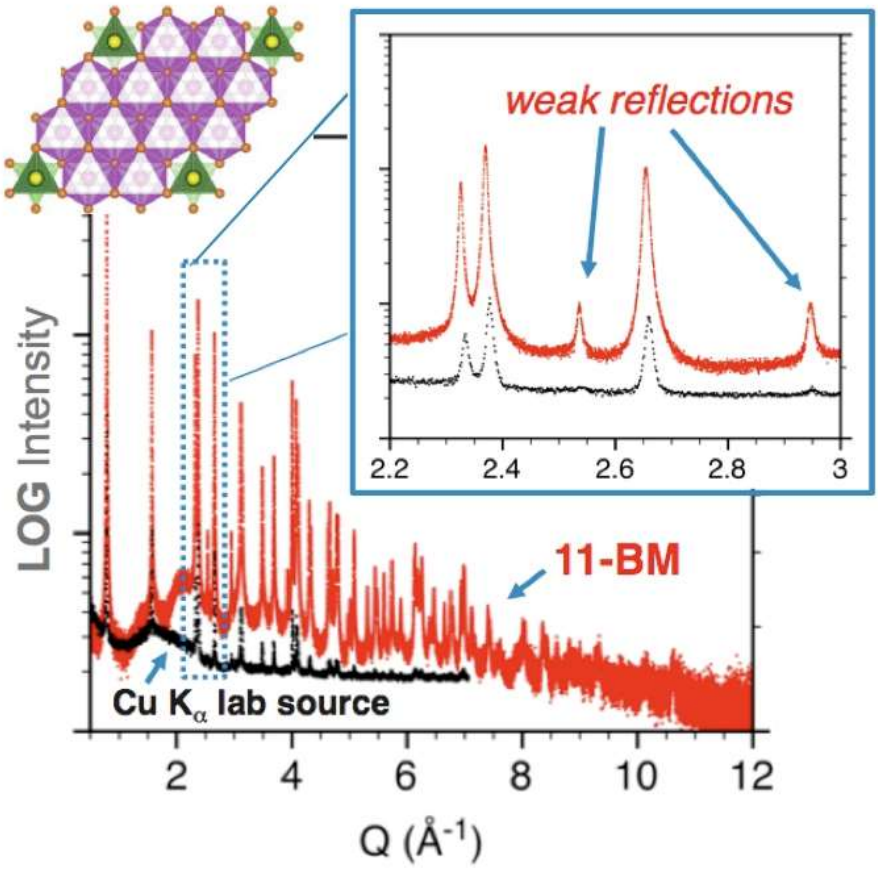

Figure A4. *Comparison of the diffraction patterns collected by laboratory diffractometer and by synchrotron radiation from 11 BM beamline*[136].

Electron Microprobe (EMP) analysis

The electron microprobe measurement for our YAG samples were measured by the microprobe SX Five (tungsten source). Samples beads were mirror polished before the measurement.

Electron microprobe is a non-destructive analysis to determine the chemical composition of small volume (typically 10-30 μm^3 or less) of a specimen, it usually works at 3-50 kV (15 kV in this work). The sample is bombarded with an electron beam and emits x-rays at characteristic wavelengths to the analyzed elements. Figure below show the electron beam path and the measured volume.

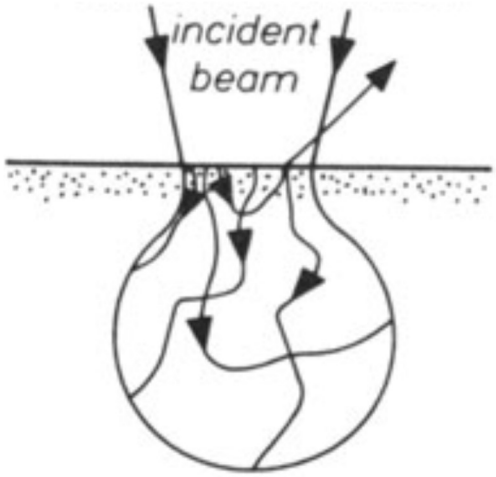

Figure A5. *A schematic of the interaction between the electron beam and sample surface (produced by Roger Theisen[137]).*

Scanning Electron Microscope (SEM)

The SEM instrument in this work is Field Emission Gun-SEM MERLIN (ZEISS). The measurement enables us to observe the microstructure of the exposed sample with a focused electron beam of electrons. The electrons interact with atoms of the sample, producing morphology or composition of the sample. In a SEM mode, the atoms of the sample are excited by electron beam and emit secondary electrons which are later detected by secondary electron detector. The number of the detected secondary electrons results in the signal intensity relating to the topography of the sample.

Scanning Transmission Electron Microscope (STEM)

Scanning Transmission Electron Microscopy−High Angle Annular Dark Field (STEM−HAADF, JEOL ARM200F (JEOL Ltd.)) imaging works as a Z−contrast mode with its signal dominated by Rutherford scattering and cross section proportional to Z^2 (Z is the atomic number). Depending on the collection angle of annular dark field (ADF) detector, the signal coming from a thin foil target with several dozens of nanometers in thickness can be approximated by an exponential function $I \propto Z^n$, where n varies in 1.6−2. This imaging mode is also able to distinguish these chemically different atomic columns, therefore in the case where the atomic column comprising of different elements (*i*), the intensity formula is modified into $I \propto \sum_i (m_i Z_i^n)$, where m_i and Z_i are respectively the ratio and atomic number of the element *i*. This enables to detect the presence of excess Y atoms in non-stoichiometric YAG, as they are supposed to be at 16a sites where is only occupied by Al for $Y_3Al_5O_{12}$ garnet structure.

Nuclear Magnetic Resonance (NMR)

The ^{89}Y NMR was measured by Bruker ADVANCE III HD Solid spectrometer (IR-NMR-CNRS-Orléans, France). The samples were grounded into powder and load into a rotor for the measurement. The nuclei of an element possess a spin angular momentum and an associated magnetic moment, when placed in a magnetic field, the nuclei has an interaction with the field. NMR allows to obtain the information on local environment of the nucleus through different chemical shift interactions, dipolar coupling, scalar coupling or quadrupole interaction. On a series of spectra, these interactions will be at the origin of the positioning, the shape and the alignment of lines, all these quantities carrying structural information to describe our compounds.

Extended X-Ray Absorption Fine Structure (EXAFS)

EXAFS measurements for $Y_{3+x}Al_{5-x}O_{12}$ ($0 \leq x \leq 0.25$) were conducted at Synchrotron Soleil site. The EXAFS supplies information on local structure surrounding a certain absorber atom, including: the distance between the absorber atom and its neighboring atoms; the type of the neighboring atoms; the number of the neighboring atoms.

The X-ray absorbing takes place when the incident X-ray energy matches the binding energy of an electron of an atom of the sample, the X-ray absorption coefficient μ can be calculated

by processing the X-ray intensity before and after the absorbing process which can described by the schematic diagram and the formula $I = I_0 e^{-\mu t}$ below.

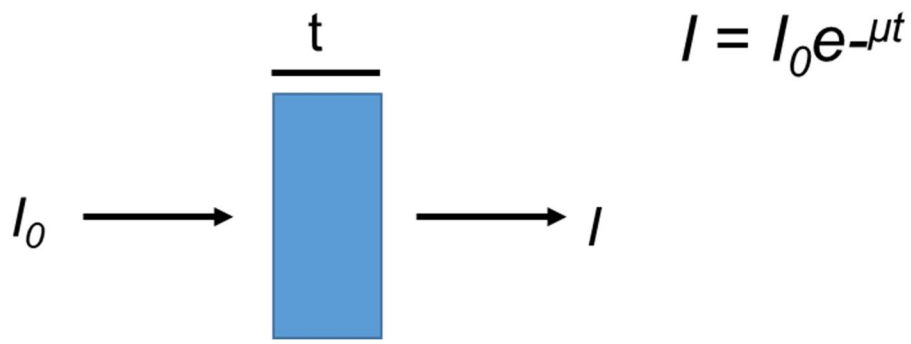

Figure A6. *Schematic of intensity change after and before the sample.*

Photoluminescence

Photoluminescence is a process in which activator absorbs excitation energy and gives out emission luminescence in visible range. Or it is process in which sensitizer is involved, the sensitizer absorbs the photons from the excitation source and transfers energy in the host lattice to the activator whose excited state level has approximately equal energy above their ground states as the sensitizer does. When the activator returns to a lower energy state, the substance gives out luminescence emission which is recorded as emission spectrum. **Figure A7** (a) and (b) respectively show the luminescence process of activator single doped and sensitizer and activator co-doped host materials. (c) shows the energy transfer process of sensitizer and activator co-doped host material, the excitation and emission process were recorded in the form of excitation and emission spectrums, respectively.

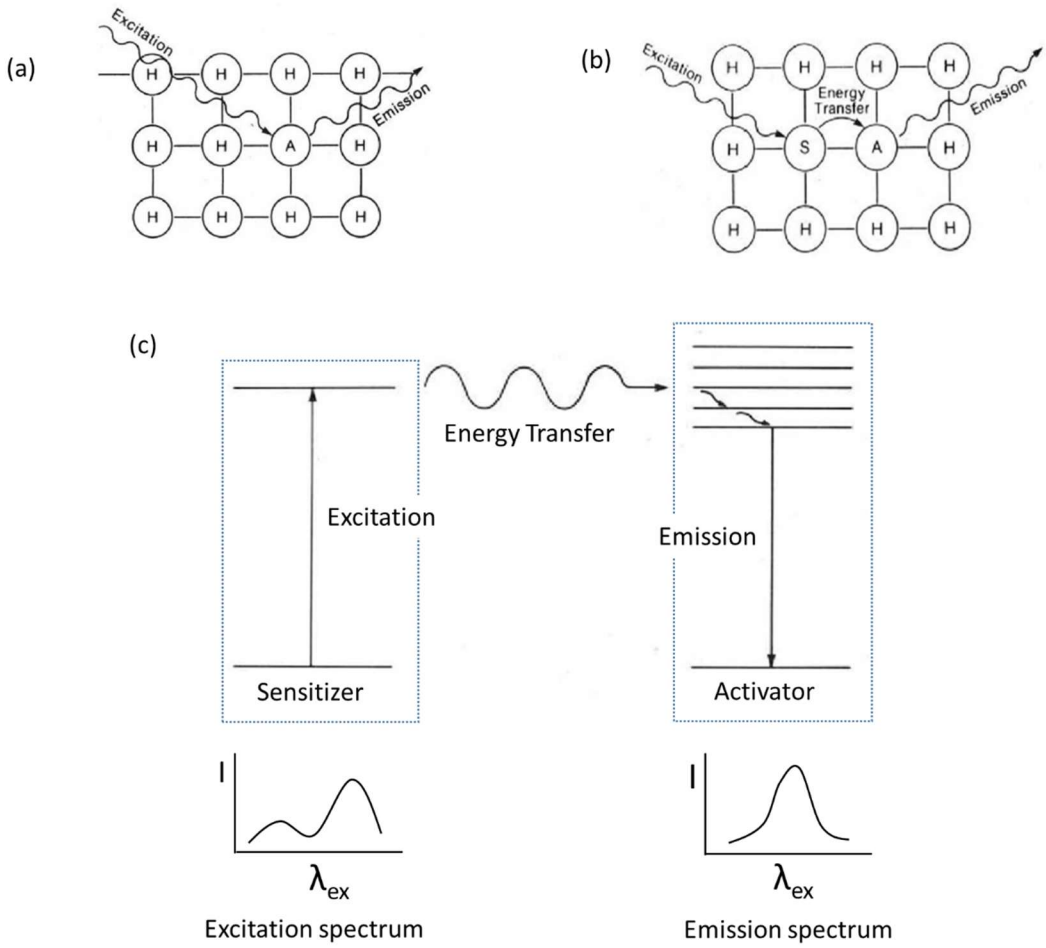

Figure A7. *Reproduced and modified* ***(a)*** *Diagram of luminescence process in the host lattice of activator doped material.* ***(b)*** *diagram of luminescence process in the host lattice of sensitizer and activator co-doped material.* ***(c)*** *Schematic diagram of energy transfer process involved in a luminescence process of sensitizer and activator doped material* [138].

Raman Spectroscopy

Raman spectroscopy was performed on polished YAG ceramic or YAG glass by Renishaw InVia Qontor spectrometer mounting a green laser (514 nm) operated at 50 mW.

Raman is a non-destructive chemical analysis technique which provides detailed information on chemical structure, for example phase, crystallinity, molecular interactions, *etc*. Its work principle is based on the interaction of the light with the chemical bonds in a sample (**figure A8**). A Raman spectrum featured many peaks showing the intensity and wavelength position of the Raman scattered light, corresponding to the specific molecular bond vibration. Each peak is related to a specific bond vibration.

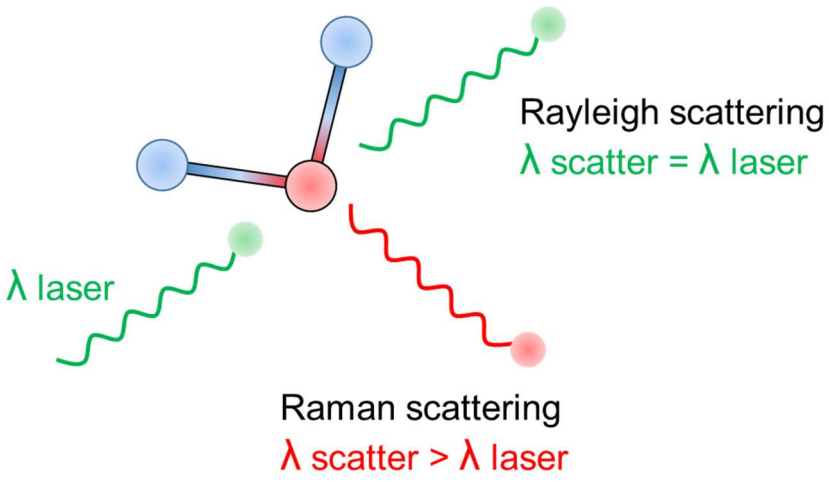

Figure A8. *Redrawn Raman principle diagram[139].*

Density Functional Theory (DFT)

Since the GIPAW method used plane waves with periodic boundary conditions, it is convenient to choose a crystal compound with known structure and known experimental isotropic chemical shift to obtain the σ_{ref} value (such that the calculated and experimental chemical shift for that compound are equal).

However, deviations from the theoretical equation GIPAW-calculated isotropic shielding and experimental isotropic chemical shift have been reported in some cases. For example, a linear relationship $\delta_{iso}^{exp} = -A \cdot \sigma_{iso}^{calc} + \sigma_{ref}$ with A~0.8 has been reported for ^{19}F. These deviations are due to the intrinsic approximations of the DFT-GIPAW method linked to the use of pseudopotentials and of the PBE functional for describing the interactions between core and valence electrons and the electronic exchange-correlation effects, respectively. Therefore, it can better use a larger family of reference crystalline compounds to obtain the σ_{ref} and A values from a linear regression analysis. This has been done for ^{89}Y using a series of reference compounds given in **table A1**. Since, the atomic positions of the $Y_{3+x}Al_{5-x}O_{12}$ structural models are been relaxed by DFT-geometry optimization of the structure, by optimizing all atomic positions while keeping symmetry and cell parameters fixed to experimental values.

Table A1. ^{89}Y GIPAW-calculated isotropic shieldings and experimental isotropic chemical shifts for a series of reference compounds. The ISCD number of the reference structures used for DFT-geometry optimization and GIPAW computation is also given.

compounds	ICSD code	site	^{89}Y $\sigma_{iso}^{calc.}$(ppm)	^{89}Y δ_{iso}^{exp} (ppm)
$Y_3Al_5O_{12}$	20090	Y1	2378.3	222
$YAlO_3$	4115	Y1	2378.8	215
$Y_4Al_2O_9$	63650	Y1 Y2 Y3 Y4	2427.4 2402.2 2438.3 2420.0	195 231 184 216
Y_2O_3	100450	Y1 Y2	2324.6 2372.2	314 273

B part – Experimental results

Figure B1(a-g) shows Rietveld refinement plots for $Y_{3+x}Al_{5-x}O_{12}$ (x = 0.05, 0.1, 0.15, 0.25, 0.3, 0.35 and 0.4) garnets whose structural information are in table 2.5, 2.6, 2.7, 2.9, 2.10, 2.11 and 2.12. The 0.05, 0.1, 0.15, 0.25 YAGs were synthesized by direct crystallisation method, x = 0.3, 0.35 and 0.4 YAGs were prepared by glass crystallisation method.

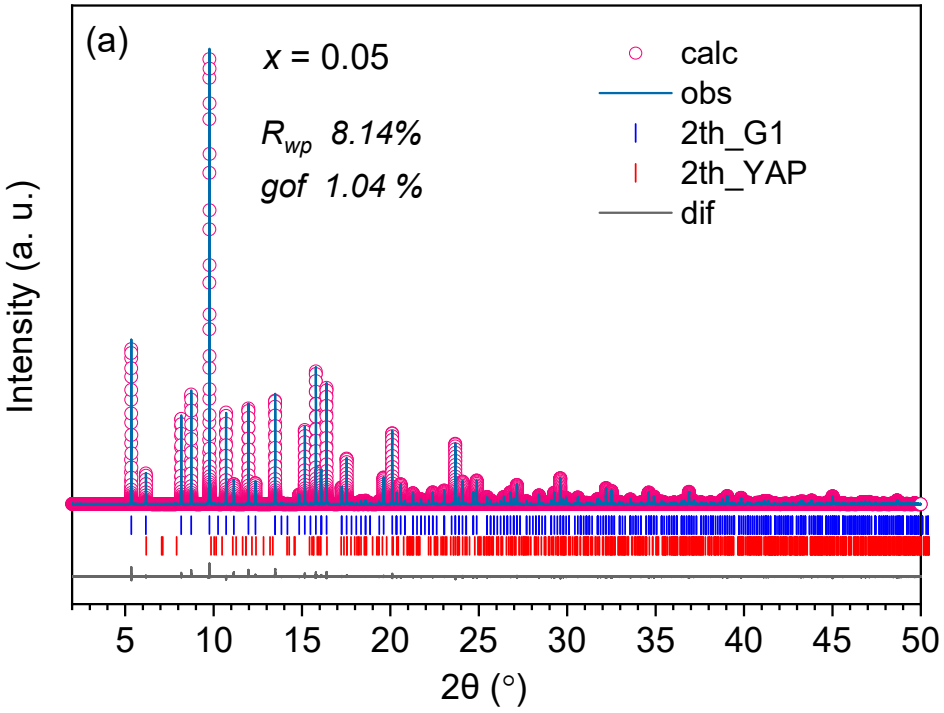
(a)
x = 0.05
R_wp 8.14%
gof 1.04 %
calc
obs
2th_G1
2th_YAP
dif
Intensity (a. u.)
5
10
15
20
25
30
35
40
45
50
2θ (°)

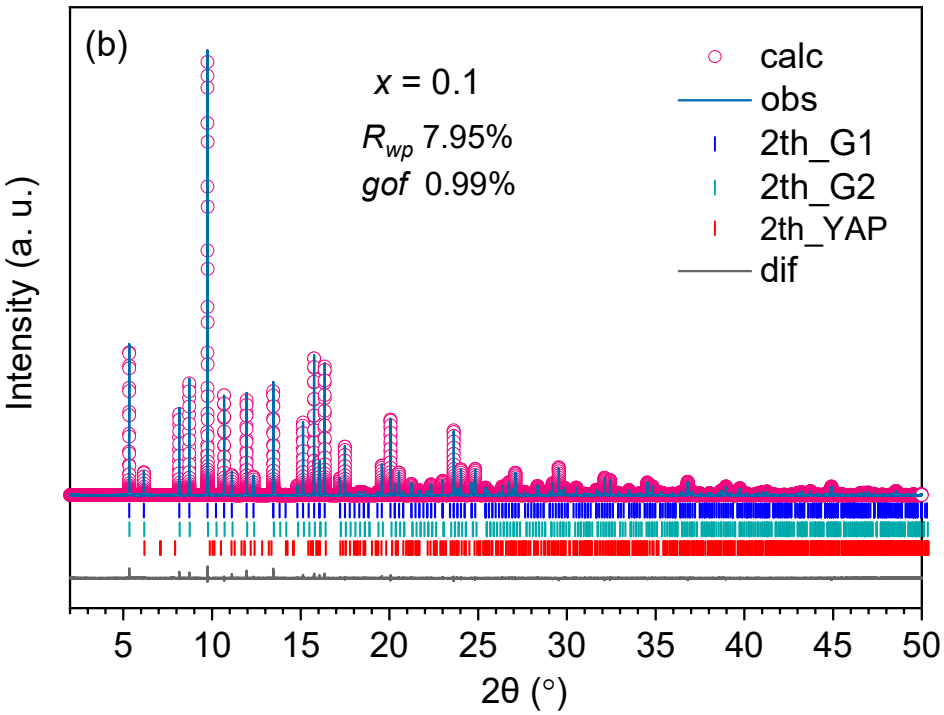
(b)
x = 0.1
R_wp 7.95%
gof 0.99%
calc
obs
2th_G1
2th_G2
2th_YAP
dif
Intensity (a. u.)
5
10
15
20
25
30
35
40
45
50
2θ (°)

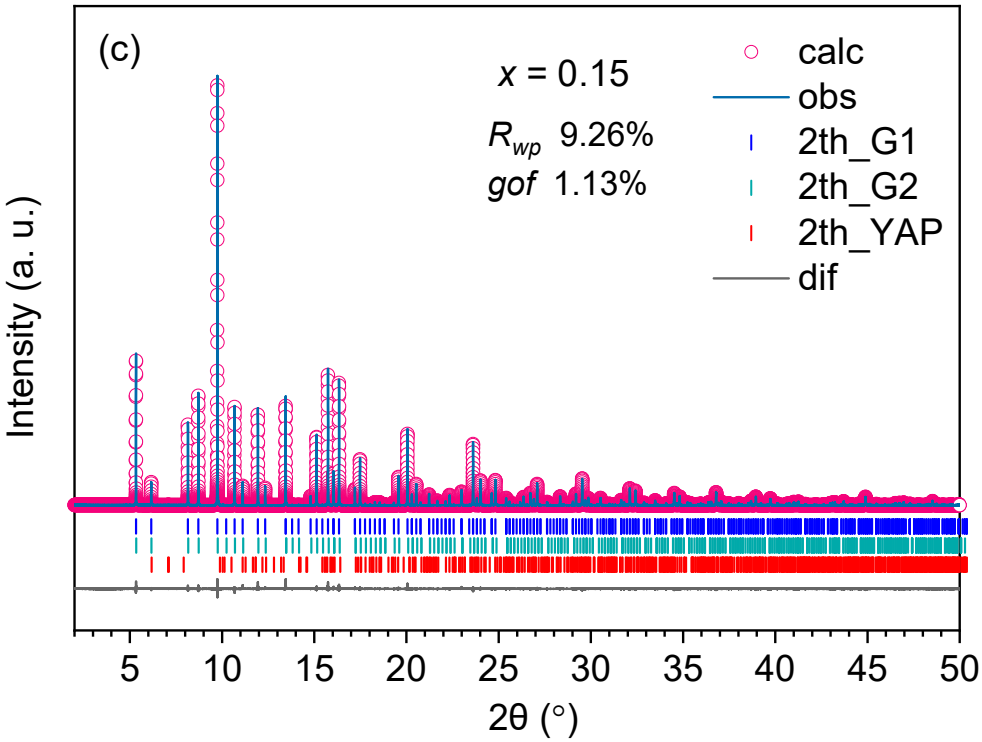
(c)
x = 0.15
R_wp 9.26%
gof 1.13%
calc
obs
2th_G1
2th_G2
2th_YAP
dif
Intensity (a. u.)
5
10
15
20
25
30
35
40
45
50
2θ (°)

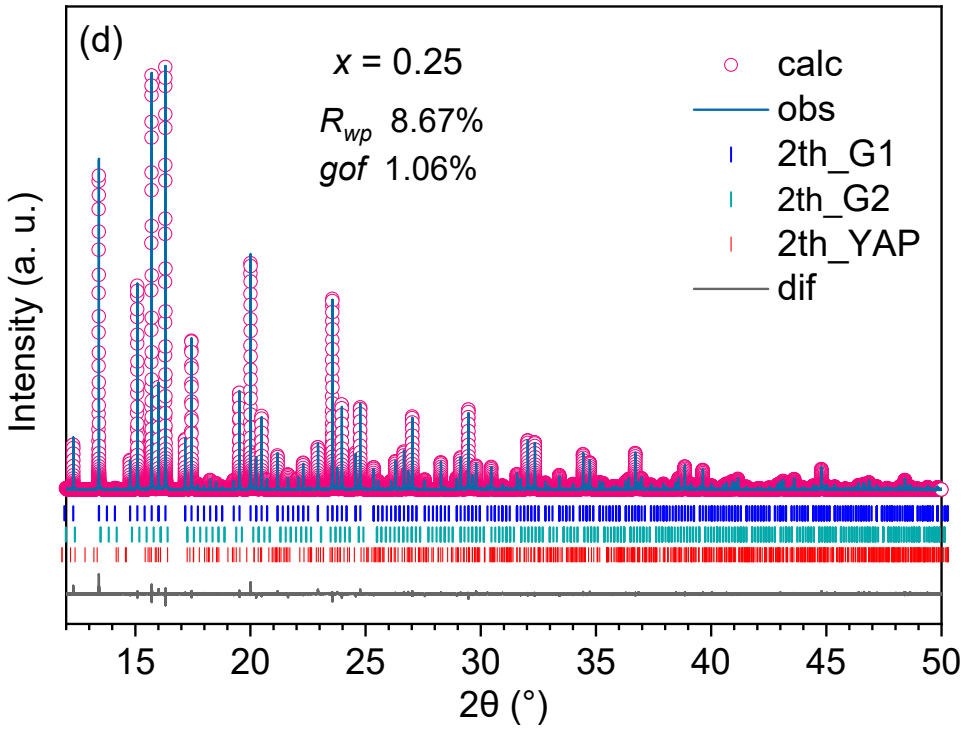
(d)
x = 0.25
R_wp 8.67%
gof 1.06%
calc
obs
2th_G1
2th_G2
2th_YAP
dif
Intensity (a. u.)
15
20
25
30
35
40
45
50
2θ (°)

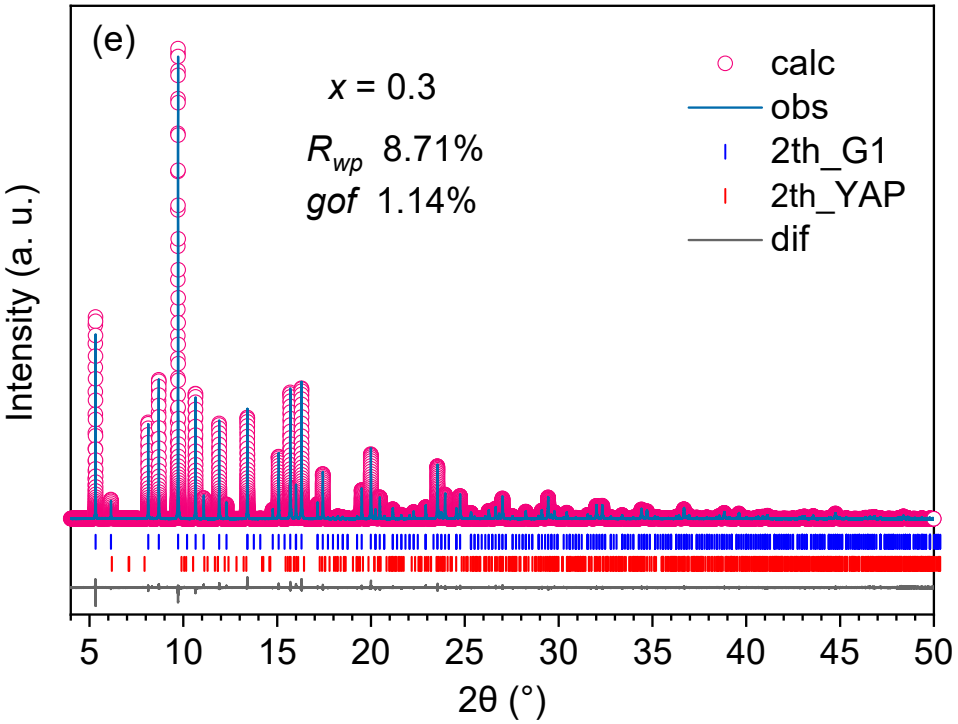
(e)
x = 0.3
R_{wp} 8.71%
gof 1.14%
calc
obs
2th_G1
2th_YAP
dif
Intensity (a. u.)
5
10
15
20
25
30
35
40
45
50
2θ (°)

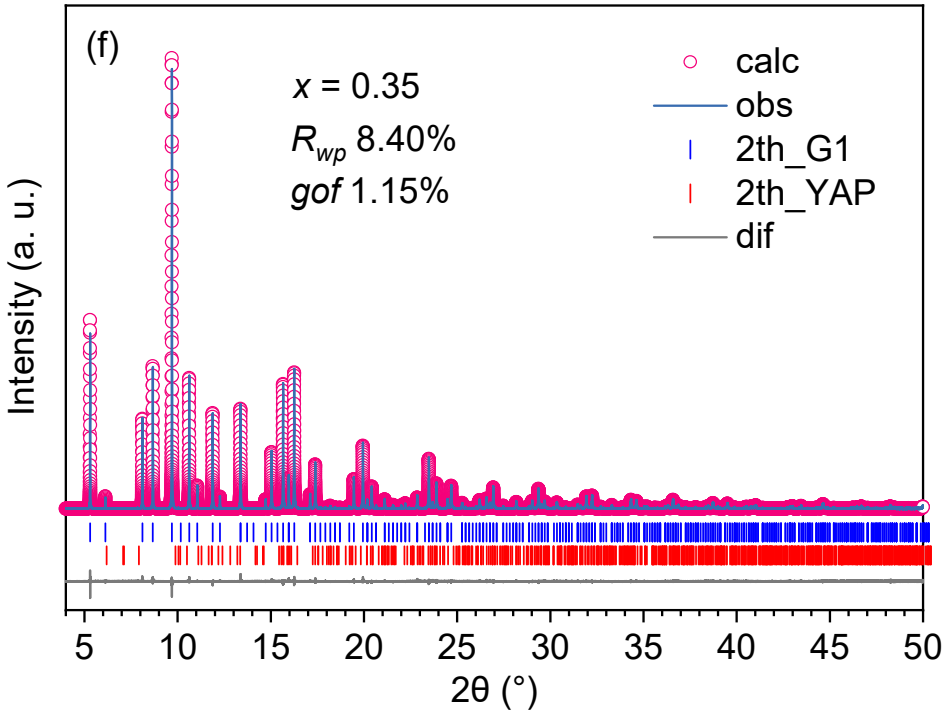
(f)
x = 0.35
R_{wp} 8.40%
gof 1.15%
calc
obs
2th_G1
2th_YAP
dif
Intensity (a. u.)
5
10
15
20
25
30
35
40
45
50
2θ (°)

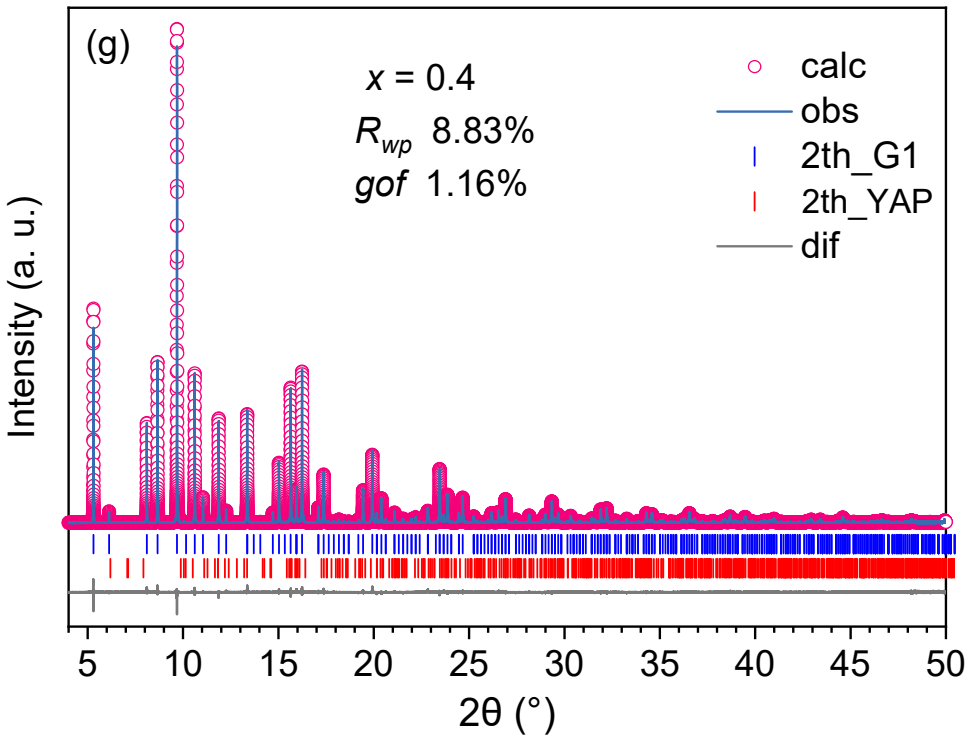

Figure B1 (a-g). *Rietveld refinement plots for $Y_{3+x}Al_{5-x}O_{12}$ (x = 0.05, 0.1, 0.15, 0.25, 0.3, 0.35 and 0.4) garnets, the refinements were performed on SPD data. The blue line and pink circle respectively represent observed and calculated data. The grey line is the difference between observed and calculated data. The blue, cyan and red tick marks respectively Bragg positions of main garnet (G1), secondary garnet (G2) and perovskite (YAP).*

Figure B2 shows the rest 3 structural models for $Y_{3.25}Al_{4.75}O_{12}$ with two defects and **figure B3** shows the 7 structural models for $Y_{3.375}Al_{4.625}O_{12}$ with three defects. The black lines in the structural models of **figure B2** and the black triangles in that of **figure B3** indicate the concerned defects. These defects were determined in the principle of “shortest distance.

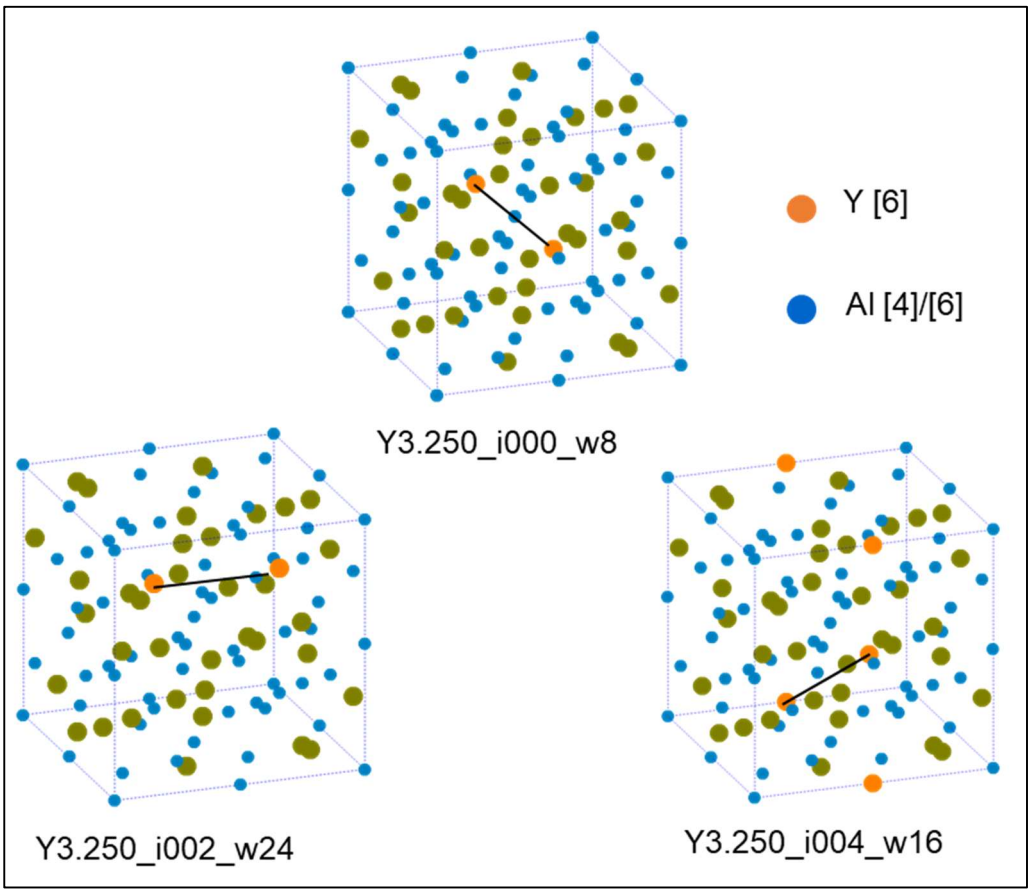

Figure B2. *Three structural models for $Y_{3.25}Al_{4.75}O_{12}$, each model has two Y defects. The black line connects the involved two Y defects. Y defects (6-coordiante) are labelled as closed orange circles and Al (4- and 6- coordinate) atoms are labelled as closed blue circles. Oxygen atoms are not shown in these models for the sake of clarity.*

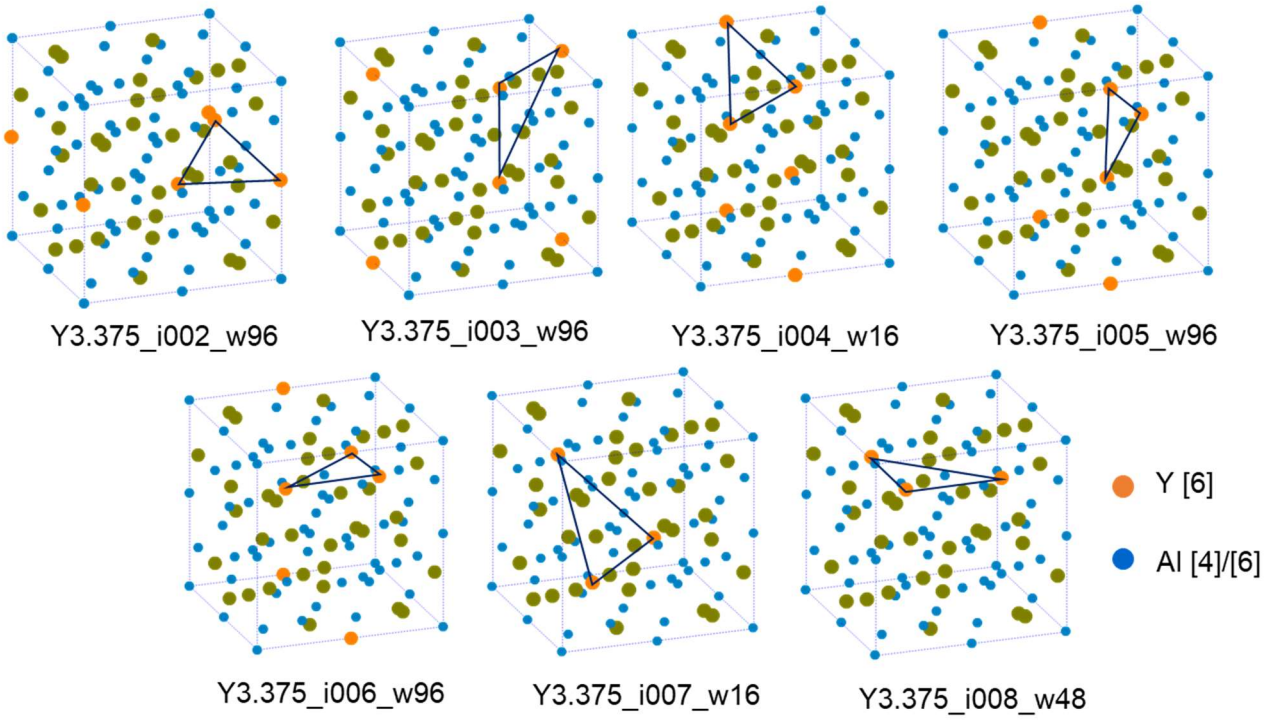

Figure B3. *Seven structural models for $Y_{3.375}Al_{4.625}O_{12}$, each model has three Y defects. The vertex of the black triangle connects the involved Y defects in the three models. Y defects (6-coordiante) are labelled as closed orange circles and Al (4- and 6- coordinate) atoms are labelled as closed blue circles. Oxygen atoms are not shown in these models for the sake of clarity.*

Reference

Reference

1. C.J. Benmore; J.K.R. Weber, Aerodynamic levitation, supercooled liquids and glass formation. *Advances in Physics: X*. (2017) *2*, 717-736.

2. T. Farmer, Structural studies of liquids and glasses using aerodynamic levitation. (2015).

3. A. Masuno, H. Inoue, Y. Arai, et al., Structural-relaxation-induced high refractive indices of $Ba_{1-x}Ca_xTi_2O_5$ glasses. *J. Mater. Chem.* (2011) *21*, 17441.

4. L.B. Skinner, A.C. Barnes, P.S. Salmon, et al., Structural and triclustering in Ba-Al-O glass. *Physical Review B*. (2012) *85*, 064201.

5. Y. Arai, K. Itoh, S. Kohara, et al., Refractive index calculation using the structural properties of $La_4Ti_9O_{24}$ glass. *J. Appl. Phys.* (2008) *103* (094905).

6. A. Masuno, H. Inoue, K. Yoshimoto, et al., Thermal and optical properties of La_2O_3-Nb_2O_5 high refractive index glasses. *Opt. Mater. Express*. (2014) *4*, 710-718.

7. Y. Watanabe, A. Masuno; H. Inoue, Glass formation of rare earth aluminates by containerless processing. *J. Non-Cryst. Solids*. (2012) *358*, 3563-3566.

8. M. Allix, S. Alahrache, F. Fayon, et al., Highly transparent $BaAl_4O_7$ polycrtsalline ceramic obtained by full crystallization from glass. *Adv. Mater.* (2012) *24*, 5570-5575.

9. M. Boyer, A.J.F. Carrion, S. Ory, et al., Transparent polycrystalline $SrREGa_3O_7$ mellite ceramics: potential phosphors for tunable solid state lighting. *J. Mater. Chem. C.* (2016) *4*, 3238.

10. X. Ma, X. Li, J. Li, et al., Pressureless glass crystallization of transparent yttrium aluminum garnet-bases nanoceramics. *Nat. Commun.* (2018) *9*, 1-9.

11. M. Boyer, X. Yang, A.J.F. Carrión, et al., First transparent oxide ion conducting ceramics synthesized by full crystallization from glass. *J. Mater. Chem. A.* (2018) *6*, 5276.

12. J. Yu, S. Yoda, A. Masuno, et al., cmprehensive structure study of glassy and metastable crystalline $BaTi_2O_5$ *Chem. Mater.* (2009) *402*, 259-263.

13. Y. Akishige, K. Fukano; H. Shigematsu, New ferroelectric $BaTi_2O_5$. *Jpn. J. Appl. Phys*. (2003) *42*, 946-948.

14. J. Fan, V. Sarou-Kanian, X. Yang, et al., $La_2Ga_3O_{7.5}$: A metastable ternery melilite with a super-excess of interstitial oxide ions synthesized by direct crystallization pf the melt *Chem. Mater.* (2020) *32*, 9016-9025.

15. M. Boyer, E. Véron, A.I. Becerro, et al., $BaGa_4O_7$, a new $A_3BC_{10}O_{20}$ crystalline phase syntheis, structure determination and luminescence properties. *CrystEngComm*. (2015) *17* (6127).

16. O. Majérus, L. Cormier, D.R. Neuville, et al., The structure of SiO_2-GeO_2 glasses: a spectroscopy study. *J. Non-Cryst. Solids*. (2008) *354*, 2004-2009.

17. C.A. Angell, Formation of glasses from liquids and biopolymers. *Science*. (1995) *267*, 1924-1935.

18. C.-h. Lee, S.-k. Jung, S. Yoda, et al., Microstructure of rapidly quenched YAG-based glass-ceramics prepared by aerodynamic levitation. *Ceram. Int.* (2015) *41*, 14475-14481.

19. K. Nagashio; K. Kuribayashi, Spherical yttrium aluminum garnet embedded in a glass matrix *J. Am. Ceram. Soc.* (2002) *85*, 2353-2358.

20. M.C. Wilding, M. Wilson, C.J. Benmore, et al., Structural changes in supercooled Al_2O_3-Y_2O_3 liquids. *Phys. Chem. Chem. Phys.* (2013) *15*, 8589.

21. S. Aasland; P.F. McMillan, Density-driven liquid-liquid phase seperation in the system Al_2O_3-Y_2O_3. *Nature*. (1994) *369*, 633-636.

22. S. Alahraché, M. Deschamps, J. Lambert, et al., Crystallization of Y_2O_3-Al_2O_3 rich glasses: synthesis of YAG glass-ceramics. *Journal of Physiques Chemistry C*. (2011) *115*, 20499-20506.

23. J.K.R. Weber, J. G.Abadie, A.D. Hixson, et al., Glass formation and polyamorphism in rare-earth oxide-aluminum oxide compositions. *J. Am. Ceram. Soc.* (2000) *83*, 1868-1872.

24. S. Kostić, Z.Ž. Lazarević, V. Radojević, et al., Study of structural and optical properties of YAG and Nd:YAG single crystals. *Mater. Res. Bull.* (2015) *63*, 80-87.

25. J. Zhou, W. Zhang, T. Huang, et al., Optical properties of Er, Yb co-doped YAG transparent ceramics. *Ceram. Int.* (2011) *37*, 513-519.

26. G. Boulon, Y. Guyot, M. Guzik, et al., Yb^{3+} ions distribution in YAG nanoceramics analyzed by both optical and TEM-EDX techniques. *J. Phys. Chem.* (2014) *118*, 15474-15486.

27. M. Gervais, S.L. Floch, N. Gautier, et al., Crystallization of $Y_3Al_5O_{12}$ garnet from deep undercooled melt effect of the Al-Ga substitution *Mater. Sci. Eng., B*. (1996) *45*, 108-113.

28. A.P. Patel, M.R. Levy, R.W. Grimes, et al., Mechanisms of non-stoichiometry in $Y_3Al_5O_{12}$. *Appl. Phys. Lett.* (2008) *93*, 191902.

29. L. Zhu, Z. Zhang, B. Liu, et al., Preparation and characterization of non-stoichiometric yttrium aluminum garnet (YAG) with antisite defects as potential scintillator. *IEEE Trans. Nucl. Sci.* (2014) *61*, 312-315.

30. Y. Zorenko, A. Voloshinovskii, V. Savchyn, et al., Excition and antisite defect-related luniscence in $Lu_3Al_5O_{12}$ and $Y_3Al_5O_{12}$. *Phys. Stat. Sol. (b)*. (2007) *244*, 2180-2189.

31. Y. Zorenko, A. Voloshinoskii, I. Konstankevych, et al., Luminescence of excitons and antistite defects in the phosphors based on garnet compounds. *Radiation Measurements*. (2004) *38*, 677-680.

32. Y. Zorenko, V. Gorbenko, I. Konstankevych, et al., Single-crystalline films of Ce-doped YAG and LuAG phosphors: advantages over bulk crystals analogues. *J. Lumin.* (2005) *114*, 85-94.

33. M. Nikl, V.V. Laguta; A. Vedda, Complex oxide scintillators: Materials defects and scintillation performance. *Phys. Stat. Sol. (b)*. (2008) *245*, 1701-1722.

34. M. Kučera, K. Nitsch, M. Kubová, et al., Ce-doped YAG and LuAG epitaxial films for scintillation detectors. *IEEE Transactions on Nuclear Science*. (2008) *55*, 1201-1205.

35. K. Nagashio, J. Sasaki; K. Kuribayashi, Phase selection in undercooled $Y_3Al_5O_{12}$ melt. *Mater. Trans.* (2004) *45*, 2723-2727.

36. M.K. Ashurov, Y.K. Voronko, V.V. Osiko, et al., Spectroscopie study of stoichiometry deviation in crystals with garnet structure. *Phys. Stat. Sol. (a)*. (1977) *42*, 101-110.

37. A. Munoz-GarcÍa, E. Artacho; L. Sejio, Atomistic and electronic structure of antisite defects in yttrium aluminum garnet: density-functional-study. *Phys. Rev. B*. (2009) *80*, 014105.

38. M. Nikl, E. Mihokova, J. Pejchal, et al., The antisite Lu_{Al} defect-related trap in $Lu_3Al_5O_{12}$: Ce single crystal. *Phys. Stat. Sol. (b)*. (2005) *242*, 119-121.

39. S. Geller, Thermal expansion of some garnets. *Mat. Res. Bull.* (1972) *7*, 1219-1224.

40. J.S. Abell; I.R. Harris, An investigation of phase stability in the Y_2O_3-Al_2O_3 system. *Journal of Materials Science*. (1974) *9*, 527-537.

41. S.J. Schneider, R.S. Roth; J.L. Wang, Solid state reaction involving oxides of trivalent cations. *J. Res. Natl. Bur. Stand. A Phys. Chem.* (1961) *65A*, 345-374.

42. M.C. Wilding, M. Wilson, P.F. McMillan, et al., Structural properties of Y_2O_3-Al_2O_3 liquids and glass: An overview. *J. Non-Cryst. Solids*. (2015) *407*, 228-234.

43. N.K. Nasikas, S. Sen; G.N. Papatheodorou, Structural nature of polyamorphism in Y_2O_3-Al_2O_3 glasses. *Chem. Mater.* (2011) *23*, 2860-2868.

44. J.L. Caslavsky; D.J. Viechnicki, Melting behaviour and metastability of yttrium aluminum garnet (YAG) and $YAlO_3$ determined by optical differential thermal analysis. *Journal of Materials Science*. (1980) *15*, 1709-1718.

45. A. Ikesue; T. Kinoshita, Fabrication and optical properties of high-performance polycrytalline Nd:YAG ceramics for solid-state lasers. *J. Am. Cream. Soc.* (1995) *78*, 1033-1040.

46. X. Yan, S. Zheng, R. Yu, et al., Preparation of YAG: Ce^{3+} phosphor by sol-gel low temperature combustion method and its luminescent properties. *Tans. Nonferrous Met. Soc. China*. (2008) *18*, 648-653.

47. Y. Zhang; H. Yu, Synthesis of YAG powders by the co-precipitation method. *Ceram. Int.* (2009) *35*, 2077-2081.

48. G. Dantelle, D. Testemale, E. Homeyer, et al., A new solvothermal method for the synthesis of size-controlled YAG: Ce single-naocrystal. *RSC Adv.* (2019) *8*, 26857-26870.

49. C. Li, H. Zuo, M. Zhang, et al., Fabrication of transparent YAG ceramics by traditional solid-state-reaction method. *Trans. Nonferrous Met. Soc. China*. (2007) *17*, 148-153.

50. K.M. Kinsman; J. McKittrick, Phase development and luminescence in chromium-doped yttrium aluminum garnet (YAG: Cr) phosphors. *J. Am. Cream. Soc.* (1994) *77*, 2866-2872.

51. D.L. Price, High-temperature levitation materials. *Cambridge University Press*. (2010).

52. D.A. Winborne, P.C. Dordine, D.E. Rosner, et al., Aerodynamic levitation temperature for containerless high temperature studies on liquid and solid samples. *Metall. Trans. B*. (1976) *7*, 711-713.

53. L. Hennet, V. Cristiglio, J. Kozaily, et al., Aerodynamic levitation and laser heating: Applications at synchrotron and neutron sources. *Eur. Phys. J. Special Topics*. (2011) *196*, 151-165.

54. F. Kargl, C. Yuan; G.N. Greaves, Aerodynmaic levitation: Thermophysical property measurement of liquid oxides. *Int. J. Microgravity Sci. Appl.* (2015) *32*, 320212.

55. O.L.G. Alderman, C.J. Benmore, J.K.R. Weber, et al., The structure of liquid UO_{2-x} in reducing gas atmospheres. *Aplied Physics Letters* (2017) *110*, 081904.

56. O.L.G. Alderman, M.C. Wilding, A. Tamalonis, et al., Iron K-edge X-ray absorption near-edge structure spectroscopy of aerodynamically levitated silicate melts and glasses. *Chem. Geol.* (2017) *453*, 169-185.

57. G.N. Greaves, M.C. Wilding, S. Fearn, et al., Detection of first-order liquid/liquid phase transitions in yttrium oxide-aluminum oxide melts. *Science*. (2008) *322*, 566-570.

58. L. Hennet, I. Pozdnyakova, V. Cristiglio, et al., Structure and dynamics of levitated liquid aluminates. *J. Non-Cryst. Solids*. (2007) *353*, 1705-1712.

59. Y.A. Mayi, M. Dal, P. Peyre, et al., Laser-induced plume investigated by finite elememnt modelling and scaling of particle entrainment in laser powder bed fusion. *J. Phys. D: Appl. Phys.* (2019) *53*, 1-15.

60. S. Fujita, Y. Umayahara; S. Tanabe, Inflence of light scattering on luminescence efficacy in Ce: YAG glass-ceramic phosphor *J. Ceram. Soc. Jpn.* (2010) *118*, 128-131.

61. F.A. Selim, D. Solodovnikov, M.H. Weber, et al., Identification of defects in $Y_3Al_5O_{12}$ crystals by positron annihilation spectroscopy. *Appl. Phys. Lett.* (2007) *91*, 104105.

62. J.E. Geusic, H.M. Macros; L.G.V. Uitert, Laser oscillations in Nd-doped yttriun aluminum, yttrium gallium and gadolinum garnet. *Appl. Phys. Lett.* (1964) *4*, 182-184.

63. W. Koechner; M. Bass, Solid state lasers. *Springer*. (2003).

64. P. Rechmann, D.S. Goldin; T. Henning, Er: YAG lasers in densistry: and overview. *Proc. SPIE*. (1998) *3248*, 2-13.

65. R. Birang, J. Poursamimi, N. Gutknecht, et al., Comparative evaluation of the effects of Nd:YAG and Er:YAG laser in dentin hypersensitivity treatment. *Lasers Med Sci*. (2007) *3*, 21-24.

66. S.D. Jackson; T.A. King, Efficient high power operation of a Nd:YAG-pumped Yb:Er-doped silica fibre laser *Optical Communications*. (1999) *172*.

67. S. Nakamura; G. Fasol, The blue laser diode: GaN based light emitters and lasers. *Spinger Berlin*. (1997).

68. N. Ishiwada, K. Tsuchiya; T. Yokomori, Applicability of Dy-doped yttrim aluminum garnet (YAG:Dy) in phosphor thermometry at diferent oxygen concentrations. *J. Lumin.* (2019) *208*, 82-88.

69. A. Hashemi, A. Vetter, G. Jovicic, et al., Temperature measurement using YAG: Dy and YAG:Sm under diode laser excitation (405 nm). *Meas. Sci. Technl.* (2015) *26*, 075202.

70. https://en.wikipedia.org/wiki/Nd:YAG_laser#/media/File:Powerlite_NdYAG.jpg.

71. L.A. Belov, S.M. Smolskiy; V.N. Kochemasov, Handbook of RF, microwave, and millimeter-wave components. (2012).

72. J. Pareja, C. Litterscheid, A. Molina, et al., Effects of doping concentration and co-doping with cerium on the luminescence properties of $Gd_3Ga_5O_{12}$: Cr^{3+} for thermometry. *Opt. Mater.* (2015) *47*, 338-344.

73. S. Aime, C. Gabella, S. Colombatto, et al., Insits into the use of paramagnetic Gd(III) complexes in MR-milecular imaging investigations. *Journal of Magnetic Resonance Imaging*. (2002) *16*, 394-406.

74. M. Guillong, I. Horn; D. Günther, A comparison of 266 nm and 193 nm produced from a single solid state Nd:YAG laser for laser ablation ICP-MS. *J. Anal. At. Spectrom.* (2003) *18*, 1224-1230.

75. F. Frankhauser; S. Kwasniewska, Clinnical effects of the Nd:YAG laser operating in the photodisruptive and thermal modes. *Ophthalmologica*. (2003) *217*, 1-16.

76. H. Sun, M. Han, M.H. Niemz, et al., Femtosecond laser corneal ablatiion threshold: dependence on tissue depth and laser pulse width. *Laser in Surgery and Medicine*. (2007) *39*, 654-658.

77. S. Gorsky, R. Zhang, A. Gok, et al., Directional light emission enchancement from LED-phosphor conventers using dielectric vogel spiral arrays. *APL Photonics*. (2018) *3*, 126103.

78. S.C. Tam, R. William, L.J. Yang, et al., A review of the laser processing of aircraft components. *J. Mater. Process. Technol.* (1990) *23*, 177-194.

79. C.Y. Yeo, S.C. Tam, S. Jana, et al., A technical review of the laser drilling of aerospace materials. *J. Mater. Process. Technol.* (1994) *42*, 15-49.

80. J.F. Ready, *Industrial Applications of Lasers*. Author, |*Title*. |Edition ed.; |Publisher: |Place Published, |Year; |`Vol.` Volume, |p Number of Pages|. ed.; Academic Press San Diego, USA, 1997.

81. T.H. Maiman, Optical and microwave-optical experiments in ruby. *Phys. Rev. Lett.* (1960) *4*, 564-566.

82. A. Golubović, S. Nikolić, R. Gajić, et al., The growth of Nd: YAG single crystals. *J. Serb. Chem. Soc.* (2001) *67*, 291-300.

83. W. Xiang, J. Zhong, Y. Zhao, et al., Growth of chracterization of air annealing Mn-doped YAG:Ce single crystal for LED. *J. Alloys Compd.* (2012) *542*, 218-221.

84. S. Nishiura, S. Tanabe, K. Fujioka, et al., Properties of transparent Ce: YAG phosphors for white LED. *Opt. Mater.* (2011) *33*, 688-691.

85. L.D. Philip, G.M. David, G.G. Neville, et al., Aerodynamic levitator furnace for measuring thermophysical properties of refractory liquids. *Rev. Sci. Instrum.* (2013) *84*, 124901.

86. C. Jaeger; F. Hemmann, EASY: A simple tool for simultaneously removing background, deadtime and acoustic ringing in quantitative NMR spectroscopy—Part I: Basic principle and applications. *Solid State Nucl. Magn. Reson.* (2014) *57-58*, 22-28.

87. T.A. Izyumov; R.P. Ozerov, Magnetic num. *PLENUM PRESS NEW YORK*. (1970), 1970.

88. M.F. Delley, G. Lapadula, Franciso, et al., Local structures and heterogeneity of silica-supported M(III) sites evidenced by EPR, IR, NMR, and luminescence spectroscopies. *J. Am. Ceram. Soc.* (2017) *139*, 8855-8867.

89. S.J. Clark, M. Segall, C.J. Pickard, et al., First principles methods using CASTEP. *Z. Kristallogr.* (2005) *220*, 567-570.

90. M.D. Segall, P.J.D. Lindan, M.J. Probert, et al., First-principle simulation: ideas, illustrations and CASTEP code. *J. Phys.: Condens. Matter*. (2002) *14*, 2717-2744.

91. P.E. Blöchl, Projector augmented-wave method. *Phys. Rev. B* (1994) *50*, 17953.

92. M. Profeta, F. Mauri; C.J. Pickard, Accurate first principles prediction of ^{17}O NMR parameters in SiO_2: assignment of the zeolite ferrierite spectrum. *J. Am. Ceram. Soc.* (2003) *125*, 541-548.

93. C.J. Picard; F. Mauri, All-electron magnetic response with pseudopotentials: NMR chemical shifts. *Phys. Rev. B*. *63*, 245101.

94. J. Xu, J. Wang, A. Rakhmatullin, et al., Interstitial oxide ion migration mechanism in aluminate melilite $La_{1+x}Ca_{1-x}Al_3O_{7+0.5x}$ ceramics synthesized by glass crystallization. *ACS Appl. Energy Mater.*. (2019) *2*, 2878-2888.

95. H. Jehn, Platinum losses during high temperature oxidation. *Journal of the Less-Common Metals*. (1981) *78*, 33-41.

96. A. Coelle, TOPAS Academic version 6. http://www.topas-academic.net/. (2020).

97. I. Levin, NIST Inorganic Crystal Structure Database (ICSD) (2018).

98. L.B. McCusker, R.B.V. Dreele, D.E. Cox, et al., Rietveld refinement guidelines. *J. Appl. Cryst.* (1999) *32*, 36-50.

99. S.J. Pennycook; L.A. Boatner, Chemically sensitive structure-imaging with a scanning transmission electron microscope. *Nature*. (1988) *336*, 565-567.

100. S.J. Pennycook; D.E. Jesson, High-resolution Z-contrast imaging of crystals. *Ultramicroscopy*. (1991) *37*, 14-38.

101. P. Hartel, H. Rose; C. Dinges, Conditions and reasons for incoherent imaging in STEM. *Ultramicroscopy*. (1996) *63*, 93-114.

102. P. Stademann, JEMS. https//www.jems-swiss.ch/(accessed May 4, 2020).

103. S.V. Aert, J. Verbeeck, R. Erni, et al., Quantative atomic resolution mapping using high-angle annular dark field scanning transmission electron microscopy *Ultramicroscopy*. (2009) *109*, 1236-1244.

104. G.T. Martinez, A. Rosenauer, A.D. Backer, et al., Quantitative composition determination at the atomic level using model-based high-angle annular dark field scanning transmission electron microscopy. *Ultramicroscopy*. (2014) *137*, 12-19.

105. K. Okhotnikov, T. Charpentier; S. Cadars, Supercell program: a combinatorial structure-generation approach for the local-level modeling of atomic substitutions and partial occupancies in crystals. *Journal of Cheminformatics*. (2016) *8*, 17.

106. P. Florian, M. Gervais, A. Massiot, et al., A multi-nuclear multiple-field nuclear magnetic resonance study of the Y_2O_3-Al_2O_3 phase diagram. *J. Phys. Chem. B*. (2001) *105*, 379-391.

107. D. Massiot, F. Fayon, M. Capron, et al., Modelling one- and two-dimensional solid-state NMR spectra. *Magn. Reson. Chem.* (2002) *40* (1), 70-76.

108. B. Ravel; M. Newville, ATHENA, ARTEMIS, HEPHAESTUS: data analysis for X-ray absorption spectroscopy using IFEFFIT. *J. Synchrotron Rad.* (2005) *12*, 537-541.

109. A.L. Ankudinov, B. Ravel, J.J. Rehr, et al., Real-space multiple-scattering calculation and interpretation of x-ray-absorption near-edge structure. *Phys. Rev. B*. (1998) *58*, 7565.

110. J.J. Rehr, J.M. deLeon, S.I. Zabinsky, et al., Theoretical x-ray absorption fine structure standards. *Jounal of the American Chemical Society*. (1991) *113*, 5135-5140.

111. Y.C. Lin, P. Erhart; M. Karlsson, Vibrational induced color shift tuning of photoluminescence in Ce^{3+}-doped garnet phosphors. *Journal of Materials Chemistry C*. (2019) *7*, 12926-12934.

112. V. Tucureanu, A. Matel; A.M. Avram, Synthesis and chracterization of YAG:Ce phosphors for white LEDs. *Opto-Electronics Review*. (2015) *23*, 239-251.

113. V. Pankratov, L. Grigorjeva, D. Millers, et al., Luminescence of cerium doped YAG nanopowders. *Radiation Measurements*. (2007) *42*, 679-682.

114. S.P. Feofilov, A.B.Kulinkin, T. Gacoin, et al., Machanism for Ce^{3+} excuation at enrgies below the zero-phonon line in YAG crystal and nanocrystals. *J. Lumin.* (2012) *132*, 3082-3088.

115. X. He, X. Liu, R. Li, et al., Effects of local structure of Ce^{3+} ions on luminescent properties of $Y_3Al_5O_{12}$: Ce nanoparticles. *Scientific Report*. (2015) *6*, 22238.

116. H.R. Abd, Z. Hassan, N.M. Ahmed, et al., Ce-doped YAG phosphor powder synthesis via microwave combustion and its application for white LED. *Opt. Mater.* (2019) *58*, 027110.

117. H. Desirena, L.A. Diaz-Torres, R.A. Rodríguez, et al., Photoluminescence characterization of porous YAG: Yb^{3+}–Er^{3+} nanoparticles. *J. Lumin.* (2014) *153*, 21-28.

118. S. Hinojosa, O. Barbosa-García, M.A. Meneses-Nava, et al., Luminescence properties and energy transfer process of co-doped Yb-Er poly-crystalline YAG matrix. *Opt. Mater.* (2005) *27*, 1839-1844.

119. E. Aleksanyan, V. Harutunyan, R. Kostanyan, et al., 5d-4f luminescence of Er^{3+} in YAG: Er^{3+}. *Opt. Mater.* (2009) *31*, 1038-1041.

120. J. Hostaša, L. Esposito, A. Malchere, et al., Polycrysalline Yb^{3+} -Er^{3+} co-doped YAG: Fabrication, TEM-EDX chracterization, spectroscopic properties, and comparison with the single crystal *J. Mater. Res.* (2014) *2288-2296*.

121. M. Liu, S.W. Wang, J. Zhang, et al., Dominant red emission ($^4F_{9/2} \rightarrow {}^4I_{15/2}$) via upconversion in YAG ($Y_3Al_5O_{12}$): Yb^{3+}, Er^{3+} nanopowders. *Opt. Mater.* (2007) *29*, 1352-1357.

122. M.-F. Joubert, Photon avalanche upconversion in rare earth laser materials. *Opt. Mater.* (1999) *11*, 181203.

123. X. Chen, Y. Wu, N. Wei, et al., Fabrication and spectroscopic properties of Yb/Er:YAG and Yb, Er:YAG transparent ceramics by co-precipitation synthesis route. *J. Lumin.* (2017) *188*, 533-540.

124. Y.K. Voronko; A.A. Sobol, Local inhomogeneity of garnet crystals doped with rare-earth ions. *Physica Status Solidi*. (1975) *27*, 657-663.

125. D. Chen, Y. Zhou, W. Xu, et al., Enhanced luminescence of Mn^{4+}:$Y_3Al_5O_{12}$ red phosphor via impurity doping. *Jounal of Matrials Chemistry C*. (2016) *4*, 1704-1712.

126. B. Wang, H. Lin, J. Xu, et al., $CaMg_2Al_{16}O_{27}$:Mn^{4+}-based Red Phosphor: A Potential Color Conveter for High-Powered Warm W-LED. *ACS Appl. Mater. Interfaces*. (2014) *6*, 22905-22913.

127. T. Murata, T. Tanoue, M. Iwasaki, et al., Fluorescence properties of Mn^{4+} in $CaAl_{12}O_{19}$ compounds as red-emitting phosphor for white LED. *J. Lumin.* (2005) *114*, 207-212.

128. I.E. Kolesnikov, A.A. Kalinichev, M.A. Kurochkin, et al., Structural, luminescnce and thermometric properties of nanocrystalline YVO_4: Dy^{3+} temperature and concentration series *Sci. Rep.* (2019) *9*, 2043.

129. L.M. Chepyga, G. Jovicic, A. Vetter, et al., Photoluminescence properties of thermographic phosphors YAG:Dy and YAG:Dy, Er doped with boron and nitrogen. *Appl. Phys. B*. (2016) *122*, 212.

130. O. Mishima, The relationship between liquid, supercooled and glassy water. *Nature*. (1998) *396*, 329-335.

131. M. Grimsditch, Polymorphism in amorphous SiO_2. *Phys. Rev. Lett.* (1984) *52*, 2379.

132. K.H. Smith; E. Shero, The equation of state of polyamorphic germania glass: A two-domain description of the viscoelastic response. *J. Chem. Phys.* (1995) *102*, 6851.

133. L.B. Skinner, A.C. Barnes, P.S. Salmon, et al., Phase separation, crystallization and polyamorphism in the Y_2O_3– Al_2O_3 system. *J. Phys.: Condens. Matter*. (2008) *20*, 205103.

134. B.R. Johnson; W.M. Kriven, Crystallization kinetics of yttrium aluminum garnet ($Y_3Al_5O_{12}$). *J. Mater. Res.* (2001) *1795-1805*.

135. W. Wisniewski, M.J. Pitcher, E. Veron, et al., Macroscopic orientation domains grown via aerodynamic levitation: a path toward single crystals. *Cryst. Growth Des.* (2021) *21*, 3554-3561.

136. https://11bm.xray.aps.anl.gov/science.html.

137. R. Theisen, Quantitative Electron Microprobe Analysis. *Springer-Verlag Berlin Heidelberg GmbH*. (1965).

138. J.A. DeLuca, An introduction to luminescence in inorganic solids. *J. Chem. Educ.* (1980) *57*, 541-545.

139. https://www.horiba.com/gbr/raman-imaging-and-spectroscopy/?gclid=EAIaIQobChMIwaval7Oa9QIVVbLVCh1UhwBrEAAYAiAAEgKhUPD_BwE.

Résumé général

Résumé général

L'objectif initial de ce travail était de synthétiser la mélilite $Y_2Al_3O_{7.5}$, qui a été inspirée par la synthèse de la céramique transparente conductrice mélilite $La_2Ga_3O_{7.5}$ [14] préparée par lévitation aérodynamique (ADL) sans conteneur couplée à un système de chauffage à deux lasers CO_2. Cela nous a intéressé de synthétiser l'hypothétique mélilite $Y_2Al_3O_{7.5}$, car dans cette composition Y^{3+} (0.9 Å) et Al^{3+} (0.39 Å) sont respectivement plus petits que La^{3+} (1.032 Å) et Ga^{3+} (0.47 Å).

En utilisant l'ADL, ~15 mg de petits fragments du mélange homogène compacté Y_2O_3-Al_2O_3 avec la stœchiométrie visée ont été chauffés de la température ambiante à ~2200-2300 °C, le processus de chauffage à cette haute température a été maintenu pendant plusieurs secondes pour obtenir une fusion homogène. Ensuite, les lasers ont été instantanément éteints et la masse fondue a commencé à se solidifier dans le processus de surfusion. Après de nombreux cycles de synthèse, trois billes différentes ont été préparées à partir de la composition $Y_2Al_3O_{7.5}$, leurs résultats de diffraction des rayons X de la poudre (DRX) impliquaient que la bille translucide était du "verre", ce qui a été confirmé comme étant un mélange de matrice vitreuse et de cristaux, la bille brute blanche opaque était de la perovskite $YAlO_3$ biphasique et du corindon Al_2O_3. De façon surprenante, la bille lisse blanche opaque était un grenat avec une structure cristalline de type $Y_3Al_5O_{12}$(YAG), ce qui indique que $Y_2Al_3O_{7.5}$ pourrait être du YAG non-stœchiométrique, c'est-à-dire $Y_{3.2}Al_{4.8}O_{12}$, qui a un rapport atomique Y/Al plus élevé que $Y_3Al_5O_{12}$.

Jusqu'à présent, le YAG non-stœchiométrique présente un grand intérêt car les défauts à l'échelle atomique dans le réseau du grenat peuvent fonctionner comme des centres de luminescence ou de piégeage d'électrons, affectant ainsi les propriétés optiques. Dans la structure du YAG stœchiométrique ($Y_3Al_5O_{12}$), Y occupe uniquement le site dodécaédrique, 40% Al occupent le site octaédrique et 60% Al occupent le site tétraédrique. Dans la structure non-stœchiométrique du YAG, le rapport Y/Al s'écarte de 3/5. Grâce à une simulation atomique et à des expériences réelles, Patel *et al.*[28] ont confirmé que le défaut Y_{Aloct} est le plus susceptible d'exister dans la structure YAG.

Dans ce travail, des efforts ont été faits pour synthétiser une céramique grenat $Y_{3+x}Al_{5-x}O_{12}$ avec une gamme de solutions solides aussi large que possible. Par la méthode de cristallisation directe à partir de la fonte, une seule phase de grenat a été obtenue à partir de compositions $0 \leq x \leq 0{,}29$. Comme la méthode de cristallisation complète du verre s'est

avérée être une voie efficace vers de nouveaux matériaux céramiques[8], nous avons essayé de préciser les conditions de formation des trois différentes phases afin de fabriquer un précurseur de verre par ADL. Pour cela, une série d'expériences de refroidissement a été faite sur la composition $Y_{3.2}Al_{4.8}O_{12.}$ Les échantillons de masses allant de 9 à 39 mg, avec un intervalle de 1 mg, ont été fondus à 2000-2300 °C, puis refroidis après avoir éteint les lasers. Les courbes de refroidissement obtenues ont été enregistrées pour analyser les conditions de formation des trois différents résultats de mise en phase. Trois types de courbes de refroidissement ont été enregistrés, correspondant à trois phases différentes. Le verre présente un processus de refroidissement graduellement décroissant, et les échantillons de $YAlO_3/Al_2O_3$ et de grenat présentent un pic de cristallisation, à partir duquel on peut voir que le grenat cristallise à ~1000 °C et $YAlO_3/Al_2O_3$ à ~ 1200 °C. Si l'on considère la gamme 2100-1300 °C, le grenat était accessible sous 400-550 °Cs^{-1}, les taux de refroidissement supérieurs à 550 °C s^{-1} et inférieurs à 400 °C s^{-1} ont respectivement donné lieu à du verre et à du $YAlO_3/Al_2O_3$ biphasé.

Les expériences de refroidissement ont indiqué que l'amélioration de la vitesse de refroidissement de l'échantillon pourrait être un moyen de fabriquer du verre avec des compositions $x \geq 0,3$. Par conséquent, l'efficacité de refroidissement des gaz Ar, O_2 et He avec différentes densités sur des compositions de 9 mg de $Y_3Al_5O_{12}$ et $Y_{3.2}Al_{4.8}O_{12}$ a été étudiée. Dans ces trois gaz de lévitation, tous les échantillons ont été synthétisés sous forme de verre. Alors que dans la gamme 2100−810 °C, l'He moins dense a donné lieu à ~ 900 °C s^{-1}, O_2 a donné lieu à ~ 450 °C s^{-1} et Ar ~ 350 °C s^{-1}. Malheureusement, la bille d'échantillon ne peut généralement pas être lévitée de manière stable dans l'He, ce qui entraîne une cristallisation hétérogène inattendue. Ainsi, O_2 a été appliqué pour fabriquer du verre avec des compositions $x \geq 0,3$. Finalement, le verre a été obtenu pour $0,3 \leq x \leq 0,4$, et les échantillons ont été préparés dans un four conventionnel à 1100 °C pendant 5h. Les analyses DRX ont confirmé que le grenat a été obtenu.

La structure moyenne des céramiques $Y_{3+x}Al_{5-x}O_{12}$ ($0,3 \leq x \leq 0,4$) a été étudiée par un affinement de structure par la méthod de Rietveld effectué sur les données de diffraction des poudres aux rayons X synchrotron à haute résolution (SPD). Les valeurs de divergence résultantes R_{wp} et la qualité de l'ajustement (*gof*) étaient respectivement inférieures à 10 % et autour de 1, indiquant le processus d'affinement satisfaisant. Le paramètre de maille du grenat pour cette gamme de composition augmente de 12.0071(1) Å à 12.354(1) Å, sa tendance d'évolution est plus élevée par rapport à celles des deux articles de L. Zhu *et al*.[29]

et M. Gervais *et al.*[27] dont le paramètre de maille le plus élevé correspondait presque à la composition x = 0,15.

Grâce à la haute résolution des données SPD, < 1 % en poids de $YAlO_3$ et < 2 % en poids de grenat secondaire, que la diffraction des rayons X (XRD) ne permettait pas de détecter, ont été tracés. L'excès de Y^{3+} a été confirmé par les résultats de l'affinement pour occuper le site octaédrique, et sa concentration dans les YAG $0 \leq x \leq 0,4$ a augmenté linéairement de 0 % à 20 %, correspondant bien à l'évolution théorique. De plus, son incorporation montre un plus grand effet sur l'augmentation de la longueur de liaison des octaèdres, que pour les dodécaèdres ou les tétraèdres.

Comme les expériences de refroidissement de $Y_{3.2}Al_{4.8}O_{12}$ indiquent que le YAG non-stœchiométrique est métastable, la stabilité thermique et la production de décomposition des grenats $Y_{3+x}Al_{5-x}O_{12}$ (x = 0,2 et 0,4) ont été étudiées par traitement thermique ex-situ et in-situ. Après que les grenats $Y_{3+x}Al_{5-x}O_{12}$ (x = 0, 0,2 et 0,4) aient été recuits à 1600 C pendant 12h, le grenat x = 0 était encore du grenat, tandis que x = 0,2 s'est décomposé en YAG et $Y_4Al_2O_9$ stœchiométriques et le grenat x = 0,4 en YAG et $YAlO_3$ stœchiométriques. Grâce à la diffraction des rayons X sur poudre à température variable in situ (VT-XRD), on a constaté que les YAG x = 0,2 et 0,4 se décomposaient à 1350 °C, quelle que soit leur stœchiométrie.

L'observation au microscope électronique à transmission à haute résolution (HRTEM) des échantillons de grenats $Y_{3+x}Al_{5-x}O_{12}$ (x = 0, 0,2 et 0,4), qui ont été soigneusement préparés au préalable sous forme de lamelles par broyage ionique, n'a montré aucun sous-grain ni aucune distorsion des grains, ce qui indique que seul le grenat cristallin était présent dans chaque échantillon. Afin d'observer la substitution locale d'atomes Y en excès, une diffraction d'électrons à zone sélectionnée (SAED) a été réalisée sur $Y_3Al_5O_{12}$, le cristal YAG sélectionné était orienté dans la direction [100]. Dans cette direction, les colonnes atomiques 1Y(dode) + 1 Al (tetra), 2Y(dode) + 2Al (tetra) et 2Al(octa) ont été classées, ce qui a permis au microscope électronique à transmission à balayage (STEM) d'observer clairement le signal atomique des sites octaédriques où l'excès de Y^{3+} pouvait entrer et sans l'interférence des atomes des autres sites polyédriques.

La mesure au microscope électronique à transmission à balayage - champ sombre annulaire à grand angle (STEM-HAADF) a été réalisée sur $Y_{3+x}Al_{5-x}O_{12}$ (x = 0, 0.2 et 0. 4). Il s'agit d'une mesure de contraste atomique (Z) dont le signal de sortie peut être présenté par la fonction exponentielle $I \propto e\rho Z^n$ (où I est l'intensité du signal, e est l'épaisseur de la zone observée, ρ est la densité de l'échantillon, Z est le numéro atomique moyen et n le coefficient exponentiel

variant dans 1,6-2). Comme la zone observée de la lamelle de chaque composition était assez petite, son épaisseur a été considérée comme constante. Dans l'image STEM-HAADF simulée de $Y_3Al_5O_{12}$ qui a été extraite du fichier CIF à l'aide du logiciel JEMS[102], il y a trois types de colonnes atomiques avec une luminosité différente, correspondant aux colonnes atomiques 1Y(dode) + 1Al (tetra), 2Y(dode) + 2Al(tetra) et 2Al(octa). Le STEM-HAADF expérimental montre presque la même situation, à l'exception des différents niveaux de luminosité des trois colonnes atomiques. La luminosité de chaque colonne atomique 2Al(octa) ne montre aucune variation évidente, ce qui implique que seuls les atomes d'Al sont présents sur le site octaédrique. Le profil d'intensité a été extrait des colonnes atomiques 2Y(dode) + 2Al(tetra) et 2Al(octa) disposées périodiquement et les intensités de pic correspondant aux colonnes 2Al(octa) sont presque constantes, ce qui correspond à l'intensité inchangée du signal dans l'image STEM-HAADF et implique que dans l'échantillon réel, seuls les atomes d'Al existent au niveau du site octaédrique. En revanche, les images STEM-HAADF simulées de $Y_{3+x}Al_{5-x}O_{12}$ (x = 0,2 et 0,4) montrent que, lorsque la valeur de x augmente ou que la teneur en Y^{3+} en excès augmente, la luminosité du signal des colonnes atomiques octaédriques devient plus forte. Cependant, dans leurs images STEM-HAADF expérimentales, les intensités de signal des colonnes atomiques octaédriques ne sont pas constantes mais différentes d'une colonne à l'autre, ce qui indique que dans les structures cristallines des YAG non-stœchiométriques x = 0,2 et 0,4, l'excès de Y^{3+} est présent au niveau du site octaédrique et que leurs distributions sont désordonnées. Ce point a été confirmé par les profils d'intensité où les intensités de pic des colonnes atomiques octaédriques sont inégales pour les deux compositions.

La théorie de la fonctionnelle de la densité (DFT) a été effectué sur $Y_{3+x}Al_{5-x}O_{12}$ (x = 0,125, 0,25 et 0,375) qui contient théoriquement respectivement 1, 2 et 3 défauts d'atomes Y pour interpréter les spectres de résonance magnétique nucléaire (RMN) et les résultats de la structure fine d'absorption de rayons X étendue (EXAFS) qui seront présentés dans le contenu suivant. Le calcul DFT sur les spectres RMN prévoit que dans la structure du YAG non-stœchiométrique, l'environnement de coordination de l'oxygène de Y peut être non seulement 8 mais aussi 6. Les déplacements chimiques de YO_8 et YO_6 se situent respectivement à 210-226 ppm et 360-440 ppm, ils peuvent donc être bien résolus.

La RMN ^{89}Y à l'état solide a été réalisée sur $Y_{3+x}Al_{5-x}O_{12}$ ($0 \leq x \leq 0,4$) au champ magnétique, les échantillons ont été dopés avec 0,1 at.% Gd pour raccourcir le temps d'enregistrement des données. Dans les spectres RMN ^{89}Y obtenus, le déplacement chimique typique de YO_8 apparaît à 215 ppm, et un nouveau déplacement chimique apparaît à 410 ppm, qui est

attribué à YO_6. On peut également observer clairement dans les spectres RMN que l'intensité du pic YO_6 devient de plus en plus intense à mesure que la valeur *x* (ou l'excès de Y^{3+}) augmente. Dans le même temps, le pic YO_8 devient de plus en plus large à mesure que les environnements de coordination secondaires autour de YO_8 deviennent plus complexes, ce qui entraîne des composantes contributives plus complexes sous le pic YO_8.

Le spectre de structure fine d'absorption des rayons X étendu (EXAFS) est sensible à l'environnement autour des atomes absorbants. Dans ce travail, la mesure a été effectuée à 17,038 keV de l'arête K de Y, ce qui permet de détecter le premier et le second environnement autour des atomes de Y, aidant ainsi à déterminer l'occupation de Y sur différents sites atomiques. La transformée de Fourier des spectres EXAFS montre un bon accord avec les spectres EXAFS simulés en utilisant les modèles de structure relaxée des calculs DFT qui ont prévu l'existence d'un excès de Y^{3+} au site octaédrique. La diminution de l'intensité du pic et le déplacement du pic impliquent que les atomes de Y sont distribués de manière désordonnée dans la structure cristalline du grenat.

Les propriétés de luminescence ont été étudiées sur du YAG stœchiométrique $Y_3Al_5O_{12}$ (appelé s-YAG) et du YAG non-stœchiométrique $Y_{3.2}Al_{4.8}O_{12}$ (appelé ns-YAG) dopés à 0,5 at.% de Mn4+, 1 at.% de Dy^{3+} et 5 at.% de Ce^{3+} et codopés à 20 at.% de Yb^{3+}-*n* Er^{3+} (*n* = 0,5, 1 et 2) afin d'étudier si la non-stœchiométrie a une influence. La structure fine des spectres d'émission normalisés est l'un des indices permettant d'évaluer les performances d'émission. Avec un dopage unique de Mn^{4+}, Ce^{3+} et Dy^{3+}, la forme du pic et le rapport d'intensité entre les YAGs s- et ns- sont presque les mêmes, alors qu'avec un codopage Yb^{3+}/Er^{3+}, ils semblent différents. Par conséquent, l'influence de la non-stœchiométrie sur les performances de luminescence a été principalement étudiée sur les YAGs dopés aux terres rares de grande taille Ce^{3+} et de petite taille Yb^{3+}/Er^{3+}.

Les spectres d'émission normalisés des YAGs s- et ns dopés au Ce^{3+} montrent que leurs larges bandes d'émission entre 455 et 750 nm se chevauchent presque. Les spectres d'émission normalisés des YAGs s- et ns co-dopés par Yb^{3+}/Er^{3+} montrent des bandes d'émission vertes et rouges entre 520-570 nm et 640-700 nm respectivement. Dans ces deux bandes d'émission, les deux pics les plus intenses du ns-YAG se déplacent vers des longueurs d'onde inférieures à celles du s-YAG. Les deux échantillons émettent ainsi des couleurs différentes, comme le montre le diagramme de chromaticité de la CIE, dans lequel le s-YAG présente une couleur jaune tandis que le ns-YAG présente une émission verte. Nous avons essayé de l'expliquer du point de vue de l'occupation atomique. L'affinement

Rietveld pour les données XRD à balayage lent des s- et ns-YAGs dopés à 5 at.% de Ce^{3+} montre que Ce^{3+} occupe uniquement le site dodécaédrique. En utilisant la même analyse structurelle sur les données SPD, on a constaté que les Yb^{3+}/Er^{3+} n'occupent que le site dodécaédrique dans la structure s-YAG, mais ils occupent non seulement le site dodécaédrique, mais également le site octaédrique dans la structure ns-YAG. Cela implique que l'excès de Y^{3+} dans le ns-YAG aide à introduire les ions Yb^{3+}/Er^{3+} dans un nouveau champ cristallin, ce qui fait que l'échantillon ns-YAG présente une couleur d'émission différente de celle du s-YAG.

Les concentrations de 0,5 %, 1 % et 2 % d'Er^{3+} ont été introduites dans des YAGs s- et ns-dopés à 20 % d'Yb afin d'identifier un niveau de dopage Er^{3+} approprié pour modifier l'efficacité d'émission. Il est apparu que la concentration de 1 at.% d'Er^{3+} conduit à l'intensité d'émission la plus élevée du spectre, et qu'une augmentation supplémentaire du niveau de dopage Er^{3+} entraîne une diminution de l'intensité d'émission. Il a également été observé que la modification de la concentration d'Er^{3+} n'a aucune influence sur la couleur d'émission du s-YAG, mais modifie légèrement la couleur d'émission du ns-YAG, ce qui pourrait être attribué à la redistribution des centres d'émission d'Er^{3+} dans la structure du ns-YAG sur les sites dodécaédriques et octaédriques. L'inhomogénéité locale a été confirmée par les spectres d'émission incohérents réalisés sur les deux côtés d'un disque d'échantillon de ns-YAG codopé à 20 % de Yb^{3+}-2 % d'Er^{3+}, mais cela n'est pas évident pour le s-YAG. Les méthodes de cristallisation directe et de cristallisation en verre intégral ont été appliquées avec succès à d'autres nouveaux grenats de type $A_3B_5O_{12}$, par exemple le grenat de gallium de gadolinium (GGG) et le grenat de gallium de samarium (SGG) non-stœchiométriques ont été synthétisés dans ce travail et développés par un autre étudiant en doctorat.

Des tentatives ont été faites afin de synthétiser du verre YAG en augmentant la vitesse de refroidissement de la bille échantillon en utilisant différents gaz de lévitation. Les données DRX des "verres" de compositions $Y_3Al_5O_{12}$ et $Y3.2Al_{4.8}O_{12}$ synthétisés dans Ar, O_2 et He impliquent que la partie cristalline dans la bille diminue lorsque la vitesse de refroidissement augmente. Les images de microscopie électronique à balayage (MEB) des billes d'échantillon polies préparées dans Ar montrent que la surface de la bille a cristallisé et que le volume est distribué avec des gouttelettes. La bille refroidie à un taux de refroidissement plus élevé a une surface cristallisée plus fine et moins de gouttelettes. Ce phénomène est plus évident pour la composition $Y_3Al_5O_{12}$ que pour $Y_{3.2}Al_{4.8}O_{12}$. Enfin, les gouttelettes sont à peine présentes sur la matrice vitreuse pour la composition $Y_3Al_5O_{12}$. Les gouttelettes dans la bille ont été confirmées comme étant des cristaux de YAG par les spectres Raman et la

cartographie. Ces résultats peuvent nous conduire à synthétiser du verre pur YAG qui pourrait présenter des propriétés optiques et des applications intéressantes.

Résumé du chapitre 1

Ce chapitre passe en revue les travaux précédemment publiés sur le matériau $Y_3Al_5O_{12}$(YAG) qui a été synthétisé à partir du système Y_2O_3-Al_2O_3. Le YAG a une structure de grenat cubique avec un paramètre de maille a = 12,008 Å et un groupe spatial *Ia-3d* (n° 230), sa cellule unitaire contient 160 atomes, dont 24 Y se situent au site de Wyckoff *c* à 8 coordonnées, 16 Al au site de Wyckoff *a* à 6 coordonnées, 24 Al au site *d* à 4 coordonnées et 96 O au site de Wyckoff *h*. $Y_3Al_5O_{12}$ est l'une des phases de la famille des grenats $A_3B_5O_{12}$, d'autres grenats comme $Gd_3Ga_5O_{12}$, $Y_3Fe_5O_{12}$ $Sm_3Al_5O_{12}$, *etc*. ont également été signalés en raison de leurs propriétés optiques, magnétiques ou thermométriques.

Au cours de la synthèse du YAG, les impuretés $YAlO_3$ orthorhombique et $Y_4Al_2O_9$ monoclinique peuvent se former si les conditions de réaction ne sont pas appropriées. D'après les travaux de synthèse de la céramique Nd:YAG de A. Ikesue *et al*.[45], les auteurs ont synthétisé le grenat par la méthode de frittage à haute température en utilisant Y_2O_3, Al_2O_3 et Nd_2O_3 comme matières premières. Dans leur travail, YAG, l'eutectique $YAlO_3$/Al_2O_3 et $Y_4Al_2O_9$ pouvaient se former, où $Y_4Al_2O_9$ se forme dans la gamme 1100-1400 °C, $YAlO_3$ dans la gamme 1200-1600 °C et YAG à des températures supérieures à 1300 °C. Par conséquent, à des températures inférieures à 1600 °C, des phases mixtes sont probablement obtenues, et une phase YAG pure peut être obtenue à une température supérieure à 1600 °C.

Le matériau YAG peut se présenter sous la forme de monocristaux, de céramiques transparentes et de poudres en fonction de leurs applications. Le monocristal de YAG dopé aux terres rares est appliqué pour les lasers à l'état solide, par exemple Nd:YAG et Er:YAG. La céramique transparente Nd:YAG rapportée par A. IKesue *et al*.[45] a été synthétisée par réaction à l'état solide à haute température avec du silicate d'éthyle comme aide au frittage, elle présente une faible perte par diffusion optique et sa dureté, ses comportements d'absorption et de fluorescence et ses caractéristiques laser sont comparables à ceux du monocristal Nd:YAG qui est généralement préparé par la méthode de Czochralski. Les méthodes chimiques humides comme le sol-gel, la co-précipitation et les méthodes

solvothermiques sont généralement utilisées pour synthétiser les poudres de YAG destinées aux applications de phosphores.

La lévitation aérodynamique (ADL) couplée à deux lasers CO_2 fonctionne sans conteneur grâce au gaz porteur, ce qui permet d'éviter la cristallisation hétérogène si l'échantillon entre en contact avec la buse, sa température de chauffage est disponible entre RT-3000 °C. Lorsqu'il est intégré à un instrument de caractérisation structurelle, tel que la diffusion des rayons X aux petits angles (S/WAXS), la diffraction des rayons X ou la diffraction des neutrons, il permet d'étudier l'évolution dynamique des matériaux.

La technique ADL a été exclusivement utilisée pour synthétiser des oxydes métalliques, des alliages et des semi-conducteurs, en utilisant cette méthode au CEMHTI. Les céramiques transparentes YAG-4%Si, $BaGa_4O_7$ et $La_2Ga_3O_{7.5}$, *etc*. ont été synthétisées par cristallisation directe, tandis que les verres $SrREGa_3O_7$, YAG-Al_2O_3 et $BaAl_4O_7$ ont été synthétisés après un processus de refroidissement rapide et ont ensuite été entièrement cristallisés dans le four pour fabriquer des céramiques. Les méthodes de cristallisation directe et de cristallisation complète des verres réalisées précédemment dans la synthèse des matériaux ont ouvert la voie à ce travail pour synthétiser le YAG non-stœchiométrique.

Résumé du chapitre 2

La céramique transparente $La_2Ga_3O_{7.5}$ publiée par J. Fan *et al*.[14] en 2020 a été synthétisée par cristallisation directe à partir de la masse fondue en utilisant la technique ADL au CEMHTI. Ce travail a commencé avec un composé cible hypothétique mélilite $Y_2Al_3O_{7.5}$, comme possible analogue de $La_2Ga_3O_{7.5}$. De plus, l'ADL est connue comme une méthode puissante pour obtenir du verre et des matériaux céramiques métastables grâce au processus de refroidissement rapide et à la synthèse sans contact. En utilisant cette technique, la céramique pourrait être obtenue directement et indirectement préparée en cristallisant complètement le verre.

Il est intéressant de noter qu'en utilisant l'ADL, $Y_2Al_3O_{7.5}$ peut être synthétisé en verre, grenat ou $YAlO_3$/Al_2O_3 biphasique, mais pas en mélilite. Le diagramme XRD de la phase grenat a été indexé par les diffractions de Bragg de l'$Y_3Al_5O_{12}$ cubique (groupe spatial *Ia-3d*), ce qui indique que cette phase pourrait en fait être du YAG $Y_{3.2}Al_{4.8}O_{12}$ non stœchiométrique. Dans la structure YAG, 60 % et 40 % des atomes d'Al sont respectivement sur des sites tétraédriques et octaédriques, tous les atomes de Y occupent le site à 8 coordonnées. Par le biais de simulations informatiques et d'expériences réelles, Patel *et al*.[28] en 2008 ont confirmé

que la non stœchiométrie la plus possible dans la structure YAG est Y^{3+} à 6-coordinations. Cela nous a motivés à étudier davantage la structure du grenat $Y_2Al_3O_{7.5}$ et nous avons essayé de synthétiser le grenat $Y_{3+x}Al_{5-x}O_{12}$ avec une valeur de *x* aussi grande que possible, car l'excès de Y^{3+} a été reconnu comme centre de luminescence et de piège à électrons influençant les propriétés optiques. En utilisant la méthode de cristallisation directe, des grenats $Y_{3+x}Al_{5-x}O_{12}$ ($0 \leq x \leq 2,9$) ont été synthétisés.

Les expériences de refroidissement sur la composition $Y_{3.2}Al_{4.8}O_{12}$ ($Y_2Al_3O_{7.5}$) ont confirmé que le fait de rendre le taux de refroidissement aussi élevé que possible pouvait aider à synthétiser du grenat ou du verre avec $x > 0,29$. Ceci a été réalisé en utilisant un gaz de lévitation moins dense que O_2, et a permis à fabriquer des verres pour des compositions $0,3 \leq x \leq 0,4$. Ces échantillons de verre ont été entièrement cristallisés dans le four à 1100 °C pendant 5h, donnant ainsi la phase grenat.

L'affinement Rietveld sur les données SPD de $Y_{3+x}Al_{5-x}O_{12}$ ($0 \leq x \leq 0,4$) implique que le paramètre de réseau de ces grenats évolue linéairement de 12,00710(1) Å à 12,13542(1) Å, et que 0-20 at.% de Y^{3+} en excès entrent dans le site octaédrique. La mesure STEM-HAADF a détecté l'existence d'un excès de Y^{3+} au niveau du site octaédrique dans les YAG non-stœchiométriques $x > 0$ en montrant un signal de contraste Z irrégulier et un profil d'intensité irrégulier extrait des colonnes atomiques octaédriques par rapport aux YAG stœchiométriques $x = 0$. Le calcul DFT a prévu le défaut Y dans les structures YAG $x = 0,125$, 0,25 et 0,375 qui pourraient contenir respectivement un, deux et trois défauts Y. Le calcul sur le déplacement des spectres RMN a montré que le défaut Y est une caractéristique importante de la structure YAG. Le calcul du déplacement chimique de la RMN implique l'existence de YO_6 et il peut être bien séparé du YO_8 typique. La RMN à l'état solide ^{89}Y mesurée dans un champ magnétique pour des grenats $Y_{3+x}Al_{5-x}O_{12}$ ($0 \leq x \leq 0,4$) dopés au Gd à 0,1at.% montre le déplacement chimique typique de YO_8 apparaissant à environ 215 ppm, et un nouveau déplacement chimique attribué à YO_6 à environ 410 ppm, en accord avec le calcul DFT. Le pic de YO_6 devient plus intense lorsque la valeur de *x* augmente, tandis que le pic de YO_8 devient plus large, car l'introduction progressive d'un excès de Y^{3+} sur le site octaédrique rend l'environnement de coordination secondaire de Y^{3+} à 8 coordonnées plus complexe. Le résultat de l'EXAFS confirme l'existence d'un excès de Y^{3+} et sa distribution dans la structure du YAG est désordonnée. Le résultat VT-XRD indique que le grenat $Y_{3.2}Al_{4.8}O_{12}$ est métastable, et bien que le grenat $Y_{3.4}Al_{4.6}O_{12}$ contienne plus d'excès de Y^{3+}, il commence aussi à se décomposer à 1350 °C comme le grenat $Y_{3.2}Al_{4.8}O_{12}$.

Résumé du chapitre 3

Le grenat $Y_3Al_5O_{12}$ (YAG) est un matériau hôte important pour les applications optiques, par exemple le Nd : YAG et le Er:YAG peuvent être utilisés comme lasers à l'état solide. Le Ce:YAG est utilisé pour les phosphores jaunes, et sa combinaison avec les LED bleues permet d'obtenir des LED blanches. Comme les terres rares de dopage sont importantes, elles sont généralement introduites dans le site dodécaédrique par Y^{3+}. Comme indiqué dans le chapitre 2, le YAG non-stœchiométrique se forme à partir d'une composition riche en Y, son excès de Y^{3+} tend à occuper le site octaédrique, ainsi les terres rares pourraient être introduites dans le site octaédrique et donner lieu à des propriétés optiques différentes de celles du YAG stœchiométrique. Dans ce travail, nous étudions principalement les grenats stœchiométriques ($Y_3Al_5O_{12}$) et non-stœchiométriques ($Y_{3.2}Al_{4.8}O_{12}$) dopés par Ce^{3+} et codopés par Yb^{3+}/Er^{3+}, car Ce^{3+} et Yb^{3+}/Er^{3+} se situent aux deux extrémités des lanthanoïdes du tableau périodique, avec des radiums significativement différents.

Les spectres d'émission normalisés des YAGs s et ns dopés à 5 at.% Ce^{3+} montrent que leurs bandes d'émission à 455-750 nm se chevauchent, ce qui indique des performances optiques similaires entre les deux échantillons de YAG. En revanche, les spectres d'émission normalisés pour les YAGs s- et ns co-dopés à 20 at.% Yb^{3+}-2 at.% Er^{3+} montrent des bandes d'émission vertes et rouges à 520-570 nm et 640-700 nm respectivement. Les deux pics les plus intenses des deux bandes d'émission du ns-YAG se déplacent vers des longueurs d'onde inférieures à celles du s-YAG, ce qui fait que le ns-YAG émet une couleur verte alors que le s-YAG émet une couleur jaune. Pour expliquer ce phénomène, une analyse structurelle des YAGs s- et ns dopés à 5 at.% Ce^{3+} et 20 at.% Yb^{3+}-2 at.% Er^{3+} a été réalisée par affinement Rietveld. Il en ressort que dans les structures cristallines des YAGs s- et ns- le Ce^{3+} occupe uniquement le site dodécaédrique, ce qui fait que les deux YAGs produisent des spectres d'émission similaires. Yb^{3+}/Er^{3+} occupent uniquement le site dodécaédrique de la structure s-YAG, mais ils occupent non seulement les sites dodécaédriques mais aussi les sites octaédriques, ce qui explique la différence de performance optique entre les YAGs s- et ns dopés par Yb^{3+}/Er^{3+}.

Afin de trouver le niveau de dopage optimal d'Yb^{3+} et d'Er^{3+}, la concentration d'Yb^{3+} a été fixée à 20 at.% et celle d'Er^{3+} à 0,5 at.%, 1 at.% et 2 at.%. Les spectres d'émission montrent que 1 at.% d'Er^{3+} donne l'intensité d'émission la plus élevée, une concentration plus élevée d'Er^{3+} provoque un effet d'extinction parmi les nombreux activateurs Er^{3+}.

Une inhomogénéité locale a été détectée par les spectres d'émission incohérents réalisés sur les deux côtés d'un disque d'échantillon ns-YAG codopé à 20 at.% Yb^{3+}-2 at.% Er^{3+}, mais cela n'est pas évident pour le s-YAG codopé à 20 at.% Yb^{3+}-2 at.% Er^{3+}. Les méthodes de cristallisation directe et de cristallisation en verre intégral ont été appliquées avec succès à d'autres nouveaux grenats de type $A_3B_5O_{12}$, par exemple le grenat de gallium de gadolinium (GGG) et le grenat de gallium de samarium (SGG) non-stœchiométriques ont été synthétisés dans ce travail.

Résumé du chapitre 4

Le cristal et le verre de YAG pur sont technologiquement importants en raison de leurs applications potentielles comme phosphores et scintillateurs, *etc.*, alors que la synthèse vers ces deux matériaux rencontre des difficultés pour exclure les inclusions inattendues. La synthèse du YAG pur peut être interrompue par la formation d'une phase secondaire de $Y_4Al_2O_9$ ou d'une phase biphasique $YAlO_3/Al_2O_3$, qui non seulement réduit la pureté de la phase mais empêche également l'échantillon de devenir transparent pour les applications de laser à l'état solide. En ce qui concerne la synthèse de verre YAG pur, il est bien connu que la bille de verre YAG préparée par ADL semble translucide. Ceci peut être expliqué par la surface de la bille qui est parfois cristallisée et, plus important encore, par de nombreuses inclusions sphériques incorporées dans la matrice vitreuse, ces inclusions sphériques peuvent être amorphes[20] ou cristallisées[19]. L'étude montre qu'une concentration plus élevée d'Al_2O_3 dans l'échantillon est une solution pour améliorer la transparence de l'échantillon de verre d'yttrium et d'aluminium, mais cela fait que la composition de l'échantillon s'écarte de celle du YAG. Les expériences de refroidissement réalisées sur la composition $Y_{3.2}Al_{4.8}O_{12}$ par ADL dans ce travail déterminent que le taux de refroidissement est critique pour la formation de verre YAG pur, c'est-à-dire que le verre YAG préfère un taux de refroidissement plus élevé que le YAG pur et le $YAlO_3/Al_2O_3$ biphasé[18].

Les données XRD du verre $Y_{3.2}Al_{4.8}O_{12}$ synthétisé dans Ar dans ce travail impliquent que la bille contient principalement des phases cristallines de verre, YAG et $YAlO_3$. L'observation au MEB de la bille polie montre une fine couche cristalline sur sa surface et de nombreuses gouttelettes distribuées dans la matrice vitreuse au sein du volume. Il est intéressant de noter que les deux constituants du volume ont une composition identique, ce qui nous a intéressé pour clarifier leur différence en plus de leur aspect, par exemple, la cristallinité. Les spectres Raman et la cartographie déterminent que les gouttelettes sont en fait des cristaux de YAG.

Cela indique que le taux de refroidissement doit être suffisamment élevé pour obtenir du verre YAG pur. Sachant qu'un gaz de lévitation moins dense peut faciliter la convection dans la masse fondue pendant le chauffage à haute température et accélérer le processus de surfusion[59], les gaz de lévitation O_2 et He ont également été utilisés en plus de Ar. La masse de l'échantillon étant importante pour la vitesse de refroidissement, la masse de toutes les billes de composition $Y_3Al_5O_{12}$ et $Y_{3.2}Al_{4.8}O_{12}$ a été contrôlée à 9 mg. Les taux de refroidissement ont été calculés et représentés par $\Delta T/\Delta t$ dans la gamme 2000−810 °C, et la séquence des taux de refroidissement correspondant aux trois gaz de lévitation est He (~ 900 °C s^{-1}) > O_2 (~ 450 °C s^{-1}) > Ar (~ 350 °C s^{-1}). Les données XRD indiquent qu'un taux de refroidissement plus élevé entraîne une diminution de la phase cristalline dans la bille de l'échantillon. L'image SEM du verre $Y_3Al_5O_{12}$ synthétisé dans l'He permet à peine de voir les gouttelettes. Cela signifie que la fabrication de verre YAG pur par ADL est prometteuse.

Weiwei CAO

Synthèse et caractérisation d'oxydes de grenat fortement non-stœchiométriques

Dans ce travail, des céramiques de grenat fortement non-stœchiométrique $Y_{3+x}Al_{5-x}O_{12}$ ($0 \le x \le 0,4$) ont été synthétisées en combinant les méthodes de cristallisation directe à partir du liquide fondu et de cristallisation du verre. Les expériences de refroidissement menées par lévitation aérodynamique (ADL) sur la composition $Y_{3.2}Al_{4.8}O_{12}$ ont impliqué que la phase grenat était accessible sous des vitesses de refroidissement de 400-550 °C s^{-1}, les taux de refroidissement > 550 °C s^{-1} et < 400 °C s^{-1} produisent respectivement des matériaux vitreux et des céramiques $YAlO_3/Al_2O_3$ biphasées. Les ns-YAGs $Y_{3.2}Al_{4.8}O_{12}$ et $Y_{3.4}Al_{4.6}O_{12}$ ont été déterminés, par des expériences de traitement thermique in-situ et ex-situ, comme métastables et décomposés à 1350 °C. L'excès de Y3+ dans les $Y_{3+x}Al_{5-x}O_{12}$ ($0 \le x \le 0,4$) YAGs a été déterminé pour occuper le site Al16a par affinement de Rietveld sur les données SPD à haute résolution, et sa concentration s'est avérée augmenter linéairement de 0 à 20 at. %, ce qui entraîne une expansion linéaire des paramètres du réseau des YAGs de 12,0071(1) Å à 12,1354(1) Å. La présence d'un excès de Y^{3+} au site *16a* a également été détectée par STEM, en montrant le signal de contraste Z de l'imagerie HAADF et le profil d'intensité. Le calcul DFT sur les modèles de structure ns-YAG a envisagé que les atomes Y se situent dans les environnements de coordinance 8- et 6-oxygène. La RMN à l'état solide de ^{89}Y a déterminé le déplacement chimique de YO_8 à 215 ppm et un nouveau déplacement chimique à 410 ppm pour YO_6. La mesure EXAFS a confirmé l'existence de Y^{3+} à 6 coordinance en identifiant les longueurs de liaison pour YO_6 qui diffèrent des deux longueurs de liaison pour YO_8 et la diminution de la coordinance moyenne de l'yttrium, *etc*.
Les terres rares Y^{3+}/Er^{3+} dopantes pour évoquer les propriétés de luminescence occupent uniquement le site dodécaédrique *24c* dans le s-YAG, alors qu'elles ont été introduites à la fois dans les sites dodécaédriques *24c* et octaédriques *16a* dans le ns-YAG par un excès de Y^{3+}, créant ainsi un nouveau chemin de transfert d'énergie $Y^{3+} \rightarrow Er^{3+}$ et modifiant la fréquence d'émission. L'inhomogénéité à micro-échelle causée par les ions Y^{3+}/Er^{3+} était prononcée dans le cas du ns-YAG par rapport au s-YAG. Le grand ion Ce^{3+} occupe uniquement le site dodécaédrique dans les s- et ns-YAGs, ce qui entraîne une fréquence d'émission inchangée.
Ce travail sur les ns-YAGs et la synthèse d'autre oxydes de grenat dans de travail devait servir de guide pour les futurs travaux portant sur l'amélioration et l'étude d'autre grenat fortement non stœchiométriques.

Mots clés : YAG, non-stœchiométrique, propriétés optiques

Synthesis and characterization of highly non-stoichiometric garnet oxides

In this work, highly non-stoichiometric $Y_{3+x}Al_{5-x}O_{12}$ ($0 \le x \le 0.4$) garnet ceramics were synthesized by combining direct crystallization from melt and glass crystallization methods. Cooling experiments conducted by aerodynamic levitation (ADL) on $Y_{3.2}Al_{4.8}O_{12}$ composition implied that garnet phase was accessible under cooling rates 400-550 °C s^{-1}, cooling rate > 550 °C s^{-1} and < 400 °C s^{-1} respectively produce glassy materials and biphasic $YAlO_3/Al_2O_3$. Tthermal stability of $Y_{3.2}Al_{4.8}O_{12}$ and $Y_{3.4}Al_{4.6}O_{12}$ ns-YAGs were studied by in-situ and ex-situ heating treatment experiments, the two metastable ns-YAGs decomposed at 1350 °C.
The excess Y^{3+} in $Y_{3+x}Al_{5-x}O_{12}$ ($0 \le x \le 0.4$) YAGs was determined to occupy Al_{16a} site by Rietveld refinement on high-resolution SPD data, and its concentration was found to increase linearly from 0 to 20 at. %, this caused the lattice parameters of YAGs to linearly expand from 12.0071(1) Å to 12.1354(1) Å. The presence of excess Y^{3+} at *16a* site was also detected by STEM, at the atomic scale, by showing Z-contrast signal from HAADF imaging and intensity profile. DFT computing on ns-YAG structure models envisaged that Y atoms locate at 8- and 6-oxygen coordinating environments. ^{89}Y solid-state NMR determined the YO_8 chemical shift at 215 ppm and a new chemical shift at 410 ppm for YO_6. EXAFS confirmed the existence of 6-coordinate Y by identifying the bond lengths for YO_6 differing from the two bond lengths for YO_8 and the decrease of average yttrium coordination, *etc*.
Rare earths Y^{3+}/Er^{3+} dopants for evoking luminescence properties only occupy the *24c* dodecahedral site in s-YAG, while they were introduced to both *24c* dodecahedral and *16a* octahedral sites in ns-YAG by excess Y^{3+}, creating new $Y^{3+} \rightarrow Er^{3+}$ energy transfer path and altering the emission frequency. Micro-scale inhomogeneity caused by Y^{3+}/Er^{3+} ions was pronounced in ns-YAG compare to s-YAG. The large Ce^{3+} ion only occupy dodecahedral site in both s- and ns-YAGs, resulting unchanged emission frequency.
The work on ns-YAGs and the synthesis of other garnet oxides presented in this work could be a guidance for further studying and improving other non-stoichiometric garnet materials.

Keywords : YAG, non-stoichiometric, optical properties

CEMHTI-CNRS UPR3079
1D Avenue de la Recherche Scientifique
45071 Orléans Cedex 2